CVD synthesis of carbon nanostructures and their applications as supports in catalysis : selective hydrogenation of cinnamaldehyde over Pt-Ru bimetallic catalysts, Electrocatalysts for electrodes in polyelectrolyte membrane fuel cells

Jacques Teddy

THESIS

Presented to obtain

The Doctor of Philosophy (Ph.D) degree from

TOULOUSE UNIVERSITY

INSTITUT NATIONAL POLYTECHNIQUE DE TOULOUSE

Specialized in: Organometallic and Coordination Chemistry

By

Jacques TEDDY

CVD SYNTHESIS OF CARBON NANOSTRUCTURES AND THEIR APPLICATIONS AS SUPPORTS IN CATALYSIS:

Selective hydrogenation of cinnamaldehyde over Pt-Ru bimetallic catalysts
Electrocatalysts for electrodes in polyelectrolyte membrane fuel cells

Defense planed on the 06 of November 2009

Reporters:	**Joël Barrault**	Director of research CNRS, LACCO, Poitier.
	Bernard Coq	Director of research CNRS, ENSCM, Montpellier.
Members:	**Philippe Kalck**	Professor, ENSIACET/INP, Toulouse.
	Philippe Serp	Professor, ENSIACET/INP, Toulouse.
	Joaquim Luis Faria	Professor, University of Porto, Portugal.
	Claudio Bianchini	Dr Claudio Bianchini, ICCOM-CNR, Florence.
Invited members:	**Karine Philippot**	HDR (CR1), LCC, Toulouse.

Abstract

In this work, we describe the synthesis, structure, physical properties and some applications in catalysis of previously known carbon allotropes, and recently discovered carbon nanostructure (Chapter I). First, FB-OM-CVD deposition was used for metal or metal oxide deposition on metal oxide supports like alumina or silica, leading to the production of supported catalysts. The resulting material was used as catalyst for catalytic chemical vapor deposition of carbonaceous nanostructures i.e single- and multi-walled carbon nanotubes (SWCNTs, MWCNTs), carbon nanofibers (CNFs), and nitrogen doped carbon nanotubes (N-MWCNTs) and nanofibers (N-CNFs) (Chapter II). After catalyst removal by a H_2SO_4 or NaOH treatments and carboxylic surface group generation by a HNO_3 treatment in the case of MWCNTs and CNFs, the carbon nanostructures were used as supports for heterogeneous catalysis. The hydrogenation of cinnamaldehyde was used as a model reaction to compare the performance of different bimetallic Pt-Ru catalysts as a function of the nature of the support. Detailed parametric studies as well as the effect of a heat treatment on the performance improvement of the Pt-Ru/MWCNT catalyst are presented. An explanation for the increase of performances upon heat treatment will be proposed after HREM, EDX, EXAFS and WAXS characterization of the catalyst (Chapter III). The prepared carbon nanostructures were also tested as supports for Pd based electrocatalysts for direct alkaline fuel cells applications in both cathodes for the ORR reaction and anodes for alcohols oxidation.

Keywords

Chemical vapor deposition, nanoparticles, catalysis, single- multi- walled carbon nanotubes, nanofibers, selective hydrogenation, cinnamaldehyde, direct alcaline fuel cells.

Résumé

Dans ce travail, nous décrivons la méthode de synthèse, la structure, les propriétés et quelques applications en catalyse de différentes formes du carbone, en particulier les nanostructures carbonées (Chapitre I). La technique de dépôt chimique en phase vapeur en réacteur à lit fluidisé a été utilisée pour le dépôt de métaux ou d'oxydes de métaux sur des supports comme l'alumine ou la silice. Le matériau résultant est utilisé comme catalyseur pour la synthèse de diverses nanostructures carbonés par dépôt chimique en phase vapeur catalytique : nanotubes de carbone mono- et multi-feuillets (SWCNTs, MWCNTs), nanofibres de carbone (CNFs), et des nanotubes de carbone (N-MWCNTs) ou nanofibres (N-CNFs) dopés en azote (Chapitre II). Après dissolution du catalyseur par un traitement à l'acide sulfurique ou par la soude, suivit dans le cas des MWCNTs et CNFs, par un traitement à l'acide nitrique pour générer des fonctions carboxyliques de surface, les nanostructures carbonées ont été utilisées comme supports de catalyseurs. L'hydrogénation du cinnamaldehyde a été choisit comme réaction modèle pour comparer les performances de différents catalyseurs bimétalliques de Pt-Ru en fonction de la nature du support. Une étude paramétrique détaillée ainsi que l'étude de l'effet d'un traitement thermique sur l'amélioration des performances du catalyseur de Pt-Ru/MWCNT sont présentés. Une explication de l'augmentation des performances catalytiques sera proposée après analyses du catalyseur par HREM, EDX, EXAFS et WAXS (Chapitre III). Les nanostructures carbonées préparées seront également testées comme supports conducteurs d'électrocatalyseurs pour l'élaboration d'électrodes de ''polyelectrolyte membrane fuel cells'' (PEMFC).

Mots clés

Dépôt chimique en phase vapeur, nanoparticules, catalyse, nanotubes de carbone mono- multi-feuillets, nanofibres, hydrogénation sélective, cinnamaldehyde, pile à combustible.

Table of contents

General conclusion and perspective

I-Carbon nanostructures for catalysis

Chapter I-Carbon nanostructures for catalysis

In 1959 Richard Feynman asked, “What could we do with layered structures with just the right layers? What would the properties of materials be if we could really arrange the atoms the way we want them?” He also noted that, they would be very interesting to investigate theoretically...I can hardly doubt that when we have some control of the arrangement of things on a small scale we will get... greater range of possible properties that substances can have, and of different things that we can do.” He also added: ‘’There's Plenty of Room at the Bottom [1]!’’ Substantial advances in fabrication and related technologies since 1959 have made it possible to manipulate matter on an atomic scale. Nanotechnology was born. A nanostructure is something or an atomic structure that has a physical dimension smaller than 100 nanometers, ranging from clusters of atoms or molecules (1 nm) to dimensional layers.

I-1-Different structures of carbon

Carbon is one of the most abundant elements in nature. It forms many allotropes, depending on its specific hybridization, and bonding to surrounding atoms. Carbon with sp^3 hybridization will form a tetrahedral lattice, thus giving rise to diamond. Carbon with sp^2 hybridization will form either graphite (arranged in hexagonal sheets), buckminsterfullerene (60 carbon atoms forming a sphere), or carbon nanotubes (long hollow tubes of carbon) depending on the conditions in which it is formed.

Some allotropes of carbon, such as graphite and diamond, occurred naturally and were known from ancient times; others such as buckyballs and nanotubes, were discovered 10-20 years ago and are just being manufactured and characterized [2]. Carbon's abundance and versatility makes it one of the most studied materials in nanotechnology research, and its allotropes have a wide range of useful properties, such as high tensile strength, thermal and electric conductivity and high melting points. Amorphous carbon and graphite are the two most common allotropes, and they make up the majority of natural carbon compounds such as coal and soot.

In the following section we describe those allotropes and the essential properties of each of them.

I-1-1-Amorphous carbon

Amorphous carbon, like most glasses has no organized crystal structure (Fig. 1). This carbon form is visually highly disordered and lacks structural integrity. The disorder allows it to have many available bonds and is responsible for building more complex carbon based molecules. Amorphous carbon forms at the edges or is the residue of other elemental compounds.

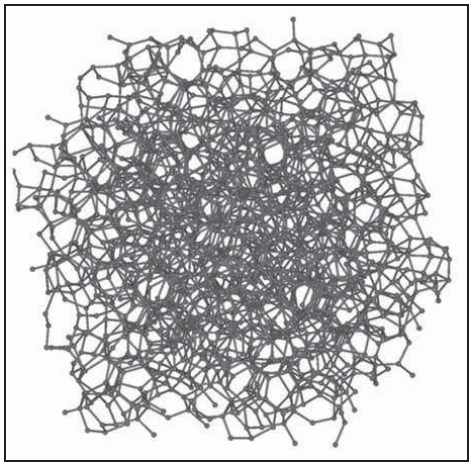

Figure 1: Coke (disordered carbon)

I-1-2-Graphite

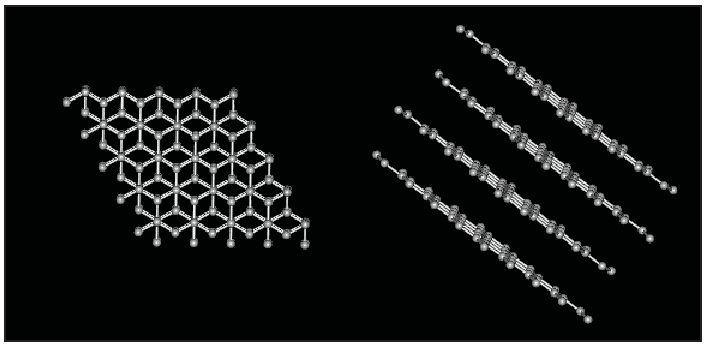

Figure 2: Structure of graphite from greek "graphein" = write (pensil, ink of china)

In 1924, J. D. Bernal successfully identified the crystal structure of graphite: carbon atoms arranged in layers (Fig. 2), each layer has strong bonds holding it together, but the layers don't bond strongly, and can be easily cleaved [3]. In graphite, sp^2 hybridization takes place, where each atom is connected evenly to three carbons (120°) in the {xy}-plane, and a weak π-bond is present along the z-axis. The C–C sp^2 bond length is 0.142 nm. The sp^2 set forms a hexagonal lattice (honeycomb) typical of a sheet of graphite with $P6_3/mmc$ space group, and ABAB stacking sequence of the layers where the plan B is shifted of $a/\sqrt{3}$ relative

to the A plan. The p_z orbital is responsible for a weak van der Waals bond, between the sheets. The spacing between these carbon layers is 0.335 nm. The free electrons in the p_z orbital move within this cloud and are no longer local to a single carbon atom (i.e. they are delocalized) giving graphite the electrical conductivity property.

A beta form of graphite was later discovered. The beta graphite-3R is rhombohedral with ABCABC stacking sequence of the layers. The beta form is unstable and reverts to the alpha form when heated above 1300 °C [4]. It is never found as a pure form but only as a tendency of ABC stacking in the primary hexagonal crystals. Natural graphite has been found to contain up to 30% of the beta form, when synthetically-produced graphite only contains the alpha form.

Pure pyrolytic graphite, where the layers are all arranged in the same plane, is an extremely strong, heat-resistant material used in high-stress, high-temperature environments. Graphite can be used as a moderator for nuclear reactors. Graphitisation is the process that coke and similar irregular carbon structures or carbon based molecules take through to become more ordered into graphite. This could be either a series of artificial treatments, or a lengthy natural process within the earths crust involving pressure and heat [5].

For catalysis applications, it is possible to find high surface area graphite, that allows good dispersion of the active phase.

I-1-3-Diamonds

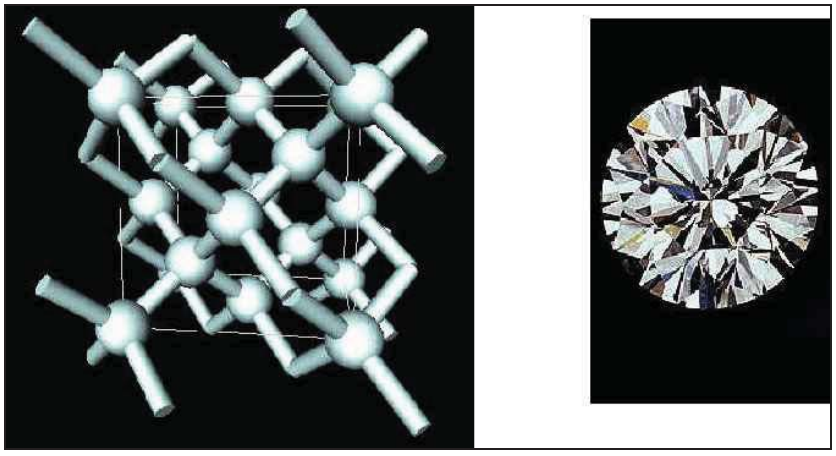

Figure 3: Diamond structure

Diamond is another natural carbon allotrope [6]. Its structure is triangularly dense, and gives it the property of being the hardest substance (hardness Mohs of 10) of all natural materials [7]. In its natural state, diamond possesses a derived structure from the cubic face

centered (fcc), named diamond type where in addition to the atoms in the corner of the cube and in the center of each facet, four of the eight tetrahedral sites are occupied, which gives finally eight atoms per elementary cell (4 in the case of a classic cfc structure), and makes each atom surrounded by 4 neighbours (Fig. 3). Diamond has been successfully grown synthetically since 1955 and diamond thin films by chemical vapor deposition have also become a twenty-first-century material [8].

I-1-4-Activated carbon

Activated carbon (AC) is a crude form of graphite. It differs from graphite by having a random imperfect structure, which is highly porous over a broad range of pore sizes from visible cracks and crevices to molecular dimensions. This structure gives the carbon it's very large surface area, often greater than 1000 m^2/g: 3 g of activated carbon develop the surface area of a football field. This gives activated carbon the strongest physical adsorption forces or the highest volume of adsorbing porosity of any material known to mankind.

Adsorption on porous carbons was described as early as 1550 B.C. in an ancient Egyptian papyrus and later by Hippocrates and Pliny the Elder, mainly for medicinal purposes. In the 18th century, carbons made from blood, wood and animals were used for the purification of liquids. All of these materials, which can be considered as precursors of activated carbons, were only available as powders. At the beginning of the 20th century the first processes were developed to produce activated carbons with defined properties on an industrial scale. It was the steam activation (V. Ostreijko, 1900 and 1901) and chemical activation (Bayer, 1915) processes. Calgon carbon corporation (USA), the parent company of Chemviron carbon [9] succeeded after World War II, in developing coal based granular AC with a substantial content of transport pore structure and good mechanical hardness. This combination allowed the use of activated carbon in continuous decolorization processes resulting to superior performance.

I-1-5-Buckminsterfullerene or C_{60}

In 1985 three researchers R. Smalley, R. Curl (Rice University, Houston, USA) and H. Kroto (University of Sussex, UK) discovered a novel form of carbon: Buckminsterfullerene or C_{60} [10-11]. The name is given to honor Richard Buckminster Fuller, who popularized geodesic domes. It is a molecule with 60 atoms of carbon distributed on the summits of a

regular polyhedron constituted of hexagonal and pentagonal facets (Fig. 4). Later other fullerenes were discovered: C_{70}, C_{80}, and others.

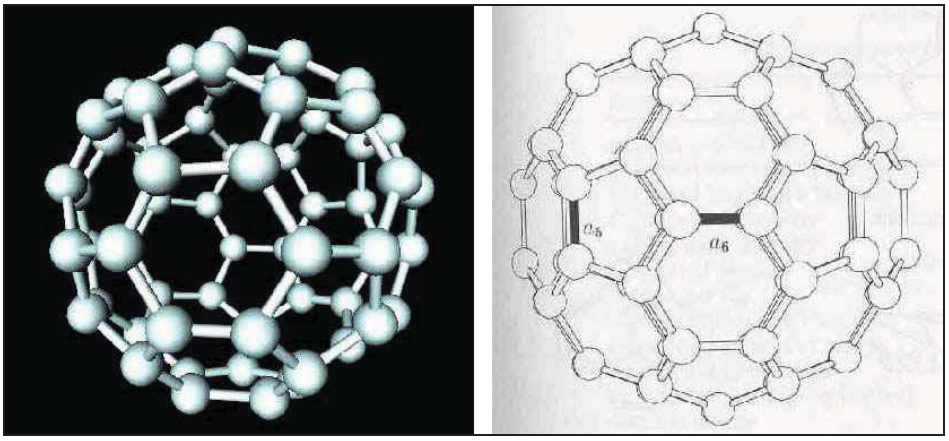

Figure 4: Fullerene structure

I-1-6-Graphitic onions

Sumio Iijima reported for the first time the existence of nested carbon nanocages, now known as graphitic onions, from HREM [12] observations. Eight years later, H. Kroto and K. McKay also proposed, for the first time, the model of graphitic onions consisting of nested icosahedral fullerenes (C_{60}, C_{240}, C_{540}, C_{960}, …) containing only pentagonal and hexagonal carbon rings. In 1992, D. Ugarte observed the transformation of polyhedral graphitic particles into almost spherical carbon onions [13] when he irradiated the specimens with fast electrons inside an electron microscope. Today graphitic onions are being produced with different methods and conditions [14-15] and their main applications are nanocapsule for drug delivery or fabrication of electronic devices.

I-1-7-Carbon nanofibers (CNF)

The nanofibers consist of graphite platelets perfectly arranged in various orientations with respect to the fiber axis, giving rise to assorted conformations. In this work we will focus on three types of CNFs: ribbon-like CNF (CNF-R) were the graphene layers are parallel to the growth axis, the platelet CNF (CNF-P) displaying graphene layers perpendicular to the growth axis and finally herringbone nanofibers (CNF-H) having layers stacked obliquely in respect to the growth axis [16] (Fig. 5). The diameters of CNFs are generally large and can easily reach 500 nm. The production of graphite fibers is old and the first reports date of more than a century. One of the first records is probably a patent dated 1889 on synthesis of filamentous carbon by Hughes and Chambers [17]. In the 1970s, the deeper studies in this

area were led by R.T. K. Baker in the USA and were motivated by the need to inhibit the growth of carbon nanofibers because of the persistent problems caused by accumulation of this material in a variety of commercial processes like steam reforming [18].

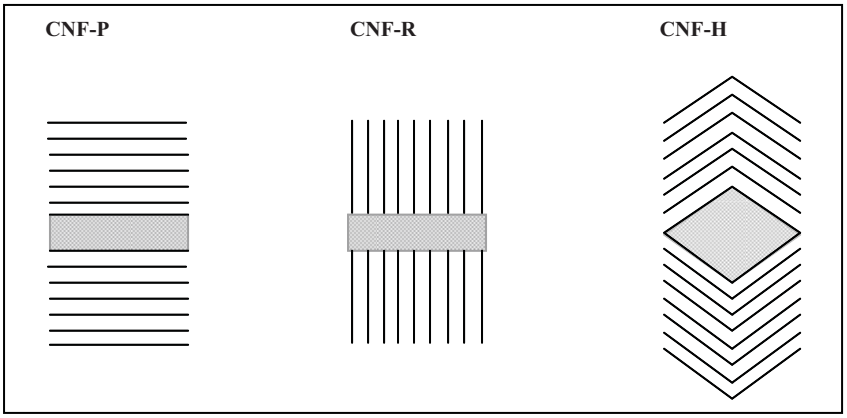

Figure 5: Different types of carbon nanofibers

I-1-8-Carbon nanotubes (CNTs)

Carbon nanotubes can be considered as elongated fullerenes. One of the first evidence that the nanofilaments thus produced could have been nanotubes, exhibiting an inner cavity, can be found in the transmission electron microscope micrographs published by Hillert and Lange in 1958 [19]. First high resolution TEM micrographs of CNTs were reported by Sumio Iijima [20-21] in the 1990's.

The main difference between CNTs and CNFs consists in the lack of a hollow cavity for the latter. Carbon nanotubes can be divided essentially into two categories: single-walled (SWCNTs) and multi-walled (MWCNTs).

Ideally, single-walled carbon nanotube consist in a perfect graphene sheet, i.e. a polyaromatic atomic monolayer made of an hexagonal display of sp^2 hybridized carbon atoms that genuine graphite is built up with, rolled up into a cylinder and closed by two caps (semi-fullerenes) (Fig. 6). The way the graphene sheet is wrapped is represented by the helicity vector (C_h) that is modulated by a pair of indices n and m. The integers n and m denote the number of unit vectors along two directions in the honeycomb crystal lattice of graphene. If m=0, the nanotubes are called zigzag. If n=m, the nanotubes are called armchair. Otherwise, they are called chiral (Fig. 6). The diameter of SWCNTs can vary between 0.4 and 2.5 nm and the length ranges from few microns to several millimeters. Due to high surface energy of these one-dimensional carbon macromolecules, SWCNTs are commonly arranged in bundles.

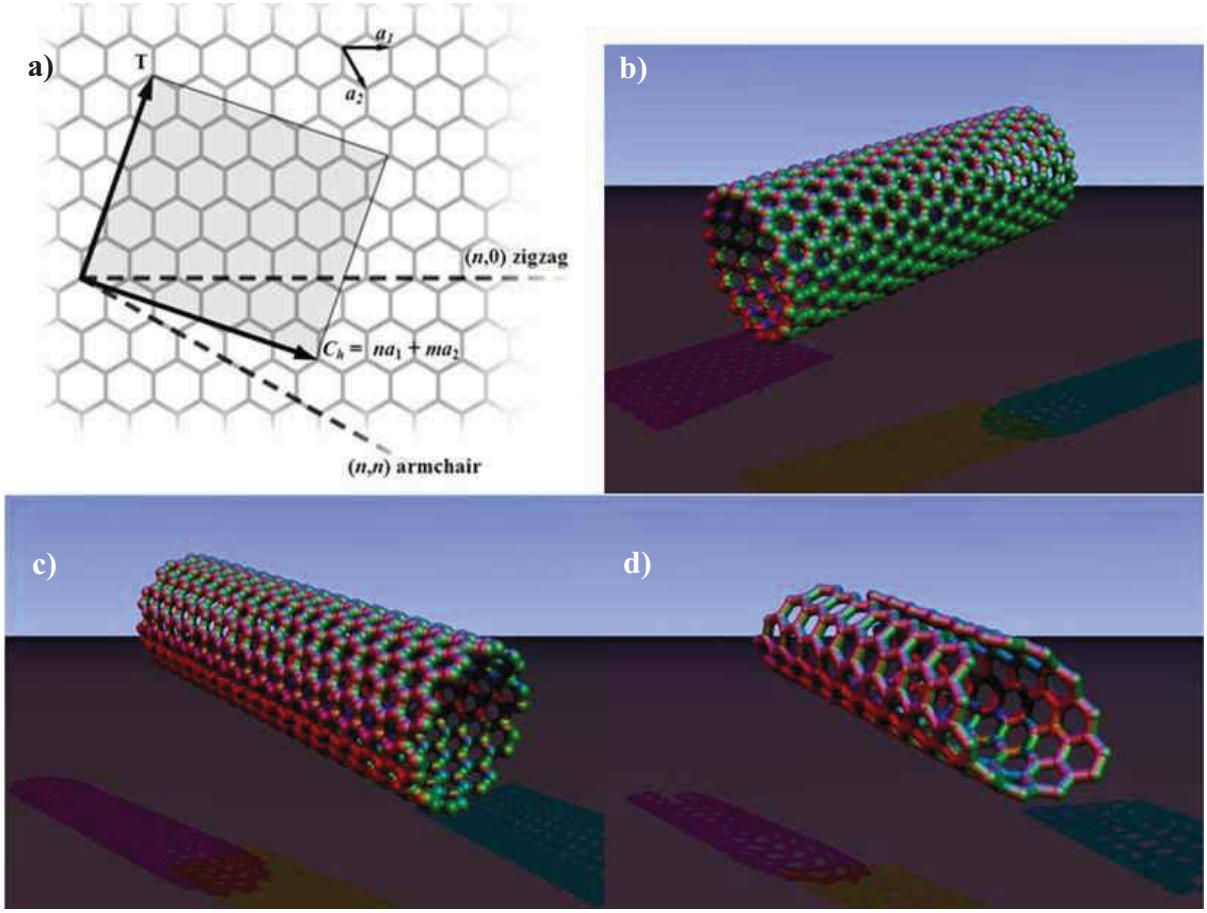

Figure 6: (a) Schematic honeycomb structure of a graphene sheet. Single-walled carbon nanotubes can be formed by folding the sheet along lattice vectors. The two basis vectors a_1 and a_2 are shown. Folding of the (n, 0), (n,n) and (n,m) vectors lead to (b) zigzag (c) armchair, and (d) chiral tubes, respectively

MWCNTs can be considered as concentric SWCNTs with increasing diameter and coaxially disposed. The number of walls present can vary from two (double-walled nanotubes) to several tens, so that the external diameter can reach 100 nm. The concentric walls are regularly spaced by 0.34 nm similar to the intergraphene distance evidenced in turbostratic graphite materials. It is worth to note that residual metallic particles coming from the production process can be found in the inner cavity of MWCNTs. It is also important to stress the fact that in most of the MWCNTs grown by catalytic CVD, the internal cavity is rarely accessible, due to the presence of bamboo-shaped compartments with graphene layers perpendicular to the tube walls.

CNTs are one of the most active fields of nanoscience and nanotechnology due to their exceptional structural characteristics and related electronic, thermal, adsorption and mechanical properties that make them suitable for many potential applications as polymer

reinforcements for composites or breakthrough materials for energy storage, electronics and catalysis. This later will be the subject of our study.

I-2-Carbon supports for heterogeneous catalysis

Catalytic processes account for more than 90 % of the chemical manufacturing processes in use throughout the world, and the role of the catalyst consists in increasing the rate and controlling the selectivity of the chemical reactions involved. It is well known in many subject areas that the structure of a material dictates its property. After presenting the various structures of old and new discovered allotropes of carbon, we will focus on their potential applications in the field of catalysis. First, discussion will be held on the advantages of carbon in general versus classical oxide supports then we will present the progress made that files to the new carbon allotropes.

I-2-1-General advantage of carbon materials *vs* metal oxides

Carbon materials have been used for a long time in heterogeneous catalysis, because they can act as direct catalysts or, more important, they can satisfy most of the desirable properties required for a suitable support [22, 23]. The specific characteristics that have attracted attention to carbon materials among different types of supports used in heterogeneous catalysis are:

i) *Resistance to acid/basic media in the range of catalytic application.*

Activated carbons are stable in both acidic and basic media, which is not true for oxides. Alumina as well as silica are dissolved at high pHs and the former is also attacked at very low pHs [24].

ii) *Possibility to control, up to certain limits, the porosity and related surface area.*

For example, activated carbon could be manufactured from suitable precursors by two methods: chemical or physical activation. Depending on the activation parameters such as temperature, pressure, time or the use of different agents, the final porosity and surface area can be tuned, and thus be adapted to the catalytic reaction demands [25].

(iii) *Easy recovery of precious metals*

A very important point for the economic use of precious metal catalysts, especially highly loaded ones, is recovery, refining and recycling of the metal. This procedure is simplified by the use of carbon as support, since this material can be burnt off, leading to highly concentrated ashes that permit an economical recovery of the precious metal [26]. This

technology is also very effective from an ecological standpoint, as it does not produce large amounts of solid waste that need to be land filled.

It is well documented that the role of the support is not only to maintain the catalytically active phase in a highly dispersed state, but may actually contribute in catalytic activity and selectivity by interacting with the active species or the substrate [27]. Thus, supporting the metal active species on different elements like C, Al, or Si may result in different catalytic performances.

The most important carbon support material is activated carbon, followed by carbon black and graphite or graphitized materials [28, 29]. However, compared to other applications such as water and gas treatment or rubber production, their use as catalyst support constitutes a minor part of the global market.

I-2-2-Novel carbon nanostructures for catalysis

Novel carbon nanostructures, mainly carbon nanotubes and nanofibers could boost up the use of carbon as support for heterogeneous catalysis. In fact, those latter solved a number of problematic issues encountered for both classical metal oxides and activated carbons.

Metal oxides and activated carbon present a rigid microporous structure. The active metal nanoparticles are formed mainly inside the pores. On the other hand, novel carbon nanostructures are mesoporous, present high external surface and dynamic structures. Active nanoparticles are highly dispersed on their surface. Hence, with novel carbon structures there should be a significant decrease in mass-transfer limitations and pores plugging so that better performances could be expected. In addition, analysis of adsorption, electronic, mechanical and thermal properties of CNTs and CNFs, with respect to catalytic requirements were encouraging.

I-2-2-a-Structural and electronic property

Exhaustive studies dealing with the electronic properties of CNTs are available in the literature [30, 31]. For CNFs, while CNF-R are often considered as conductive substrates that can exert electronic perturbations similar to those of graphite [32], few data are available for CNF-P and CNF-H, but due to the orientation of the graphene layers they are expected to be less conductive.

SWCNTs behave as pure quantum wires, in which the electrons are confined along the tube axis. Electronic properties are mainly governed by two factors: the tube diameter and the

helicity (Fig. 6). In particular, armchair SWCNTs display a metal-like conductivity and zigzag ones behave as semi-conductors. The curvature of the graphene sheets induces strong modifications of the electronic properties; indeed a comparison to graphite shows modification of the π-electron cloud [33]. The rolling-up of the graphene sheet to form the tube causes a rehybridization of carbon orbitals (non-planar sp^2 configuration), thus leading to modification of the π density in the graphene sheet (Fig. 7).

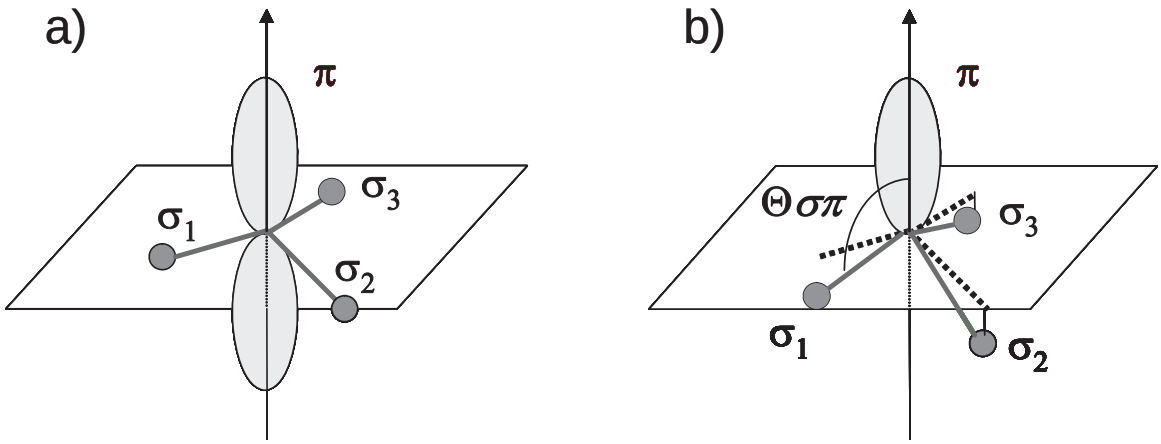

Figure 7: Carbon hybridization in a) graphene and b) CNTs

It is also worth noting that the theoretically predicted electronic properties are often modified by the presence of defects such as pentagons, heptagons, vacancies or impurities [34]. In addition, production techniques do not currently allow the selective production of only one type of SCWNTs, and the final purity of the obtained material, i.e. after purification steps, is often far from being satisfactory.

Studies on MWCNT electronic properties have shown that they behave like an ultimate carbon fiber [31]: at high temperature their electrical conductivity can be described by the semi-classical models already used for graphite, whilst at low temperature they reveal 2D-quantum transport features. A reliable prediction of their electronic properties is even more difficult than in the case of SWCNTs due to the higher complexity of their structure, and experimental measurements on MWCNT resistivity have not given reliable values (Table 1) due to different CNT purities and measuring conditions.

In catalysis, the electrical conductivity of CNTs (Table 1) as well as the curvature of the surface of these materials and the presence of an inner cavity is expected to affect the metal-support interaction in a different manner if compared to activated carbon and graphite. Thus, a theoretical study has shown that the binding sites are related to the support structure (Fig. 8): the studies conducted on nickel show that the nature of the most stable anchoring

sites varies significantly passing from graphite to SWCNTs, due to the different curvature of the surfaces where the active species are deposited [35].

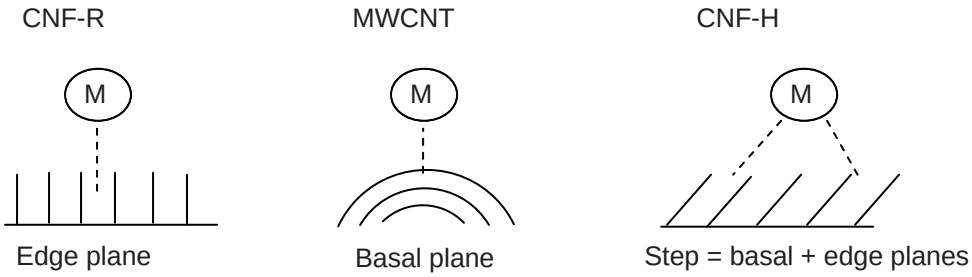

Figure 8: Different metal-support interaction as a function of the support structure

Moreover, it has been demonstrated that mechanically bent SWCNTs present kink sites that are chemically more reactive than the others [36]. Such local chemical reactivity can be also present in open-tip CNTs, and stable tip structures can be obtained by putting in contact transition metals with the open ends of SWCNTs [37]. The curvature does also affect significantly the values of magnetic moments on the nickel atoms on the nanotube wall, and the charge transfer direction between nickel and carbon can be inverted. Charge transfer, resulting in SWCNT holes doping, has also been evidenced during the room temperature spontaneous reduction, or galvanic displacement, of gold(III) and platinum(II) ions on the surface of SWCNTs [38].

The metal nanoparticles size strongly depends on the metal-CNT/CNF interaction (Fig. 8), with stronger interactions giving rise to smaller nanoparticles. Due to their peculiar morphology, CNF-P and CNF-H allow for the best dispersions. Of course, strong variations in the interaction energies will be observed according to the metal used. Although strong interactions have been measured for palladium and platinum, such interactions are weaker for gold [39]. The shape of the nanoparticles also depends on these interactions, and it has been proposed that metal nanoparticles grown on CNT surfaces may undergo a bending deformation along the transverse direction to the CNT because of the nanoparticle-CNT interaction and of the large curvature of small diameter CNTs [40]. Finally, the presence of relatively well-defined and nanometric inner hollow cavities can also induce differences of reactivity between the convex (external) and concave (internal) surfaces. Thus, it has been experimentally proven that hematite nanoparticles located inside the MWCNT pores are more easily reduced (600 °C) by the support than those on the outer surface (800 °C) [41].

	SWCNTs	MWCNTs	CNFs
Diameter[a] (nm)	0.5-2 (1-1.5)	5-200 (10-40)	10-500 (50-100)
Length	few µm up to 20 cm	few to hundreds µm	few to hundreds µm
d_{002} (Å)	-	3.39-3.48	3.36-3.44
Apparent density (g/cm^3)	0.5-1 (film)	0.02-0.3[e]	0.3-1.4
S_{BET} (m^2/g)	400-900	150-450	10-250
Porosity (cm^3/g)	microporous V_{micro}: 0.15-0.3	mesoporous V_{micro}: 0.5-2	mesoporous V_{micro}: 0.2-2
Young modulus (TPa)	1.05-1.3	0.5-1.2	0.3-0.7
Tensile strength (GPa)	45 to 150	3-30 to 150[b]	3-12
Electrical resistivity (Ω.cm)	6.10^{-4}	$0.6\text{-}2.10^{-4}$	1.5-3
Electrical conductivity (S/cm)	550	80-1000	300
Thermal conductivity[c] (W/K.m)	1000-6000[d]	300-3000	800-2000

[a]Typical values in parentheses. [b]Defect free MWCNTs. [c]Axial thermal conductivity at room temperature. [d]For a single rope of SWCNTs. [e]The lower value is for a powder and the upper one for short MWCNTs.

Table 1: Physical properties of carbon nanostructures

I-2-2-b-Adsorption properties

The interaction of carbon nanotubes with their environment, and in particular with gases or liquids adsorbed either on their internal or external surfaces is attracting increasing attention due to the possible influence of such adsorption on the CNT electronic properties (application as chemical sensors), and to the possibility of using these materials for efficient gas storage or for gas separation [42].

Studies concerning nitrogen adsorption on CNTs [43-45] have highlighted the porous nature of these materials. In MWCNTs, pores can be mainly divided into inner hollow cavities of small diameter (narrowly distributed, mainly 3-10 nm), external walls, and aggregated pores (widely distributed, 20-100 nm) formed by interaction of isolated MWCNTs, the latter being much more important for adsorption issues. Although adsorption among the graphenes (intercalation) has been proposed in the case of hydrogen adsorption in MWCNTs or CNF-P, it is unlikely that many molecules can do the same, owing to steric hindrance, or to too long diffusion paths. Thus, MWCNTs are essentially a mesoporous material that also presents some macroporosity (pores > 50nm). Chemical activation such as treatments with KOH or NaOH can efficiently give rise to microporosity; indeed, surface areas as high as 1050 m^2/g have been reported [46]. An efficient one step treatment based on the solid/solid reaction between NaOH and CNTs has been reported to simultaneously purify and open MWCNTs [47]. Thus, it appears that opening or cutting, and chemical treatments of carbon nanotubes, can considerably affect their surface area and pore structure. CNFs share this behavior with MWCNTs, except for the presence of narrower pores due to the presence of inner cavities in MWCNTs. For SWCNTs, N_2 adsorption has clearly evidenced the microporous nature of these materials. Adsorption of gases into a SWCNT bundle can occur inside the tubes, in the interstitial triangular channels among the tubes, on the outer surface of the bundle or in a groove formed at the contact between adjacent tubes on the outside of the bundle. Most experiments show that the specific surface area of SWCNTs is often larger than that of MWCNTs or CNFs (Table 1). Typically, the total surface area of as-grown SWCNTs ranges from 400 to 900 m^2/g (micropore volume, 0.15 – 0.3 cm^3/g), whereas for as-produced MWCNTs values ranging between 150 and 300 m^2/g are often reported. For CNFs, the surface area can range from 10 to 250 m^2/g, and the mesopore volume varies between 0.5 and 2 cm^3/g [48].

Model studies have pointed out that the convex surface of CNTs is more reactive than the concave one and that this difference in reactivity increases when the tube diameter decreases [49]. Compared to the highly bent fullerenes, CNTs are only moderately curved, and are hence expected to be much less reactive towards dissociative chemisorption. Dissociation of molecules on graphite edge sites, which constitutes the major part of the CNF surface, and are present at the tip of open-ended CNTs, can indeed occur. Models have also predicted an enhanced reactivity at the kink sites of bent CNTs [50]. In addition, it is worth noting that unavoidable imperfections such as vacancies, Stone-Wales defects, pentagons, heptagons and dopants, are believed to play a key role in tailoring the adsorption properties

[51]. The observed trends in the binding energies of gases with different van der Waals radii suggest that the groove sites of SWCNTs are the preferred low coverage adsorption sites owing to their high binding energies. Furthermore, several studies have shown that, at low coverage, the binding energy of the adsorbate on SWCNTs is between 25 % and 75 % higher than the monolayer binding energy on graphite. The observed changes in binding energy can be related to an increase in the coordination possibilities in binding sites, such as the groove sites in SWCNT bundles [52, 53]. For CNFs (25 m^2/g) and CNTs (186 m^2/g) it has been shown that the adsorption capacity towards volatile organic compounds is significantly lower than for high surface area graphite (100-300 m^2/g), the enthalpy of adsorption following the same trend [54].

In summary, it appears that carbon nanotubes present peculiar adsorption properties if compared to graphite or to activated carbon, mainly due to their peculiar morphology. The role of defects, of the opening/closing of the tubes, of chemical purification or of the presence of impurities as catalyst particles that can govern the adsorption properties have not yet been examined in detail.

I-2-2-c-Mechanical properties

CNTs are unique materials because of the particularly strong bonds in the curved graphene sheet that are stronger than in diamond as revealed by the difference in C-C bond length (0.142 and 0.154 nm, for graphene and diamond, respectively). This makes CNTs particularly stable towards deformation with a Young modulus in the order of tera-Pascal [55], and a resistance to traction of 250 GPa [56]. Defective MWCNTs produced by CVD provided a measured range of 3-30 GPa [57]. As for their flexural modulus, MWCNTs would exhibit higher values than SWCNTs [58], with flexibility decreasing when the number of walls increases. Concerning CNFs, most authors claim that they present lower mechanical strength due to the peculiar arrangement of the graphene layers [59].

I-2-2-d-Thermal property

The thermal stability and conductivity of these materials is an important feature that ought to be taken into account under real reaction conditions. The most common and simple method to study the resistance of a carbonaceous material towards heating in air is by thermogravimetric analysis (TGA). CNTs or CNFs are more stable towards oxidation than activated carbon, but more reactive than graphite. However, the concentration of surface defects and the presence of residual metal on or inside the nanotubes, which can catalyze

carbon gasification, could lower the temperature at which the maximum gasification rate is observed. This makes difficult an objective comparison between these materials. It is however generally accepted that amorphous carbon burns first, followed by SWCNTs and then MWCNTs, even if in most cases TGA is unfortunately not able to clearly separate the different oxidation steps. High resistance towards air oxidation is often reported for CNFs [60, 61] and should be related to the purity of the material.

Finally, the thermal control on nanocatalysts becomes increasingly important as the size of the system diminishes. Therefore, for exothermic reactions the thermal conductivity of CNTs or CNFs should play a critical role in controlling the performance of the catalyst. Despite the importance of thermal management, there has been little progress, mainly due to technical difficulties, in measuring the thermal conductivity of individual CNTs. The measured thermal conductivities of graphite along the basal plane range from 940 to 2000 W/K.m, and that perpendicular to the basal plane are two or three orders of magnitude lower. For CNTs, a similar behavior is very likely to be observed for their axial and transverse conductivities. Although experimental data and theoretical predictions are scattered by one order of magnitude (Table 1), probably depending on CNT type and size, most of the studies concerning CNT thermal conductivity agree about very high values comparable to diamond and to in-plane graphite sheet and about a significantly improved thermal conductivity for CNT-polymer composites. Although the CNTs present in catalyst pellets exhibit defects and are aggregated, so that the thermal conductivity of these dense-packed CNTs significantly decreases if compared to single tubes, it is still much higher than that of other supports used in catalysis, and this property should be taken into account when exploring specific catalytic reactions.

To conclude, it appears that their aforementioned properties make CNTs and CNFs attractive competitive catalyst supports if compared to other supports. Indeed, resistance to abrasion, thermal and dimensional stabilities, and specific adsorption properties are important factors controlling the final activity and reproducibility of the catalytic system. In particular, CNTs and CNFs could replace activated carbons in liquid-phase reactions since the properties of the latter cannot be easily controlled, and since their microporosity has often slowed down catalysts development.

I-3-Direct application of carbon nanomaterials as catalysts

I-3-1-Fullerene

C_{60} Fullerene molecules were deposited on titania and were found promising catalysts for decreasing the rate of the electron-hole recombination occurring in the reactions of the photooxidation of pollutants and the photocatalytic splitting of water [62]. Novel recyclable heterogeneous catalysts generating singlet-oxygen under visible-light irradiation have been prepared by linking C_{60} fullerene to amino-functionalized silica gels. The catalysts facilitate various types of photooxygenerations including Diels–Alder reaction, ene reaction, and oxidation of phenol and sulfide in a solid-solvent system and even in a solvent-free system (Fig. 9) [63].

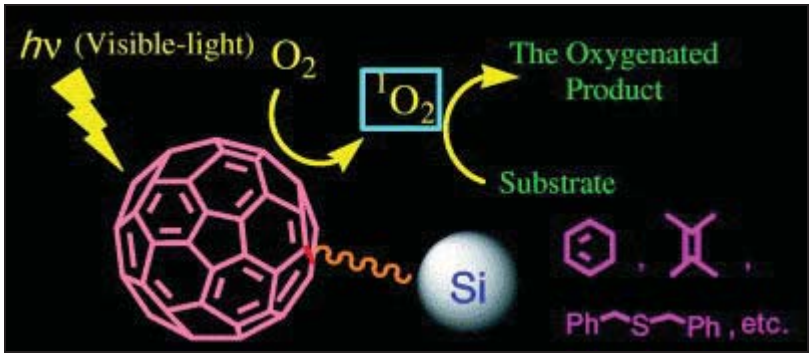

Figure 9: C_{60} based photocatalyst for various oxidation reactions

I-3-2-CNTs and CNFs

CNT or CNF have been used as catalysts for some specific reactions including methane decomposition to produce hydrogen free from CO and CO_2 [64], oxidative dehydrogenation of ethylbenzene to styrene [65-70], of propane to propene [71], deNO_x reactions [72, 73], selective oxidation of H_2S [74, 75], oxidation of aniline [76] and p-toluidine [77], catalytic wet air oxidation of phenol [78], esterification [79], and hydroxylation [80]. Nitrogen-doped CNT have been used as solid basic catalysts for Knoevenagel condensation [81]. Nitrogen and boron doped carbon are also reported as catalysts for the oxygen reduction reaction on the cathodic side of fuel cells [82]. Finally, the possibility of hydrogen generation via splitting of H_2O confined in SWCNTs by the use of a camera flash has been reported [81, 83]. In this reaction, the camera flash induces an ultra-photothermal effect that permits to reach high temperatures and causes the dissociation of water molecules into H_2 and O_2.

Even though carbon materials can act alone as catalysts, they are usually reported as supports for active metallic species.

I-4-Carbon nanostructures as supports for active nanoparticles

I-4-1-Surface chemistry of CNTs and CNFs

From a general point of view, both experimental and theoretical results conclude that in order to attain a high dispersion of the metallic phase, a surface activation or functionalization, meaning the creation of functional groups on the surface of CNTs or CNFs, is essential. Indeed, as-produced CNTs do not possess a high amount of functional groups on their surface, and only surface defects such as vacancies, dangling bonds at open ends, Stone-Wales defects and rehybridization defects, can be considered as anchoring sites for metals [84]. The result is a poor dispersion of the metallic phase, and the impossibility to reach high metal loadings [85]. The broad spectrum of CNT and CNF applications has permitted the development of reliable methods for their chemical and electrochemical functionalization [86], and today chemical reactions on these materials receive an increasing attention. Without going into detail, the most common methods used for metal particles anchoring are: acid oxidation [87], gas phase (air [87] or CO_2 [88]) oxidation, oxidation by common oxidizing agents (hydrogen peroxide [87], permanganate [89], osmium tetroxide [90], ozone [91]), the use of polymeric additives [92], and physical methods such as ball-milling [93, 94] or sonication [95]. Besides introducing anchoring sites for particles, these treatments can also modify the behaviour of CNTs and CNFs towards wetting, and the capability of the precursor to get reduced on the support. Thus HNO_3-oxidized CNTs become hydrophilic, whereas untreated CNTs are hydrophobic. This is important for their use as supports in liquid phase reactions since it is possible to design them so as to obtain a support with optimal wetting properties according to the reaction medium employed. Furthermore, worthy of note is that the presence of oxygenated groups could inhibit the easy reduction of the metal on the support. In summary, the CNT or CNF surface chemistry and structural features strongly depend on the chosen treatment.

The HNO_3 or HNO_3/H_2SO_4 treatments are the most widely used for nanoparticle anchoring, and it has been shown that surface oxygen functionalities, mostly carboxylic and anhydride carboxylic groups are introduced at defect sites on the outer and possibly inner walls of CNTs or CNFs [87, 96-98]. In refluxing acids, the oxidation proceeds via carbonyl and other oxide groups to carboxylic or anhydride groups. The HNO_3/H_2SO_4 treatment creates the higher density of carboxylic groups on the surface [87, 99]. A concentration of 1-1.4 oxygen-containing surface groups per nm^2 has been measured by chemical titration in the case of oxidized CNFs [59]. Prolonged reflux induces the opening of MWCNT tips, damages the

walls and slightly increases the specific surface area. For SWCNTs, careful and slow oxidation in diluted nitric acid is needed to create surface oxygenated groups, mostly carboxylic acid functions, and to minimize bulk damage of the material. XPS analyses have demonstrated that H_2SO_4 treatment can lead to the formation of sulphur-containing species on the surface of MWCNTs [100] and SWCNTs [101, 102]. The sonication of MWCNTs in HNO_3/H_2SO_4 at 60 °C permits a homogeneous treatment of the material with 6 % atomic oxygen on the surface [100]. In this case, carbonyl, ester and phenol groups have been detected by infrared spectroscopy, with only few carboxylic groups [103]. A prolonged sonication can lead to fragmentation of the tubes and cause mechanical damage to their surface. Yet, the introduction of a large number of functionalities can significantly reduce the mechanical and electronic properties of CNTs, and an alternative method to strong acid treatments employs heteroatom doping, like nitrogen [104], sulphur, fluor or boron. Doping is a promising direction to improve properties of nanostructures. It causes significant changes in their morphology, hardness, electrical conductivity, and chemical reactivity [105]. Nevidomskyy et al. [106] predicted that nitrogen doping in carbon nanotubes will result in chemically active, localized areas of higher electron density. Doping is usually done at the same stage of the nanostructure synthesis.

Interestingly, $-SO_3H$ sulfonic groups, which can be of interest for proton conduction in fuel cells electrocatalysts have been introduced on CNT surface by treatment in fuming sulfuric acid [107]. Dependind on CNT quality, these drastic liquid phase oxidation treatments can generate contaminating debris, which can be removed by CO_2 oxydation [108] or base treatments [109]. This latter treatment, if performed with NaOH may introduce sodium carboxylate or alcoolate functionalities.

Besides the classical nitric acid treatments, other oxidative agents have been used to prepare functionalised CNTs. Rao et al. have compared the effects of concentrated nitric acid, aqua regia, $HF-BF_3$, aqueous OsO_4 and $KMnO_4$ (acid/alkali) solutions on MWCNT structures [110]. All these oxidants open the nanotubes but the essential structural features are still present at the end of the treatment. The advantage of $HF-BF_3$ superacid and OsO_4 is that reactions can be conducted at room temperature. In the case of osmylation, theoretical calculations have predicted the formation of osmate ester adducts via complexation on the CNT walls via a base-catalyzed cycloaddition reaction [111]. The concentration of the surface acid groups after 24 hours of treatment under reflux has been measured to be 2.5 10^{20} sites per gram of MWCNTs for HNO_3, 6.7 10^{20} for H_2SO_4, 7.6 10^{20} for aqua regia and 8-10 10^{20} for $KMnO_4$ (acid/alkali) solution. The localized etching of CNT surface by iron catalyzed steam

gasification is an effective manner to increase the surface roughness and the number of surface defect [112].

Amongst the different methods proposed to cut nanotubes, ball-milling [93, 113, 114] is the most popular. The ball-milling treatment allows the segmentation of CNTs to shorter tubes obeying a second-order exponential length-decrease rule [114]. Segmented CNTs present typical length-distributions ranging between 200 and 800 nm. Detailed HREM observations on segmented CNTs and on their tips have shown a high percentage of carbon nanotubes that have partially or completely collapsed openings [113]. These results point to the limitations of this method to produce small-diameter, open-ended CNTs.

I-4-2-Deposition methods

Several chemical methods such as incipient wetness impregnation (IWI), ion exchange, chemical vapor deposition, organometallic grafting, impregnation with colloidal solutions, deposition/precipitation but also electrochemical techniques have been used to prepare CNT or CNF supported catalysts (Table 2) [115, 116].

System	Preparation method	S_{BET}[a] (m^2/g)	Loading (w/w %)	Mean particle size (nm)	Ref
RuO_2/CNF-H	Impregnation on oxidized CNFs	184	9	1.35	117
Ru/CNF	Impregnation on oxidized CNFs	(140)	4	2.9	118
Ru/MWCNT	IWI on oxidized MWCNTs	170 (224)	4.8	4.2	119
Pd/CNF	Impregnation on oxidized CNFs	(100)	10	3-5	120
Pd/MWCNT	Impregnation on oxidized CNT	-	20	3-5	121
Pd/SWCNT	Colloidal Pd solution on functionalized SWCNTs	-	5.7	5	122
Pt/MWCNT	Impregnation on oxidized MWCNTs	(400)	3	< 2	123
Pt/CNF-H	Impregnation	180	4	2.5	124
Pt/SWCNT	Colloidal Pt solution on functionalized SWCNTs	-	30	2-3	125
PtRu/MWCNT	Impregnation on oxidized	(100)	25 Pt–25	2-3	126

	MWCNTs		Ru		
Ni/ CNF-H	Deposition precipitation on oxidized CNFs	(150)	20	8	127
Co/MWCNT	CVD on oxidized MWCNTs	(140)	5.8	7	128
Rh/MWCNT	Impregnation on oxidized MWCNTs	140 (180)	1	5-10	72

[a] Values in parentheses are the S_{BET} of the supports.

Table 2: Representative examples of metals or oxides supported on CNT or CNF

By observation of the dispersion of the metallic phase on these supports, better results are obtained using CNF-H, followed by MWCNTs, and then SWCNTs. This order is due on one side to the peculiar orientation of the graphene layers in CNFs that provides many potential sites for metal anchoring and on the other side to the difficulty in getting a good dispersion on SWCNTs since they tend to arrange in bundles. One can see in Table 2 that high dispersions are often obtained with Ru and Pt, whereas Ni, Co, and to a lesser extent Pd give rise to larger particles, pointing to differences in metal-support interactions.

Incipient wetness impregnation methods involve the impregnation of the oxidized CNTs or CNFs with a solution of a metal salt or of an organometallic complex, followed by drying and reduction to give metal particles anchored to the carbon functionalized surface. The reduction is generally carried out either by H_2 or sodium borohydride. This method is the most commonly employed owing to its simplicity, cost and easy scale-up. Generally speaking, this method leads to well-dispersed catalysts and enables high loadings. The use of organometallic precursors is preferred when very small particle are needed [129], and the use of supercritical CO_2 provides a green alternative to organic solvents [130]. When high dispersions and high loadings are targeted, deposition by precipitation or the use of colloids solutions are often more effective [131]. As for this latter approach, different strategies have been adopted to stabilize the nanoparticles: i) specific CNT surface functionalization such as creation of thiol groups improves nanoparticle anchoring [132]; ii) the use of surfactants stabilises the colloids and permits high dispersions and high loadings [133]; and iii) the use of polymer additives improves CNT dispersibility [134].

Chemical vapor deposition is a recognized method to prepare well-dispersed catalysts [135], and it has been explored for the preparation of CNT and CNF based catalysts [136-138]. However this method has two important limitations: i) if it is conducted by two successive steps, it only affords low loadings [136, 137]; and ii) it is difficult to scale-up since

deposition must be carried out in fluidized bed and CNTs and CNFs are difficult to fluidize without external activation such as vibration.

Electrodeposition is the process by which metal particles are produced by the reduction of a metal salt solution at a cathode. The electrodeposition method presents limitations due to the difficulty in controlling the metal loading because of the concurrent reduction of protons and to the difficulty in reaching small particle sizes [139, 140].

Well dispersed supported catalysts have been prepared by surface organometallic grafting of various compounds. Two approaches can be adopted: i) the surface reaction between a complex and the functionalized CNT/CNF surface, which is the most common method; or ii) the synthesis of a complex between a metal salt and modified CNT/CNF surface as the ligand. The first approach has been adopted to anchor different species onto CNTs or CNFs, such as $[IrCl(CO)(PPh_3)_2]$ [141], $[RhCl(PPh_3)_3]$ [142], $[HRh(CO)(PPh_3)_3]$ [143], $[Rh(COD)(NH_2(CH_2)_2NH(CH_2)_3Si(OCH_3)_3)]$ [144], an octaamino bisphtalocyanine erbium complex $[OAErPc_2]$ [145], $[Ru{=}CHPh(Cl)_2((Pcy_3)_2]$ [146], [ruthenium(4,4'-dicarboxy-2,2'-bi-pyridine)$(2,2'\text{-bipyridyl})_2](PF_6)_2$ [147], a vanadyl salen complex [115], zirconium based metallocenes [149-151], and nickel metallacarboranes [152]. The grafting of the metal complex may occur via oxidative addition of a –OH or –COOH group [141], with η^2-coordination by the C=C bonds of the CNTs [141] or via surface reaction between a group on the functionalized CNT surface (amino group or thiol) and a ligand present on the metal complex [145, 147, 148, 152]. In the latter case there is no direct bond between the metal and the CNT surface. The second approach was used to attain the immobilization of a rhodium complex on HNO_3/H_2SO_4 treated CNFs [153-157].

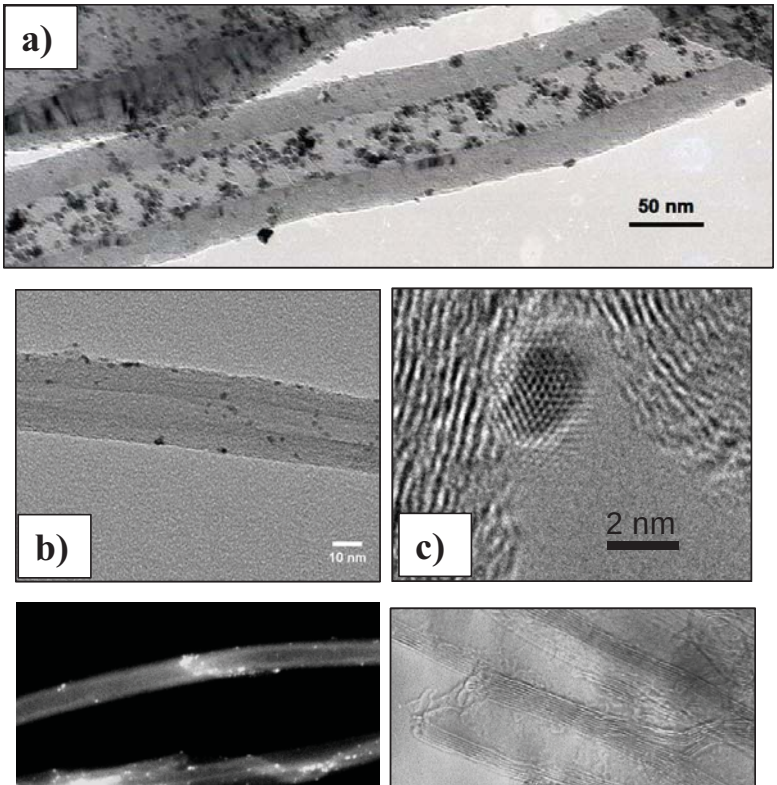

Figure 10: MWCNT-based catalysts: a) TEM micrograph of Pt nanoparticles inside MWCNTs, b) STEM micrograph of PtRu/MWCNT, c) HREM micrograph of PtRu/MWCNT, d) STEM-HAADF2 micrograph of PtRu/MWCNT and e) TEM micrograph of TiO_2-MWCNT composite catalyst. Adapted from [159]

The coordination chemistry of CNTs is still in its infancy and further studies must be conducted for the in-depth characterization of the grafted moieties. Preliminary theoretical works studying the interaction of CNTs with transition metal complexes have appeared for $[IrBr(CO)(PPh_3)_2]$ [154], $[M(\eta^5\text{-}C_5H_5)_2]$ (M= Fe,Co) [155], and $[M(C_{16}H_{10})(PH_3)_2]$ (M= Pt, Ni) [156]. It is reported that some metals, such as ruthenium, interact more strongly than others with the graphene layers of CNTs or with the surface of CNFs and that metal adhesion follows the order: Ru > Rh > Pd ≥ Pt [157, 158].

To conclude, it appears well established that different effective synthetic routes are at the disposal of chemists to prepare supported metal catalysts with high dispersions on CNTs or CNFs (Fig. 10).

I-4-3-Exemples of catalytic performance of CNT- and CNF-based catalysts

Owing to the advantageous properties of CNTs and CNFs as supports, several studies have been carried out on different catalytic reactions. In particular much attention has been dedicated to liquid-phase reactions with MCWNT and CNF supported catalysts, since their high external surface area and their mesoporosity would result in a significant decrease in mass-transfer limitations when compared to AC. It is worth noting that only few studies on SWCNT supported catalytic systems have been reported, due either to their microporosity or to the fact that it is still very difficult to obtain the large amounts of pure material required to conduct catalytic studies. A wide range of reactions are under study using carbon nanostructures as support for catalysis, like hydrogenation reactions, reactions involving CO/H_2 (Fischer-Tropsch reactions [160], methanol [161] or higher alcohol [162] synthesis,

and hydroformylation [163]), polymerization reactions to yield a polymer-functionalized CNT composite material [164], carbon nanotubes synthesis on preformed carbon nanostructures by catalytic decomposition of hydrocarbons[165], ammonia synthesis and decomposition[166], environmental catalysis and oxidation reactions[167], and finally fuel cell electrocatalysis.

In this section we will focus on the results obtained using carbon nanotubes and nanofibers for two types of applications: hydrogenation reactions and fuel cell electrocatalysts and, when possible, we will try to rationalize these results by comparison with other carbonaceous supports.

I-4-3-a-Hydrogenation reactions

One of the most studied catalytic reactions is hydrogenation, both in the liquid and gas phases, and two types of reactions have been considered: alkenes hydrogenation and α,β-unsaturated aldehydes selective hydrogenation.

I-4-3-a-i-Alkenes hydrogenation

Baker's research team has conducted several studies on ethylene, but-1-ene and buta-1,3-diene hydrogenation on nickel catalysts supported on different types of CNFs (CNF-R, CNF-P or spiral-like CNF), γ-alumina and activated carbon [168-170]. The authors state that the nickel crystallite activity and selectivity can undergo important modifications by interactions with the support. Indeed, it was found that the catalyst supported on CNFs gives higher conversion than those measured employing γ-alumina and AC, even though the metallic particle size was larger for CNF supported catalysts (6.4-8.1 nm on CNFs, 5.5 nm on AC and 1.4 on Al_2O_3). These results point to the fact that catalytic hydrogenation might be extremely sensitive to the nature of the metal-support interaction. HREM studies have been performed to get a deeper insight on metallic particle morphology: on CNF support the deposited crystallites were found to adopt very thin, hexagonal structures, and the relevant growth pathways are generally believed to be followed in situations in which strong metal-support interactions are present to cause the spreading of the metal onto the support surface. By contrast, a globular particle geometry prevails when nickel is supported on γ-Al_2O_3, providing a somewhat weaker metal-support interaction. Pt/CNF-H catalysts were also

reported to be nearly 1.2 times more active than Pt/AC or Pt/Al_2O_3 for hydrogenation of toluene [171], the CNF support allowing high Pt dispersion and higher concentration of Pt(0).

Rhodium nanoparticles (1.1-2.2 nm) supported on oxidized CNF-H were used in the hydrogenation of cyclohexene [172]. These catalysts turned out to be extremely active even under low hydrogen pressures at low metal loadings (1% w/w) and low cyclohexene concentrations (1% v/v). The authors claimed that the activity is almost independent of the nanoparticle size and that other factors, such as the possible clustering of the support material in the liquid phase and the presence of oxygen-containing species on the support surface are responsible for the observed results. Unfortunately, no comparison with other AC supported catalysts was provided. Ruthenium nanoparticles (2-4 nm) on CNFs (CNF-P or CNF-H) and MWCNTs showed excellent catalytic activity for arenes, and for toluene hydrogenation on a 1.7 % w/w Ru/CNF-P, the sum of the turn over numbers for five repeated runs was over 180000 [173]. A 5 % w/w platinum catalyst deposited on CNTs (100 m^2/g) was found to be significantly more active than a commercial or home-made 5 % Pt/AC and a 5 % Pt/graphite for the hydrogenation of trans-stilbene and trans-β-methylstyrene [174]. A rhodium complex grafted onto MWCNTs was also reported to be very active in cyclohexene hydrogenation [175, 176]. Such catalyst is more active than that supported on activated carbon, and interestingly TOF dramatically increases upon recycling. Pd/CNT catalysts were found to be active in cyclooctene [177] and benzene [178] hydrogenation, and for the latter a catalyst having Pd nanoparticles in the inner cavity of the tubes is more active than a Pd/AC system. If deposited on CNFs, palladium is also active for phenol hydrogenation [179], and while Pd/AC favored partial hydrogenation to cyclohexanone, Pd/CNF affords complete hydrogenation to the alcohol. Rh/CNF catalysts are also active for this reaction in *sc*CO_2 with high selectivity to cyclohexanone [180]. Bimetallic RhPd [181] and PtPd [182] systems supported on MWCNTs are active in the hydrogenation of aromatics and polyaromatics. Irrespectively of the reactant molecule, such PtPd catalysts show higher TOF than the corresponding oxide-supported systems [182]. Nitrobenzene has been hydrogenated to aniline at ambient temperature and under atmospheric pressure on 3 wt % Pt/CNT (170 m^2/g) presenting 3 nm Pt nanoparticles; a good activity was observed [183]. Different hydrogenation mechanisms have been proposed on the basis of the nature of the organic intermediates observed. Due to a higher dispersion, the catalysts were more active than their counterparts on AC [184]. For p-chloronitrobenzene hydrogenation, the use of bimetallic PtM/CNT catalysts (M = Mn, Fe, Co or Ni) permits higher activity than monometallic Pt catalysts as well as higher selectivity to p-chloroaniline [185]. Interestingly, it has been reported that reduced Pd/CNT (H_2, 1 h, 500 °C)

can effectively reduce NO at 300 °C [186]. The CNTs act as reducing agent that provides both hydrogen (adsorbed during reduction of the supported catalyst) and carbon in the NO reduction, and surface adsorbed species such as OH, NO, NO_2 and NO_3 are detected on the catalyst surface. Thus an important factor to take into consideration in hydrogenation reactions is the ability of CNTs and CNFs to take up significant amount of H_2, especially when they are used in association with Pd and/or Pt. Indeed, the spillover of physisorbed hydrogen from the metal nanoparticles enhances hydrogen storage if compared with pristine CNTs. The selective partial hydrogenation of acetylene to ethylene was reported on NiB/CNT catalysts [187]. The activation of CNTs with NH_3 (particle size 9 nm) provides better dispersions than the treatment with HNO_3 (particle size 16 nm). The use of CNT-NH_3 which favors high dispersion, results in the acceleration of the hydrogenation rate and in the increase of the selectivity towards ethylene. The selective hydrogenation of cyclohexadiene to cyclohexene over a homogeneous Rh catalyst immobilized in an ionic liquid phase supported on CNFs was used as test reaction to demonstrate the feasibility of the supported ionic liquid phase catalysis approach on nanostructured carbon support [188, 189]. Palladium catalysts supported on MWCNTs, CNF-H and CNF-R have been compared in the selective hydrogenation of 1,3-butadiene [190]. CNF supports and in particular the CNF-R permit to obtain highly dispersed Pd particles (3 nm), and the strong interaction between Pd and the graphene-edge sites of these supports does stabilize the oxidation state +2 of the metal via electron transfer from the metal to the support. The overall activity and selectivity of these catalysts decrease when the fraction of Pd^{2+} increases and the best results have been obtained on MWCNTs. Finally, cinchona modified Pt/SWCNT catalysts were found to be efficient for the asymmetric hydrogenation of ethyl pyruvate [191].

I-4-3-a-ii-α,β-unsaturated aldehydes hydrogenation

The hydrogenation of α,β-unsaturated substrates on CNF or CNT supported catalysts has been the subject of several studies. Although, the C=C bond is easier to hydrogenate than the carbonyl one, the unsaturated alcohol is often the desired product. Gas-phase hydrogenation of crotonaldehyde to crotyl alcohol was conducted on 5% w/w Ni catalysts supported on CNF-P, CNF-R and γ-alumina [192]. Even though the mean particle size greatly differs according to the support used, from a narrow distribution centered at 1.4 nm for γ-Al_2O_3 to a broad distribution centered at 7 nm for CNFs, the higher activity and selectivity to crotyl alcohol were obtained on the CNF supported catalysts. Possible reasons for these

differences are: i) different Ni crystallographic face exposure according to the support; and ii) the possibility of charge transfer. High activity and selectivity were also obtained with 2 wt % Pt/MWCNT (87 m^2/g) catalysts in the selective hydrogenation of citral [193]. Though it presents lower dispersion (6 nm) than Pt systems deposited on high surface area graphite (305 m^2/g, Pt 3.4 nm) or carbon black (135 m^2/g, Pt 1.8 nm), the Pt/MWCNT system is more selective towards the formation of the unsaturated alcohol at iso-conversion. A Pt supported catalyst on purified SWCNTs has been found to be active and selective in the hydrogenation of prenal (3-methyl-2-butenal) to prenol (3-methyl-2-butenol) [194].

The selective hydrogenation of cinnamaldehyde has been studied on different supported catalysts including monometallic Pd [122, 195-198], Pt [123, 199, 200], Ru [201, 202], and bimetallic PtCo [203, 204], PtNi [205], PtRu [206] and PdRu [207] systems. In general, the catalytic systems obtained by deposition on CNTs or CNFs are more active than their counterparts on AC or oxides, and only few systems are selective towards the unsaturated alcohol. Palladium systems are very active in the selective hydrogenation of the C=C bonds. On CNF-H (50 m^2/g), Pd catalysts (4 nm) are more active than commercial Pd/AC (900 m^2/g) catalysts [195, 196]. Similar results were obtained when Pd was deposited on the surface and into the cavity of large diameter MWCNTs (20 m^2/g), and on the surface of aligned MWCNTs attached to the surface of a structured silica reactor [197, 198]. As for SWCNTs, it is worth noting that a commercial Pd/AC catalyst (Pd particle size 14.5 nm) is more active than Pd/SWCNT (Pd particle size 5.6 nm) [122]. On MWCNTs, it has been observed that high selectivity to cinnamyl alcohol can be reached during cinnamaldehyde hydrogenation if Pt nanoparticles are located in the inner cavities of large diameter CNTs, (CNT inner diameter 60-100 nm, Pt 5nm)[208], while lower values have been determined with Pt on the outer surface of small diameter tubes (CNT inner diameter <10 nm, Pt <2nm) [123]. However, the Pt particle size was not the same in these two samples, and that might also affect selectivity [209]. A marked support effect on activity and selectivity has been reported for Pt/CNF [199, 200]. While Pt/CNF (177 m^2/g, Pt < 2 nm) containing a significant amount of oxygenated groups show only a moderate activity and selectivity in C=C bond hydrogenation (20-30%), the same catalysts heat treated to remove the oxygen-containing groups present an activity increased by a factor of 25, and a selectivity to hydrocinnamaldehyde of 40 to 70 %. This important finding highlights the importance of substrate adsorption onto the support in the mechanisms of hydrogenation [200]. The possible role of hydrogen storage on these supports has not been addressed yet. Different results have been obtained with ruthenium [201, 202]. On unpurified MWCNTs (27 m^2/g) generated by

arc discharge evaporation of graphite, a high activity compared to Ru/Al_2O_3 (Ru 3.5 nm) has been obtained together with an exceptionally high selectivity to cinnamyl alcohol (90 %) [201]. More recent results on purified MWCNTs (Ru < 2 nm) [204], or CNF (Ru < 2 nm) [202], report selectivity ranging between 30 and 50 %.

For Ru/CNF, the crucial role of cinnamaldehyde adsorption on the support has been reported, CNFs with low amounts of oxygen-containing groups showing increased activity and higher selectivity to hydrocinnamaldehyde (73 %). Bimetallic Pt-based systems permit a better control of selectivity. PtNi/MWCNT (135 m^2/g, particles 2-5nm) are more selective towards hydrocinnamaldehyde formation than Pt/MWCNT, showing values of 88 and 25 %, respectively [210]. The use of PtCo/MWCNT [204] or PdRu/SWCNT [211] permits to orientate selectivity towards cinnamyl alcohol formation to nearly 90 % and 57 %, respectively. Finally, the use of PtRu/MWCNT (175 m^2/g, particles 2 nm) leads to activities higher than with PtRu/AC, and a selectivity to cinnamyl alcohol higher than 90 %, after heating the catalysts to remove the oxygen-containing groups [206]. This result confirms the importance of the surface chemistry of the support with regard to the final performance of the catalysts.

I-4-3-b-Fuel cell electrocatalysts

The field to which the specific features of CNTs and CNFs could bring the most significant advancements is perhaps fuel cell electrocatalysis [212, 213]. In this paragraph we will summarize the main advantages linked to the use of nanotubes or nanofibers for these applications.

The structure and properties of the carbon support, which constitutes the electrode material, have a direct impact on the performance of fuel cells. This material must present: i) a high electronic conductivity; ii) a high mesoporosity to permit high metal dispersion; iii) a suitable morphology to optimize and stabilize the three-phase boundary reactive sites; and iv) a good hydrophobicity for water removal and mass transport improvement. In comparison with the more widely used Vulcan XC-72R carbon black support, which has an electronic conductivity of 4 S/cm and a specific surface area of 240 m^2/g with a significant amount of micropores, CNTs and CNFs have significantly higher electronic conductivities, and present higher mesoporous volumes for comparable or higher surface areas.

More than one hundred articles and numerous patents have been published on the use of CNTs or CNFs as catalyst supports for DMFC and PEMFC. The most studied reaction is methanol oxidation (anode catalyst), followed by oxygen reduction (cathode catalyst), and, to a lesser extent, hydrogen oxidation (anode catalyst). Platinum is the most used metal,

followed by Pt-Ru systems. Other Pt-containing bimetallic $PtWO_3$ [214, 215], PtNbPOx [216], PtFe [217], PtSn [218] and trimetallic PtRuIr [219] systems have also been reported. Surprisingly, only a few studies have been conducted on the use of cheaper metals such as Pd [220, 221], Ag [222], Au [223], Co [224] and MnO_4 [225]. All kinds of CNTs and CNFs have been used for these reactions, including CNF-H, CNF-P, CNF-R [226, 227] MWCNTs, SWCNTs, DWCNTs [228], and nitrogen-doped CNTs [229]. In most of these works, high dispersions of the metallic phase have been obtained [212, 213].

Although it is not possible to compare all these studies mainly because of the different origin of CNTs and CNFs samples (pointing to the crucial importance of CNT and CNF standardization), the general tendency observed is that the catalysts prepared on CNTs or CNFs are more active and in some cases present a better resistance to poisoning [230] than those prepared on conventional carbon supports as Vulcan XC-72. With some systems it is also possible to obtain similar or better performances with significant reduction of Pt loadings [231, 232]. When compared to the commonly used carbon black support, the increase in the power density of a single stack is comprised between 20-40 %, even if 70 [228], 100 % [233] or even higher values [234, 235] have been reported. Only a few studies concern systematic comparison of the different types of CNTs and CNFs. If we consider the electronic conductivity and specific surface area of the supports, we would expect the following order: SWCNTs > DWCNTs > MWCNTs > CNFs. In general, and this result could be rationalized on the basis of the electronic conductivity of the support, the activity of metal supported MWCNT systems is superior to CNF-based catalysts. For DWCNTs, which present a higher specific surface area than MWCNTs [228], better performances have been reported. For SWCNTs contrasting results have been reported, and further work is needed to shed light on the potentiality of these materials.

The advances made by the use of CNTs and CNFs as supports for fuel cell applications are generally attributed to: i) the possibility to reach high metal dispersions and high electroactive surface area; for Vulcan XC-72 R the catalyst particles can sink into the microporosity, thus reducing the number of three-phase boundary active sites; ii) the peculiar 3D mesoporous network formed by these materials, which provide an improved mass transport; and iii) their excellent conducting properties that improve electron transfer.

I-5-Conclusion

Large scale industrial production of nanotubes or nanofibers is underway for now: Arkema in France, Nanocyl in Belgium, Bayer in Germany, CoMocat and HIPCo processes in the United States…. Although the production processes are more and more controlled, it is still very difficult to maintain homogeneity in all the features (structure, purity, …) of these materials, so that precise comparison between different samples of different origin can hardly be made. Progress on that matter should arise from a better understanding of the growth processes of CNTs and CNFs and from the control of catalyst synthesis and high temperature activation. Additionally, the crucial aspects concerning standardization and toxicity of CNTs and CNFs should be addressed.

Concerning the preparation of supported catalysts, several methods have been successfully used, and the role of surface pre-treatments, as in the case of activated carbon, as well as the influence of the structure (CNTs or CNFs) on the final metal dispersion has been clearly demonstrated [236, 237]. Experimental as well as theoretical works would be necessary in order to have a better understanding of charge transfer phenomena and strength of metal support interaction in CNT and CNF catalytic systems.

The possibility of shaping these nanomaterials offers some interesting perspectives, including for the design of structured microreactors [238]. The catalytic studies conducted on CNT or CNF based systems have shown encouraging results in terms of activity and selectivity. In particular, high selectivity has been obtained on catalytic systems displaying different metal-support interaction and/or charge transfer phenomena than those evidenced on other supports such as activated carbon or alumina. High activities arise from the mesoporous nature of this support that avoids mass transfer limitations. For electrocatalysis, which constitutes an important field of application, the combination of specific support morphology and electrical conductivity often permit to reach high electrocatalytic activity.

I-6-References

1) R.P. Feynman, Eng. Sci. 23 (1960) 22

2) http://www.invsee.asu.edu/nmodules/Carbonmod/

3) M. Terrones, H. Terrones, Phil. Trans. R. Soc. Lond. A 361 (2003) 2789

4) IUPAC Compendium of Chemical Terminology 2nd Edition (1997)

5) S.Y. Boey, D.J. Bacon, Carbon 24 (1986) 557

6) http://magma.nationalgeographic.com

7) http://ist-socrates.berkeley.edu/~eps2/wisc/Lect6.html

8) C. Benndorf, P. Joeris, R. Kroger, Pure and Appl. Chem., 66 (1994) 1195
9) http://www.chemvironcarbon.com/
10) H.W. Kroto, J.R. Heath, S.C. O'Brien, R.F. Curl, R.E. Smalley, Nature 318 (1985) 162
11) H.W. Kroto, Angew. Chem. Int. Ed. Engl. 31 (1992) 111
12) P.J.F. Harris, in Carbon nanotubes and related structures: new materials for the XXI century, 1st edn, Cambridge University (1999) pp. 1–293
13) D. Ugarte, Nature 359 (1992) 707
14) S-S Hou, D-H Chung, T-H Lin, Carbon 47 (2009) 938
15) S. Hua, P. Bai, F. Tian, S. Cao, J. Sun, Carbon 47 (2009) 876
16) P. Serp, M. Corrias, P. Kalck, Appl. Catal. A: Gen., 253 (2003) 337
17) T.V. Hughes, C.R. Chambers, US Patent No. 405, 480, 1889
18) M.S. Kim, N.M. Rodriguez, R.T.K. Baker, J. Catal. 134 (1992) 253
19) M. Hillert, N. Lange, Zeitschr. Kristall. 111 (1958) 24
20) S. Iijima, Nature 354 (1991) 56
21) S. Iijima, T. Ichihashi, Nature 363 (1993) 603
22) F. Rodriguez-Reinoso, in Porosity in Carbons: Characterization and Applications, ed. J. W. de Patrick. Edward Arnold, London, (1995) 253
23) L.R. Radovic, F. Rodriauez-Reinoso, in Chemistry and Physics of Carbon, 25, ed. P.A. Thrower. Marcel Dekker, New York (1997) 243
24) P. Roisson, J.-P. Brunelle, P. Nortier, in Catalyst Supports and Supported Catalysts, A.B. Stiles (Ed.), Butterworth, Boston, 1987, p. 11
25) F. Rodriguez-Reinoso, M. Molina-Sabio, Carbon 30 (1992) 1111
26) C. Hagelücken, Erzmetall 49 (1996) 122
27) S.A. Stevenson, J.A. Dumesic, R.T.K. Baker, E. Ruckenstein, in Metal-Support Interactions in Catalysis, Sintering and Redispersion, Van Nostrand Reinhold, New York, 1987
28) A.J. Bird, in Catalyst Supports and Supported Catalysts, A.B. Stiles (Ed.), Butterworths, Boston, 1987, p. 107
29) L.R. Radovic, F. Rodriguez-Reinoso, in Chemistry and Physics and Carbon, P.A. Thrower (Ed.), Vol. 25, Marcel Dekker, New York, 1997, p. 243
30) J.E. Fischer, A.T. Johnson, Current Opinion in Solid State and Material Science 4 (1999) 28
31) J.P. Issi, J.C. Charlier, The science and technology of carbon nanotubes, in K. Tanaka, T. Yamabe, K. Fukui (Ed.), Elsevier (1999) p.107

32) C.A. Bessel, K. Laubernds, N.M. Rodriguez, R.T.K. Baker, J. Phys. Chem. 105 (2001) 1115

33) T. Dumitrică, C.M. Landis, B.I. Yakobson, Chem. Phys. Lett. 360 (2002) 182

34) J.C. Charlier, Acc. Chem. Res. 35 (2002) 1063

35) M. Menon, A.N. Andriotis, G.E. Froudakis, Chem. Phys. Lett. 320 (2000) 425

36) S. Park, D. Srivastava, K. Cho, Nano Lett. 3 (2003) 1273

37) G. Mpourmpakis, G.E. Froudakis, A.N. Andriotis, M.E. Menon, Appl. Phys. Lett. 87 (2005) 193105

38) H.C. Choi, M. Shim, S. Bangsaruntip, H. Dai, J. Am. Chem. Soc. 124 (2002) 9059

39) A. Maiti, A. Ricca, Chem. Phys. Lett. 395 (2004) 7

40) J. Zhong, G.M. Stocks, Appl. Phys. Lett. 87 (2005) 133105

41) W. Chen, X. Pan, M.G. Willinger, D.S. Su, X. Bao, J. Am. Chem. Soc. 129 (2007) 7421

42) M. Monthioux, P. Serp, E. Flahaut, C. Laurent, A. Peigney, M. Razafinimanana, W. Bacsa, J.-M. Broto. Introduction to carbon nanotubes. In "Springer handbook of nanotechnology" Second revised and extended Edition B. Bhushan (ed.), Springer-Verlag, Heidelberg, Germany (2007) 43

43) Q.H. Yang, P.X. Hou, S. Bai, M.Z. Wang, H.M. Cheng, Chem. Phys. Lett. 345 (2001) 18

44) S. Inoue, N. Ichikuni, T. Suzuki, T. Uematsu, K. Kaneko, J. Phys. Chem. 102 (1998) 4689

45) M. Eswaramoorthy, R. Sen, C.N.R. Rao, Chem. Phys. Lett. 304 (1999) 207

46) E. Raymundo-Piñero, P. Azaïs, T. Cacciaguerra, D. Cazorla-Amorós, A. Linares-Solano, F. Béguin, Carbon 43 (2005) 786

47) E. Raymundo-Piñero, T. Cacciaguerra, P. Simon, F. Béguin, Chem. Phys. Lett. 412 (2005) 184

48) N.M. Rodriguez, J. Mater. Sci. 8 (1993) 3233

49) Z. Chen, W. Thiel, A. Hirsch, ChemPhysChem. 1 (2003) 93

50) S. Park, D. Srivastava, K. Cho, Nano Lett. 3 (2003) 1273

51) X. Lu, Z. Chen, P. Schleyer, J. Am. Chem. Soc. 127 (2005) 20

52) H. Ulbricht, G. Moos, T. Hertel, Phys. Rev. B 66 (2002) 075404-1

53) H. Ulbricht, G. Kriebel, G. Moos, T. Hertel, Chem. Phys. Lett. 363 (2002) 252

54) E. Díaz, S. Ordóñez, A. Vega, J. Colloids Interface Sci. 305 (2007) 7

55) R. Pagani, C&EN. 1 (1999) 31
56) M.M.J. Treacy, T.W. Ebbesen, J.M. Gibson, Nature 381 (1996) 678
57) R.P. Gao, Z.L. Wang, Z.G. Bai, W.A. de Heer, L.M. Dai, M. Gao, Phys. Rev. Lett. 85 (2000) 622
58) M.F. Yu, O. Lourie, M.J. Dyer, K. Moloni, T.F. Keley, R.S. Ruoff, Science 287 (2000) 637
59) J.H. Bitter, in "Nanocatalysis", D.Y. Murzin (ed.), Research Signpost, Kerala, India (2006) 99
60) E. Díaz, S. Ordóñez, A. Vega, J. Colloids Interface Sci. 305 (2007) 7
61) C. Park, R.T.K. Baker, J. Phys. Chem. B 103 (1999) 2453
62) V. Apostolopoulou, J. Vakros, C. Kordulis, A. Lycourghiotis, Colloids and Surfaces A: Physicochemical and Engineering Aspects, In Press, Accepted Manuscript
63) T. Hino, T. Anzai, N. Kuramoto, Tetrahedron Lett. 47 (2006) 1429
64) N. Muradov, Catal. Commun. 2 (2001) 89
65) G. Mestl, N.I. Maksimova, N. Keller, V.V. Roddatis, R. Schlögl, Angew. Chem. Int. Ed. 40 (2001) 2066
66) D.S. Su, N. Maksimova, J.J. Delgado, N. Keller, G. Mestl, M.J. Ledoux, R. Schlögl, Catal. Today 102-103 (2005) 110
67) J.J. Delgado, R. Viera, G. Rebmann, D.S. Su, N. Keller, M.J. Ledoux, R. Schlögl, Carbon 44 (2006) 809
68) M.F.R. Pereira, J.L. Figueiredo, J.J.M. Órfão, P. Serp, P. Kalck, Y. Kihn, Carbon 42 (2004) 2807
69) P. Li, T. Li, J.H. Zhou, Z.J. Sui, Y.C. Dai, W.K. Yuan, D. Chen, Micropor. Mesopor. Mater. 95 (2006) 1
70) T.J. Zhao, W.Z. Sun, X.Y. Gu, M. Rønning, D. Chen, Y.C. Dai, D.K. Yuan, A. Holmen, Appl. Catal. A 323 (2007) 135
71) Z.J. Sui, J.H. Zhou, Y.C. Dai, W.K. Yuan, Catal. Today 106 (2005) 90
72) J.Z. Luo, L.Z. Gao, Y.L. Leung, C.T. Au, Catal. Lett. 66 (2000) 91
73) H. Ogihara, S. Takenaka, I. Yamanaka, K. Otsuka, Carbon 42 (2004) 1609
74) V.V. Shinkarev, V.B. Fenelonov, G.G. Kuvshinov, Carbon 41 (2003) 295
75) G.G. Kuvshinov, V.V. Shinkarev, A.M. Glushenkov, M.N. Boyko, D.G. Kuvshinov, China Particuology 4 (2006) 70
76) M. Croston, J. Langston, R. Sangoi, K.S.V. Santhanam, Int. J. Nanosci. 1 (2002) 277

77) M. Croston, J. Langston, G. Takacs, T.C. Morrill, M. Miri, K.S.V. Santhanam, P. Ajayan, Int. J. Nanosci. 1 (2002) 285
78) S. Yang, W. Zhu, X. Li, J. Wang, Y. Zhou, Catal. Commun. 8 (2007) 2059
79) F. Peng, L. Zhang, H. Wang, P. Lv, H. Yu, Carbon 43 (2005) 2405
80) Z. Kang, E. Wang, B. Mao, Z. Su, L. Gao, L. Niu, H. Shan, L. Xu, Appl. Catal. A 299 (2006) 212
81) S. van Dommele, K.P. de Jong, J.H. Bitter, Chem. Commun. (2006) 4859
82) H. Niwa, K. Horiba, Y. Harada, M. Oshima,T. Ikeda, K. Terakura, J. Ozaki, S. Miyata, J. Power Sources 187 (2009) 93
83) D.Z. Guo, G.M. Zhang, Z.X. Zhang, Z.Q. Xue, Z.N. Gu, J. Phys. Chem. B 110 (2006) 1571
84) S.H. Yang, W.H. Shin, J.W. Lee, S.Y. Kim, S.I. Woo, J.K. Kang, J. Phys. Chem. B 110 (2005) 13941
85) P. Serp, M. Corrias, P. Kalck, Appl. Catal. A 173 (2003) 337
86) D. Tasis, N. Tagmatarchis, A. Bianco, M. Prato, Chem. Rev. 106 (2006) 1105
87) T.G. Ros, A.G. van Dillen, J.W. Geus, D.C. Koningsberger, Chem. Eur. J. 5 (2002) 1151
88) N. Zhao, C. He, Z. Jiang, J. Li, Y. Li, Mater. Lett. 61 (2007) 681
89) B.C. Satishkumar, A. Govindaraj, G. Mofokeng, G.N. Subbanna, C.N.R. Rao, J. Phys. B: At. Mol. Opt. Phys. 29 (1996) 4925
90) S. Banerjee, S.S. Wong, J. Am. Chem. Soc. 126 (2004) 2073
91) S. Agrawal, M.S. Raghuveer, H. Li, G. Ramanath, Appl. Phys. Lett. 90 (2007) 193104
92) W. Li, C. Gao, H. Qian, J. Ren, D. Yan, J. Mater. Chem. 16 (2006) 1852
93) G. Maurin, I. Stepanek, P. Bernier, J.F. Colomer, J.B. Nagy, F. Henn, Carbon 39 (2001) 1273
94) N. Pierard, A. Fonseca, Z. Konya, I. Willems, G. Van tendeloo, J.B. Nagy, Chem. Phys. Lett. 335 (2001) 1
95) Y. Xing, L. Li, C.C. Chusuei, R.V. Hull, Langmuir 21 (2005) 4185
96) A. Kusnetzova, I. Popova, J.T. Yates, M.J. Bronikowski, C.D. Huffman, J. Liu, R.E. Smalley, H.H. Hwu, J.G. Chen, J. Am. Chem. Soc. 123 (2001) 10699
97) T. Kyotani, S. Nakazaki, W.H. Xu, A. Tomita, Carbon 39 (2001) 771
98) M.L. Toebes, J.M.P. Van Heeswijk, J.H. Bitter, A.J. van Dillen, K.P. de Jong, Carbon 42 (2004) 307
99) G. Ovejero, J.L. Sotelo, M.D. Romero, A. Rodriguez, M.A. Ocaña, G. Rodriguez, J. Garcia, Ind. Eng. Chem. Res. 45 (2006) 2206

100) Z. Liu, X. Lin, J.Y. Lee, W. Zhang, M. Han, L.M. Gan, Langmuir 18 (2002) 4054
101) J.L. Hudson, M.J. Casavant, J.M. Tour, J. Am. Chem. Soc. 126 (2004) 11158
102) J.J. Stephenson, J.L. Hudson, S. Azad, J.M. Tour, Chem. Mater. 18 (2006) 374
103) R.V. Hull, L. Li, Y. Xing, C.C. Chusuei, Chem. Mater. 18 (2006) 1780
104) A. Zamudio, A.L. Elías, J.A. Rodríguez-Manzo, F. Lopez-Urías, G. Rodríguez-Gattarno, F. Lupo, M. Rühle, D.J. Smith, H. Terrones, D. Diaz, M. Terrones, Small 2 (2006) 346
105) R. Chetty, S. Kundu, W. Xiaa , M. Brona, W. Schuhmann, V. Chirila,W. Brandl, T. Reineckec, M. Muhlera, Electrochimica Acta 54 (2009) 4208
106) A.H. Nevidomskyy, G. Csanyi, MC. Payne, Phys. Rev. Lett., 9 (2003) 1055021
107) F. Barroso-Bujans, J.L.G. Fierro, S. Rojas, S. Sánchez-Cortes, M. Arroyo, M.A. López-Manchado, Carbon 45 (2007) 1669
108) S. Delpeux, K. Szostak, E. Frakowiak, F. Béguin, Chem. Phys. Lett. 400 (2005) 374
109) R. Verdejo, S. Lamoriniere, B. Cottam, A. Bismarck, M. Shaffer, Chem. Commun. 2007 513
110) B.C. Satishkumar, A. Govindaraj, G. Mofokeng, G.N. Subbanna, C.N.R. Rao, J. Phys. B: At. Mol. Opt. Phys. 29 (1996) 4925
111) X. Lu, F. Tian, Y. Feng, X. Xu, N. Wang, Q. Zhang, Nano Lett. 2 (2002) 1325
112) W. Xia, V. Hagen, S. S. Kundu, Y. Wang, C. Somsen, G. Eggeler, G. Sun, G. Grundmeier, M. Stratmann, M. Muhler, Adv. Mater. 19 (2007) 3648
113) Z. Kónya, J. Zhu, K. Niesz, D. Mehn, I. Kiricsi, Carbon 42 (2004) 2001
114) A. Kukovecz, T. Kanyó, Z. Kónya, I. Kiricsi, Carbon 43 (2005) 994
115) R. Bacsa, P. Serp, In “Carbon metananotubes” M. Monthioux (ed.), Wiley, Germany, (2009) in press
116) V. Georgakilas, D. Gournis, V. Tzitzios, L. Pasquato, D.M. Guldi, M. Prato, J. Mater. Chem. 17 (2007) 2679
117) X. Fu, H. Yu, F. Peng, H. Wang, Y. Qian, Appl. Catal. A 321 (2007) 190
118) W.Z. Li, C. Liang, Z. Feng, P. Ying, D. Wang, C. Li, J. Mol. Catal. A 211 (2004) 103
119) S.J. Wang, S.F. Yin, L. Li, B. Q. Xu, C.F. Ng, C.T. Au, Appl. Catal. B 52 (2004) 287
120) W. Yang, S. Yang, J. Guo, G. Sun, Q. Xin, Carbon 45 (2007) 397
121) R.B. Rakhi, A. Leela Mohana Reddy, M.M. Shaijumon, K. Sethupathi, S. Ramaprabhu, J. Nanopart. Res. 10 (2008) 179
122) A. Corma, H. Garcia, A. Leyva, J. Mol. Catal. A 230 (2005) 97
123) H. Ma, L. Wang, L. Chen, C. Dong, W. Yu, T. Huang, Y. Qian, Catal. Commun. 8 (2007) 452

124) R.T.K. Baker, N. Rodriguez, A. Mastalir, U. Wild, R. Schlögl, A. Wootsch, Z. Paál, J. Phys. Chem. B 108 (2004) 14348
125) A. Kongkanand, K. Vinodgopal, S. Kuwabata, P.V. Kamat, J. Phys. Chem. B 110 (2006) 16185
126) W. Li, X. Wang, Z. Chen, M. Waje, Y. Yan, J. Phys. Chem. B 110 (2006) 15353
127) M.K. van der Lee, A.J. van Dillen, J.H. Bitter, K.P. de Jong, J. Am. Chem. Soc. 127 (2005) 13573
128) H. Zhang, J. Qiu, C. Liang, Z. Li, X. Wang, Y. Wang, Z. Feng, C. Li, Catal. Lett. 101 (2005) 211

129) S. Hermans, J. Sloan, D.S. Shepard, B.F.G. Johnson, M.L.H. Green, Chem. Commun. (2002) 276
130) X. Li, I.M. Hsing, Electrochem. Acta 51 (2006) 525
131) G. An, P. Yu, L. Mao, Z. Sun, Z. Liu, S. Miao, Z. Miao, K. Ding, Carbon 45 (2007) 536
132) R. Zanella, E.V. Basiuk, P. Santiago, V.A. Basiuk, E. Mireles, I. Puente-Lee, J.M. Saniger, J. Phys. Chem. B 109 (2005) 16290
133) Y. Wang, X. Xu, Z. Tian, Y. Zong, H. Cheng, C. Lin, Chem. Eur. J. 12 (2006) 2542
134) W. Li, C. Gao, H. Qian, J. Ren, D. Yan, J. Mater. Chem. 16 (2006) 1852
135) P. Serp, P. Kalck, R. Feurer, Chem. Rev. 102 (2002) 3085
136) W. Xia, O.F.K. Schlüter, C. Liang, M.W.E. van den Berg, M. Guraya, M. Muhler, Catal. Today 102-103 (2005) 34.
137) C. Liang, W. Xia, H. Soltani-Ahmadi, O.F.K. Schlüter, R.A. Fischer, M. Muhler, Chem. Commun. (2005) 282.
138) J.D. Kim, B.S. Kang, T.W. Noh, J.G. Yoon, S.I. Baik, Y.W. Kim, J. Electrochem. Soc. 152 (2005) D23
139) K. Lee, J. Zhang, H. Wang, D.P. Wilkinson, J. Appl. Electrochem. 36 (2006) 507
140) H. Liu, C. Song, L. Zhang, J. Zhang, H. Wang, D.P. Wilkinson, J. Power Sources 155 (2006) 95
141) S. Banerjee, S.S. Wong, Nano Lett. 2 (2002) 49
142) S. Banerjee, S.S. Wong, J. Am. Chem. Soc. 124 (2002) 8940
143) G. Leendert Bezemer, J.H. Bitter, H.P.C.E. Kuipers, H. Oosterbeek, J.E. Holewijn, X. Xu, F. Kaptjein, A.J. van Dillen, K.P. de Jong, J. Am. Chem. Soc. 128 (2006) 3956
144) L. Lemus-Yegres, I. Such-Basáñes, C. Salinas-Martínez de Lecea, P. Serp, M.C. Román-Martínez, Carbon 44 (2006) 605

145) H.B. Xu, H.Z. Chen, M.M. Shi, R. Bai, M. Wang, Mater. Chem. Phys. 94 (2005) 342
146) Y. Liu, A. Adronov, Macromolecules 37 (2004) 4755
147) F. Frehill, J.G. Vos, S. Benrezzak, A.A. Koos, Z. Konya, M.G. Ruther, W.J. Blau, A. Fonseca, J.B. Nagy, L.P. Biro, A.I. Minett, M. in het Panhuis, J. Am. Chem. Soc. 124 (2002) 13694
148) C Baleizão, B. Gigante, H. Garcia, A. Corma, J. Catal. 221 (2004) 77
149) S. Park, S.W. Yoon, K.B. Lee, D.J. Kim, Y.H. Jung, Y. Do, H.J. Paik, I.S. Choi, Macromol. Rapid Commun. 27 (2006) 47
150) K. Wiemann, W. Kaminski, F.H. Gojny, K. Schulte, Macromol. Chem. Phys. 206 (2005) 1472
151) S. Bredeau, L. Boggioni, F. Bertini, I. Tritto, F. Monteverde, M. Alexandre, P. Dubois, Macromol. Rapid Commun. 28 (2007) 822
152) Z. Yinghuai, S.L.P. Sia, K. Carpenter, F. Kooli, R.A. Kemp, J. Phys. Chem. Solids 67 (2006) 1218
153) T.G. Ros, A.J. van Dillen, G.W. Geus, D.C. Koningsberger, Chem. Eur. J. 8 (2002) 2868
154) F. Mercuri, A. Sgamelloti, J. Phys. Chem. B 110 (2006) 15291
155) E.L. Sceats, J.C. Green, J. Chem. Phys. 125 (2006) 154704-1
156) F. Nunzi, F. Mercuri, A. Sgamelloti, J. Phys. Chem. B 106 (2002) 10622
157) Y.V. Naidich, V.M. Perevertailo, O.B. Loginova, Izvestia Akad. Nauk. SSSR. Metally 4 (1979) 37
158) Y. Okamoto, Chem. Phys. Lett. 407 (2005) 354
159) P. Serp, in Carbon materials for catalysis, Edition: P. Serp, J.L. Figueiredo, John Wiley and sons, Inc. (2009)
160) G. Leendert Bezemer, J.H. Bitter, H.P.C.E. Kuipers, H. Oosterbeek, J.E. Holewijn, X. Xu, F. Kaptjein, A.J. van Dillen, K.P. de Jong, J. Am. Chem. Soc. 128 (2006) 3956
161) X. Dong, H.B. Zhang, G.D. Lin, Y.Z. Yuan, K.R. Tsai, Catal. Lett. 85 (2003) 237
162) H.B. Zhang, X. Dong, G.D. Lin, X.L. Liang, H.Y. Li, Chem. Commun. (2005) 5094
163) H. Zhang, J. Qiu, C. Liang, Z. Li, X. Wang, Y. Wang, Z. Feng, C. Li, Catal. Lett. 101 (2005) 211
164) S. Qin, D. Qin, W.T. Ford, D.E. Resasco, J.E. Herrera, J. Am. Chem. Soc. 126 (2004) 170
165) W. Qian, T. Liu, F. Wei, Z. Wang, H. Yu, Carbon 41 (2003) 846
166) Y. Cai, J.D. Lin, H.B. Chen, H.B. Zhang, G.D. Lin, D.W. Liao, Chinese Chem. Lett. 11 (2000) 373

167) C.-Y. Yen, Y.-F. Lin, C.-H. Hung, Y.-H. Tseng, C.-C.M. Ma, M.-C. Chang, H. Shao, Nanotechnology 19 (2008) 045604
168) C. Park, R.T.K. Baker, J. Phys. Chem. B 103 (1999) 2453
169) A. Chambers, T. Nemes, N.M. Rodriguez, R.T.K. Baker, J. Phys. Chem. B 102 (1998) 2251
170) C. Park, R.T.K. Baker, J. Phys. Chem. B 102 (1998) 5168
171) M. Zhou, G. Lin, H. Zhang, Chin. J. Catal. 28 (2007) 210
172) T.G. Ros, D.E. Keller, A.J. van Dillen, J.W. Geus, D.C. Koningsberger, J. Catal. 211 (2002) 85
173) M. Takasaki, Y. Motoyama, K. Higashi, S.H. Yoon, I. Mochida, H. Nagashima, Chem. Asian J. 2 (2007) 1524
174) T. Onoe, S. Iwamoto, M. Inoue, Catal. Commun. 8 (2007) 701
175) F. Winter, G. Leendert Bezemer, C. van der Spek, J.D. Meeldijk, A.J. van Dillen, J.W. Geus, K.P. de Jong, Carbon 43 (2006) 327
176) L.J. Lemus-Yegres, M.C. Román-Martínez, I. Such-Basáñez, C. Salinas-Martínez de Lecea, Microp. Mesop. Mater. 109 (2008) 305
177) W. Xia, O.F.K. Schülter, C. Liang, M.W.E. van den Berg, M. Guraya, M. Muhler, Catal. Today 102-103 (2005) 34
178) A.M. Zhang, J.L. Dong, Q.H. Xu, H.K. Rhee, X.L. Li, Catal. Today 93-95 (2004) 347
179) C. Park, M.A. Keane, J. Colloids Interface Sci. 266 (2003) 183
180) H. Wang, F. Zhao, S.I. Fujita, M. Arai, Catal. Commun. 9 (2008) 362
181) B. Yoon, C.M. Wai, J. Am. Chem. Soc. 127 (2005) 17174
182) B. Pawelec, V. La Parola, R.M. Navarro, S. Murcia-Mascarós, J.L.G. Fierro, Carbon 44 (2006) 84
183) C.H. Li, Z.X. Yu, K.F. Yao, S.F. Ji, J. Liang, J. Mol. Catal. A 226 (2005) 101
184) Y. Zhao, C.H. Li, Z.X. Yu, K.F. Yao, S.F. Ji, J. Liang, Mater. Chem. Phys. 103 (2007) 225
185) X.X. Han, Q. Chen, R.X. Zhou, J. Mol. Catal. A 277 (2007) 210
186) S.J. Wang, W.X. Zhu, D.W. Liao, C.F. Ng, C.T. Au, Catal. Today 93-95 (2004) 711
187) C.Y. Hu, F.Y. Li, L. Hua, R.B. Zhang, J. Serb. Chem. Soc. 71 (2006) 1153
188) M. Ruta, I. Yuranov, P.J. Dyson, G. Laurenczy, L. Kiwi-Minsker, J. Catal. 247 (2007) 269
189) L. Rodriguez-Perez, E. Teuma, A. Falqui, M. Gomez, P. Serp, Chem. Commun., 35 (2008) 4201

190) V.V. Chesnokov, I.P. Prosvirin, N.A. Zaitseva, V.I. Zaikovskii, V.V. Molchanov, Kinet. Catal. 43 (2002) 838
191) L. Xing, F. Du, J.J. Liang, Y.S. Chen, Q.L. Zhou, J. Mol. Catal. A 276 (2007) 191
192) F. Salman, C. Park, R.T.K. Baker, Catal. Today 53 (1999) 385
193) E. Asedegbega-Nieto, A. Guerrero-Ruiz, I. Rodríguez-Ramos, Carbon 44 (2006) 804
194) V. Lordi, N. Yao, J. Wei, Chem. Mater. 13 (2001) 733
195) C. Pham-Huu, N. Keller, L.J. Charbonniere, R. Ziessel, M.J. Ledoux, Chem. Commun. (2000) 1871
196) C. Pham-Huu, N. Keller, G. Ehret, L.J. Charbonniere, R. Ziessel, M.J. Ledoux, J. Mol. Catal. A 170 (2001) 155
197) J.P. Tessonnier, L. Pesant, G. Ehret, M.J. Ledoux, C. Pham-Huu, Appl. Catal. A 288 (2005) 203
198) I. Janowska, G. Winé, M.J. Ledoux, C. Pham-Huu, J. Mol. Catal. 267 (2007) 92
199) M.L. Toebes, Y. Zhang, J. Hájek, T. A. Nijhuis, J.H. Bitter, A.J. Van Dillen, D.Y. Murzin, D. C. Koninsberger, K.P. De Jong, J. Catal. 226 (2004) 215
200) M.L. Toebes, T.A. Nijhuis, J. Hajek, J.H. Bitter, A.J. van Dillen, D.Y. Murzin, K.P. de Jong, Chem. Eng. Sci. 60 (2005) 5682
201) J.M. Planeix, N. Coustel, B. Coq, V. Brotons, P.S. Kumbhar, R. Dutartre, P. Geneste, P. Bernier, P.M. Ajayan, J. Am. Chem. Soc. 116 (1994) 7935
202) M.L. Toebes, F.F. Prinsloo, J.H. Bitter, A.J. van Dillen, K.P. de Jong, J. Catal. 214 (2003) 78
203) V. Brotons, B. Coq, J.M. Planeix, J. Mol. Catal. A 116 (1997) 397
204) Y. Li, Z.G. Li, R.X. Zhou, J. Mol. Catal. A 279 (2008) 140
205) Y. Li, G.H. Lai, R.X. Zhou, Applied. Surf. Sci. 253 (2007) 4978
206) H. Vu, F. Gonçalves, R. Philippe, E. Lamouroux, M. Corrias, Y. Kihn, D. Plee, P. Kalck, P. Serp, J. Catal. 240 (2006) 18
207) J. Qiu, H. Zhang, X. Wang, H. Han, C. Liang, C. Li, React. Kinet. Catal. Lett. 88 (2006) 269
208) E. Castillejos, P-J Debouttière, L. Roiban, A. Solhy, V. Martinez, Y. Kihn, O. Ersen, K. Philippot, B. Chaudret, P. Serp, Angew. Chem., 121 (2009) 2567
209) P. Gallezot, D. Richard, Catal. Rev. - Sci. Eng. 40 (1998) 81
210) Y. Li, G.H. Lai, R.X. Zhou, Applied. Surf. Sci. 253 (2007) 4978
211) J. Qiu, H. Zhang, X. Wang, H. Han, C. Liang, C. Li, React. Kinet. Catal. Lett. 88 (2006) 269

212) K. Lee, J. Zhang, H. Wang, D.P. Wilkinson, J. Appl. Electrochem. 36 (2006) 507
213) H. Liu, C. Song, L. Zhang, J. Zhang, H. Wang, D.P. Wilkinson, J. Power Sources 155 (2006) 95
214) B. Rajesh, K. Ravindranathan Thampi, J.M. Bonard, N. Xanthopoulos, H.J. Mathieu, B. Viswanathan, J. Phys. Chem 107 (2003) 2701
215) B. Rajesh, V. Karthik, S. Karthikeyan, K. Ravindranathan Thampi, J.M. Bonard, B. Viswanathan, Fuel 81 (2002) 2177
216) J.-S. Huang, X.-G. Zhang, J.-M. Luo, J.-Y. Sun, W.-J. Yang, J. Solid State Electrochem. 12 (2008) 113
217) W. Li, C. Liang, J. Qiu, H. Li, W. Zhou, G. Sun, Q. Xin, React. Kinet. Catal. Lett. 82 (2004) 235
218) X. Zhao, W. Li, L. Jiang, W. Zhou, Q. Xin, B. Yi, G. Sun, Carbon 42 (2004) 3251
219) S. Liao, K.A. Holmes, H. Tsaprailis, V.I. Birss, J. Am. Chem. Soc. 128 (2006) 3504
220) W. Yang, S. Yang, J. Guo, G. Sun, Q. Xin, Carbon 45 (2007) 397
221) D.J. Guo, H.L. Li, J. Colloids Interface Sci. 286 (2005) 274
222) D.J. Guo, H.L. Li, Carbon 43 (2005) 1259
223) P. Santhosh, A. Gopalan, K.P. Lee, J. Catal. 238 (2006) 177
224) A.L.M. Reddy, N. Rajalakshmi, S. Ramaprabhu Carbon 46 (2008) 2
225) Y.G. Wang, L. Feng, F. Li, H.M. Xiong, Y.Y. Xia, Chem. Mater. 19 (2007) 2095
226) C.A. Bessel, K. Laubernds, N.M. Rodriguez, R.T.K. Baker, J. Phys. Chem. 105 (2001) 1115
227) M. Tsuji, M. Kubokawa, R. Yano, N. Miyamae, T. Tsuji, M.S. Jun, S. Hong, S. Lim, S.H. Yoon, I. Mochida, Langmuir 23 (2007) 387
228) W. Li, X. Wang, Z. Chen, M. Waje, Y. Yan J. Phys. Chem. B 110 (2006) 15353
229) T. Maiyalagan, B. Viswanathan, U.V. Varadaraju, Electrochem. Commun. 7 (2005) 905
230) L. Li, G. Wu, B.-Q. Xu, Carbon 44 (2006) 2973
231) J.-H. Wee, K.-Y. Lee, S.H. Kim, J. Power Sources 165 (2007) 667
232) J.M. Tang, K. Jensen, M. Waje, W. Li, P. Larsen, K. Pauley, Z. Chen, P. Ramesh, M.E. Itkis, Y. Yan, R.C. Haddon, J. Phys. Chem. C 111 (2007) 17901
233) Y. Xing, J. Phys. Chem. B 108 (2004) 19255
234) J.M. Liu, H. Meng, J.I. Li, S.J. Liao, J.H. Bu, Fuel Cells 5 (2007) 402
235) Y.L. Hsin, K.C. Hwang, C.T. Yeh, J. Am. Chem. Soc. 129 (2007) 9999
236) Z. Yu, Ø. Borg, D. Chen, E. Rytter, A. Holmen, Topics Catal. 45 (2007) 69
237) J. Lu, Carbon 45 (2007) 1599

238) N. Ishigami, H. Ago, Y. Motoyama, M. Takasaki, M. Shinagawa, K. Takahashi, T. Ikuta, M. Tsuji, Chem. Commun. (2007) 1626

II-Carbon nanostructures synthesis by catalytic chemical vapor deposition

Chapter II-Carbon nanostructures synthesis by catalytic chemical vapor deposition

In this chapter, we describe the elaboration of supported nanoparticles of iron, nickel, and cobalt by the metalorganic chemical vapor deposition (MO-CVD) method and their use as catalysts for the catalytic chemical vapor deposition of novel nanostructured carbon materials. Iron pentacarbonyl or nickelocene were used as iron or nickel sources for metalorganic chemical vapor deposition. An iron oxide supported on alumina was used for the synthesis of single- double- and multi-walled carbon nanotubes [1]. Metallic iron nanoparticles supported on alumina associated react with organic compounds (acetonitile, pyridine…) to yield nitrogen doped carbon nanofibers. Nickel metallic nanoparticles supported on alumina were used for nanofibers synthesis [2]. A cobalt oxide catalyst supported on silica was prepared by incipient wetness impregnation and gave in association with acetonitrile nitrogen doped multi-walled carbon nanotubes [3].

II-1-Introduction

II-1-1- Introduction to CVD techniques on powders

Chemical vapor deposition is an important technique for surface modification of powders through either grafting or deposition of thin films and coatings. It consists of bringing a reactive gas in contact with the solid particles to be treated. Different technologies exist to ensure such contact making CVD a flexible technique to adapt according to application demands [4]. Different gas-solid contact gave different CVD nominations and processes but the basic principle remains the same. Each contact mode has advantages and drawbacks.

The basic techniques are the fixed bed and the flat hearth (Fig. 1), where gas flows respectively through and over powders whose particles do not move relative to each other. In this case if the gas flow rate is sufficiently low, the gas merely percolates through the voids between the stationary particles.

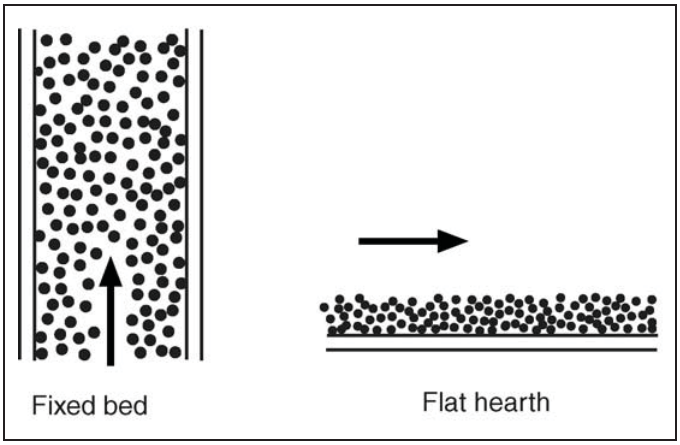

Figure 1: Basic fixed bed CVD techniques

There are numerous drawbacks related to these processes: i) as in the case of chemical vapor infiltration, diffusion limitations may affect the efficient contact between the gas reactants and the inner particles, ii) it is impossible to perform deposition on the entire surface of each particle due to contact points among them and with the reactor walls, iii) when high growth rates are expected, clogging phenomena can occur, and iv) the scale-up of these processes is problematic.

A relative improvement of the previous techniques was to impose a movement of the particles relative to each other (Fig. 2). In such cases, it is expected that each particle will present its entire surface to the gaseous reactant during the process. We can distinguish different techniques such as the rotary cylinder, pneumatic conveying, the vertical moving beds and, the most frequently employed technique the fluidized bed (FB-CVD).

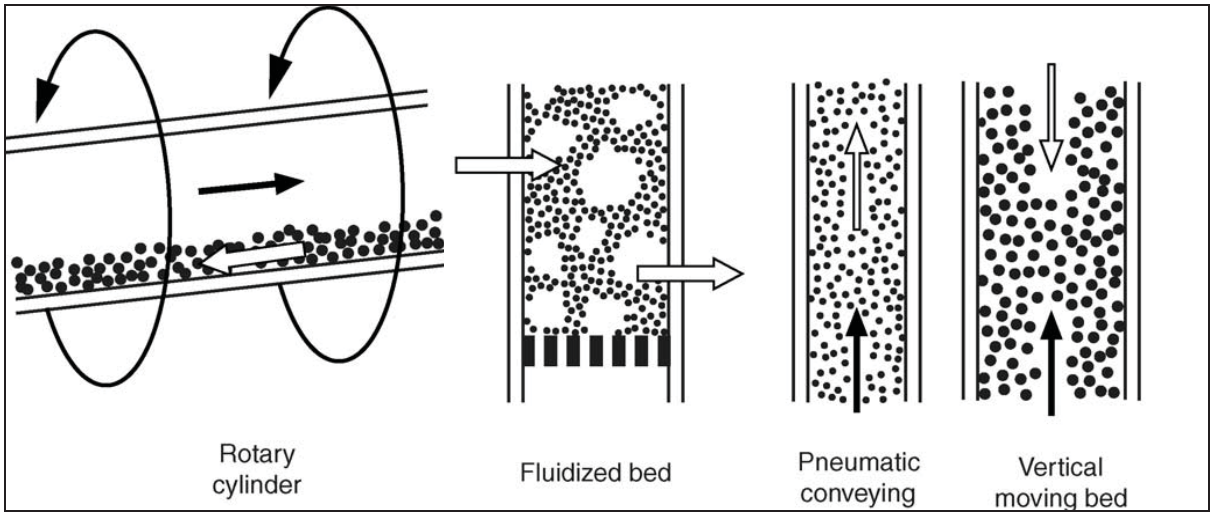

Figure 2: Improvement of CVD contactors for powders [5]

The choice of both reactors type and operating conditions are of extreme importance to ensure success in the desired application.

The fluidized bed technology is interesting since the movement of the particles is achieved by the carrier and/or the reactive gases, and no additional cost effective apparatus are needed. For this latter, due to a high degree of gas-solid mixing, diffusive phenomena only occur near the boundaries of bubbles, and mass transfer rates are mainly convective ensuring homogeneous deposition. The high degree of contact between gases, powders and reactor walls in FB-CVD lead to high heat transfer rates, thus ensuring advantageous isothermal conditions both radially an axially in the bed [6].

A detailed presentation of the FB-CVD technique for catalyst preparation was reported in the thesis of Emmanuel Lamouroux [7], and numerous books dedicated to fluidization [8, 9] describe the behavior of a fluidized-bed. In summary, fluidized bed regime is when solid particles over a gas distributing plate (called the grid or the distributor) are made to behave like a fluid by passing gas through it at a flow rate over a critical value.

In our work, we defined two main objectives: the catalyst elaboration, and carbon nanostructure synthesis. In both cases a fluidized bed chemical vapor deposition apparatus was used.

II-1-2- FB-CVD for catalyst preparation

Except for the cobalt catalyst all of the catalysts were prepared by the fluidized bed metalorganic chemical vapor deposition technique (FB-MOCVD).

The choice of a dry technique instead of traditional wet methods such as impregnation, ion exchange, or sol-gel was based on different reasons. Corresponding processes use environmentally harmful solvents, involves several steps such as drying, oxidation or reduction, potentially leading to redistribution of the metal deposit over the support and non reproducibility of the as prepared materials. Additionally, for wet methods an organic additive may be needed (surfactant, ligand, polymers) to achieve nanoparticles stability [10]. Such distribution and size control would not last at the high temperatures required for carbon nanostructure synthesis (650 and 1000 °C).

For the CVD technique a good dispersion of the metal nanoparticles and the control of their size for a given metal loading relay on precursor vapor pressure, which governs the nucleation rate, temperature, pressure, and metal-support interaction [4, 7].

Those advantages of CVD over liquid phase impregnation procedure for catalyst preparation often result in better catalytic activity [11-18].

On the other hand, drawbacks do exist for CVD- based processes. One can mention the difficulty to optimize the process, which can be attributed to the large number of tunable parameters, and the possible toxicity of precursors and of their decomposition products that may limit the large scale applications.

In this work, we will try to promote the FB-CVD technique, which in spite of all its advantages, remains relatively under employed compare to the conventional techniques of catalyst preparation [19-21].

II-1-2-1-Precursor's choice

The use of reactive metalorganic complexes and not metal salts as metal precursors often provides to clean deposit at low temperature, since the metal to ligand bonding is fragile and easily broken. The choice of such precursors must take into account several issues depending on application demands: i) it must be easy to prepare and commercially available, ii) the less toxic the compound, the better it is, iii) it must be gas transportable, have good volatility to yield appropriate vapor pressure by sublimation or evaporation so as to ensure good nucleation and growth rate of nanoparticles, iv) the decomposition temperature and eventual contaminations (C, N,…) must be as low as possible, v) the oxidation state of the complex should be taken into account depending on the desired oxidation state of the deposit, and vi) finally, the precursor must be economically affordable for large scale production. One should also consider that for the same metal, different metalorganic precursors could lead to different catalytic activity and structural properties. Taking into account those previous issues and as a continuity of previous work performed in our laboratory, iron pentacarbonyl [$Fe(CO)_5$] [7] and nickellocene [22] were used as iron and nickel sources, respectively. Some of the features of such choices are reminded below:

Iron pentacarbonyl [$Fe(CO)_5$]

Over the years, iron carbonyl have played a central role in the development of carbonyl chemistry, and represent one of the largest classes of transition metal carbonyl compounds.

Iron pentacarbonyl is a straw-colored liquid with a musty odor. It is toxic [23] but does not react with air at room temperature. It has a relative high vapor pressure (21 torr at 20°C) which can be represented in Equation 1:

$$\text{Log } P_{\text{Torr}} = 8{,}4959 - (2096{,}7/T) \qquad \text{(Eq. 1)}$$

At temperature above 100 °C iron pentacarbonyl undergoes thermal decomposition [24]. This pyrolysis has been investigated as a means of producing thin, coherent metal oxide iron films. In the presence of air or pure oxygen, [$Fe(CO)_5$] oxidation leads to iron(III) oxide attributed to be Fe_2O_3 [23].

Nickelocene [$Ni(Cp)_2$]

Nickelocene or cyclopentadienyl nickel is a dark powder that can only tolerate brief exposure to air before noticeable decomposition. It decomposes at its melting point (173 °C), and the sublimation temperature was found experimentally at 65 °C. The nickel is in the Ni^{2+} oxidation state. The use of metallocene as precursor for thermal vapor deposition of metals such as titanium, vanadium, iron, nickel and ruthenium has been reported before [25]. However, its thermolysis is known to give two radical species identified by mass spectroscopy at m/e=65 and 123 and a molecule having m/e=130. Those species could react with each other yielding different organic species poisoning the catalyst [26]. In order to have a metallic Ni deposition, free of any organic contaminations, H_2 can be added as an assisting reactive gas to enhance decomposition (section II-4).

II-1-3- Carbon nanostructure synthesis

In the literature, due to its scale up ability and relative mild conditions, catalytic chemical vapor deposition (C-CVD) technique is largely used for carbon nanostructure synthesis using supported metal nanocatalysts [1-3, 27].

In our laboratory, two processes have been chosen for C-CVD, the flat hearth process and a fluidized bed reactor. For primary studies on single-walled carbon nanotubes synthesis, low yields are expected so that the flat hearth process would ease the product recuperation after synthesis. As for the other carbon nanostructures synthesis, a fluidized bed CVD apparatus was used.

II-2- SWCNT C-CVD synthesis from iron oxide /Al_2O_3 catalysts

II-2-1- State of the art

Based on the evaluation of carbon solubility and carbide stability from the carbon-metal binary phase diagrams, it has been suggested that Fe, Co, and Ni are the only active elements capable of catalyzing SWCNT growth among 70 elements that include most of the

transition metals [28]. Such synthesis could be performed under different gas mixtures, temperatures and pressions. Most commonly, the active metals are associated to one or many co-catalyst such as Mo, V, Ru or others [29]. Catalytic nanoparticles could be formed in situ by decomposition of a metal precursor and yield directly SWCNTs [30] or previously supported on a stable metal oxide such as alumina, silica or magnesium oxide.

Isolated SWCNTs were produced by disproportion of CO at 1200 °C over Mo nanoparticles of a few nanometers in size supported on alumina [31]. This was the first experimental evidence of SWCNTs produced by pre-formed catalytic particles and the tube diameters ranged from 1 to 5 nm, closely similar to the size of the catalytic particle found attached to the tip of the tube. The molybdenum catalyst used in these experiments was prepared by mixing bis(acetylacetonato) dioxomolybdenum with fumed alumina nanoparticles (1:10 by weight).

The first large scale SWCNT production process was based on the disproportionation of CO. The CoMoCAT process developed by the research group of Prof. D. Resasco at the University of Oklahoma is based on a bimetallic catalyst of Co and Mo supported on silica gel and CO disproportionation (decomposition into C and carbon dioxide) at 700-950 °C [32].

Then the high-pressure carbon monoxide (HiPCO) process, developed at Rice University, has been reported to produce single-walled carbon nanotubes from gas-phase reactions of iron carbonyl and carbon monoxide at high pressures (10-100 atm) [33].

On laboratory scale research continued. Fe/Ni/Mg catalyst was used in the arc discharge process [34]. J. Kong et al studied the carbon products of the CVD using CH_4 as carbon source upon different metal oxide catalysts supported on silica or alumina by wet impregnation method [35]. Representative results are assembled in Table 1.

Catalyst Composition	Support material	SWCNTs	Description of synthesis material
Fe_2O_3	Alumina	Yes	Abundant individual SWCNTs, some bundles, occasional double-walled tubes
Fe_2O_3	Silica	Yes	Abundant SWCNT bundles
CoO	Alumina	Yes	Some SWCNT bundles and individual SWCNTs
CoO	Silica	No	No tubular materials synthesis
NiO	Alumina	No	Mainly defective multi-walled structures with partial metal filling
NiO	Silica	No	No tubular materials synthesis
NiO/CoO	Alumina	No	No tubular materials synthesis
NiO/CoO	Silica	Yes	Some SWCNT bundles

Table 1: Different carbonaceous products as a function of different catalysts [35]

Gold nanoparticles catalyst prepared by block copolymer templating technique for the synthesis of SWCNTs and MWCNTs have been recently reported [36], but such catalysts make the process very expensive for large scale SWCNT production. Single-walled carbon nanotubes were synthesized on SiO_2/Si substrates by thermal chemical vapor deposition using an Al/Fe/Mo triple layer catalyst, methane (CH_4) as carbon source, and a mixture of Ar/H_2 (10% H_2) as the carrier gas [37].

Recent papers appeared describing the benefits of using as catalyst a solid solution of transition metal oxide(s) and non reducible (at practical temperature) oxides. These solid solutions of mixed oxides must be calcined at relatively high temperatures to avoid the presence of oxide phases. Bacsa et al describe a catalyst made by the selective reduction (T > 800 °C) in H_2/CH_4 of solid solution between one or more transitional metal oxides and a non-reducible oxide such as Al_2O_3, $MgAl_2O_4$ or MgO. Those solid solutions were prepared by combustion synthesis, employing combustion of both precursors and a fuel as urea [38].
Alternative to CH_4 and CO, alcohols are being used as carbon sources [39].

In summary, parameters of SWCNT synthesis; i.e supported catalyst *vs* non supported catalyst, choice of active metals Fe, Ni, Co (monometallic, bimetallic) with or without co-catalyst (Mo, V, Ru), their oxidation state, and the relative reactive atmosphere (CO, CH_4 or ethanol) associated to them, make such synthesis largely tunable and complex.

In general, three characteristics are examined in order to determine whether a process will be commercially feasible for the production of a desired carbon nanotube type on an industrial scale. The first is catalyst selectivity, e.g. will the catalyst yield primarily single-walled carbon nanotubes or primarily multi-walled carbon nanotubes or other forms of carbon products? Specifically, the catalyst selectivity towards single-walled carbon nanotubes can be measured through evaluation of Raman spectra signatures of fibril-containing products, which are informative for differentiating single and double–walled carbon nanotubes from multi-walled carbon nanotubes [40]. Indeed, a sample having sufficiently small diameter nanotubes, to be single-walled has to exhibit a Raman spectrum with "radial breathing mode" (RBM) peaks between 150 and 300 wave numbers, the area under the RBM peaks at least 0.1% of the area under a characteristic G band peak, and the intensity of the G band peak at least twice that of a characteristic D band peak (I_G/I_D of at least 2) [41]. Selectivity determination is also completed by TEM observations and thermogravimetric analysis.

The second is catalyst yield (mass of carbon product generated divided by the mass of catalyst used) that should be as high as possible.

The third is the effective cost, security and environmental issues related to such process. Cobalt and nickel compounds are toxic and relatively expensive. Iron is cheaper and less toxic. CO large scale manipulation could be dangerous and is preferably being replaced by methane. So, the studies should be better focused on iron based catalysts and carbon sources other than CO.

In previous studies of our group, MWCNT synthesis was performed on iron catalysts supported on alumina elaborated by MO-CVD [42]. Bimetallic Fe-Mo catalysts supported on alumina by MO-CVD catalyzed the SWCNT synthesis [43]. In this work, we investigated the SWCNT synthesis from monometallic iron oxide catalyst supported on alumina. The same type of catalyst will also be used for MWCNT synthesis. Our aim is to control the number of walls and diameter of the produced nanotubes as a function of the imposed synthesis conditions.

The key element of such catalyst's choice, relay on the ionic interaction between Al^{3+} of γ-alumina and Fe^{3+} ions which are known to be chemically similar [44], and should favour a very strong metal support interaction, yielding small iron oxide nanoparticles on alumina that should be suitable for SWCNT growth at high temperatures. Of course, the atmosphere

used during SWCNT synthesis, and in particular the presence or not of hydrogen, may impact the course of the reaction since hydrogen may induce some sintering and favour methanation.

II-2-2- SWCNT synthesis on iron oxide supported on alumina

In the literature most of the studies dealing with the synthesis of SWCNTs are limited to the presentation of the synthesis process and characterization of SWCNTs but few focuses on catalytic activity. Production of SWCNTs with high yield remains a challenge. First we will be interested in finding conditions of good selectivity towards SWCNTs then we will try to increase the catalytic activity as high as possible without loosing selectivity.

We have prepared three iron oxide/Al_2O_3 catalysts (2, 4 and 6% w/w) by MO-CVD from iron pentacarbonyl in the presence of a low partial pressure of oxygen and water. The MO-CVD reactor is presented in Fig. 3 and the detailed preparation procedure in chapter V.

Figure 3: FB-CVD apparatus for the catalysts elaboration

Based on our collected data from the literature, a loading of 2% wt of iron should be a good compromise between having enough iron nanoparticles to obtain good activity, and optimum nanoparticles size and distribution for the best selectivity towards SWCNTs. Below 2%, activity may be too low, and above large nanoparticles may start yielding other carbon nanostructures as carbon nanofibers, multi-walled carbon nanotubes and encapsulated metal particles.

After the MO-CVD deposition, the fresh 2% Fe/Al_2O_3 MO-CVD catalyst was first tested under different atmospheres assembled in Table 2. The corresponding flat hearth reactor is presented in Fig. 4 and the detailed preparation procedure is given in chapter V.

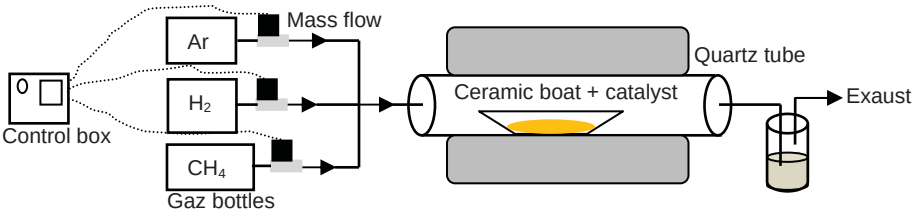

Figure 4: Flat hearth CVD apparatus for SWCNT synthesis

Test	CH_4 sccm	Ar sccm	H_2 sccm	I_G/I_D	RBM
1	100	200	0	0.76	*
2	100	190	10	0.86	**
3	100	180	20	0.86	**
4	100	150	50	0.90	None
5	100	100	100	0.86	None
6	200	0	100	0.76	None
7	200	100	0	1.08	***

T_d=900°C; heating rate = 30 °C/min; $t_{deposition}$=30min; *little **average ***a lot

Table 2: Different gas mixtures of CH_4, H_2, and Ar for SWCNT synthesis

Identification of the composition of the resulting carbon deposit was made by Raman spectroscopy and TEM observations.

In the TEM micrographs of all these samples, whatever the reactive atmosphere used, a mixture of SWCNTs, fibers and carbon encapsulated nanoparticles was observed (Fig. 5).

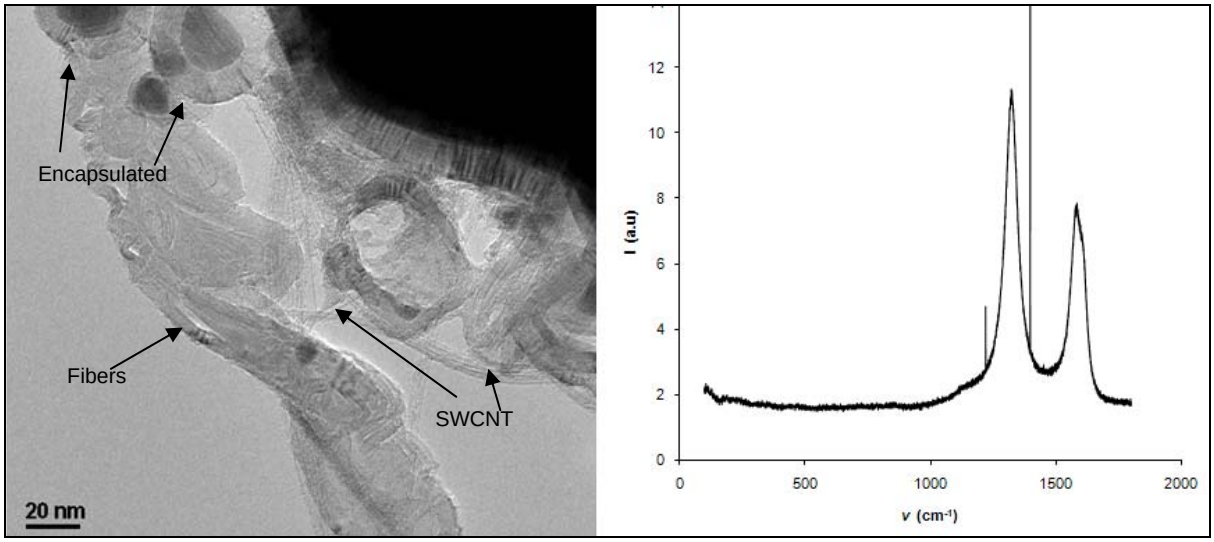

Figure 5: TEM micrograph (left) and Raman spectrum (right) of the sample 7

This was in accordance with the Raman spectra recorded at 632 nm were the ratio of the intensity of the G to the D band (I_G/I_D) was very low, typically below 1. The absence of radial breathing modes (RBM) could be correlated either to the non excitation under the wave number of the Raman laser (632 nm) or to the real absence of the SWCNT structure.

Based on the experience of our laboratory, SWCNTs oxidize under air in the range 470-510 °C [1]. Calcination temperatures of the deposited carbon structures were either too high (550 °C) to be considered as SWCNTs or were spread over a large window (470-550 °C). The catalytic activity ranged between 1.9 h^{-1} (test 6) and 3.7 h^{-1} (test 7).

Based on TEM, Raman and TGA results, the as prepared MO-CVD catalyst of 2% iron oxide supported on alumina was not selective towards SWCNT synthesis. The causes of the failure could be correlated to its structure or to the reactive gas mixture, or both.

As far as the reactive atmosphere was concerned, essential parameters such as hydrogen and methane partial pressure were varied inside the reactor (Table 2). Hydrogen is described in the literature as an agent to improve selectivity via methanation: etching back the carbon deposit to CH_4 [45]. In our case no improvement of the I_G/I_D ratio in the Raman spectra occurred by increasing the H_2 partial pressure in the reactor (test 2 to 5 in Table 2).

The process of the carbon nanostructure formation involves critical steps of carbon enrichment of metal nanoparticles, its diffusion, and precipitation onto their surface (Fig. 6). Each step rate, and the size of the formed carbon nuclei depends on the carbon partial pressure of the atmosphere, the nature of the catalytic metal involved, the nanoparticles size and reaction temperature.

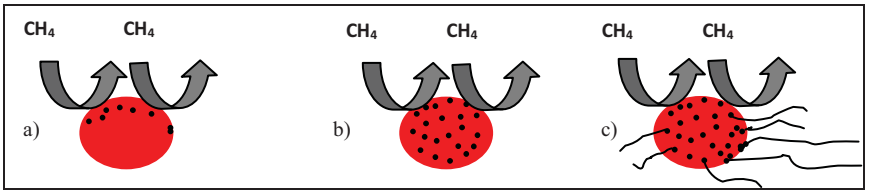

Figure 6: Different steps of carbon transformation during the nanostructure formation: a) Carbon enrichement on the surface, b) Carbon diffusion, c) Carbon precipitation

A thermodynamic model, which does not take into account the presence of the support, has been developed to describe the CNT growth from a droplet of supersaturated carbon melt in a metal catalyst, and the relevant calculations enable the construction of a phase diagram showing that the CNT type depends on the melt supersaturation with carbon and on the droplet radius [46]. At low carbon supersaturation the encapsulation of the nanoparticles occurs, MWCNTs are formed if the supersaturation is increased and at high carbon supersaturation SWCNTs can be produced (Fig. 7).

Figure 7: Type of carbon nanostructure obtained as a function of the carbon supersaturating ratio of the NPs

In our case, doubling the partial pressure of CH_4 in the reactor in order to increase the sursaturation of the iron nanoparticles with carbon did not improve the selectivity.

The lack of selectivity could stem out of the catalyst structure. The catalytic performances of a supported catalyst are related to numerous factors like the preparation method, nanoparticles size, crystallographic and electronic structure, phases present during growth, oxidation state, or simply the adhesion and accessibility of the active phase on the alumina support [47].

II-2-3- Activation of the 2% Fe/Al_2O_3 MO-CVD catalyst

The preparation of supported catalysts by classical wet methods usually comprises a calcinations step at high temperatures to eliminate contaminants [48]. Inspired by such methods, the freshly deposited MO-CVD catalyst was heated at 900 °C under static air for different periods of time and the effect of such treatment on SWCNT selectivity was studied under the condition of high partial pressures of hydrogen (100 sccm) and methane (200 sccm). The results are summarized in Table 3.

Test	$t_{activation}$ (h)	I_G/I_D	RBMs	$g_C/g_{catalyst}$	$T_{oxidation}$ (°C)	g_C/g_{Fe}	TOF (h^{-1})
6	0	0.76	None	0.019	544	0.95	1.9
8	1	0.80	**	0.017	490;539	0.85	1.7
9	3	1.10	**	0.010	520	0.5	1.0
10	5	0.75	None	0.019	540	0.95	1.9
11	10	5.10	***	b.d	-	b.d	b.d

2% Fe/Al_2O_3, 200 sccm CH_4; 2 sccm Ar; 100 sccm H_2; T_d=900 °C; b.d=below detection

Table 3: Effect of time spent at 900°C on the catalyst selectivity towards SWCNT

Based on the Raman spectroscopy, as a function of the time spent at 900°C there is a slight selectivity improvement from 0 to 5 h. At 10 h of activation, a high selectivity is observed, the G band being 5 times more intense than the D one (Table 3) and clear and very intense RBMs were observed in the range of 100-200 cm^{-1} (Fig. 8).

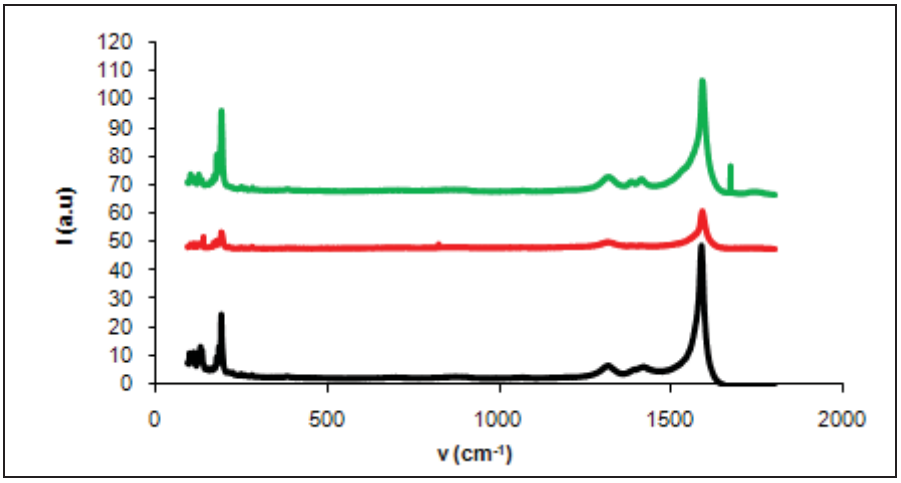

Figure 8: Raman spectra of sample 11

In the TEM micrographs of sample 11 only bundles of SWCNTs were observed (Fig. 9).

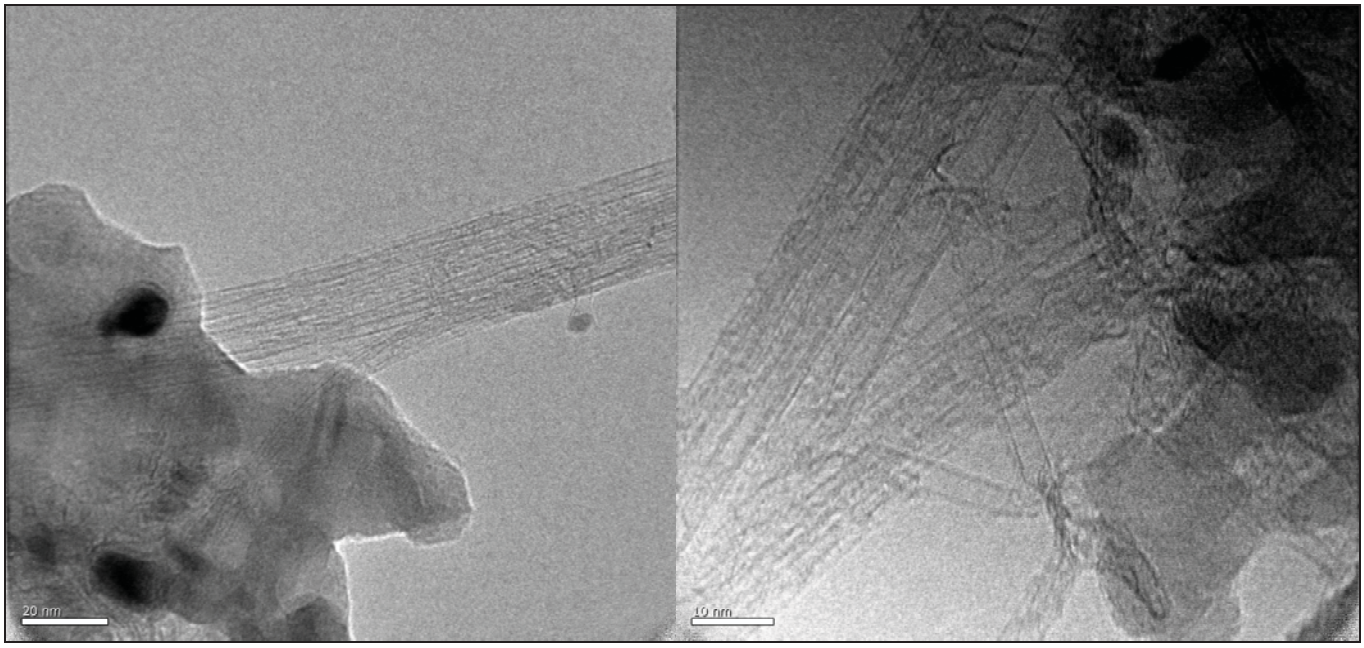

Figure 9: TEM micrographs of sample 11

However, the carbon yield of sample 11 was too low to be detectable by TGA. The difficulty rose due to the gain of weight by the sample in the TGA analysis from 25 to 1000 °C, probably due to iron reoxidation (Fig. 10). Nevertheless, a weak signal (0.3%) between 406 and 490°C could be due to SWCNT oxidation.

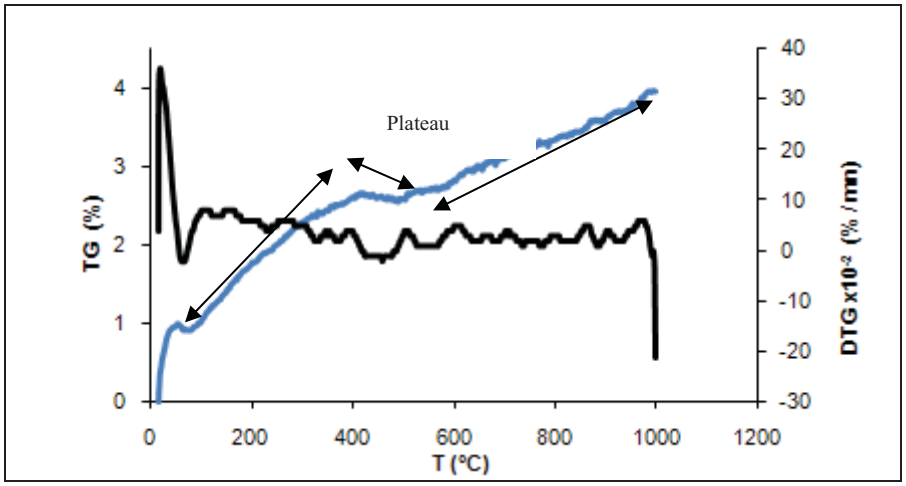

Figure 10: TGA thermogram of sample 11

To have an overlook and another accurate confirmation of the population of the SWCNTs over the catalyst grain we performed SEM observations. In the SEM micrograph represented in Fig. 11 we can see the grain of the catalyst decorated by few bundles of SWCNTs confirming the low yields.

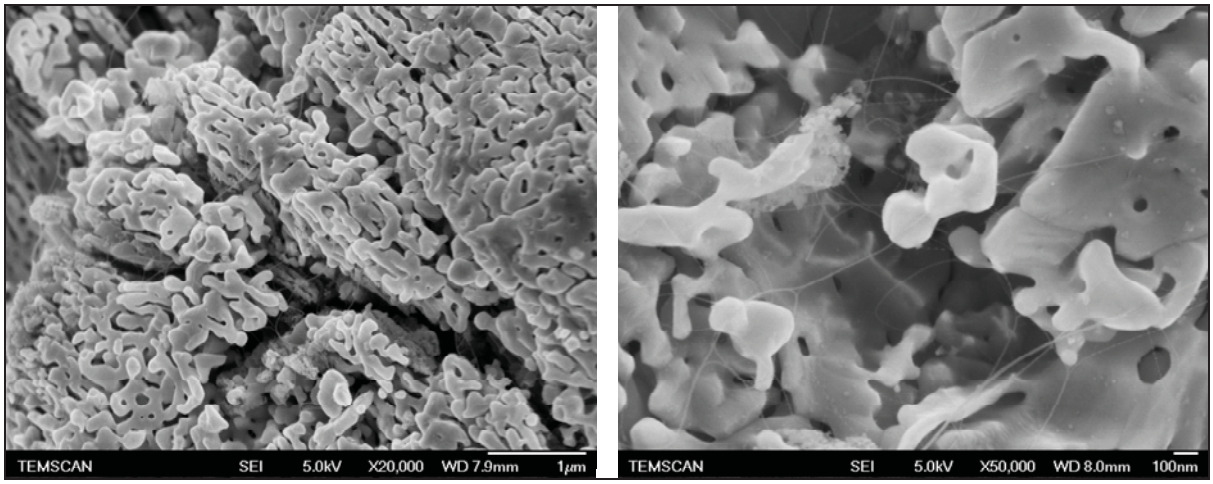

Figure 11: SEM micrographs of sample 11 based on the catalyst activated at 900°C, 10 h

An appropriate time of calcination under static air at 900°C was fixed at 10 h and from now on this step will be called the activation.

We found a good condition associated to the 2% Fe/Al_2O_3 catalyst giving high selectivity towards SWCNTs but low catalytic activity. The next step should be focused on raising the catalytic activity towards SWCNT production, while trying to keep high selectivity. But before that, a characterization of the catalyst before and after the activation was performed to explain the increase in selectivity.

II-2-4-Caracterisation of the Fe/Al_2O_3 catalysts

The 2% Fe/Al_2O_3 catalyst was characterized by Mossbauer spectroscopy, specific surface measurement (BET), temperature programmed reduction (TPD) and XRD, before and after activation at 900°C for 10 h. For a better understanding of the behavior of iron oxide on alumina we extended the study to 4 and 6 % loadings.

II-2-4-a-ICP-MS

Catalyst	%C	%H	%N	%Fe
2%MO-CVD	0.05	0.2	0	2
2% MO-CVD activated	0.1	0	0.01	2

Table 4: ICP-MS results on the 2% Fe/Al_2O_3

First, we have evidenced by ICP-MS analysis that a temperature of 220 °C is sufficient to decompose the $[Fe(CO)_5]$ precursor in the MO-CVD process and that the carbon

contamination was low. Thus, the activation step is not related to carbon decontamination or to a complete decomposition of the iron pentacarbonyl.

II-2-4-b-Specific surface area measurements (BET)

BET specific surface area measurements were carried out on the 2% MO-CVD catalyst after different periods of activation at 900°C.

Time at 900 °C (h)	BET ($m^2.g^{-1}$)	Mean pore diameter (nm)	Total pore volume ($cm^3.g^{-1}$)	Classification
0	141.8	6.3	0.2	mesoporous
3	83.0	11.4	0.2	mesoporous
10	21.4	39.1	0.2	mesoporous

Table 5: Specific surface area, mean pore diameter and total pore volume evolutions of the 2% Fe/Al_2O_3 catalyst as a function of calcinations duration at 900°C

Large modifications on the surface of the catalyst occur after activation. The surface area decreases from 142 m^2/g for the fresh MO-CVD to 21 m^2/g for the activated catalyst (Table 5). The mean pore diameter increased, so that the active phase should be more accessible to the reactive atmosphere. The total pore volume remained constant; this could be related to collapsing of pores upon activation leading to their opening. We should not underestimate an increase in strength of the interaction between alumina and iron oxide during the activation at 900 °C [48]. In that case Fe-Al bonding should be favored relative to the Fe-Fe bonding. Thus, the iron phase, filling the pores after MO-CVD, may migrate to the surface, and be redistributed more uniformly in the defect sites of the alumina lattice to form a subsurface solid solution. The iron distribution in the pores is changed, contributing to their opening.

II-2-4-c-TPR analysis

The temperature programmed reduction experiment (Fig. 8) shows 3 peaks at 300 (A), 490 (B), and 700 °C (C) for both fresh and activated MO-CVD catalysts. The difference was in the intensity of those peaks, for which we got a 40 % drop of H_2 consumption upon activation. This leads to the conclusion that the active phase has undergone a transition upon activation either to a much more stable state of iron, since it was very hard to reduce, or that part of the active phase is buried into the support and not accessible to hydrogen.

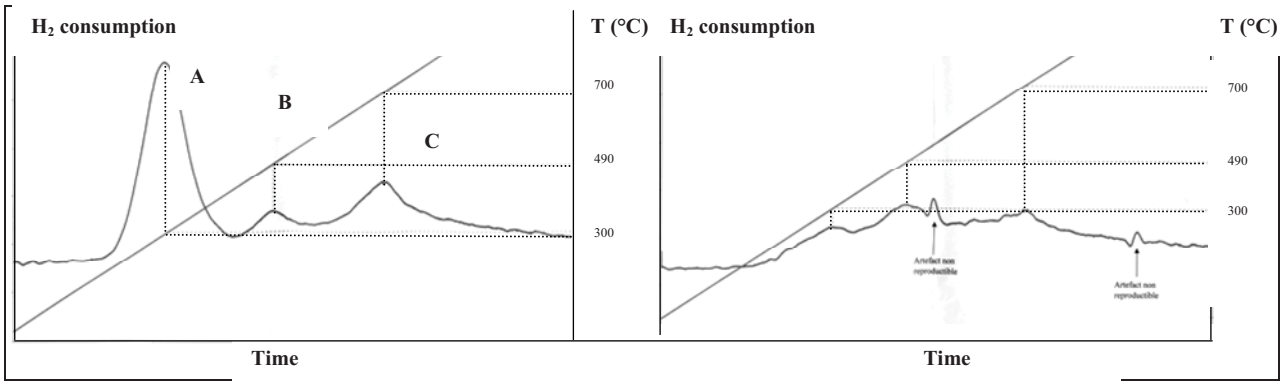

Figure 12: TPR analysis of the fresh (left) and activated (right) MO-CVD 2% Fe/Al_2O_3

Iron is a very versatile element [49] and assessing each transition to a specific iron species is complicated. Nevertheless main possibilities are drawn out. MO-CVD at 220°C is supposed to yield γ-Fe_2O_3 maghemite nanoparticles on alumina [50-52, 75]. At 300 °C (peak A) Fe_2O_3 is transformed to magnetite (Fe_3O_4) [53], and at 490 °C magnetite is transformed to Fe(II) species (peak B) probably wustite (FeO) or a spinel type solid solution $Fe_xAl_yO_4$ [54]. Then, at 700 °C (peak C), Fe(II) is transformed to Fe^0 or another spinel type solid solution $Fe_nAl_mO_4$ [54].

The possible transitions of iron are summarized in scheme 1.

Maghemite **Magnetite** **Wustite/Solid-Solution**

$$\gamma\text{-}Fe_2O_3 \xrightarrow[300\ °C]{A} Fe_3O_4 \xrightarrow[490\ °C]{B} FeO \text{ or } Fe_xAl_yO_4 \xrightarrow[700\ °C]{C} Fe^0 \text{ or } Fe_nAl_mO_4$$

Scheme 1: Probable transitions of iron oxide supported on alumina

As a conclusion, TPR analysis confirmed that the iron in the fresh MO-CVD catalyst was not heat stable. Transitions presented in scheme 1 could occur during SWCNT synthesis upon heating the catalyst from 25 to 900 °C in reducing atmosphere. This could generate a heterogeneous catalyst with different iron species presenting different catalytic activity and selectivity, and leading to different carbon nanostructures deposition, thus to low selectivity towards SWCNTs. After activation, the catalyst was much more stable, and possibly hard to reduce. This may explain the low selectivity and yield obtained with the 2% activated catalyst.

II-2-4-d-XRPD analysis

For all 2, 4 and 6 % fresh Fe/Al_2O_3 MO-CVD catalysts, no peak relative to any iron form was detectable (Fig. 13a). This was a confirmation of the high dispersion of iron oxide on the alumina surface and the formation of very small iron nanoparticles with the MO-CVD technique at 200°C. Since a copper X ray source was used, a scattering effect [22] could also explain the difficulties in the detection of the small iron nanoparticles proved to exist by Mossbauer spectroscopy (vide infra).

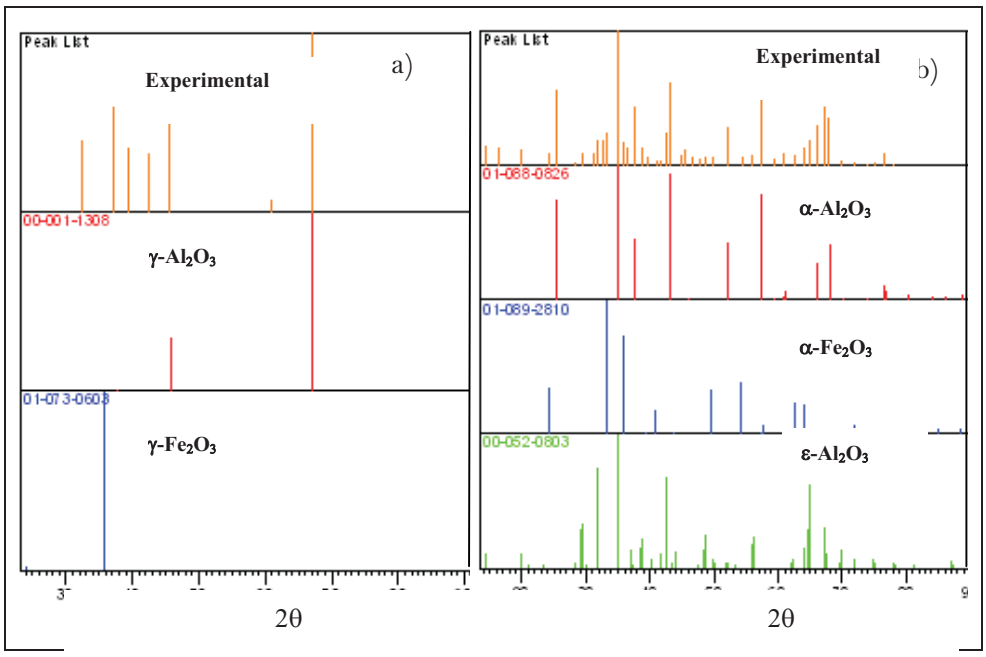

Figure 13: XRD diffractogram of the 6% catalyst a) fresh MO-CVD b) activated

After activation (900°C, 10 h), the peaks relative to alumina got more intense, an indication of the crystallization of γ-alumina to α-alumina and ε-alumina or a mixture of both. Iron-alumina interactions may have lowered the γ- to α-alumina crystallization temperature that is at 1200 °C for pure γ-alumina [115]. As for iron peaks, for the 2% Fe/Al_2O_3 activated catalyst they remained undetectable, started to appear at 4% and are clearly present for 6% (peaks of α-Fe_2O_3 at 2θ=24, 33, 35, 42, 49, 54, 63 and 64°) in the form of nanocrystals of hematite (Fig. 13b).

By XRD, we have a confirmation that the iron oxide forming the nanocrystallite was hematite, and Fe^{3+} was not reduced upon thermal activation to Fe^{2+} solid solution species or any other form of reduced iron. Concerning the probable subsurface solid solution, a broad band was always present for the fresh and under the peaks of the activated catalyst suggesting a random distribution of Fe^{3+} cations in the vacancies of the alumina surface [115].

II-2-4-e-Mössbauer spectroscopy

II-2-4-e-1-State of art

Mössbauer spectroscopy is a very sensitive and largely used technique to study the chemical state of iron [53, 54, 55]. The technique enabled us to clarify the difference between the fresh MO-CVD catalyst and the activated (900 °C, 10 h) one, and to identify the active species for SWCNT synthesis.

Parameters such as isomeric shifts, quadrupole splitting, or magnetic hyperfine splitting of the Mössbauer spectrum of iron oxide supported on alumina are variable due to the versatility of iron and their dependence on the nature of the support (specific surface area, surrounding surface groups, and number of vacancies). This makes the exact comparison with the literature values difficult. Based on the TPR analysis we reviewed the main characteristics of the possible iron species involved, such as magnetic behavior, oxidation state and location on the alumina matrix.

Fe^{3+} can easily occupy vacant sites or even substitute Al^{3+} ions in the γ-alumina lattice due to high interactions and chemical similarities [55-60]. According to the basic theory of Mössbauer spectroscopy for Fe_2O_3 supported on γ-Al_2O_3, if the Fe^{3+} cations are incorporated into the vacant surface sites of the support and exist as isolated Fe^{3+} ions, then this iron will exist as paramagnetic Fe^{3+} cations, giving Mössbauer spectra of a quadrupole splitting doublet [55-60].

It is known that for an oxide dispersed on a support there will be a threshold dispersion capacity [57] and this latter depends on the surface area, the loading, the number of vacant sites and the interaction force between the support and the supported species.

When Fe^{3+} ions start to aggregate, forming crystallite nanoparticles of iron oxide, many possibilities can arise depending on the oxidation state, crystalline state, size, and temperature of the sample [61]:

Hematite (α-Fe_2O_3) is paramagnetic at temperature above its Curie temperature of 683 °C. At room temperature it is weakly ferromagnetic and undergoes a phase transition at -13 °C (the Morin temperature T_M) to the antiferromagnetic state. The Morin temperature of hematite decreases if the particle size decreases or if the substitution with alumina increases and tends to vanish for particles smaller than 8-20 nm. Iron is in the $Fe^{(III)}$ oxidation state.

Magnetite (Fe_3O_4) is ferrimagnetic at room temperature and has a Curie temperature of 577 °C. The iron exist in both $Fe^{(III)}$ and $Fe^{(II)}$ oxidation states.

Maghemite (γ-Fe_2O_3) is ferrimagnetic at room temperature, unstable at high temperatures (starts to crystallize to hematite at 400°C) and loose its susceptibility with time. Iron is in the $Fe^{(III)}$ oxidation state.

From the magnetic specifications presented above, the Mössbauer spectrum of hematite, magnetite or maghemite should present a magnetic splitting sextuplet at room temperature. However, if the particles are too small, typically less than 10 nm, the magnetic ordering will not be seen and the nanoparticles magnetic behavior will be transformed to superparamagnetic doublet because of the fast relaxation of the magnetic moment of such small particles. Aggregation of ultrafine maghemite particles (supposed to be superparamagnetic) leads sometimes to magnetic coupling between particles and ordering of the magnetic moment, whish is termed superferromagnetism [61].

In summary, and based on the previous citations, conclusions from Mössbauer spectroscopy should be drawn out by comparing spectra at different temperatures, in our case at 20 and -268 °C. This enables us to distinguish the doublet relative to small superparamagnetic Fe_2O_3 nanoparticles at room temperature, yielding a magnetic hyperfine splitting sextuplet superimposed on a doublet at -268 °C, from the one relative to a sub-monolayer of iron oxide, dispersed as Fe^{3+} ions in the vacant sites of alumina, with a persisting paramagnetic doublet at -268 °C [57].

The observation of a sextuplet at room temperature is attributed to large Fe_2O_3 crystallites, which show collective magnetic excitation.

II-2-4-e-2-Fresh MO-CVD catalysts

For all fresh MO-CVD catalysts, doublets were observed at room temperature that were transformed to sextuplets superimposed on the doublets at -268 °C (Table 6 and Fig. 14).

T = 20 °C						
%Fe	Form	%	IS(mm/s)	QS(mm/s)	W(mm/s)	Conclusions
2	Doublet	100	0.32	0.82	0.25	Fe^{3+} submonolayer
4	Doublet	100	0.33	0.83	0.26	
6	Doublet	100	0.33	0.82	0.26	
T = -268 °C						

%Fe	Form	%	IS(mm/s)	QS(mm/s)	W(mm/s)	Conclusions
2	Doublet	26.6	0.42	1.12	0.79	Fe^{3+} submonolayer
4	Doublet	12.1	0.49	1.74	0.71	
6	Doublet	57.8	0.39	0.67	0.43	≠environments ≠QS
%Fe	Form	%	IS(mm/s)	$H_{m,f}$ (KOe)		Conclusions
2	Sextet	73.4	0.46	458.1		Fe_2O_3 crystallite
4	Sextet	87.8	0.45	474.35		
6	Sextet	42.1	0.45	527.19		≠size ≠ $H_{m,f}$

Table 6: MS parameters of the MO-CVD catalysts with different iron loadings

This indicates that the MO-CVD technique is effective to produce very small nanocrystallites of iron oxide (sextet at -268 °C), with mean diameter less than 10 nm that could be suitable for SWCNT synthesis. Those latter are superimposed on a sub-monolayer of Fe^{3+} (doublet) for all 2, 4 and 6% iron loadings. One can ask about the oxidation state of iron in such nanoparticles and if it was the same for all iron loadings. By increasing the iron loading, the isomeric shifts of the nano-crystallites remained the same at 0.46 mm/s, and the hyperfine magnetic splitting H_{mf} increased linearly in the range 458-527 KOe (Fig. 15). This meant that the iron oxide species forming the nanoparticles were the same, most probably maghemite (γ-Fe_2O_3) according to literature [51] and increased in size with the increase of the iron loading [62, 63].

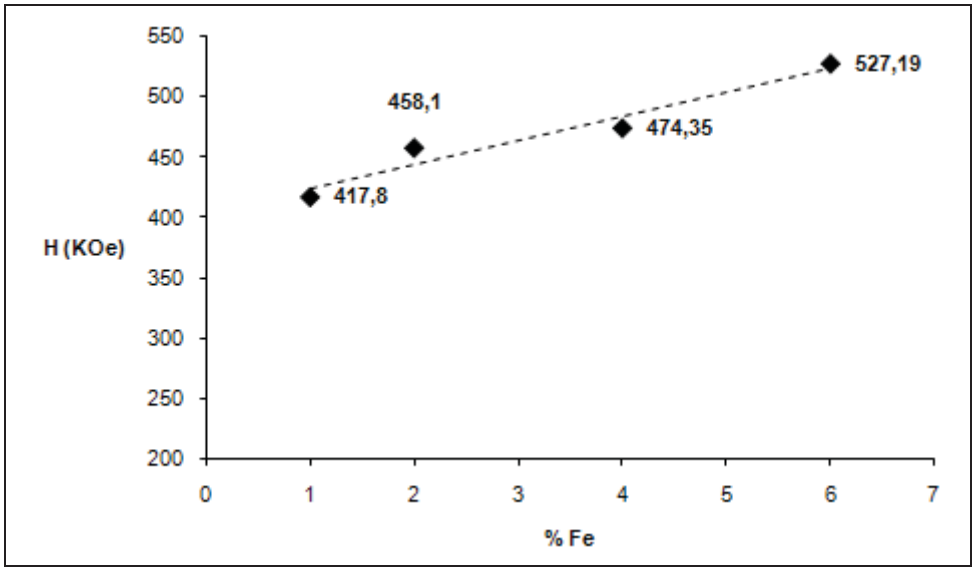

Figure 14: $H_{m,f}$ of the nanoparticles as a function of the iron loadings

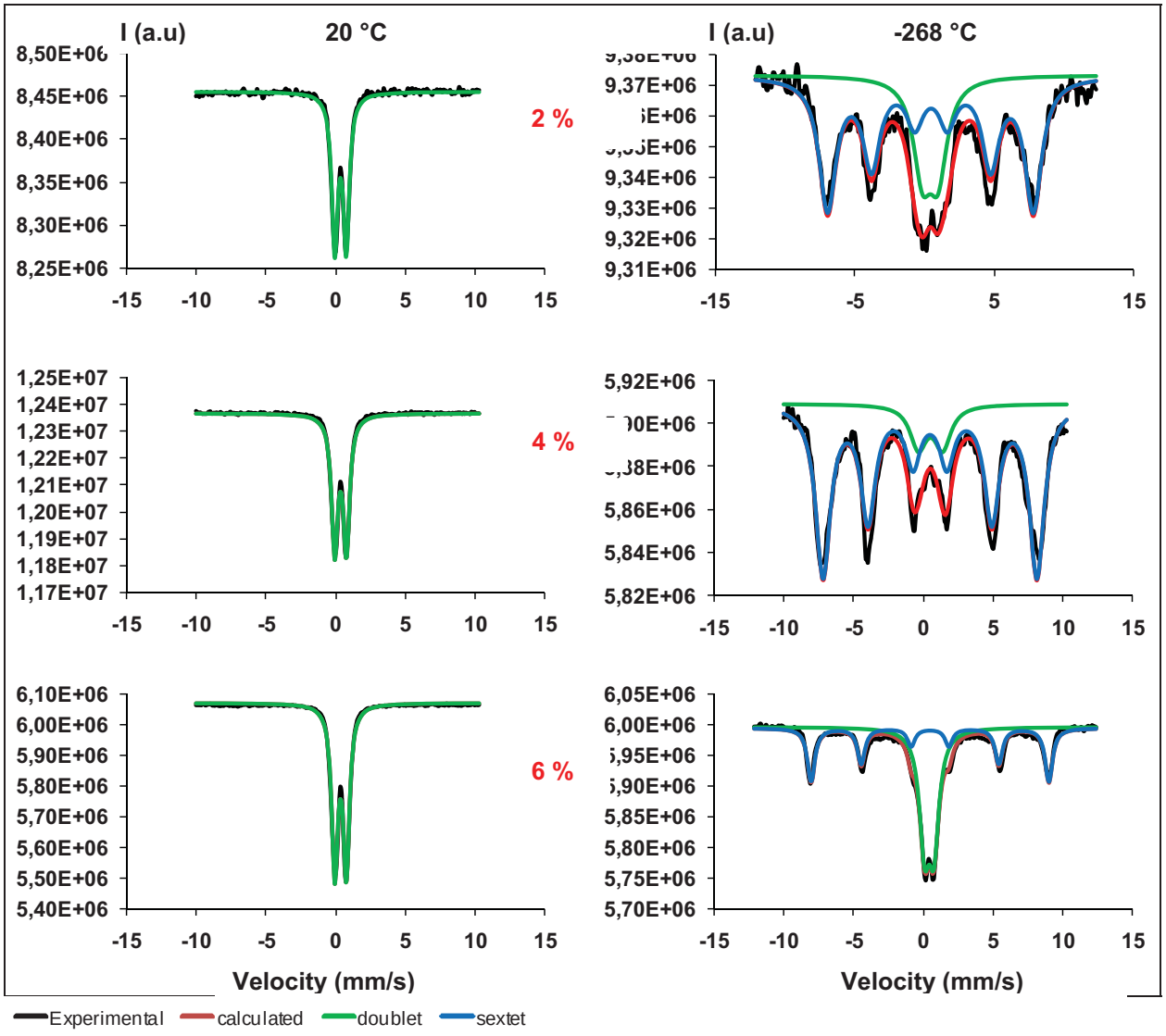

Figure 15: Mössbauer spectra of the fresh MO-CVD catalysts at 20°C (left) and -268 °C (right)

Interesting results about the iron distribution on alumina as a function of iron loading can be taken out from the ratio of the sextet to the doublet contributions. (% sextet / % doublet). The proportion of the crystallite to the monolayer species increased from 2.7 (73% sextet / 26% doublet) to 7.2 (88% sextet / 12% doublet) when we doubled the loading of iron from 2 to 4%, then decreased to 0.7 (42% sextet / 57% doublet) at 6%. This indicates that a change in the law of iron distribution on the alumina surface occurred for the 6%. This is also supported by the difference in the quadruplet splitting (QS) of all the paramagnetic doublets of the catalysts at T = -268 °C, indicating that the structure of the monolayer of Fe^{3+} or its environment was not the same.

In fact, from 2 to 4% iron loadings, iron nanoparticles nucleation and growth was favored: the additional amount of iron got mostly distributed on the surface of previously deposited iron, leading to the increase in size of the crystallite. In the 6% sample, iron nanoparticles nucleation is more favored and we forced the formation of a more extended Fe^{3+}monolayer. The increment of iron was more distributed in the sub-monolayer of the alumina lattice confirming that there were still sites available on that latter. This result seems logical since the deposition time was the same and an increase in the precursor supersaturation is known to favor the nucleation of nanoparticles. We can add to that the iron supersaturation has an influence on iron deposit morphology and distribution on alumina. The structure of the fresh MO-CVD catalysts is represented in Scheme 2.

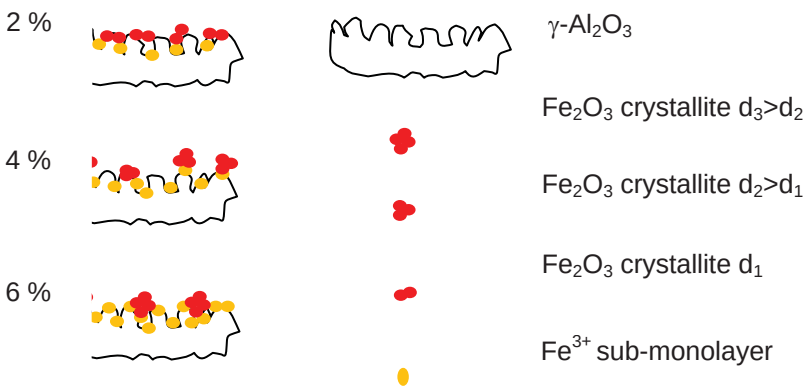

Scheme 2: Structure of the fresh MO-CVD catalysts, d_1, d_2, d_3 being the nanocrystallite size in the 2, 4, and 6 % catalysts.

II-2-4-e-3-Activated catalysts

Upon thermal activation (900 °C, 10 h) the different catalysts showed different spectra depending on iron loadings (Table 7 and Fig. 16).

The activated catalyst with 2% iron loading presents a remarkable change in the distribution of iron on the alumina. Indeed a population of 100% doublet was observed at room temperature and remained 100% at -268 °C since no sextet was observed. This indicates that a redistribution of the $Fe^{(III)}$ iron atoms of the nano-crystallites in the alumina lattice occurred yielding a surface with only a paramagnetic sub-monolayer of Fe^{3+} ions located in the vacant sites of alumina. It was reported that calcinations in air of amorphous oxides at the appropriate temperature produces the cubic and stable α-corundum form of $Al_{1,8}Fe_{0,2}O_3$ [64].

T=20 °C						
%Fe	Form	%	IS(mm/s)	QS(mm/s)	W(mm/s)	Conclusions
2	Doublet	100	0.29	0.84	0.33	Fe^{3+} submonolayer
4	Doublet	95	0.30	0.67	0.26	≠ environment ≠ QS
6	Doublet	72	0.30	0.62	0.22	
%Fe	Form	%	IS(mm/s)	$H_{m,f}$ (KOe)		Conclusions
2	Sextet	0	-	-		Hematite
4	Sextet	5	0.37	506.6		same size
6	Sextet	28	0.36	505.12		
T = -268 °C						
%Fe	Form	%	IS(mm/s)	QS(mm/s)	W(mm/s)	Conclusions
2	Doublet	100	0.42	0.85	0.53	=IS = oxidation state
4	Doublet	100	0.40	0.68	0.55	≠ QS ≠ hematite size
6	Doublet	0	-	-	-	Submonolayer coupled to the ultrafine crystallite
%Fe	Form	%	IS(mm/s)	$H_{m,f}$ (KOe)		Conclusions
2	Sextet	0	-	-		Fe^{3+} submonolayer
4	Sextet	0	-	-		Antiferromagnetic
6	Sextet	100	0.45	478.87		Superferromagnetic

Table 7: Mössbauer parameters of the activated MO-CVD catalysts with different iron loadings

Starting from the catalyst with 4% Fe/Alumina, a sextuplet contribution appear in the Mössbauer spectrum at room temperature, then becomes clearly present in the catalyst at 6% iron loading. This indicates the presence of magnetic nano-crystallite of Fe_2O_3 in addition to the $Fe^{(III)}$ sub-monolayer on alumina. In fact by increasing the iron loading we step over the threshold of iron solubility in the alumina lattice, and 5 % (at 4 % loading) and 27.6 % (at 6 % loading) magnetic nanoparticules remained after activation. The size of such nanoparticles should be larger than 10 nm since no superparamagnetic doublet appeared in the Mossbauer spectrum at room temperature. Such big nanoparticles are not expected to have a catalytic activity for the SWCNT synthesis. The ratio of crystallites ferromagnetic nanoparticles to paramagnetic Fe^{3+} monolayer was 0.05 for the 4% catalyst and 0.36 for the 6% catalyst, thus could cause selectivity problems.

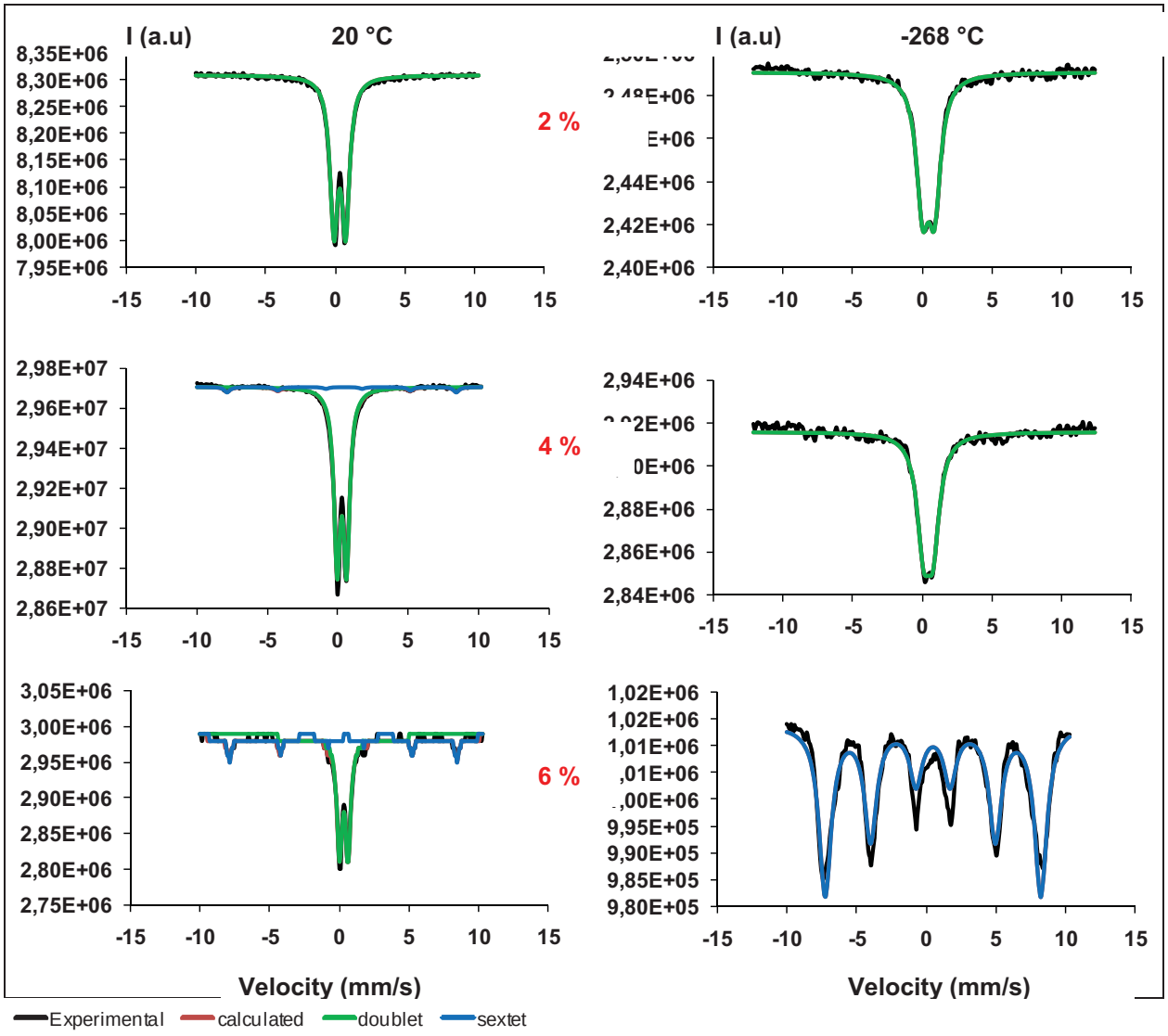

Figure 16: Mössbauer spectra of the activated catalysts at 20 °C(left) and -268 °C (right)

For all 2, 4 and 6% fresh or activated catalysts, the chemical state of iron does not change since $Fe^{(III)}$ is the only present species, and that the thermal activation does not induce a reduction of iron by formation of an $Fe^{(II)}$ solid solution as proposed in the literature [54].

Iron is distributed, on the surface of alumina as iron oxide nanoparticles (when existing) attributed to hematite (α-Fe_2O_3) and as a sub-monolayer of ionic Fe^{3+} in the vacant sites of the alumina lattice.

The size of the hematite nanoparticles of the 4 and 6% catalysts is similar since the same hyperfine magnetic field values of 505-506 KOe is observed at room temperature. Nevertheless there is a difference in the magnetic behavior in the Mössbauer spectrum at -268 °C. The hematite of the 4% catalyst being more than 10 nm in size has undergone the Morin transition from ferromagnetic at RT (sextet) to an antiferromagnetic behavior (doublet) at -268 °C.

In the 6% catalyst we observe a 100% sextet at -268 °C, indicating the persistence of the magnetic ordering of the corresponding hematite. The chemical and structural environment of the hematite of the 6% catalyst is not the same as that of the 4% catalyst. The appearance of a lonely sextet at -268 °C and the disappearance of the doublet of the monolayer could only be explained by a superferromagnetic behavior. In fact, the high iron loading in the submonolayer as seen in the 6% fresh MO-CVD catalyst, induces a decrease of the distance between Fe^{3+} ions, and this ultrafine submonolayer of Fe^{3+} started to aggregate after activation to ultrafine maghemite particles(γ-Fe_2O_3), leading to magnetic coupling between such nanoparticles and ordering of the magnetic moment [61].

This is a proof that the aptitude to crystallization of iron oxide on alumina is a function of the iron loading. As the loading increases, the iron-alumina interaction decreases, the iron-iron interaction increases and the crystallization capability increases.

II-2-4-e-4-Conclusion on catalyst activation

TPR analysis informed us about the possible iron species existing on the alumina support and their thermal transitions. It also marked the difficulty to reduce the catalyst after activation or the poor accessibility of the active phase. Essential information concerning the oxidation state, crystallography, nature of the species and their locations on the alumina lattice was obtained from Mössbauer spectroscopy. Iron deposited by MO-CVD was always in the Fe^{3+} oxidation state, localized in a sub-monolayer of vacant sited of alumina in addition to very small nanoparticles of hematite. From the magnetic behavior, estimation concerning

the size evolution of those nanoparticles before and after activation could be drawn out. At last, XRD confirmed the Mössbauer spectroscopy conclusions and emphasized that there was no reduction to magnetite or other reduced iron forms after thermal activation and that the nanoparticles when existing were hematite.

A model of the structure of each catalyst after activation is proposed in Scheme 3.

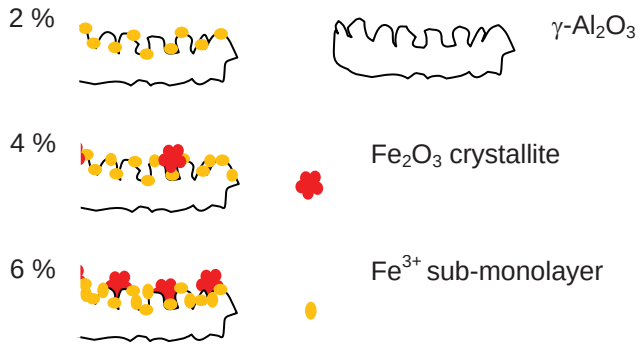

Scheme 3: Structure of the activated MO-CVD catalysts

Now that we got information on the detailed composition of the catalysts at different iron loading and before and after activation, the role played by the activation on the increase of the selectivity could be clarified. First, for both 2 and 4% loadings the dominant iron phase after activation was the ionic Fe^{3+} sub-monolayer of a solid solution like species. In such structure iron oxide is much more stable at 900 °C than the Fe_2O_3 nanoparticles due to strong interaction with alumina. In fact, Fe^{3+} substitutes an Al^{3+} ion in the alumina matrix due to chemical similarities. Thus, reactivity of the sub-monolayer is not the same than that of the nanoparticles. Activation redistributed the iron atoms of nanoparticles on the alumina in the form of a submonolayer. This leads to a homogeneous reactivity and higher selectivity. At 6% iron loading, the alumina cannot dissolve more iron from hematite nanoparticles, and thus in this catalyst we could expect lower selectivity towards SWCNTs.

An accurate confirmation of these conclusions could stem from a study of the state of iron after SWCNT synthesis, and identification of the active species.

II-2-5-Identification of the active species

The identification of the iron active species for SWCNT synthesis was performed essentially by Mössbauer spectroscopy.

State of art

With respect to catalytic formation of carbon nanotubes, identifying the active center is of critical importance in improving the growth rate, and selectivity towards SWCNTs. A summary of the most frequently encountered species and their Mössbauer parameters and magnetic behavior are summarized in Table 8.

Species	T °C	Form	IS (mm/s)	QS(mm/s)	$H_{m,f}$ (KOe)	Ref
α-Fe_2O_3	20	Doublet	0.35	0.81	-	62
Fe_3C		Sextet	0.19	0.02	206	
α–Fe^0		Sextet	-0.06	-0.01	330	
α-Fe^0		Sextet	-0.02	-	328	
(Super)para Fe^{2+}	-268	Doublet	1.23	0.45/1.31	-	69
(Super)para Fe^{2+}	20	Doublet	1.04	0.20/0.48	-	
(Super)para Fe^{3+}	-268	Doublet	0.47	0.44	-	
(Super)para Fe^{3+}	20	Doublet	0.31/0.40	0.46/1.1	-	
$MgFe_2O_4$-like	-268	Sextet	0.41	-	492	
Fe(III) S=5/2	-	Doublet	0.46	0.86	-	70
Fe(II) S=2	-	Doublet	1.24	2.69	-	
α-Fe^0	20	Sextet	0.01	-	**33.2T**	71
Fe_3C		Sextet	0.19	-	**20.8T**	
$(Al.Fe)_2O_3$		Doublet	0.31	0.53	-	
γ-Fe^0-C		Singlet	-0.12	-	-	
(Super)para Fe^{3+}	-193	Doublet	0.39	0.53	-	72
Ferro-α-Fe^0		Sextet	0.11	-	340	
Ferro-Fe_3C		Sextet	0.31	-	246	
Non ferro-Fe^0		Singlet	0.03	-	-	
$Fe_{1-y}O$ (Fe^{II})	20	Doublet1	0.94	0.74	-	10
$Fe_{1-y}O$ (Fe^{II})		Doublet2	0.95	0.43	-	
$Fe_{1-y}O$(Fe^{III})		Doublet3	0.50	0.80	-	
$Fe_{1-y}O$ (Fe^{III})		Singlet	0.33	-	-	
Fe_3C	-173	Sextet	0.29	0	246	73
γ-Fe^0		Singlet	-0.02	0	0	
α-Fe^0		Sextet	0.10	0	340	
FeO		Doublet	0.62	0.60	0	

Table 8: Mössbauer parameters of iron species encountered in carbon nanotube synthesis

As seen in Table 8, numerous iron species are encountered in CVD synthesis of carbon nanotubes and many speculations on the active species exist but none has received complete acceptance. Ruston et al. [65] reported the formation of iron carbide (Fe_3C) in the bulk of iron foil which was found to support fiber growth. However, they identified the fiber growth crystal as Fe_7C_3 by X-ray diffraction. Investigating the initiation and growth of filamentous carbon from α-iron in H_2, CH_4, CO_2 and CO gas mixture, Sacco et al. [66] proposed that Fe_3C acted as catalyst for carbon deposition and subsequent filament and nanotube growth. Baker and Chludzinski suggested FeO instead of Fe_3C in carbon nanofiber synthesis that showed much higher activity than Fe [67]. Audier and Coulon [68] reported that the reduced iron metal catalyzed the growth of isolated SWCNTs.

Based on the literature, we concluded some identification keys for the large number of probable iron species (Table 8). Iron carbide Fe_3C and α-Fe^0 exhibit a hyperfine magnetic field sextet. The lowest hyperfine magnetic splitting encountered in the range of 200 and 250 KOe is attributed to Fe_3C, followed by the metallic α-Fe^0 in the range of 300-340 KOe. The γ-Fe^0 shows only a singlet with IS around 0 and is either paramagnetic or superparamagnetic [73]. Iron oxide in the reduced Fe^{2+} form present, a doublet with high IS (around 1 mm/s) and QS values at around 2 mm/s distinguishable from the doublet of Fe^{3+} which present lower values.

Carbon deposition was performed in the C-CVD reactor by exposing the 2, 4 and 6% activated catalysts to a mixture of 200/100 sccm of CH_4/H_2 for 30 minutes at 900 °C. The Mössbauer spectra of the composite materials are presented in Figure 17 and their parameters in Table 9.

T= 25 °C							
Test	%Fe	Form	%	IS(mm/s)	QS(mm/s)	W(mm/s)	Conclusions
11	2	Doublet1	100	0.273	0.631	0.278	Doublet1: Fe^{3+}
27	4	Doublet1	66	0.274	0.586	0.213	Doublet 2: Fe^{2+}
		Doublet2	34	0.89	1.909	0.306	
37	6	Doublet1	74.9	0.249	0.696	0.266	
Test	%Fe	Form	%	IS(mm/s)	Conclusions		
11	2	Singlet	0	0	-		
27	4	Singlet	0	0			
37	6	Singlet	25.1	-0.033	γ-Fe^0		
T= -268 °C							
Test	%Fe	Form	%	IS(mm/s)	QS(mm/s)	W(mm/s)	Conclusions
11	2	Doublet	67	0.343	0.548	0.47	Fe^{3+} monolayer
27	4	Doublet1	87	0.30	0.55	0.40	Fe^{3+} monolayer
		Doublet2	13	1.25	2.30	0.23	Fe^{2+}
37	6	Doublet	7.4	0.36	0.71	0.20	Fe^{3+} monolayer
Test	%Fe	Form	%	IS(mm/s)	$H_{m,f}$ (KOe)		Conclusions
11	2	Sextet	33	0.57	484		Fe_3O_4
27	4	Sextet	0	0	0		-
37	6	Sextet1	31	0.47	520.1		Fe_2O_3
		Sextet2	22	0.32	252.8		Fe_3C
		Sextet3	11	0.09	342		α-Fe^0
Test	%Fe	Form	%	IS(mm/s)	Conclusions		
11	2	Singlet	0	0	-		
27	4	Singlet	0	0			
37	6	Singlet	29	0.18	γ-Fe^0		

Table 9: Mossbauer parameters of the samples after SWNT synthesis with different iron loading

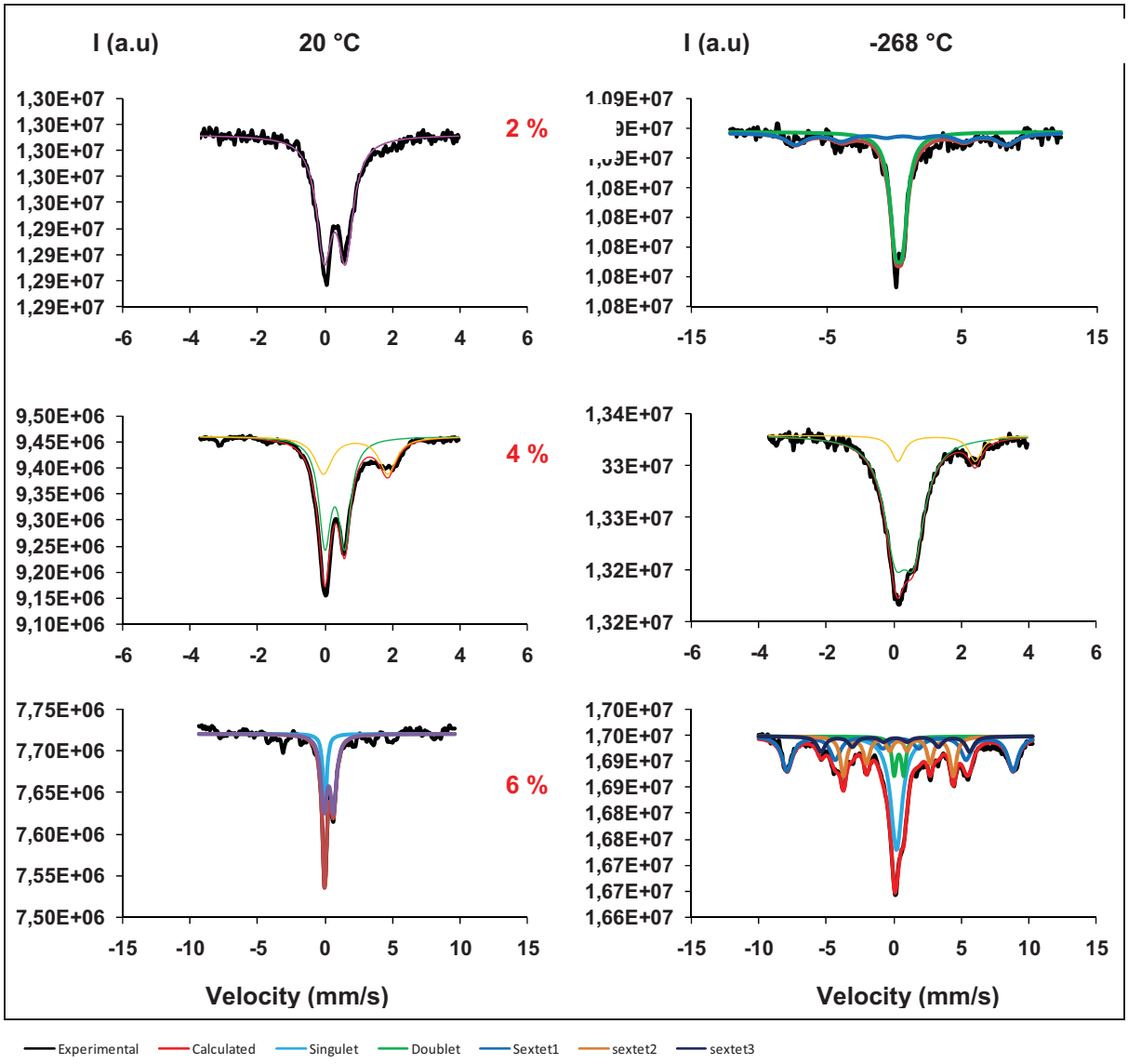

Figure 17: Mössbauer spectra of the samples after SWCNT synthesis at 20 °C (left) and -268 °C (right)

2% catalyst (Test 11)

In the 2 % catalyst at room temperature a doublet could be fitted. At -268 °C a very broad and different doublet appeared as well as a sextet of low intensity. From the previous observations it seems that we have two different iron species to identify, resulting from the $Fe^{(III)}$ monolayer of the activated catalyst. The parameters of the doublet at room temperature are so close to the $Fe^{(III)}$ of the activated 2 % catalyst (IS=0.273 and 0.29 mm/s). In addition, the broadening of the doublet at -268 °C is a signature of an incomplete reduction of the $Fe^{(III)}$ iron monolayer [70]. The assignment of the sextet at -268 °C to the presence of any iron carbide or metallic iron was discarded because the hyperfine magnetic field value (484 KOe) was too high for carbides (236 KOe) and metallic iron (360 KOe). This hyperfine magnetic

field and the isomeric shift value of 0.57 are close to the mostly reported values of the supported Fe_3O_4, FeO and $(Al,Fe)O_4$ species. Based on the as mentioned facts, it seems that the two iron species correspond to a magnetite structure formed by the reduction of some $Fe^{(III)}$ of the sub-monolayer to $Fe^{(II)}$, and some agglomerated $Fe^{(III)}$ iron (sextet). The remaining unreduced superparamagnetic $Fe^{(III)}$ in the sub-monolayer of the alumina produces the doublet. The two different iron species *i.e* superparamagnetic $Fe^{(III)}$ of the monolayer and paramagnetic $Fe^{(II)}$ of the magnetite, contribute both in the doublets and produce its broadening.

The $Fe^{(II)}$ species seems to be the active species for SWCNT synthesis [73] or a mandatory intermediate. Since the reduction of $Fe^{(III)}$ in the submonolayer to $Fe^{(II)}$ is very hard, due to strong $Fe^{(III)}$-Al interactions, the catalytic activity for the synthesis of SWCNTs was limited.

4% catalyst: (Test 27)

In the Mössbauer spectrum of the 4% catalyst after carbon deposition, the same iron species as for the 2% catalyst were detected. At room temperature, a first doublet with IS of 0.27 (mm/s), very similar to the doublet of the previous 2 % activated catalyst was attributed to the unreduced $Fe^{(III)}$ of the sub-monolayer. At -268 °C, this first doublet did not vary a lot. A second doublet was present at room temperature and remained at -268 °C. The parameters of this latter are in accordance with a superparamagnetic $Fe^{(II)}$ species. In fact the $Fe^{(III)}$ iron in the 4% activated catalyst is more reducible than the one in the 2% activated catalyst, leading to a reduction of 13.2% of the $Fe^{(III)}$ sub-monolayer to $Fe^{(II)}$ active species. The absence of magnetite, an intermediate of incomplete reduction of $Fe^{(III)}$, leads to the disappearance of the sextet. It is well known that the reduction species depend strongly on the iron loading [74, 79].

6% catalyst: (Test 37)

Finally, at 6% iron loading all the species involved in iron oxide reduction appeared: $Fe^{(III)}$; $Fe^{(II)}$; and $Fe^{(0)}$. This is in accordance with the previous conclusions, as the iron loading increased, $Fe^{(II)}$ starts to appear, then $Fe^{(0)}$. In fact at 6% iron loading part of the iron oxide became more easily reducible [79] leading to different iron species.

It has been reported that the preparation of supported Fe catalysts can lead to strong metal-support interaction, which makes its transformation into the metallic state difficult [53,

76], leading to partial transformation of Fe as well as stabilization of the $Fe^{(II)}$ oxidation state [77].

The appearance of the carbide species and its absence in the 2 and 4 % catalyst leads us to think that such species are formed from the reduced $Fe^{(II)}$ species and not from the $Fe^{(III)}$ of the monolayer. $Fe^{(II)}$ could be generated by the partial reduction of the monolayer or from the easily reducible $Fe^{(III)}$ of the large nanoparticles or both.

$$Fe_3O_4 + CH_4 + 2H_2 \longrightarrow Fe_3C + 4\ H_2O$$ [78]

Many associated reactions could explain the formation of Fe^0 species, starting from the reaction of Fe_2O_3, or $FeAl_2O_4$ with hydrogen [53, 79]:

$$Fe_2O_3 + 3\ H_2 \longrightarrow 2\ Fe^0 + 3\ H_2O$$

$$FeAl_2O_4 + H_2 \longrightarrow Fe^0 + Al_2O_3 + H_2O$$

The 6% activated catalyst did not yield any SWCNT but only fibers. Such catalyst presents high activity and selectivity towards MWCNTs under the condition of MWCNT synthesis (Carbon source C_2H_4, T=650 °C). Thus, Fe_3C species could be suitable for MWCNT synthesis under the MWCNT conditions (see section II-2-3) but yields fibers under the SWCNT conditions. It seams that the $Fe^{(II)}$ iron species imbedded in a solid solution of $FeAl_2O_4$ [79] is suitable for SWCNT synthesis [70].

II-2-6-Parametric study to improve SWCNT yield

II-2-6-1-H_2 concentration

In order to improve the yield of SWCNT while keeping the selectivity at its optimum, we varied the concentration of H_2 in the reactor from 100 to 0 sccm keeping the total flow constant at 300 sccm and the CH_4 mass flow at 200 sccm.

Figure 18 and Table 10 indicate that the partial pressure of H_2 plays an important role in achieving selectivity toward SWCNTs. However, no satisfactory results was obtained between the condition were there is 100 sccm of H_2 (H_2 condition) and its absence (Ar condition). In fact, a slight lowering of the hydrogen partial flow led to a high drop of the I_G/I_D ratio but without increase in carbon yield. The catalytic activity only start to increase to 3.5 h^{-1} for a H_2/Ar ratio of 10/90 associated to a partial pressure of CH_4 imposed by 200 sccm mass flow. But again selectivity was not acceptable since the I_G/I_D ratio was 0.8.

Test	H_2 (sccm)	Ar (sccm)	I_G/I_D	$g_c/g_{catalyst}$	$T_{oxidation}$ (°C)	g_C/g_{Fe}	TOF (h^{-1})	TEM
11	100	0	5.16	b.d	b.d	b.d	b.d	SWCNTs
12	90	10	1.54	0.006	534	0.3	0.6	SWCNTs
13	80	20	0.95	0.009	544	0.45	0.9	Not done
14	50	50	0.88	0.012	520	0.59	1.2	Not done
15	10	90	0.82	0.035	538	1.79	3.5	Not done
16	0	100	1.3	0.069	508/565	3.43	6.9	Graphite sheets + SWCNTs

200 sccm CH_4; T_d=900°C; t_d=30min

Table 10: Effect of H_2 partial pressure on the activity and selectivity of the 4% catalyst

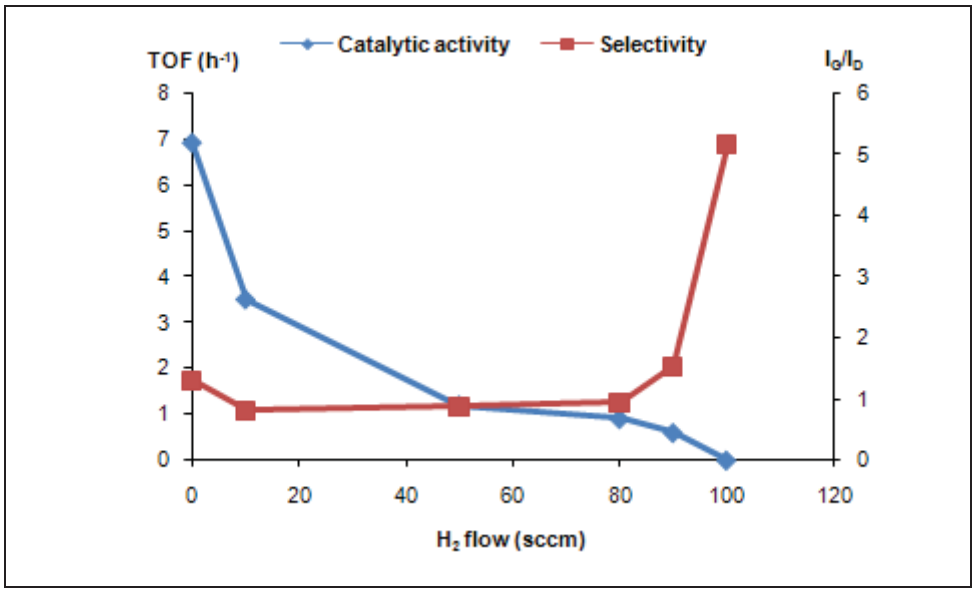

Figure 18: Variation of selectivity and activity as a function of H_2 partial pressure

In the literature, the presence of H_2 and its partial pressure relative to CH_4 (CH_4 /H_2 ratio) is reported to play an important role on the selectivity towards SWCNTs [45]. Nevertheless high H_2 concentrations are also known to decrease the yield of SWCNTs using iron oxide catalysts at 900 °C [80, 81]. This could be due either to SWCNT etching after deposition or to inhibition of CH_4 decomposition (Eq. 2).

$$SWCNT + H_2 \rightleftharpoons CH_4 \qquad \text{Eq. 2}$$

We decided to do a closer investigation on the test without hydrogen by TEM to identify the nature of the interesting yield of 0.069 $g_C/g_{catalyst}$ obtained under the (Ar) condition.

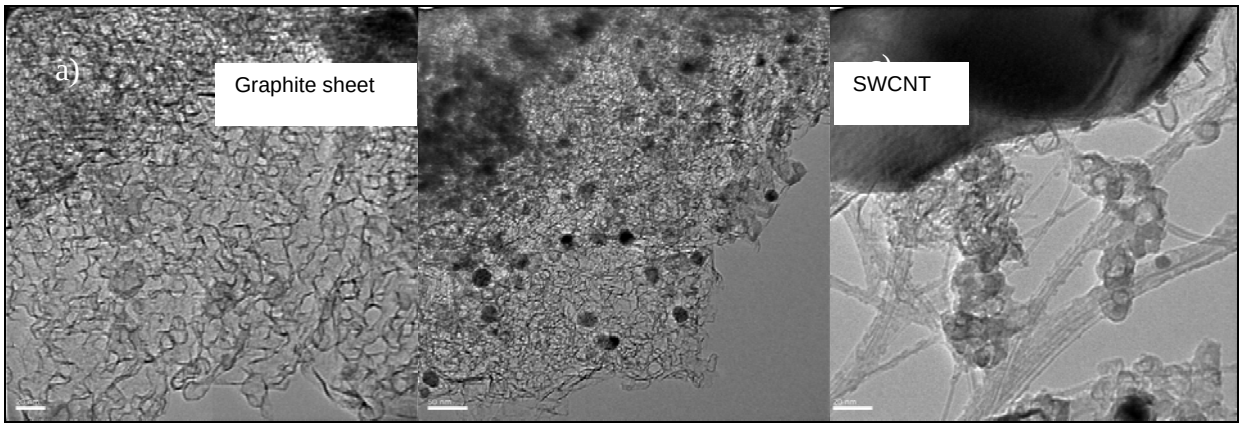

Figure 19: HREM micrographs of the test 16 after catalyst removal

To get an easier look on the carbon products, the catalyst was removed by a solution of 20% HF. In the micrographs (Fig. 19) we observed some single-walled carbon nanotubes assembled in bundles and some graphitic structures that we named graphite sheets. This was in accordance with the TGA analysis where we observed two decomposing temperatures: 508 and 565 °C (Fig. 20). The weight percentage of each of the species was however difficult to estimate.

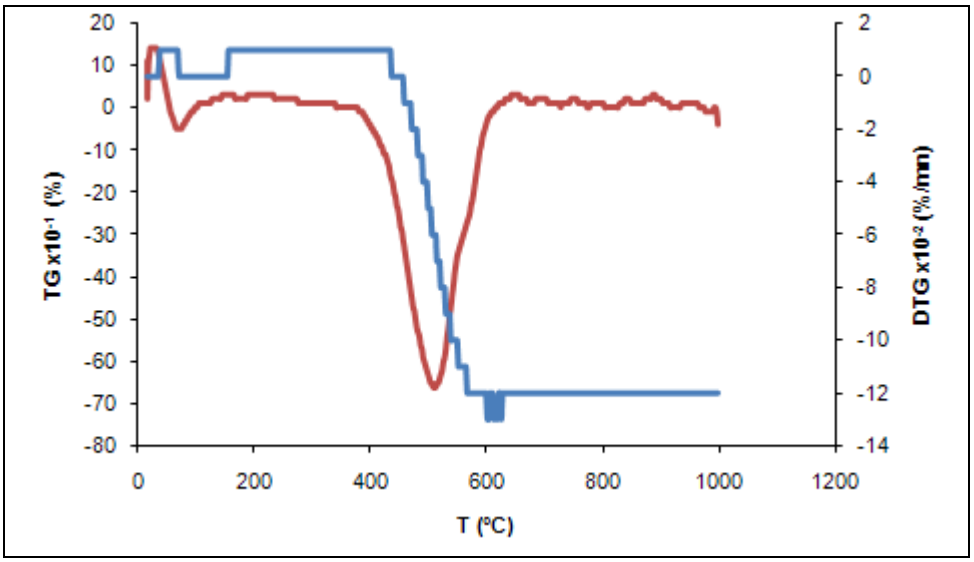

Figure 20: TGA thermogram of sample 16

From the SEM micrographs, we could confirm the high activity under the (Ar) condition as we see abundant SWCNT bundles covering the surface of the catalyst grain.

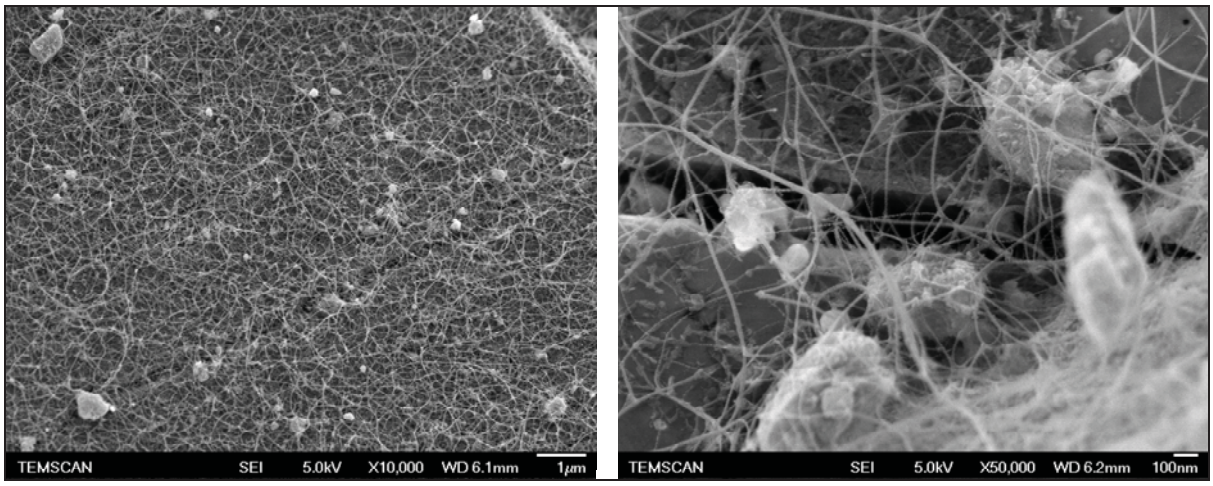

Figure 21: SEM micrographs of sample 16

Unfortunately, the Raman spectra of such sample completed the TEM and TGA conclusions on selectivity, as three spectra taken from different areas of the sample yield very different I_G/I_D ratios: 0.95; 2.46 and 0.65 (Fig. 22).

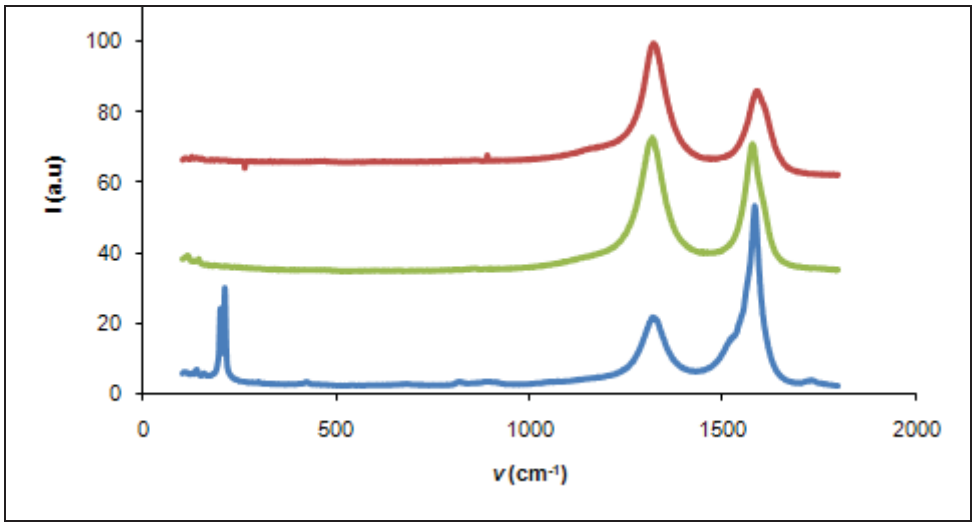

Figure 22: Raman spectra taken at 3 sampling zones of the 16 sample

Once again, we found a condition for the 2% catalyst yielding SWCNTs but with an average selectivity. From now on, the 200/100 sccm CH_4/H_2 will be called the (H_2) condition and 200/100 sccm CH_4/Ar the (Ar) condition.

II-2-6-2-Effect of the activation temperature

In an attempt to increase the yield of SWCNTs while keeping a good selectivity, the activation temperature was lowered to 700 °C and 500 °C keeping the duration of the

treatment at 10h. Those new activated catalysts were tested under the (Ar) and (H_2) conditions.

Test	Condition	$T_{activation}$ °C	I_G/I_D	$g_C/g_{Catalyst}$	$T_{Oxidation}$ (°C)	g_C/g_{Fe}	TOF (h^{-1})
11	H_2	900	5.16	b.d	b.d	b.d	b.d
17		700	0.96	0.024	540	1.2	2.4
18		500	0.98	0.026	547	1.3	2.6
16	Ar	900	1.3	0.074	506	3.7	7.4
19		700	0.56	0.074	511	3.7	7.4
20		500	0.57	0.069	515/545	3.5	6.9

200 sccm CH_4; T_d=900°C; t_d=30min

Table 11: Selectivity and activity as a function of $T_{activation}$ under (Ar) and (H_2) conditions

Under the (H_2) condition the catalytic activity increased from being undetectable to 2.4-2.6 h^{-1} but the selectivity dropped dramatically: I_G/I_D from 5 to 1 (Table 11). Curiously, under the (Ar) condition, the catalytic activity remained unchanged, and the selectivity dropped. The activation temperature has an effect on the catalytic activity of the catalyst under the (H_2) condition but not under the (Ar) condition. It is possible that the iron species formed in situ are not the same in both cases, hence the behavior as a function of the activation temperature was not the same.

However, no significant improvement in selectivity or activity was observed by lowering the activation temperature. This latter is an important factor and should be strictly kept at 900 °C. In fact, a calcination temperature range of 900-1000 °C is reported to be appropriate for improving the catalyst performances [82]. Below 900°C iron species are heterogeneous and not well dispersed, beyond 1000 °C a compact surface of alumina could be generated, which is not adapted for gas diffusion and that prevent SWCNT growth.

II-2-6-3-Variation of the supersaturating g_C/g_{Fe} ratio (Z)

The saturation of the supported iron nanoparticles by carbon is an essential factor in the determination of activity and selectivity towards one type of carbon nanostructure [83, 84]. SWCNTs are produced when the right compromise is reached between the

decomposition rate of the carbon source, the diffusion rate of carbon through the particles, and the carbon precipitation rate (Fig. 6). The iron content in the reactor was varied by the introduction of different weight of catalyst in the boat inside the reactor keeping the partial pressure of each reactive gas constant. As seen in Table 12 doubling the C/Fe ratio decreased the selectivity (I_G/I_D=1) but do not increase the activity that remains below detection. Lowering the C/Fe ratio to the half or to the quarter increased the activity to around 1.6 h^{-1} but the selectivity was lost (I_G/I_D=0.7-0.9). Thus, the optimum C/Fe ratio was verified at Z=3354 g_C/g_{Fe}/h and no interesting results appeared otherwise.

Test	Catalyst weight (mg)	Z(g_C/g_{Fe}/h) sent	I_G/I_D	$g_C/g_{Catalyst}$	$T_{Oxidation}$ (°C)	g_C/g_{Fe}	TOF (h^{-1})
21	50	1677	1.09	b.d	b.d	b.d	b.d
11	100	3354	5	b.d	b.d	b.d	b.d
22	200	6709	0.93	0.013	521	0.65	1.3
23	400	13418	0.71	0.016	475;533	0.8	1.6

200 sccm CH_4; 100 sccm H_2; 0 sccm Ar; T_d=900°C; t_d=30min

Table 12: Effect of Z on activity and selectivity

II-2-6-4-Increasing the metal loading to 4% Fe/Al_2O_3

As concluded by the previous characterization of the catalysts **(II-2-4-d)**, a considerable amount of iron is dissolved in the sub-lattice of alumina support in the form of ionic Fe^{3+} solid solution, which is very hard to reduce. In fact we can consider that for the 2% catalyst the real active iron species towards CH_4 decomposition is largely less than 2% [79], because Al-Fe interaction is stronger than Fe-Fe and Fe-C ones for low iron concentration [53]. To counter balance this effect we increased the iron loading to 4% iron.

II-2-6-4-a-Verification of the role of activation

First of all, we verified if the activation of the catalyst was still needed, under the (H_2) and (Ar) conditions (Table 13). Under both the (Ar) and (H_2) conditions the activation of the catalyst under static air at 900°C for 10h was still mandatory. Based on the Raman spectroscopy, the I_G/I_D ratio increased from 1 to 2.4 under the (Ar) condition and from 0.9 to 3.1 under the (H_2) condition. The full analysis of the samples 25 and 27 is described in the next section.

Test	t(h), 900°C	H_2 sccm	Ar sccm	I_G/I_D	$g_C/g_{Catalyst}$	g_C/g_{Fe}	TOF (h^{-1})	TEM
24	0	0	100	1.1	0.16	0.4	8	Not done
25	10	0	100	2.38	0.054	1.35	2.7	SWCNTs
26	0	100	0	0.94	0.048	1.2	2.4	Not done
27	10	100	0	3.13	b.d	b.d	b.d	SWCNTs

200 sccm CH_4; T_d=900°C; t_d=30min

Table 13: Effect of the activation on the 4% catalyst

II-2-6-4-b-Effect of H_2 partial pressure

Like for the 2% catalyst we varied the H_2 partial pressure in the reactor (variation of the mass flow of H_2) keeping the CH_4 partial pressure constant (200 sccm CH_4) and the total flow at 300 sccm by adjusting the Ar flow.

The results were the following:

Test	H_2 sccm	Ar sccm	I_G/I_D	$g_C/g_{Catalyst}$	$T_{oxidation}$ (°C)	g_C/g_{Fe}	TOF (h^{-1})	TEM
25	0	100	2.38	0.054	501	1.35	2.7	SWCNTs+ E[a]
28	10	90	1.52	0.031	470	0.775	1.55	SWCNTs+ E[a]
29	50	50	1.6	0.003	476	0.075	0.15	Not done
30	90	10	1.53	0.008	501	0.2	0.4	Not done
27	100	0	3.13	b.d	b.d	b.d	b.d	SWCNTs

200 sccm CH_4; T_d=900°C; t_d=30min; [a]Encapsulated nanoparticles

Table 14: Effect of H_2 partial pressure on activity and selectivity

The same observations as for the 2% Fe/Al_2O_3 catalyst remained for the 4% one, a high H_2 partial pressure would lead to high selectivity towards SWCNTs but low carbon yields. Nevertheless, the selectivity of the activated 4% catalyst under the (Ar) condition (I_G/I_D =2.38) in spite of being lower than the one under the (H_2) condition (I_G/I_D =3.1) starts to be acceptable (Fig. 23). The role of hydrogen partial pressure in achieving high selectivity with the 4% Fe/Al_2O_3 catalyst seems less pronounced that with the 2% Fe/Al_2O_3, for which I_G/I_D varied from 5 (H_2) to 1 (Ar).

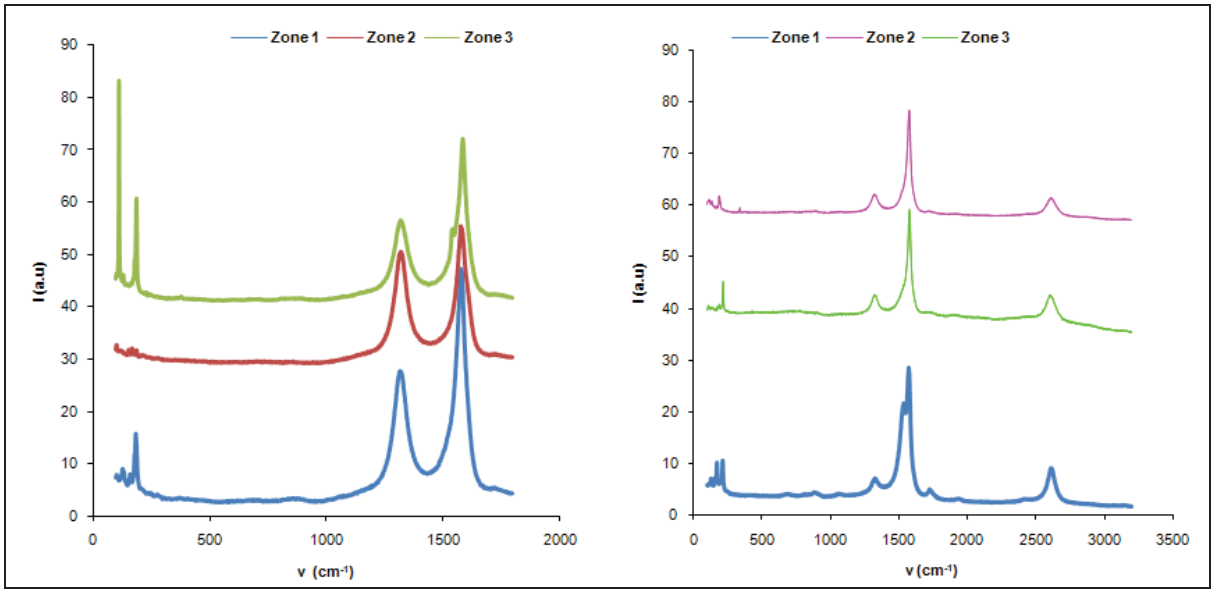

Figure 23: Raman spectra of the 25(left) and 27(right) samples

This was in accordance with the Mössbauer spectroscopy results made on the 2 and 4% catalysts (**section II-2-4-d**). The only difference between the 2 and 4% iron loadings after activation was the appearance of 5% bigger nanoparticles in the 4% activated catalyst indicating the saturation of the alumina matrix with iron in the sub-monolayer form. In fact, increasing the metal loading to 4% was a right choice, allowing to avoid the addition of hydrogen in the reactor, which is detrimental to SWCNT growth [81]. Thus, removing hydrogen led to an increase in the yield of carbon deposition to $0.054 g_C/g_{Catalyst}$ (TOF=2.7 h^{-1}).

The iron loading was expected to affect activity and selectivity towards SWCNT, by mean of particle size and distribution but one should keep in mind that structure and interactions with alumina are also important. For low iron loadings, we can expect strong Fe-Al interactions, leading to reduction difficulties: in that case H_2 is needed. At 4% iron loading, the iron saturated the anchoring sites of alumina lattice in the form of a sub-monolayer, thus Fe-Al interaction are weaker, and H_2 generated by CH_4 decomposition is sufficient for reduction to $Fe^{(II)}$, and no further H_2 addition is needed.

In the HREM micrographs (Fig. 24), SWCNTs appeared clearly in both (Ar) and (H_2) conditions. Both conditions were selective towards SWCNTs, but the sample with (H_2) was as expected purer.

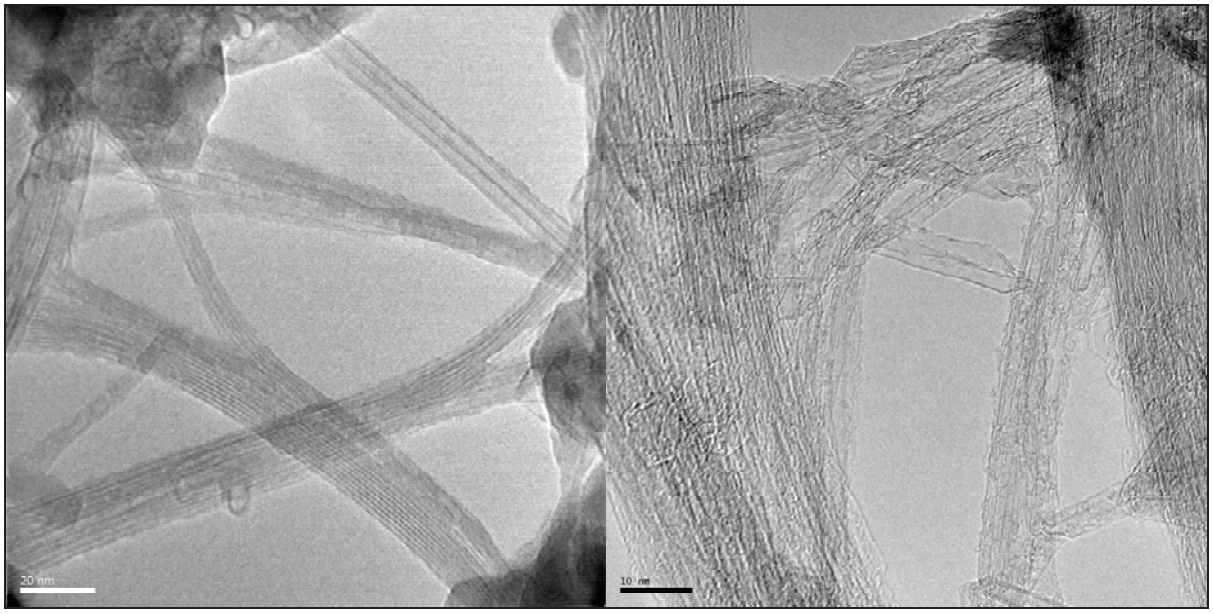

Figure 24: TEM micrograph of samples 25 (left) and 27 (right)

Under the (H_2) condition, the distribution of the tube's diameter was narrow with a majority between 0.5 and 2.5 nm, confirming the SWCNT/DWCNT structure (Fig. 25). The average diameter was 1.3 nm. Imprecise diameter distribution based on radial breathing modes of the Raman spectrum performed with only one wave number (632 nm) and using equation 2 was almost similar to the distribution observed in TEM (1.2-2.4 nm) and an average diameter of 1.7nm.

$$\omega_{RBM} = 234/d_{SWNT} + 10\ (cm^{-1})\ \text{(Equation 2) [85]}$$

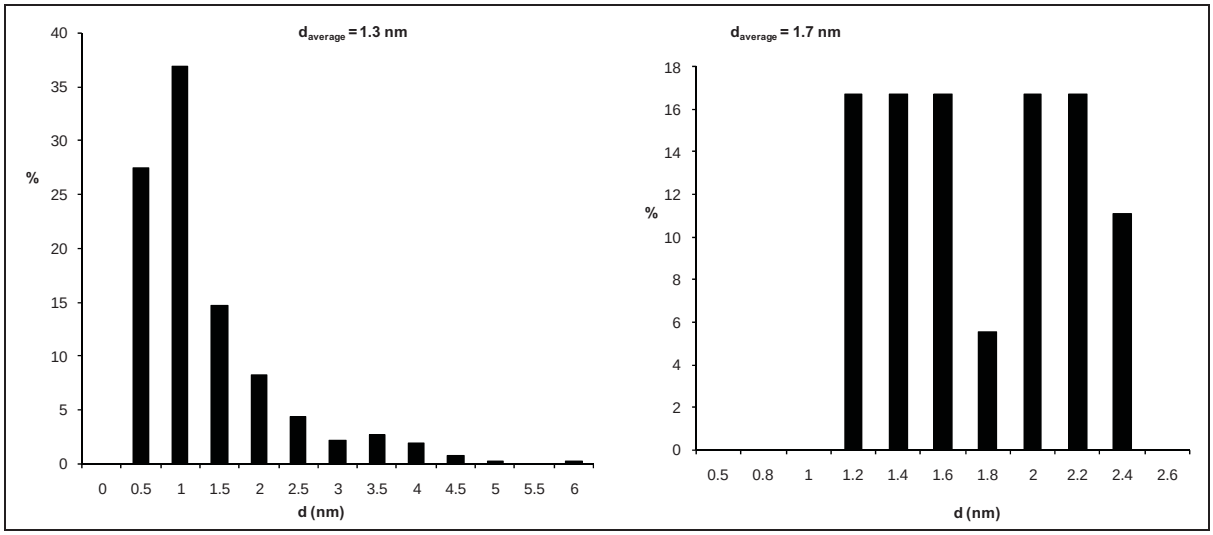

Figure 25: Diameter distribution in sample 27 from TEM (left) and Raman at 632 nm (right)

Under the (Ar) condition, the distribution of the tube's diameter (Fig. 26) was also narrow, between 1 and 3.5 nm; but larger than the one under the (H_2) condition. The average diameter was 2.2 nm. Imprecise diameter distribution based on Raman RBMs was almost similar to the TEM observed distribution (1-2.2 nm), but the average diameter varied and was 1.6 nm. This indicated that a missing part of the SWCNTs does not yield RBMs at the 632 nm wave length.

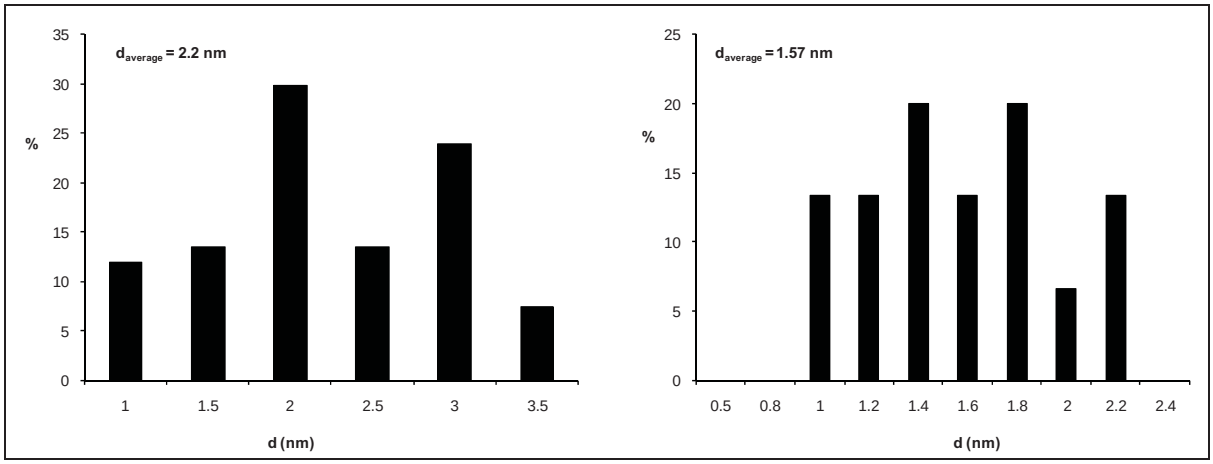

Figure 26: Diameter distribution in the sample 25 from TEM (left) and Raman at 632 nm (right)

TGA (Fig. 27) and SEM (Fig. 28) analysis indicate low SWCNT yields under the (H_2) condition. For the (Ar) condition catalytic activity starts to be acceptable (TOF=2.7 h^{-1}), and a yield of $0.05 g_C/g_{Catalyst}$ was obtained and was assumed to be SWCNTs considering the previous TEM observations and the oxidizing temperature of 500 °C (Fig. 28).

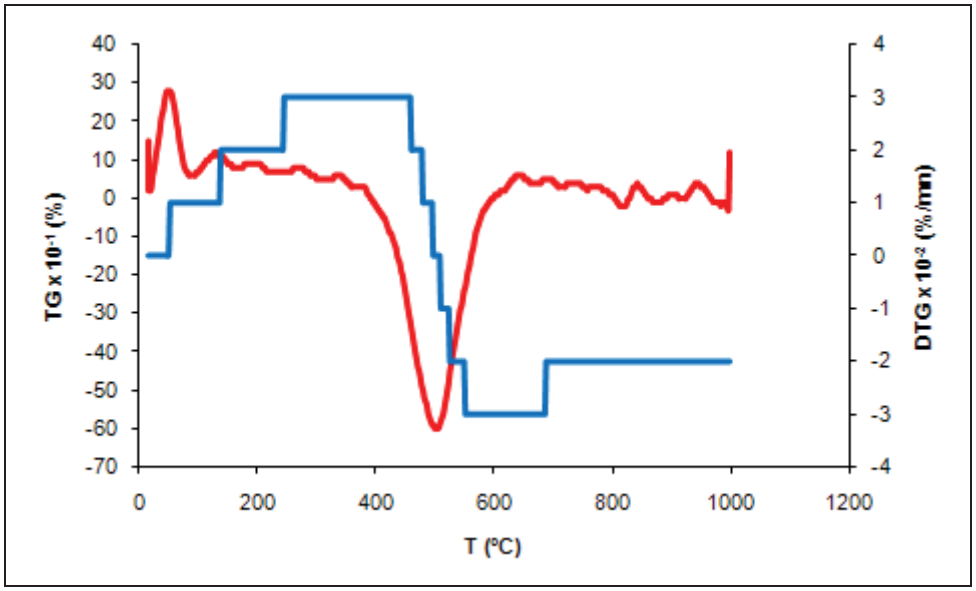

Figure 27: TGA thermogram of sample 25

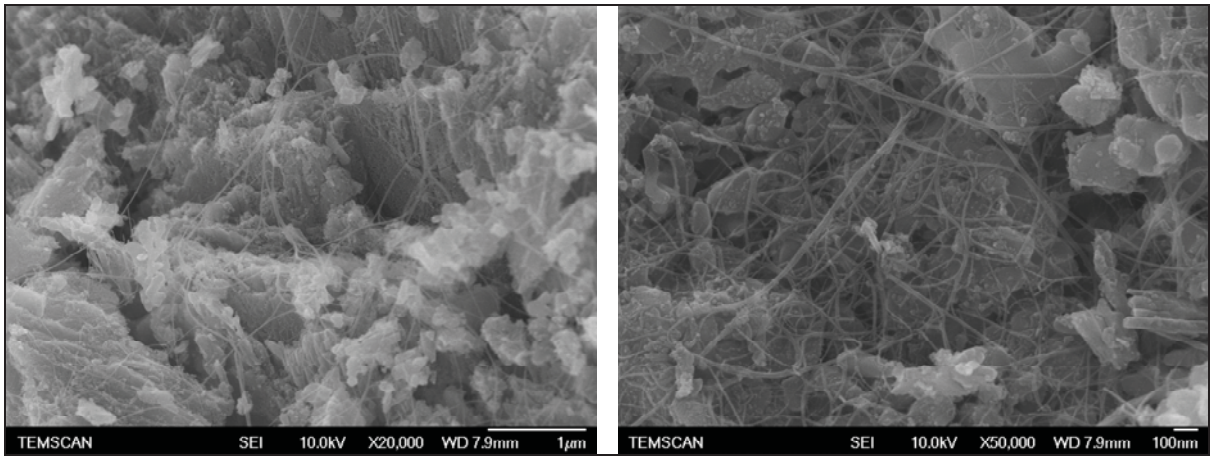

Figure 28: SEM micrographs of the sample 27

Now that we found relatively good conditions at 200/100 (sccm) CH_4/Ar with the 4% activated Fe/Al_2O_3 catalyst, associating better catalytic activity and good selectivity, further studies were performed for optimization.

II-2-6-4-c-Effect of CH_4 partial pressure

The 4% Fe/Al_2O_3 activated catalyst was tested under different CH_4 partial pressures [83] by varying the methane mass flow in the reactor and keeping constant the total mass flow at 300 sccm by adjusting the Ar flow. The results are assembled in Table 15.

Test	CH_4 scc	Ar scc	I_G/I_D	Z (g_C/g_{Fe}/h)	$g_C/g_{Catalyst}$	$T_{oxidation}$ (°C)	g_C/g_{Fe}	TOF (h^{-1})	TEM

	m	m							
31	75	225	2.83	157	0.041	485	1.02	2.05	Not done
32	150	150	3	314	0.058	494	1.45	2.9	SWCNTs+E[a)]
25	200	100	2.38	419	0.054	501	1.35	2.7	SWCNTs+E[a)]
33	225	75	2.03	471	0.063	519	1.58	3.15	Not done

T_d = 900 °C; t_d = 30 min; [a)]Encapsulated nanoparticles

Table 15: Effect of CH_4 partial pressure on activity and selectivity of the 4% catalyst

Selectivity towards SWCNTs slightly increases (I_G/I_D of 2.83 to 3 in Raman spectroscopy), then decreases linearly with the partial pressure of CH_4 (Fig. 29).

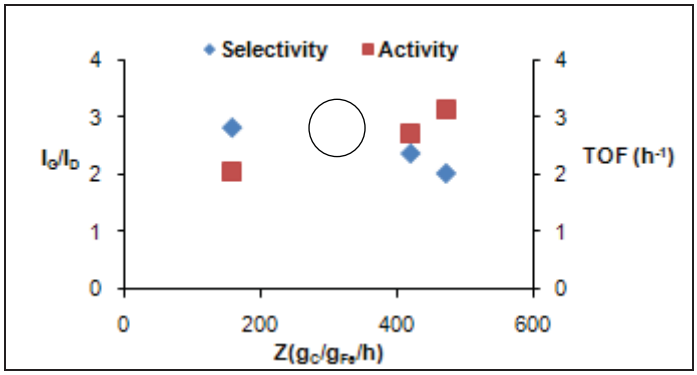

Figure 29: Activity and selectivity variations as a function of CH_4 partial pressure

The decrease in selectivity could be correlated to the increase of the calcinations temperature observed by TGA on the deposited carbon (Fig. 30).

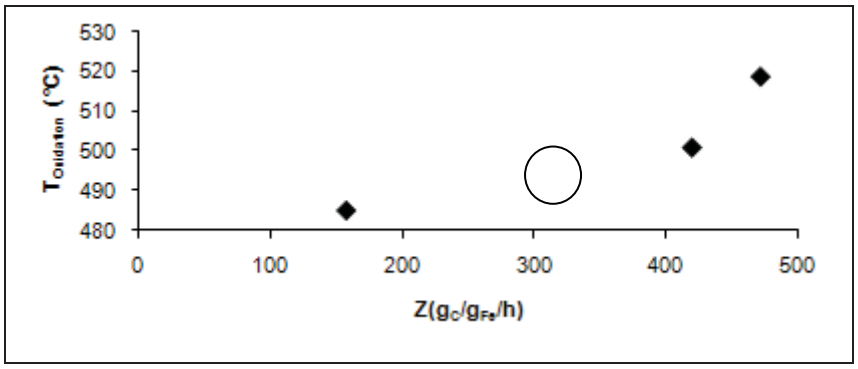

Figure 30: Variation of the SWCNT oxidation temperature as a function of P_{CH4}

The activity increased linearly with the CH_4 partial pressure, indicating a positive order for this parameter in the rate of SWCNTs growth (Fig. 29). The most interesting

condition of this study was the Z of 314 $g_C/g_{Fe}/h$ (test 32) for which we observed the highest selectivity (I_G/I_D =3) and a good activity (TOF=2.9) with carbon yield of 0.058 $g_C/g_{catalyst}$.

Adjusting the partial pressure of CH_4 optimizes the C/Fe supersaturating ratio that limits the formation of other forms of carbon than SWCNTs, and thus leading to higher selectivity [83]. From the TEM micrographs, we can see that the formation of encapsulated nanoparticles could not be avoided. Those latter could be formed at the last cooling step of SWCNT synthesis, by expulsion of the residual carbon dissolved in the iron nanoparticle. The characterizations of sample 32 are assembled in Fig. 31.

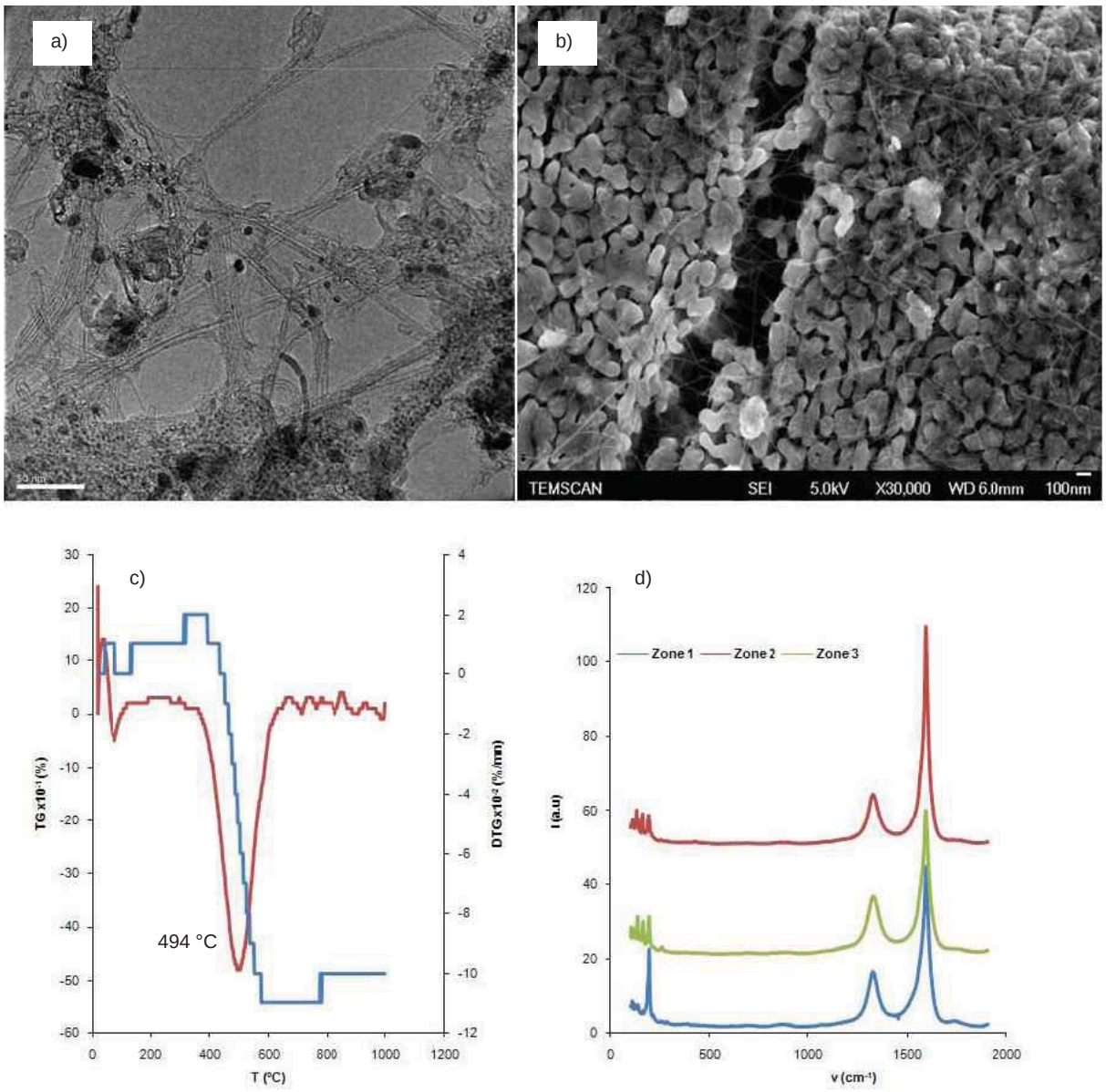

Figure 31: a) TEM micrograph, b) SEM, c) TGA and d) Raman spectra of sample 32

The diameter distribution of the SWCNT/DWCNT of sample 32 ranged from 1.5 to 3.5 nm with an average diameter of 2.6nm. The average diameter according to the Raman RBMs was 1.8 nm (Fig. 32).

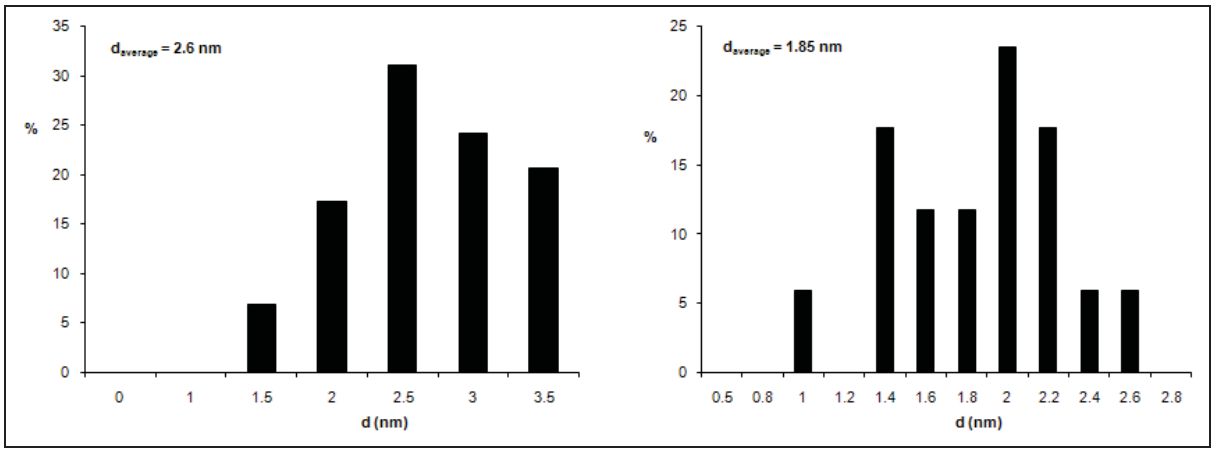

Figure 32: Diameter distribution in sample 32: TEM (left), and Raman at 632 nm (right)

II-2-6-4-d-Influence of the total flow rate

The CH_4 partial pressure was kept constant (Z of 314 $g_C/g_{Fe}/h$) and the total mass flow rate (w) was varied.

Test	W sccm	CH_4 sccm	Ar sccm	I_G/I_D	$g_C/g_{Catalyst}$	$T_{oxidation}$ (°C)	g_C/g_{Fe}	TOF (h^{-1})	TEM
25	300	200	100	2.38	0.054	501	1.35	2.7	SWCNTs
34	200	130	70	2	0.057	497	1.42	2.85	SWCNTs
35	100	67	33	1	0.049	499	1.22	2.45	Not done

Table 16: Effect of total gas flow on activity and selectivity

As seen in table 16 progressive decrease of the total mass flow (w) from 300 to 200 and 100 sccm decreases the I_G/I_D ratio. We notice the appearance of different D bands in the Raman spectra as a function of the decrease in the total mass flow and this is particularly clear for the w = 100 sccm sample (Fig. 33). Different D bands could exist that are related to the presence of amorphous carbon or to different deformations of the surface of SWCNTs or interaction of the SWCNTs with iron and alumina [86-87]. SWCNTs are proven to exist by the presence of RBMs and TEM analysis (Fig. 34). The result is a heterogeneous sample.

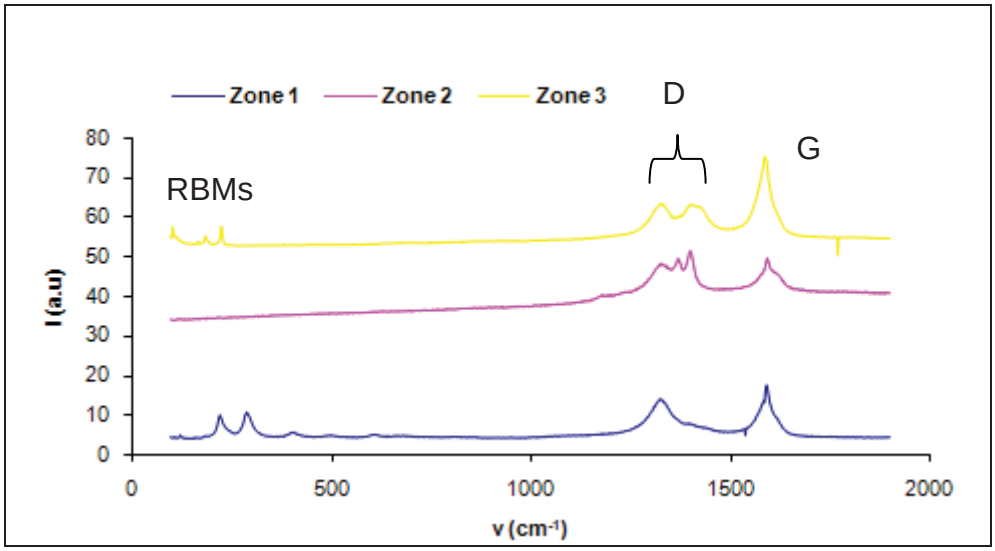

Figure 33: Raman spectra of sample 35 in different sampling zones

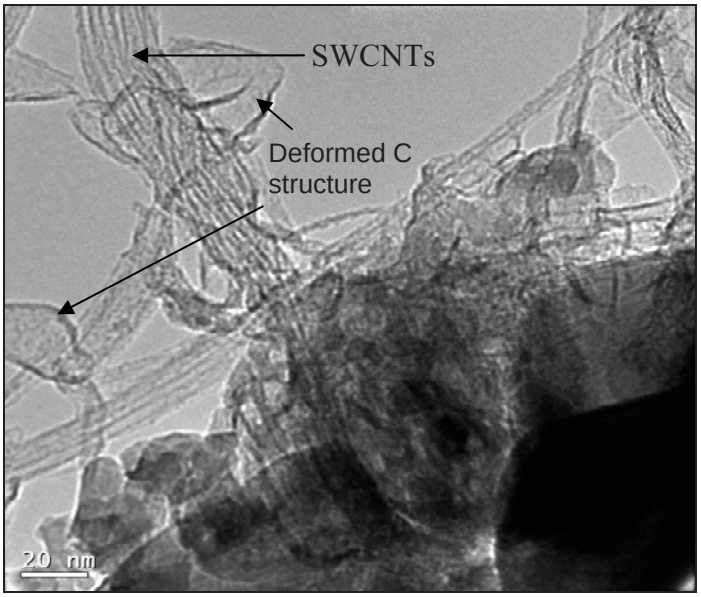

Figure 34: TEM micrograph of sample 34

The catalytic activity did not vary a lot and was around 2.4-2.8 h^{-1}. This indicates that the total mass flow for the synthesis of SWCNTs was at its optimum at 300 sccm, and changes affect selectivity or disorders the surface of SWCNTs without remarkable increase in catalytic activity.

II-2-7-Increasing the metal loading to 6% Fe/Al_2O_3

Finally, we increased the metal loading to 6% to see if there would be further increase in the catalytic performances. After activation, the catalyst was tested under the (H_2) condition. Catalytic activity increased from being below detection in the case of 1, 2 and 4% of iron, to 1.8 h^{-1} for the 6% iron loading. But a lost of selectivity was observed as the I_G/I_D

ratio decreased with the increase of iron loading from 5 at 2% to 3 at 4%, and finally 1.3 at 6% Fe/Al_2O_3 (Table 17).

Test	% Fe	CH_4 sccm	H_2 sccm	Ar sccm	I_G/I_D	$g_C/g_{Catalyst}$	T (°C)	TEM
36	1	200	100	0	2.30	b.d	b.d	SWCNTs
11	2	200	100	0	5.3	b.d	b.d	SWCNTs
27	4	200	100	0	3.13	b.d	b.d	SWCNTs
37	6	200	100	0	1.28	0.054	550	Fibers

Table 17: Catalytic activity and selectivity as a function of the iron loading under the (H_2) condition

This may be due to the decrease in the C/Fe ratio. However, increasing the methane partial pressure did not enhance the selectivity (test 38, 39 of Table 18).

Test	CH_4 sccm	H_2 sccm	I_G/I_D	$g_C/g_{Catalyst}$	$T_{oxidation}$ (°C)	g_C/g_{Fe}	TOF (h^{-1})	$I_G/I_{D\ distribution}$
37	200	100	1.28	0.054	550	0.9	1.8	1.4-1.47-0.98
38	270	30	1.5	0.032; 0.018	496;561	0.83	1.6	2.86-0.65-1.02
39	290	10	0.7	0.049	507	0.82	1.6	0.83-0.62-0.67

Table 18: Activity and selectivity of the 6% activated catalyst with different methane partial pressures

As previously stated in section **II-2-4-d**, from 1 to 4 % iron loadings the active iron species was the same after activation: a sub-monolayer of $Fe^{(III)}$ on the alumina lattice. The supersaturating C/Fe ratio had a slight effect on selectivity that remained acceptable $I_G/I_D>2$ but catalytic activities remained constant and relatively low. At 6% loading the nature of the active species changed, and we observed in addition to the $Fe^{(III)}$ monolayer, some Fe_2O_3 crystallites leading to a decrease of the selectivity. We think that the Fe_2O_3 crystallites are responsible of the appearance of the thick nanofiber present with the 6% activated catalyst [71]. We can now say that the effect of the nature of the iron active species is more important than the C/Fe supersaturating ratio since SWCNTs were notably absent in the TEM micrographs of Figure 35.

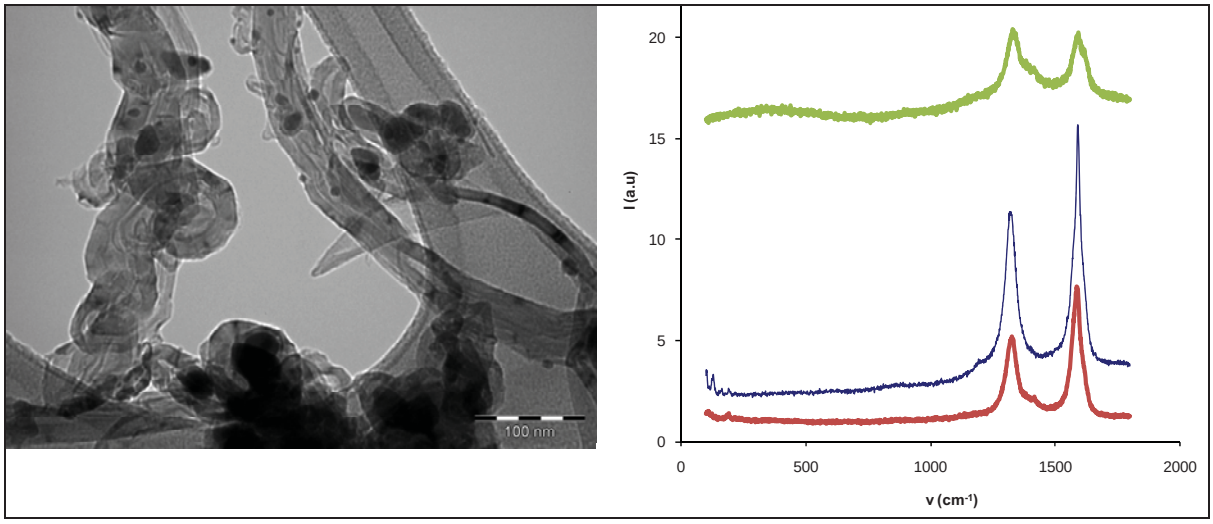

Figure 35: TEM micrograph (left) and Raman spectra (right) of sample 37

II-2-8- Conclusion

For all 1, 2, 4 and 6% w/w iron catalysts, MO-CVD yield a deposition of iron oxide in the vacant sites of the alumina as submonolayer and on its surface in the form of crystallites of Fe_2O_3. The proportion of this latter increased with the iron loading. In contact with the reactive atmosphere, each iron species yields different carbon nanostructures. While the sub-monolayer species are suitable for SWCNT growth (ultrafine dispersion of iron), the crystallites yield thick carbon nanofibers [71]. Activation of the catalyst (10h, 900 °C) redistributes the iron in favor of the submonolayer. For an alumina surface, there is a threshold for iron solubility. For the activated 6% w/w iron catalyst we step over this limit and selectivity decreases with the formation of thick carbon nanofibers. A scheme of those hypotheses is presented in Fig 36.

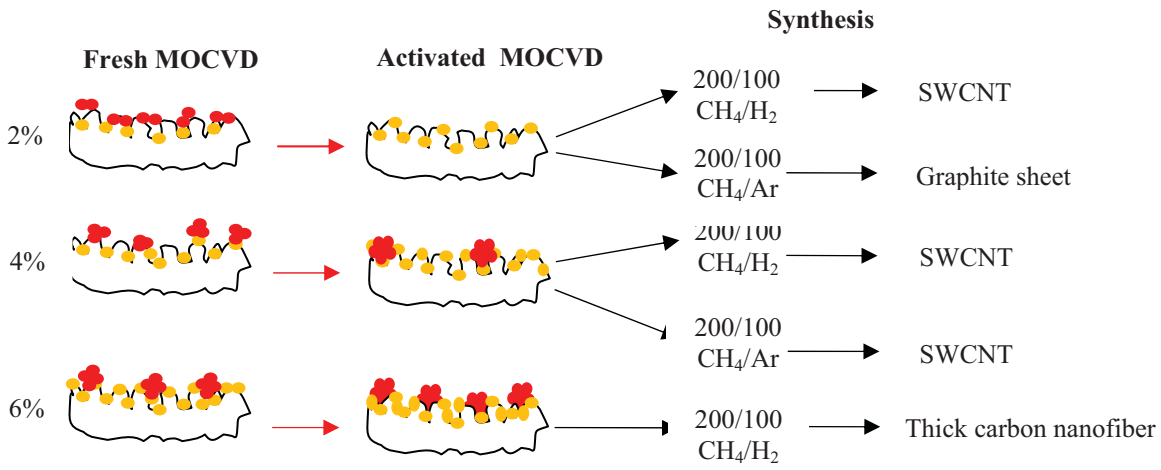

Figure 36: Global conclusions on the SWCNT synthesis

Another essential conclusion is the role played by the iron to alumina interaction in imposing the suitable reactive atmosphere and determining the selectivity. For the activated 2% catalyst, such interaction is strong; H_2 is needed for the reduction of iron to yield SWCNTs. Without H_2 carbon sheets are formed. At 4% loading the Al-Fe interaction is weakened by the saturation of the surface with iron, H_2 is no more essential to achieve selectivity towards SWCNTs since the iron oxide became more reducible.

Additionally, the choice of alumina as support [80], permits a good dispersion of iron and optimum reducibility at 4% iron loading after activation. This catalyst in contact with the appropriate gas mixture of CH_4/Ar yields $FeAl_2O_4$ nanoparticles with an appropriate size for SWCNT production with good catalytic activity and selectivity. We found optimum conditions for the production of SWCNTs that combines good selectivity ($I_G/I_D = 3$) and good catalytic activity (0.05 $g_C/g_{Catalyst}$, TOF = 2.8 h^{-1}) with the activated 4% Fe/Al_2O_3 under 150/150 sccm of CH_4/Ar at 900 °C.

II-3- Multiwalled carbon nanotubes synthesis (MWCNTs)

The MWCNT synthesis was conducted on the freshly prepared MO-CVD 4% w/w Fe_2O_3/Al_2O_3 catalyst according to the conditions of Table 19.

Test	Condition	T (°C)	$m_{catalyst}$ (g)	TEM	TGA				Raman
				$d_{average}$ (nm)	$g_C/g_{catalyst}$	g_C/g_{Fe}	TOF (h^{-1})	$T_{oxidation}$ (°C)	I_G/I_D
MW1	Classical	650	2	8.7	0.15	3.75	3.7	524/647	0.58
MW10	Classical	700	2	5.7	0.11	2.69	2.7	647	-
MW9	Classical	750	2	13.9	0.15	3.78	3.8	522/610	-
MW2	Hyperion	650	0.1	6.7	0.15	3.73	7.5	581	0.63
MW3	Hyperion	650	0.5	6.9	0.16	4.13	8.3	628	0.63
MW8	Hyperion	700	0.5	6.5	0.28	6.99	14.0	636	0.76
MW7	Hyperion	750	0.5	6.7	0.04/0.23	6.79	13.6	483/638	-

Classical condition: 60 sccm C_2H_4; 120 sccm H_2; 160 sccm N_2; $t_{Reaction} = 60$ min
Hyperion condition: 200 sccm C_2H_4; 100 sccm H_2; $t_{Reaction} = 30$ min

Table 19: Conditions and results for MWCNT synthesis

From the literature two main conditions were selected: i) the one developed in our laboratory [22] called the classical condition and ii) the Hyperion condition were high flow rates of C_2H_4 are used [22, 88].

Under the classical condition (MW1), two oxidation temperatures at 524 and 647 °C of the as prepared material were observed by TGA analysis (Table19), indicating a non homogeneous sample. This was confirmed by TEM observations (Fig. 37), where few fibers were observed in addition to MWCNTs. Additionally, the catalytic activity was low (TOF=3.7 h^{-1}) with carbon yield of 3.75g_C/g_{Fe}.

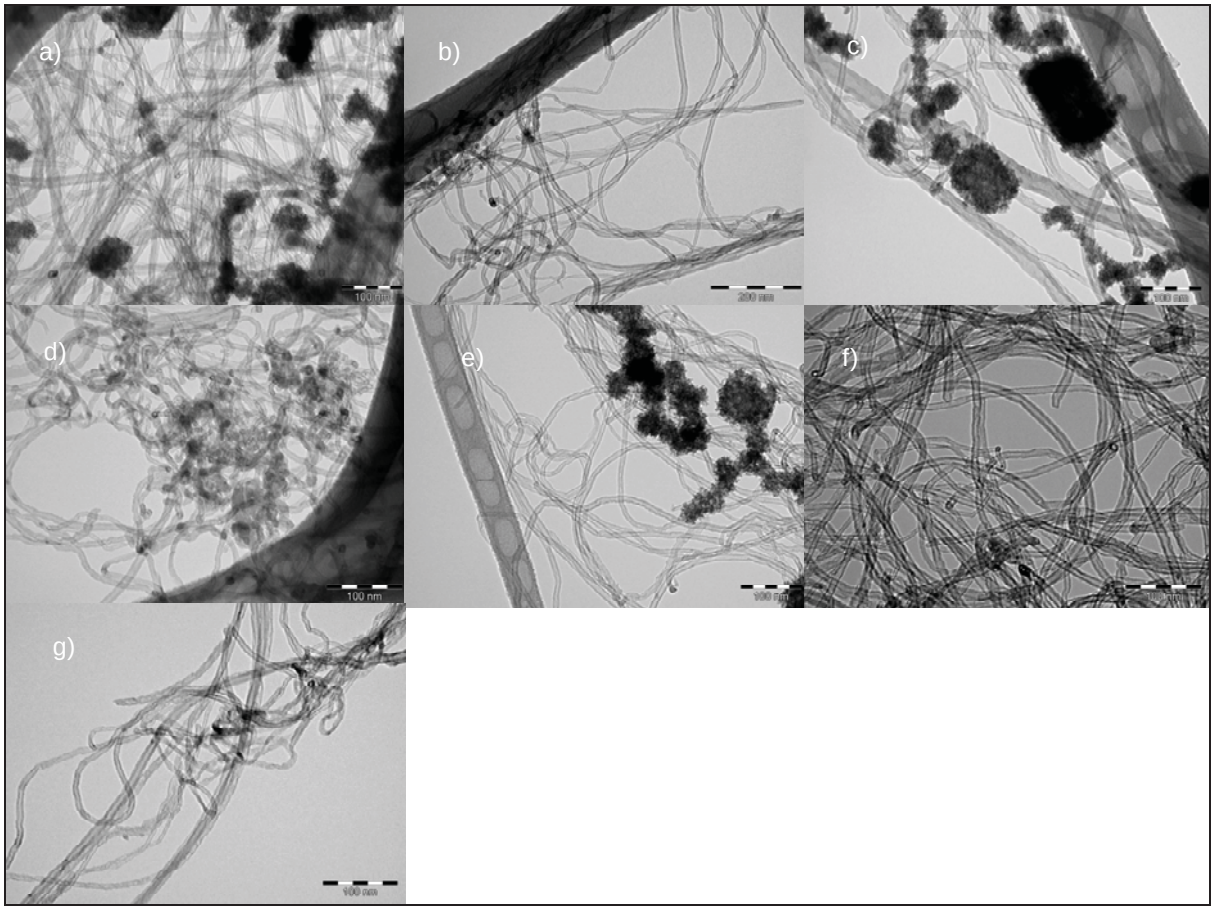

Figure 37: TEM micrographs of the MWCNT at different synthesis conditions a)MW1, b)MW10, c) MW9, d)MW2, e)MW3, f)MW8, g)MW7

Under the Hyperion condition, the sample (MW2) was proved to be more homogeneous by TEM observations (Fig. 37) and TGA analysis (Table 19) as only one oxidation temperature at 581 °C was observed. The catalytic activity doubled to 7.5 h^{-1} in comparison with the 3.5 h^{-1} obtained under the classical conditions. Increasing the amount of catalyst in the reactor from 0.1 to 0.5g (MW3) led to the increase of catalytic activity from 7.5 to 8.3 h^{-1}.

The effect of reaction temperature was evaluated for both the classical and the Hyperion conditions, aiming to get better MWCNT yields and selectivity. For the modified classical tests no interesting results were observed upon increasing the temperature to 700 °C and 750 °C (Table 19). Nevertheless, under the modified Hyperion conditions, an increase in the deposition temperature improves the catalytic activity from 8.3 to 14 h^{-1} and carbon yield from 4.13 at 650 °C to around 7 g_C/g_{Fe} at 700 °C. At 750 °C a mixture of carbon structures starts to appear in the sample as seen in the TEM micrographs of Figure 37 and was confirmed by the observation of two oxidation temperatures in TGA (Table 19).

The distribution of the external diameters of each sample and the average external diameter were calculated based on the TEM micrographs (Fig. 38).

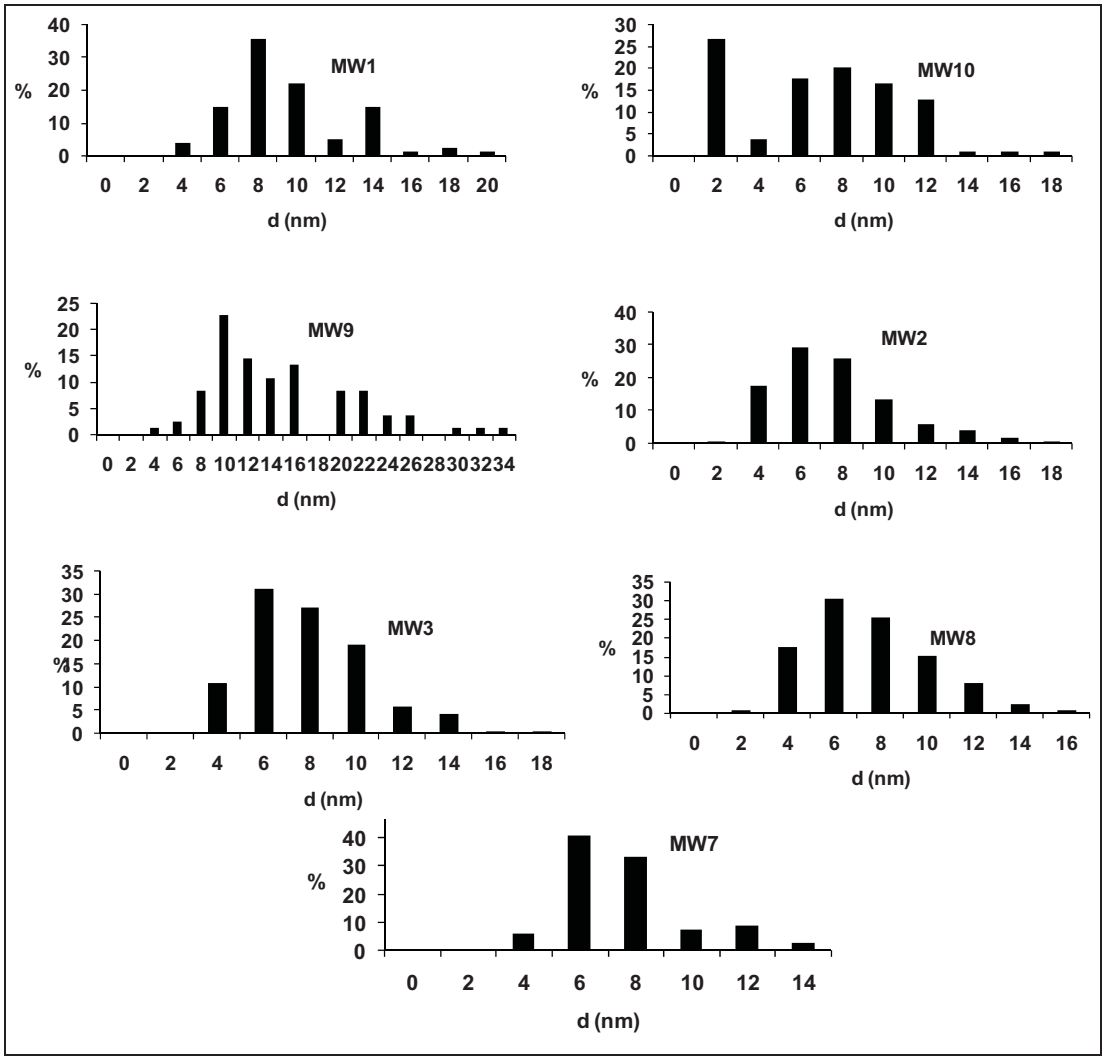

Figure 38: Distribution of MWCNT external diameter

For all samples, the external diameter distribution was almost the same, between 2 and 14 nm. In the classical conditions the average diameters were variable between 5.7 and

13.9 nm. For the Hyperion conditions, the average diameter was narrower and remained unchanged at around 6 nm.

The higher selectivity and yield and narrower external diameter distribution under the Hyperion condition could be explained by a higher supersaturating ratio effect (C/Fe) similar to the case of SWCNT (Fig. 6). In fact, under such conditions a lower mass of catalyst (0.5 g) and a higher partial pressure of ethylene (200 sccm) are introduced in the reactor.

In summery and taking into account the selectivity towards MWCNTs, narrow external diameter distribution and good yields, the best condition associated to the fresh 4% MO-CVD catalyst for the synthesis of MWCNTs were the modified Hyperion conditions (MW8) with 0.5 g of catalyst introduced in the reactor at a deposition temperature of 700 °C.

II-4- Carbon nanofibers synthesis (CNFs)

Nickel based catalysts are known from the literature to generally yield carbon nanofibers [89-91]. In this optic a metallic Ni/Al_2O_3 catalyst was prepared. Many conditions of chemical vapor deposition using nickelocene as nickel source exist and involve different sublimation temperature, decomposition temperature and result in different Ni species on the support (Table 20).

Gas mixture	$T_{sublimation}$ (°C)	$T_{deposition}$ (°C)	Species deposited	Ref
Ar	30	550	Nickel oxide film	[92]
$Ar+H_2$	100-120	190-230	Metallic nickel film	[93]
$Ar+H_2$	130	180-350	Metallic nickel film	[94]
$Ar+H_2$	120	200-350	Metallic nickel film	[95]

Table 20: CVD of nickelocene [$Ni(Cp)_2$] under different conditions yielding different structures

The Ni^0/Al_2O_3 catalyst was prepared by MO-CVD under the condition of Table 21 using the reactor presented in Figure 39. The detailed procedure for Ni deposition is described in chapter V.

m Al_2O_3 (g)	m $Ni(Cp)_2$ (g)	T_S (°C)	T_C (°C)	H_2 (sccm)	N_2 (sccm)	Total (sccm)	$t_{deposition}$ (h)	P (mbars)	%Ni
50	9	135	220	350	300	650	5	0.5	5.95

Table 21: Condition of Ni^0/Al_2O_3 CVD deposition from $Ni(Cp)_2$

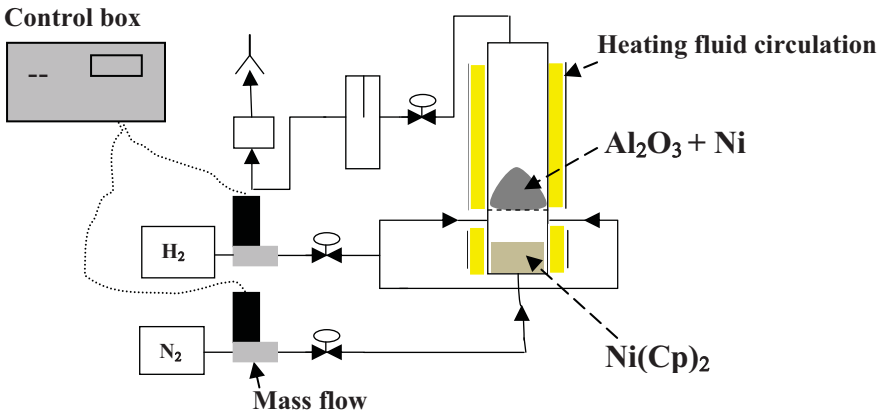

Figure 39: Apparatus for CVD of nickelocene on alumina

This catalyst was tested under different conditions of C_2H_4 and H_2 partial pressures (Table 22).

Test	Catalyst	t (min)	C_2H_4 (sccm)	H_2 (sccm)	N_2 (sccm)	$g_C/g_{Catalyst}$	g_C/g_{Ni}	TOF (h^{-1})	MET
F1	fresh	60	105	120	160	0.19	3.2	3.2	CNF ≠ diameter
F2	oxidized	60	105	120	160	0.42	7.1	7.1	CNF =diameter
F3	oxidized	120	50	120	160	0.26	4.4	2.2	CNF ≠ diameter
F4	oxidized	60	105	0	160	0.59	9.9	9.9	CNF ≠ diameter

$T_{Reaction}$=700 °C; $m_{Catalyst}$ = 4 g

Table 22: Different conditions of fiber synthesis on the Ni^0/Al_2O_3 catalyst

Under the classical conditions, the as prepared 5.9% Ni^0/Al_2O_3 yields carbon nanofibers but without control of diameters. By TEM observation (Fig. 40) besides fishbone fibers with perfect graphitic ordering, less ordered platelet type and some helical fibers are found. The measured activity was relatively low (TOF =3.2 h^{-1}).

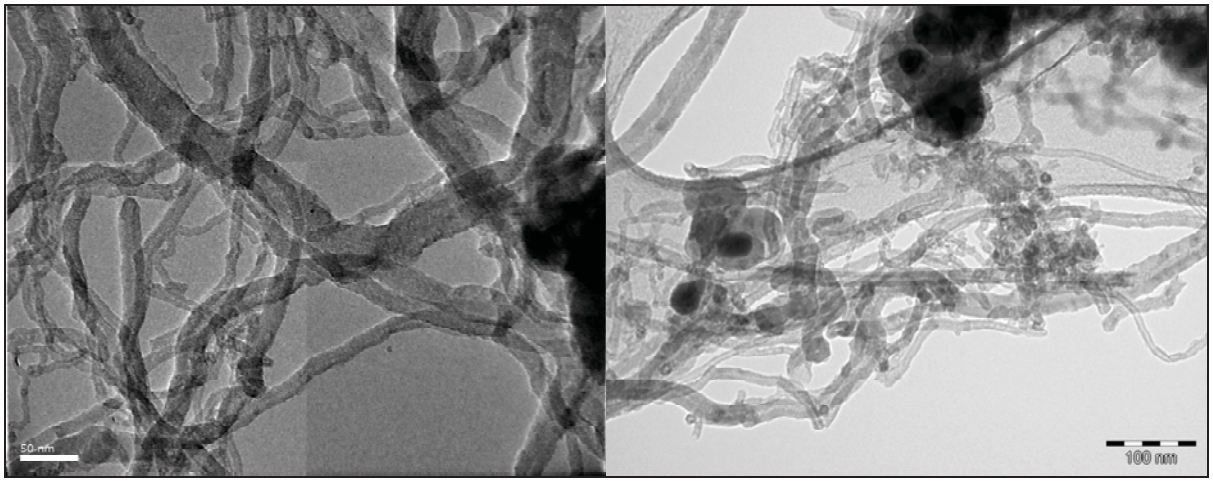

Figure 40: TEM micrographs of the F1 sample

Taken into account the broad diameter distribution of the resulting carbon nanofibers, and the high amount of carbon contamination of the catalyst, 5% measured by elemental analysis, indicating a non complete decomposition of nickelocene at 220 °C, an oxidation step at 700 °C for 4 h was necessary [96]. After oxidation, the catalyst's activity increased from 3.2 to 7.1 h^{-1} (test F2). From TEM micrographs, we observed nanofibers of fishbone fibrils type as dominant and narrow distribution in the diameter, calculated and represented in the histogram of Figure 41. The average diameter of such CNFs was 7.8 nm, which is relatively small for such material.

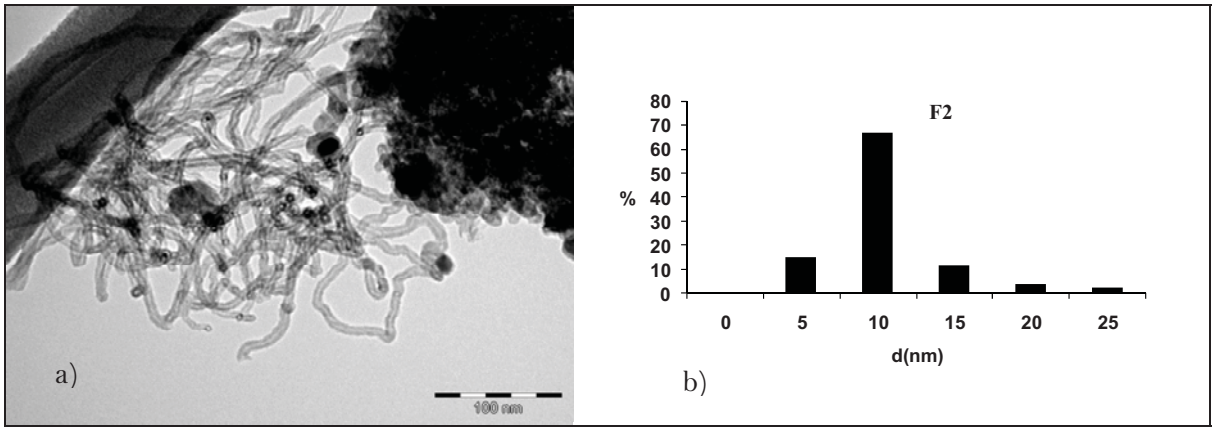

Figure 41: a) TEM micrograph and b) external diameter distribution of the F2 sample

Two additional tests were conducted on the activated catalyst, one by lowering the supersaturating ratio (C/Ni) by decreasing the partial pressure of C_2H_4 (test F3) and another by removing the H_2 gas from the reactive gas mixture (test F4). Both modifications yield to a broad diameter distribution.

Once again, for carbon nanofibers synthesis we have evidenced the importance of: i) the catalyst preparation, i.e conditions of the Ni^0/Al_2O_3 deposition by MO-CVD, related structure and purity of the nanoparticles (activation at 700°C) and ii) the associated conditions of gas mixture and C/Ni supersaturating ratio in the FB-CVD carbon nanostructure synthesis. For large scale production and in order to produce CNFs with narrow diameter distribution and good yield, the conditions of Table 23 were retained.

MO-CVD		Activation		FB-CCVD	
$m(Al_2O_3)$	50 g	T	700°C	$m_{Catalyst}$	4 g
$m(Ni(Cp)_2)$	9 g	t	4 h	T	700 °C
$T_{Sublimation}$	135 °C	Gaz	Air	t	1 h
T_{Column}	220 °C			C_2H_4	105 sccm
H_2/N_2	350/300 sccm			H_2	120 sccm
t_d	5 h			N_2	160 sccm
P	0.5 mbars				

Table 23: Optimum conditions for CNF synthesis

II-5-Nitrogen doped carbon nanostructures

The experimental field of doped MWCNTs and CNFs is more advanced than that of doped SWCNTs. Nanotube doping can be achieved by two different ways: either directly during the synthesis or by post treatment of pre-synthesized carbon nanostructures. In this work, we were interested in the first approach. For a long time it was assumed to be a difficult task to synthesize nitrogen doped MWCNTs, and the first papers that appeared dealt with relatively low doping concentration [97,98]. For SWCNTs a maximum of 1% is reported [99], whereas for MWCNTs average concentrations could reach 15-20% only when aerosol assisted CVD methods were used [100].

Table 24 summarizes the results obtained using different techniques of synthesis, catalysts and C/N sources.

Method	C,N source	Catalyst	N %	Ref
Aerosol assisted CVD	CH_3CN/THF	-	20	[100]
Pyrolysis	Dimethylformamide	iron	2–16	[101]
Pyrolysis	Pyridine	cobalt	~2	[102]
Pyrolysis	2-amino-4,6-dichloro-*s*-triazine	cobalt	<1–2	[103]
CVD	Acetylene/ammonia/	ferrocene	3-7 T (750-950 °C)	[104]
Microwave plasma CVD	CH_4/N_2	Fe particle coated on Si or SiO_2	15–17	[105]
Pyrolysis	Iron phthalocyanine	Iron phthalocyanine	10	[106]
Classical CVD	Acetylene/ammonia	-	2–6	[107]
Pyrolysis	Melamine	iron	4–5	[108]
Pyrolysis	Melamine	nickel	3–5	[108]
Pyrolysis	Acetonitrile	Ni:Co ratio 0:1	0.70	[109]
		Ni:Co ratio 3:7	0.50	
		Ni:Co ratio 1:1	1.2	
		Ni:Co ratio 7:3	0.6	
		Ni:Co ratio 1:0	1.2	

Table 24: Nitrogen concentration in MWCNTs as a function of nitrogen and carbon precursors synthesized using CVD or CVD-type methods

II-5-1-Synthesis of nitrogen doped carbon nanofibers (N-fibers)

Nitrogen doped carbon nanofibers were grown from acetonitrile or pyridine over a 2.5% w/w Fe/Al_2O_3 catalyst. The comparative study of the performances of these two compounds for doping, as a function of the deposition temperatures are presented in Tables 25 and 26.

TEM micrographs revealed that the fibers present a bamboo-like structure whatever the nature of the nitrogen compound used, or the deposition temperatures (Fig. 42). The catalytic activity increased with the increase of the deposition temperature, irrespectively of the carbon and nitrogen source used [3]. The diameter distribution of the nitrogen doped

CNFs were calculated from the TEM micrographs and are shown in Fig. 43. In the case of acetonitrile, the average diameters of the N-fibers varied between 7.7 and 19.5 nm as a function of the deposition temperature, and for pyridine it was narrower, between 8.8 and 11.9 nm (Table 25).

Test	T_d	Compound	$d_{average}$ (nm)	$g_C/g_{Catalyst}$	TOF (h^{-1})	$T_{oxidation}$	TEM
AN4	600	CH_3CN	7.7	7.82	3.91	483	Bamboo fibers
AN1	650	CH_3CN	19.5	9.5	4.75	487	Bamboo fibers
AN2	700	CH_3CN	14.6	13.3	6.65	487	Bamboo fibers
AN3	750	CH_3CN	15.3	20.72	10.36	503	Bamboo fibers
PN18	600	Pyridine	8.8	1 .9	0.95	470/530	Bamboo fibers
PN17	650	Pyridine	10	10.4	5.2	565	Bamboo fibers
PN15	700	Pyridine	11.9	27.6	13.8	561	Bamboo fibers
PN16	750	Pyridine	9.6	14	7	575	Bamboo fibers

T_b = 30 °C; t_d = 1 h; $m_{catalyst}$ = 2 g; H_2 = 120 sccm; N_2 = 160 sccm, TOF = $g_{N\text{-}Fibers}/g_{Fe}/h$

Table 25: Conditions for the synthesis of nitrogen doped CNFs

		XPS					Elemental analysis		
Test	T °C	%C	$B.E_{C(sp2)}$	%N	$B.E_{N(average)}$ eV	C/N	%C	%N	C/N
AN4	600	97.4	284.1	2.6	398.9	37.46	79.8	3.6	22.16
AN1	650	98.3	284.3	1.7	404	57.82	80.4	7.1	11.32
AN2	700	96.2	284.6	3.8	400.1	25.31	78.4	6.4	12.25
AN3	750	96.8	284	3.2	400.7	30.25	80.9	5.9	13.71
PN18	600	100	283.6	0	0	0	85.6	0.6	142
PN17	650	100	284.2	0	0	0	90.9	1.3	70
PN15	700	100	284.5	0	0	0	93.6	1.6	58.5
PN16	750	100	284.2	0	0	0	92.5	1.5	61.6

Table 26: Concentration of nitrogen determined by XPS and elemental analysis as a function of the temperature and nitrogen source

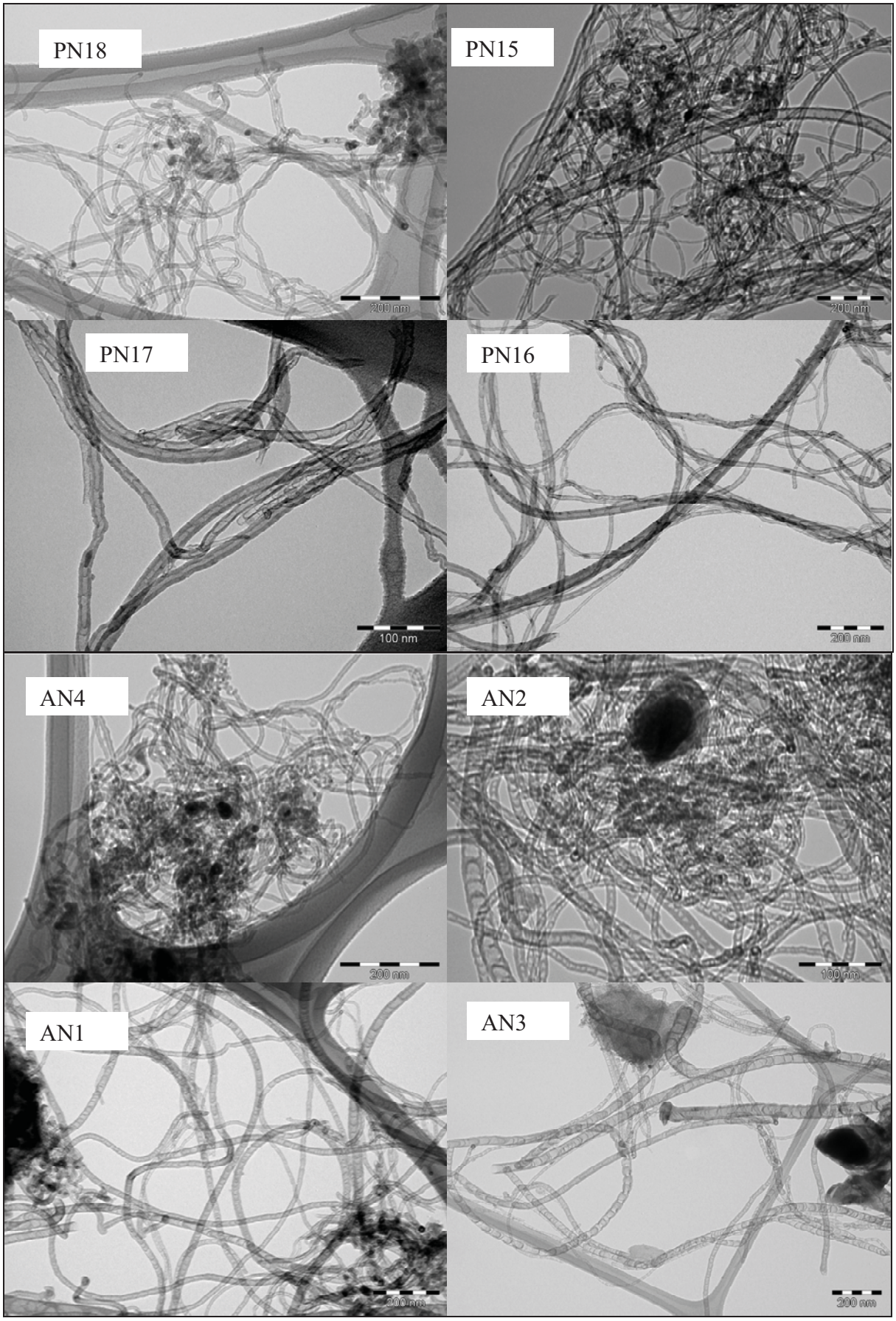

Figure 42: TEM micrographs of the N-CNFs produced under different synthesis conditions

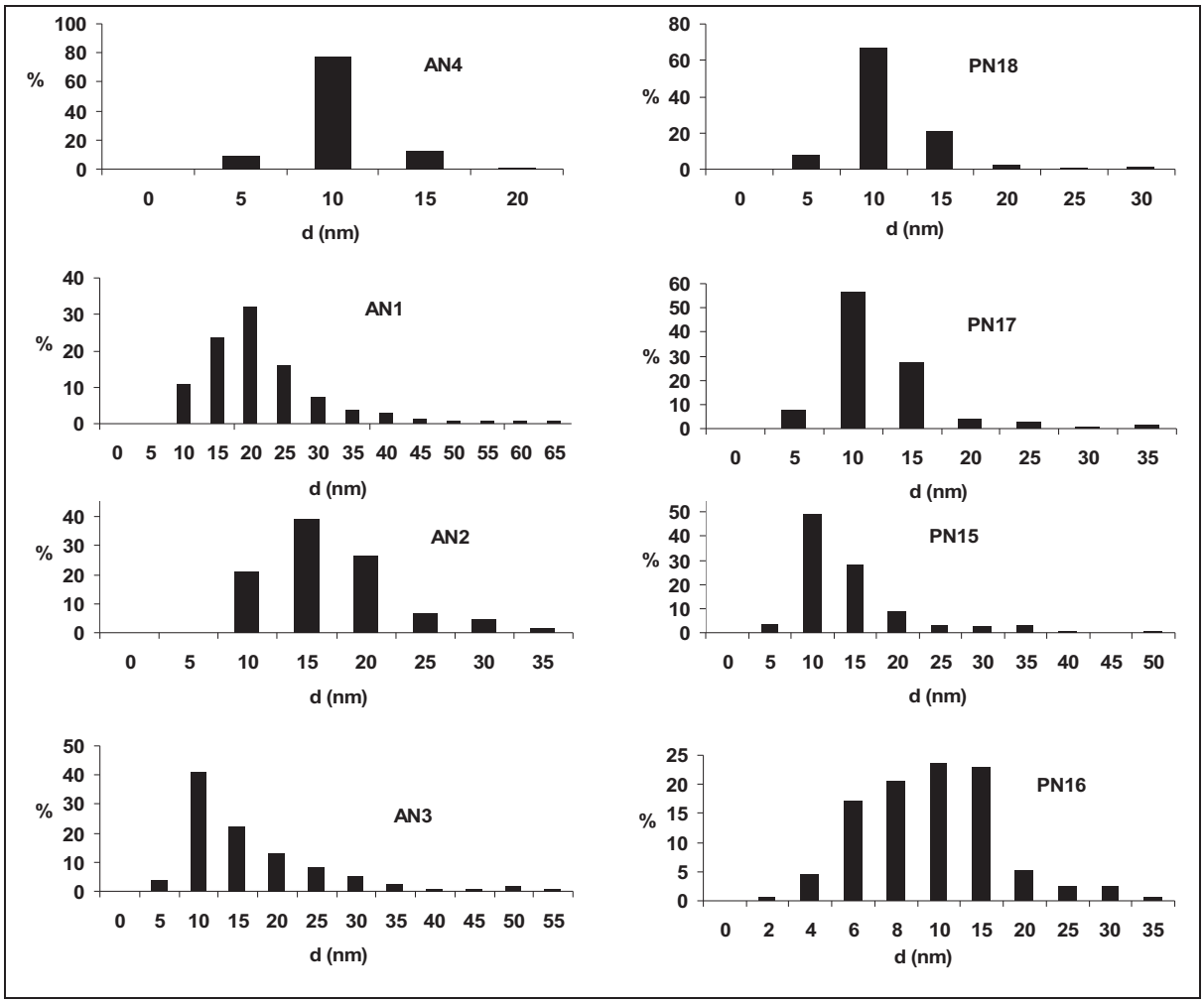

Figure 43: Diameter distribution of the N-CNFs produced under different conditions

The amount of nitrogen doping was determined by X-ray photoelectron spectroscopy and elemental analysis. The nitrogen doping values of XPS (surface analysis technique) are much lower than those of the elemental analysis (global analysis technique). The depth of the XPS beam is less than 8 nm. This indicates that the doping is not limited to the surface of the fibers but reach the whole bamboo structure. The results are assembled in Table 26.

The amount of nitrogen doping of the acetonitrile based N-fibers was higher than the one obtained for fibers grown from pyridine. As for the influence of the deposition temperature on the amount of nitrogen doping, in both acetonitrile and pyridine cases the nitrogen doping increase by increasing the temperature from 600 to 650 °C, but later starts to decrease in the case of acetonitrile and tends to be constant in the case of pyridine (Table 26). This could be related to the thermodynamic stability of metal carbides *vs* metal nitrides, the formation of carbides being favored over nitrides at high temperatures [3].

It is reported that doped carbon nanostructures are less stable and oxidize at lower temperatures than undoped ones [110]. The oxidation temperatures of pyridine based N-fibers were higher than those of acetonitrile, *i.e* 565 *vs* 487 °C, as expected, confirming the higher nitrogen concentration in the case of acetonitrile based CNFs. We should add that the type of nitrogen insertion could also affect stability to oxidation.

Unfortunately the nitrogen doping of the pyridine based N-fibers was too low to be detected by XPS and thus the study on the type of nitrogen doping as a function of deposition temperature will be limited to the acetonitrile based N-CNFs. In the literature, the XPS peak between 395 and 405 eV of the nitrogen atoms is fitted with four different contributions. They were assigned to pyridinic nitrogen ($398.4 < N_P < 399$ ev), quaternary nitrogen ($401.1 < N_Q < 401.7$ ev), pyrrolic nitrogen ($400 < N_{PYR} < 400.6$ ev) and nitrogen oxides ($402 < N_{ox} < 405$ ev) [111-113]. A schematic representation of each nitrogen type is represented in Figure 44.

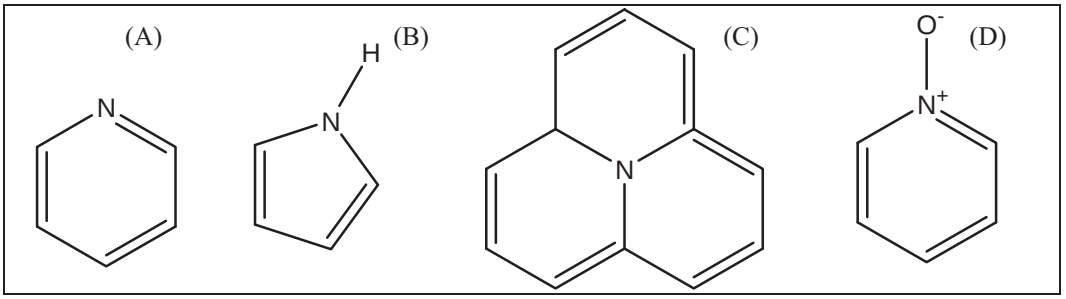

Figure 44: Type of nitrogen species found in N-CNFs: (A) N_P (pyridinic), (B) N_{PYR} (pyrrolic), (C) N_Q (quaternary) and (D) N_{ox} (oxidized pyridinic)

In our case the fitted XPS spectra of acetonitrile based N-CNFs as a function of temperature of synthesis are presented in Figure 45 and the proportion of each species are summarized in Table 27.

		XPS				
Test	T (°C)	% N_P	% N_{PYR}	% N_Q	% N_{ox}	Dominant species
AN4	600	77	0	15.6	7.4	Pyridinic
AN1	650	28.8	31.3	12.3	27.6	Pyrrolic
AN2	700	34.7	0	53.1	12.1	Quaternary
AN3	750	24.8	34.8	19.2	21.1	Pyrrolic

Table 27: Proportion of each type of nitrogen containing species

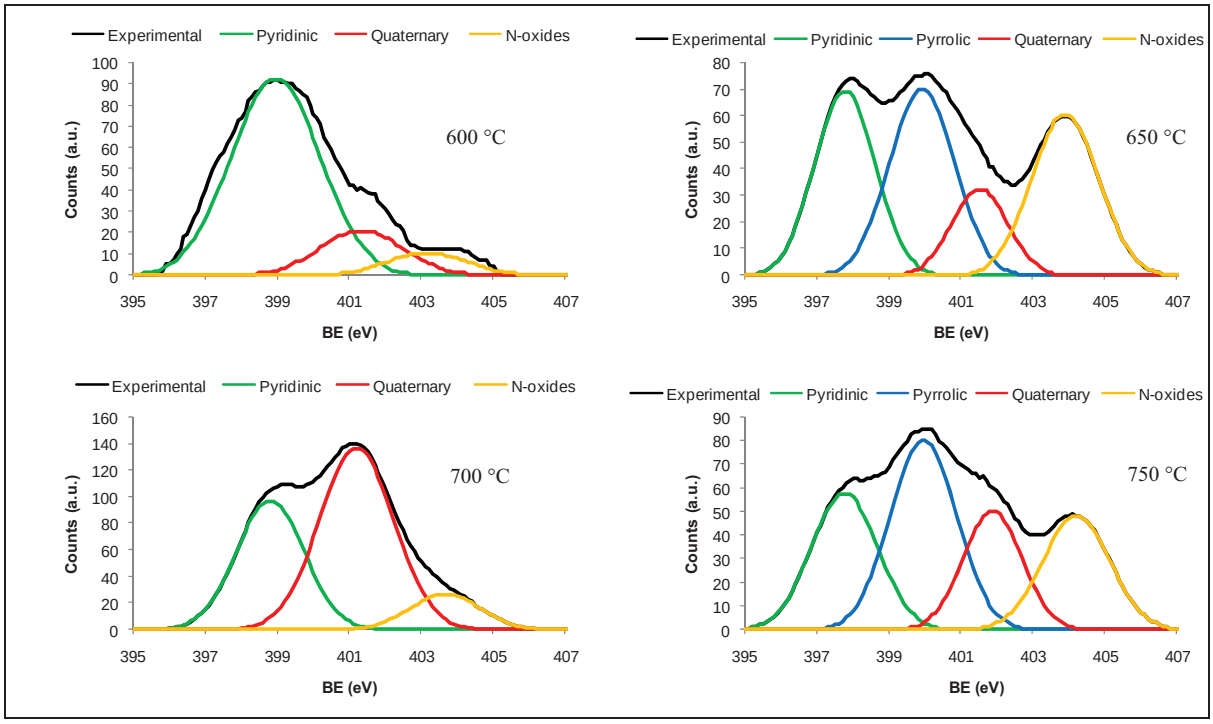

Figure 45: XPS fitted spectra as a function of the synthesis temperature

The type of nitrogen present in the graphene layers was variable, depending on the temperature of synthesis. We pass from predominant pyridinic group at 600 °C to pyrrolic ones at 650 °C and quaternary type at 700 °C. This is in accordance with the results of Bitter et al [3], who observed that the increase in temperature of synthesis favors the quaternary nitrogen groups over the pyridinic ones.

Taking into account the toxicity of pyridine and its low amount of nitrogen doping, in spite of the narrowing and small diameters of the resulting N-CNFs, the choice of this molecule as precursor to produce nitrogen doped CNFs was excluded for a large scale production. The acetonitrile conditions AN2 were selected as a compromise between the best yield ($13.3 g_C/g_{Catalyst}$, TOF = 6.65 h^{-1}), nitrogen doping (3.8% by XPS and 6.4% by elemental analysis), and narrow diameter distribution ($d_{average}$= 14.6 nm).

II-5-2-Nitrogen doped multiwalled carbon nanotubes (N-MWCNTs)

A 5 % w/w cobalt catalyst supported on silica prepared by incipient wetness impregnation was used for the N-MWCNTs synthesis. After impregnation, the catalyst was oxidized under air at 350 °C for 3 h. The catalyst before and after oxidation was tested under the condition reported in Table 28.

Tests	$T_{deposition}$ (°C)	Catalyst	TGA		
			$g_C/g_{Catalyst}$	$T_{oxidation}$ (°C)	TOF (h^{-1})
NMW1	700	Co/SiO_2	0.17	438	3.4
NMW2	700	Co/ SiO_2 calcined	0.45	460	9

Compound= CH_3CN, T_b=30 °C; t_d=1 h; $m_{catalyst}$=2 g; H_2=120 sccm; N_2= 160 sccm,

$TOF = g_{N\text{-}MWNT}/g_{Co}/h$

Table 28: Condition of N-MWCNT synthesis

A spectacular increase in the N-MWCNTs yield was observed after catalyst activation, probably due to the decomposition of the cobalt precursor and the formation of the active nanoparticles. This indicates that the structural aspect of the catalyst plays an important role in the determination of the catalytic activity, Co/SiO_2 nanoparticles being more active (TOF = 9 h^{-1}) than the cobalt compound supported on silica (TOF = 3.4 h^{-1}).

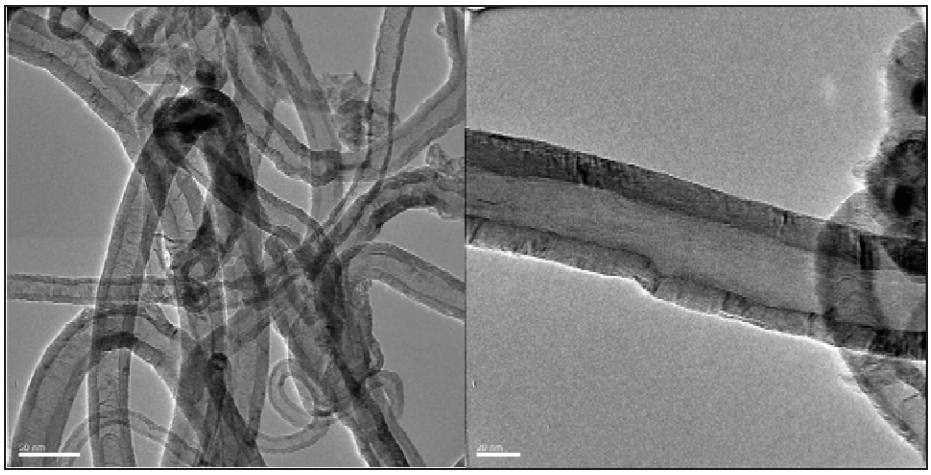

Figure 46: TEM micrographs of the NMW2 sample

By TEM analysis the carbonaceous nanostructures resulting from the oxidized Co catalyst were identified as multiwalled carbon nanotubes based on their parallel walls and the presence of a hollow cavity (Fig. 46).

The average external diameter of such nitrogen doped MWCNTs was 24 nm and the distribution was large, ranging from 8 to 45 nm (Fig. 47).

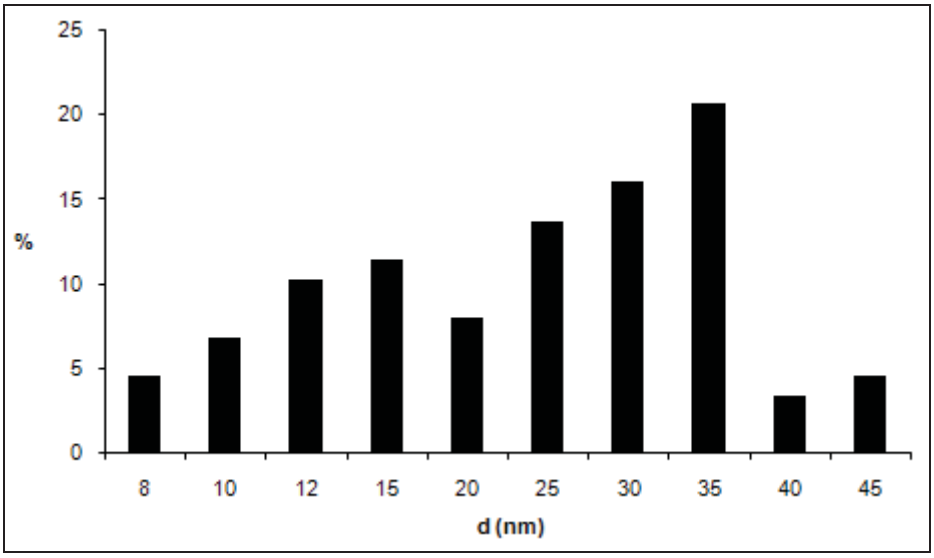

Figure 47: External diameter distribution of the N-MWCNTs

The nitrogen doping for sample NMW2 was confirmed by XPS and elemental analysis, giving 0.6% and 1.6%, respectively. Low doping values were expected using cobalt catalysts (Table 24). In general, an increase in the nitrogen doping induces an evolution from parallel walls (MWCNTs) to a fishbone CNFs [114].

Test	XPS					Elemental analysis	
	$B.E_{C(sp2)}$ (ev)	%C	$B.E_N$ (eV)	%N	N-Type	%C	%N
NMW2	284.2	99.4	400.8	0.6	N-O	94.7	1.6

Table 29: Concentration of nitrogen by XPS and elemental analysis of the N-MWCNT

The NMW2 conditions were selected for the production on a large scale of nitrogen doped carbon nanotubes.

II-5-3-Conclusion on nitrogen doping

An iron based catalyst was tested to produce nitrogen doped MWCNTs using acetonitrile as a source of carbon and nitrogen, but carbon nanofibers were always obtained. In fact, nitrogen doping afect the carbon nanotubes growth on iron based catalysts and transforms them to bamboo-like CNFs [3, 114]. In fact, we succeeded in producing nitrogen doped MWCNTs on cobalt based catalysts [3]. Cobalt based catalysts are known to be strongly selective to yield carbon nanotubes and even after nitrogen doping a nanotube structure remained. Nitrogen doping was low in this case and one may think that an increase in nitrogen doping could result in the transformation of the tubes into fibers. But the same conditions of synthesis were used for the iron and cobalt system so we can also suppose that

the nitrogen doping of the carbon nanotube was low because of the use of the cobalt species (Table 23). This difference in morphology can be explained by the thermodynamic stabilities of the different metal carbides or nitrides, leading to pulsating growth in the case of iron as opposed to a more continuous growth in the case of cobalt [3].

II-6-Caracterization of the pure carbon nanostructures used in catalysis

The catalyst was removed from the samples with a sulfuric acid treatment according to the procedure detailed in chapter V, and in the case of MWCNTs and CNFs a nitric acid treatment was also imposed on purified MWCNTs and CNFs to create surface binding groups, mainly carboxylic but also phenols, aldehydes…, resulting in the production of CNF-COOH and MWNT-COOH samples. These bonds would play the role of anchoring sites for the carbonaceous support decoration with well dispersed metal nanoparticles. General characteristics of the carbonaceous supports are presented in Table 30. All the carbon nanostructures are proved to be pure at around 90 % by TGA, ICP-MS and elemental analysis, and TEM analysis revealed different average diameters. In the future, a challenge could be to create different structures with the same diameter distribution.

Support	TGA		Elemental analysis		ICP-MS		TEM	Specific surface area (BET)			Raman
	T_{ox} (°C)	%[a]	C	N	% M	% S	d (nm)	BET (m^2/g)	Vp cm^3/g	dp (average) (nm)	I_G/I_D
MWCNT	582	95	95	0	0.94	0.02	6.5	180	2.05	46	0.77
MWCNT-COOH	655	98	94	0.08	0.44	0.02		214	2.16	54	0.56
N-MWCNT	486	97	95	1.6	2.23	<0.3	24	119	0.56	18.7	0.83
CNF	609	92	91	0.02	4.56	0.05	7.8	437	0.70	6.44	0.97
CNF -COOH	637	93	87	0.6	3.42	0.47		560	0.78	5.6	0.84
N-CNF	502	88	81	6.4	5.43	0.46	14.6	204	0.74	14.5	0.86

a)Weight loss, M = Fe, Ni or Co, S = Al or Si

Table 30: General characteristics of the carbon supports selected for catalysis

The BET specific surface area of such nanomaterials ranged between 120 and 520 m^2/g and particularly that of CNF was high. The microporosity of those CNFs was evident in

the MP plot, mainly between 1.5 and 2 nm, and indicates that even though it is a fishbone fiber, a significant part between the walls is accessible.

XRD analysis was performed on the carbon nanostructures and revealed common diffraction peaks at 25 and 43 attributed to carbon but later different diffraction peaks characteristic of different crystal structures specially for CNF-COOH and N-CNF due to nitrogen insertion and different graphene orientations.

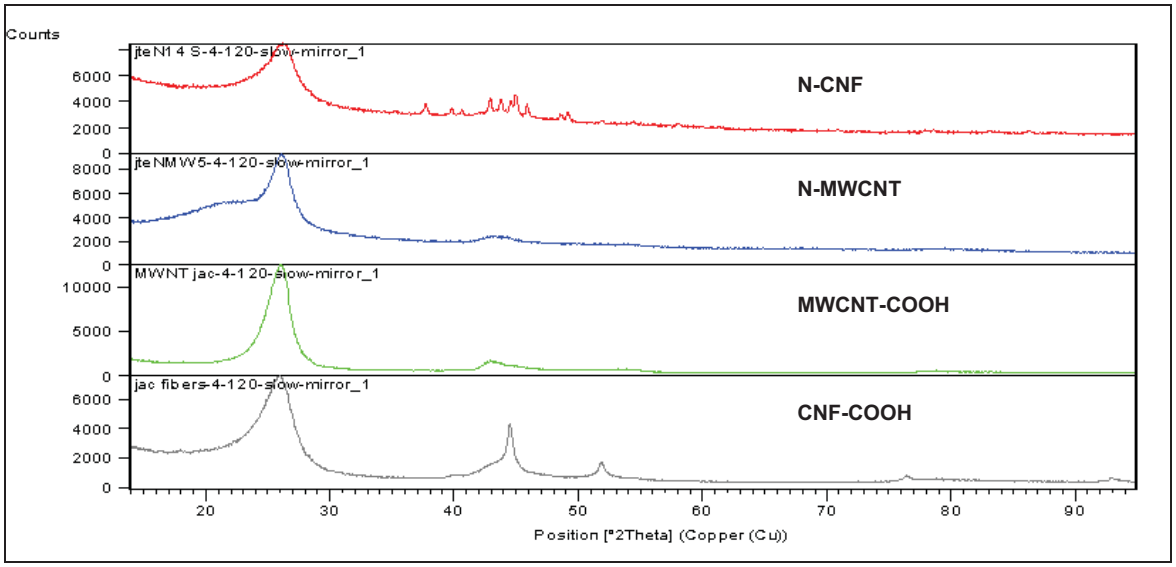

Figure 48: XRD diffractograms of MWCNT-COOH, N-MWCNT, CNF-COOH and N-CNF

Those carbon nanostructures will be used as supports for heterogeneous catalysis and electrocatalysis in chapter III and IV.

II-7-Conclusion

In this chapter we found some optimum transition metal supported catalysts and associated conditions for the catalytic chemical vapor deposition of carbonaceous nanostructures. Carbon nanofibers, multiwalled carbon nanotubes, bamboo like CNF doped with nitrogen and MWCNTs doped with nitrogen could be produced in good yields and good selectivity at the laboratory scale. As for single walled carbon nanotubes, large production on the scale of grams was restricted due to technical problems. A scale up process could be optimized in the future using the optimum condition (100 mg of 4% iron oxide supported on alumina activated 10 h at 900 °C, in association with 150/150 sccm of CH_4/Ar at 900 °C) as starting base. We should note that a further optimization of each of the previously reported

condition associated to each of the carbonaceous structure synthesis could also be developed for massive production in the future. This work was limited to laboratory scale production, since the aim was to evaluate these nanocarbons as support for catalysis.

II-8-References

1) E. Lamouroux, P. Serp, Y. Khin, P. Kalck, Catal. Commun. 7 (2006) 604.

2) J. Teddy, R. Philippe, E. Lamouroux, M. Corrias, Y. Kihn, B. Caussat, P. Gaillard, C. Mazzocchia, P. Kalck, P. Serp, Submited to ChemCatChem.

3) S. Dommele, A. Romero-Izquirdo, R. Brydson, K.P. de Jong, J.H. Bitter, Carbon 46 (2008) 138.

4) C. Vahlas, B. Caussat, P. Serp, G.N. Angelopoulos, Mater. Sci. Eng. R 53 (2006) 1.

5) D. Kunii, O. Levenspiel, Fluidization Engineering, Butterworth-Heinemann, Newton, MA, 1991.

6) D. Geldart, Gas Fluidization Technology, John Wiley & Sons, Chichester, New York, Brisbane, Toronto, Singapore, 1986.

7) E. Lamouroux, PhD thesis, Institut National Polytechnique, 2005.

8) C.K. Gupta, D. Sathiyamoorthy, Fluid Bed Technology in Materials Processing, CRC Press, Boca Raton, FL, 1999.

9) J.F. Davidson, R. Clift, D. Harrison (Eds.), Fluidization, Academic Press, London, 1985.

10) A. Glaria, M.L. Kahn, P. Lecante, B. Barbara, B. Chaudret, Chem. Phys. Chem 9 (2008) 776.

11) T.A. Kainulainen, M.K. Niemela, A.O.I. Krause, Catal. Lett. 53 (1998) 97.

12) P. Serp, L. Château, R. Feurer, A. Kiennemann, P. Kalck, J. Mol. Catal. 136 (1998) 269.

13) T. Miyao, I. Shishikura, M. Matsuoka, M. Nagai, Chem. Lett. (1996) 561.

14) K. Tomishige, K. Asakura, Y. Iwasawa, J. Catal. 157 (1995) 472.

15) K. Tomishige, K. Asakura, Y. Iwasawa, Chem. Lett. (1994) 235.

16) K. Tomishige, K. Asakura, Y. Iwasawa, J. Catal. 149 (1994) 70.

17) K. Tomishige, K. Asakura, Y. Iwasawa, Catal. Lett. 20 (1993) 15.

18) K. Tomishige, K. Asakura, Y. Iwasawa, J. Chem. Soc., Chem. Commun. (1993) 184.

19) B.C. Liu, S.C. Lyu, S.I. Jung, H.K. Kang, C.-W. Yang, J.W. Park , C.Y. Park, C.J. Lee, Chem. Phys. Lett. 383 (2004) 104.

20) S Chiashi, Y Murakami, Y Miyauchi, S Maruyama, Chem. Phys. Lett. 386 (2004) 89.

21) H. Dai, A.G. Rinzler, P. Nikolaev, Chem. Phys. Lett. 260 (1996) 471.

22) R. Philippe, PhD thesis, Institut National Polytechnique, 2006.

23) G. Wilkinson, Comprehensive Organometallic Chemistry, Pergamon Press, Volume 4, (1982) P. 244.

24) J. Phillips, B. Clausen, J.A. Dumesic, J. Phys. Chem. 84 (1980) 1814.

25) P. Schissel, D.J. Mcadoo, E. Hedaya, D.W. Mcneil, J. Chem. Phys. 49 (1968) 5061.

26) A.G. Harrison, L.R. Honnen, H.J. Dauben, F.L. Lossing, J. Am. Chem. Soc., 82 (1960) 5593.

27) A.M. Cassell, J.A. Raymakers, J. Kong, H. Dai, J. Phys. Chem. B 103 (1999) 6484.

28) C.P. Deck, K. Vecchio, Carbon 44 (2006) 267.

29) Harutyunyan , et al, United States Patent, , 10/992,277, (2004).

30) C.N.R. Rao, A. Govindaraj, Acc. Chem. Res. 35 (2002) 998.

31) H. Dai, A.G. Rinzler, P. Nikolaev, A. Thess, D.T. Colbert, R.E. Smalley, Chem. Phys. Lett. 260 (1996) 471.

32) W.E. Alvarez, B. Kitiyanan, A. Borgna, D.E. Resasco, Carbon 39 (2001) 547.

33) P. Nikolaev, M.J. Bronikowski, R.K. Bradley, F. Rohmund, D.T. Colbert, K.A. Smith, R.E. Smalley, Chem. Phys. Lett. 313 (1999) 91.

34) T. Zhao, Y. Liu, C. Zhu, X. Zhao, J. Nanomat. 2007 (2007) 4.

35) J. Kong, A.M. Cassell, H. Dai, Chem. Phys. Lett. 292 (1998) 567.

36) S. Bhaviripudi, E. Mile, S.A. Steiner, A.T. Zare, M.S. Dresselhaus, A.M. Belcher, J. Kong, J. Am. Chem. Soc. 129 (2007) 1516.

37) Y.S. Chen, J.H. Huang, J.L. Hu, C.C. Yang, W.P. Kang, Carbon 45 (2007) 3007.

38) R. Bacsa, C. Laurent, A. Peigney, W. Bacsa, Chem. Phys. Lett. 323 (2000) 566.

39) Y. Murakami, S. Chiashi, Y. Miyauchi, M Hu, M. Ogura, T. Okubo, S. Maruyama, Chem. Phys. Lett. 385 (2004) 298.

40) A.M. Rao, Science 257 (1997) 187.

41) M.S. Dresselhaus, G. Dresselhaus, A. Jorio, A.G. Souza Filho, M.A. Pimenta, R. Saito, Acc. Chem. Res. 35 (2002) 1070.

42) R. Philippe, B. Caussat, A. Falqui, Y. Kihn, P. Kalck, S. Bordère, D. Plee, P. Gaillard, D. Bernard, P. Serp, J. Catal. 263 (2009) 345.

43) E. Lamouroux, P. Serp, Y. Kihn, Ph. Kalck, Appl. Catal. A: Gen. 323 (2007) 162.

44) K. Chen, L. Dong, Q. Yan, Y. Chen, J. Chem. Soc, Faraday Trans. 93 (1997) 2203.

45) F.B. Rao, T. Li, Y.L. Wang, Physica E 40 (2008) 779.

46) N.I. Alekseev, Tech. Phys. 49 (2004) 1166.

47) A.R. Harutyunyan, E. Mora, T. Tokune, Appl. Phys. Lett. 90 (2007) 163120.

48) G. Ning, F. Wei, Q. Wen, G. Luo, Y. Wang, Y. Jin, J. Phys. Chem. B 110 (2006) 1201.
49) J.P. Jolivet, E. Tronc, C. Chanéac, C.R. Geoscience 338 (2006) 488.
50) L. Zhang, G.C. Papaefthymiou, J.Y. Ying, J. Phys. Chem. B 105 (2001) 7414.
51) D. Predoi, V. Kuncser, G. Filoti, Romanian reports in physics 56 (2004) 373.
52) E. Tronc, C. Chanéac, J.P. Jolivet, J. Solid State Chem. 139 (1998) 93.
53) X. Gao, J. Shen, Y. Hsia, Y. Chen, J. Chem. Soc. Faraday Trans. 89 (1993) 1079.
54) T. Ren-Yuan, Z. Su, W. Chengyu, L. Dongbai, L. Liwu, J. Catal. 106 (1987) 440.
55) M. Petrera, G. Gubitosa, A. Gennaro, N. Burriesci, Gazz. Chim. Ital. 110 (1980) 465.
56) K. Chen, L. Dong, Q. Yan, Y. Chen, J. Chem. Soc, Faraday Trans. 93 (1997) 2203
57) Y. Xie, X. Xu, B. Zhao, Y. Tang, Catal. Lett. 13 (1992) 239
58) M.C. Hobson, H.M. Gager, J. Catal. 16 (1970) 254.
59) T.C. Huang, H.H. Wei, Hyperfine Interactions 28 (1986) 887.
60) M. Carbucicchio, J. Chem. Phys 70 (1979) 784.
61) A.S. Teja, P.Y. Koh, Progress in crystal growth and characterization of materials XX (2008) 1.
62) S. Herreyre, P. Gadelle, P. Moral, J.M.M. Millet, J. Phys. Chem. Solids 58 (1997) 1539.
63) P. Ayyub, M. Multani, M. Barma, J. Phys. C: Solid State Phys. 21 (1988) 2229.
64) C. Laurent, A. Peigney, A. Rousset, J. Mater. Chem. 8 (1998) 1263.
65) W.R. Ruston, M. Warzee, J. Hennaut, J. Waty, Carbon 7 (1969) 47.
66) A. Sacco, P. Thacker, T.N. Chang, J. Catal. 85 (1984) 224.
67) R.T.K. Baker, J.J. Chludzinski, J. Catal. 64 (1980) 464.
68) M. Audier, M. Coulon, Carbon 23 (1985) 317.
69) P. Coquay, E. Grave, A. Peigney, J. Phys. Chem. B 106 (2002) 13186.
70) N. He, Y. Kuang, Q. Dai, Y. Miao, Mater. Sci. Eng. C 8-9 (1999) 151.
71) V.G. Resende, E. De Grave, A. Peigney, C. Laurent, J. Phys. Chem. C 112 (2008) 5756.
72) A. Peigney, P. Coquay, E. Flahaut, J. Phys. Chem. B 105 (2001) 9699.
72) A. Glaria, M.L. Kahn, P. Lecante, B. Barbara, B. Chaudret, Chem. Phys. Chem 9 (2008) 776.
73) A. Khasanov, J. He, J. Gaillard, K. Yang, Appl. Phys. Lett. 93 (2008) 013103.
74) J.F. Bengoa, A.M. Alvarez, M.V. Cagnoli, N.G. Gallegos, S.G. Marchetti, Appl. Catal. A: Gener. 325 (2007) 68.
75) R. Zboril, M. Mashlan, D. Petridis, Chem. Mater. 14 (2002) 969.
76) M.L. Cubeiro, H. Morales, M.R. Goldwasser, M. Josefina, Appl. Catal. A: Gener. 189 (1999) 87.

77) L. Guczi, Catal. Rev. Sci. Eng. 35 (1993) 1.

78) F. Stephens, D.L. Williamson, J. P. Hager, Nuclear instruments and methods in physics research B76 (1993) 354.

79) M. Verlest, K.R. Kanaan, C. Laurent, A. Rousset, J. Mater. Res 7 (1992) 3072.

80) K. Hasegawa, S. Noda, H. Sugime, K. Kakehi, S. Maruyama, Y. Yamaguchi, J. Nanosci. Nanotech. 8 (2008) 6123.

81) G. Zhang, D. Mann, L. Zhang, A. Javey, H. Dai, PNAS 102 (2005) 16141.

82) G. Ning, F. Wei, Q. Wen, G. Luo, Y. Wang, Y. Jin, J. Phys. Chem. B 110 (2006) 1201.

83) E. Lamouroux, P. Serp, P. Kalck, Catal. Rev. Sci. Eng. 49 (2007) 341.

84) A. Peigney, C. Laurent, A. Rousset, J. Mater. Chem. 9 (1999) 1167.

85) L. Zhang, Y. Tan, D.E. Resasco, Chem. Phys. Lett. 422 (2006) 198.

86) Z. Niu, Y. Fang, J. Colloid and Interface Sci. 303 (2006) 224.

87) J.F. Colomer, J-M. Benoit, C. Stephan, Chem. Phys. Lett. 345 (2001) 11.

88) H. G. Tennet, US Pat 4 663 230, 1987, Hyperion Catalysis International, Inc.

89) J.D. Fowlkes, A.V. Melechko, P.D. Rack, M.L. Simpson, Carbon 44 (2006) 1503.

90) S.T. Retterer, A. Melechko, D.K. Hensley, M.J. Doktycz, Carbon 46 (2008) 1378.

91) C.C. Chen, J.H. Lin, Carbon 46 (2008) 365.

92) G.T. Stauf, D.C. Driscoll, P.A. Dowben, S. Barfuss, M. Grade, Thin Solid Films 153 (1987) 421.

93) C.H.J. Van Den Brekel, R.M.M. Fonville, G. Verspui, Proceedings of the Electrochem. Soc. 7 (1981) 142.

94) O.N. Andreev, O.P. Bespal'ko, Metalloorganitcheskaya Khimiya 1 (1988) 1184.

95) Y.A. Kaplin, J. Gen. Chem. USSR 50 (1980) 100.

96) M.L. Toebes, J.H. Bitter, A.J. van Dillen, K.P. de Jong, Catal. Today 76 (2002) 33.

97) M. Terrones, H. Terrones, Y.Q. Zhu, J.P. Hare, H.W. Kroto, D.R.M. Walton, Ph.K. Ohler-Redlich, M. Rühle, J.P. Zhang, A.K. Cheetham, Appl. Phys. Lett. 75 (1999) 3932.

98) M. Yudasaka, R. Kikuchi, Y. Ohki; S.Y. Oshimura, Carbon 35 (1997) 195.

99) M. Glerup, J. Steinmetz, D. Samaille, O. Stéphan, S. Enouz, A. Loiseau, S. Roth, P. Bernier 387 Chem. Phys. Lett. (2004) 193.

100) M. Glerup, M. Castignolles, M. Holzinger, G. Hug, A. Loiseau, P. Bernier, Chem. Commun. 20 (2003) 2542.

101) C. Tang, Y. Bando, D. Golberg, F. Xu, Carbon 42 (2004) 2625.

102) R. Sen, B.C. Satishkumar, A. Govindaraj, K.R. Harikumar, G. Raina, J.-P. Zhang, A.K. Cheetham, C.N.R. Rao, Chem. Phys. Lett. 287 (1998) 671.

103) M. Terrones, N. Grobert, J. Olivares, J.P. Zhang, H. Terrones, K. Kordatos, W.K. Hsu, J.P. Hare, P.D. Townsend, K. Prassides, H.W. Kroto, D.R.M. Walton, Nature 388 (1997) 52.
104) C.J. Lee, S.C.L Yu, H.-W Kim, J.H. Lee, K.I. Cho, Chem. Phys. Lett. 359 (2002) 115.
105) E.-G. Wang, Adv. Mat. 11 (1999) 1129.
106) X.B. Wang, W.P. Hu, Y.Q. Liu, C.F. Long, Y. Xu, S.Q. Zhou, D. Zhu, L. Dai, Carbon 39 (2001) 1533.
107) Y.T. Lee, N.S. Kim, S.Y. Bae, J. Park, S.-C. Yu, H. Ryu, H.J. Lee, J. Phys. Chem. B 107 (2003) 12958.
108) S. Trasobares, O. Stéphan, C. Colliex, W.K. Hsu, H.W. Kroto, D.R.M. Walton, J. Chem. Phys. 116 (2002) 8966.
109) A.G. Kudashov, A.V. Okotrub, L.G. Bulusheva, I.P. Asanov, Y.V. Shubin, V.S. Danilovich, O.G. Abrosimov, J. Phys. Chem. B 108 (2004) 9048.
110) C.J. Lee, S.C. Lyu, H.-W Kim, J.H. Lee, K.I. Cho, Chem. Phys. Lett. 359 (2002)115.
111) J.R. Pels, F. Kapteijn, J.A. Moulijn, Q. Zhu, KM. Thomas, Carbon 33 (1995) 1641.
112) W.J. Gammon, O. Kraft, A.C. Reilly, B.C. Holloway, Carbon 41 (2003) 1917.
113) S.R. Kelemen, M.L. Gorbaty, P.J. Kwiatek, Energeia 6 (1995) 1.
114) C.P. Ewels, M. Glerup, J. Nanosci. Nanotech. 5 (2005) 1345.
115) M. Liu, H. Li, L. Xiao, W. Yu, Y. Lu, Z. Zhao, J. Magn. Magn. Mater., 294 (2005) 294.

III-Application of carbonaceous nanostructures in catalysis: selective hydrogenation of cinnamaldehyde to cinnamylalcohol

Chapter III: Application of carbonaceous nanostructures in catalysis: selective hydrogenation of cinnamaldehyde to cinnamylalcohol

III-1-State of the art

III-1-1-Terminology

Abbreviation	Full name
AC	Activated carbon
CAL	Cinnamaldehyde
COL	Cinnamyl alcohol
CNFs	Carbon nanofibers
HCAL	Hydrocinnamaldehyde
HCOL	Hydrocinnamyl alcohol
MWCNTs	Multi-walled carbon nanotubes
$n_{CAL}i$	Initial number of moles of CAL
$n_{CAL}t$	Number of moles of CAL at a time t
n_{Pt}, n_{Ru}	Number of moles of Pt or Ru introduced in the reactor
n_{COL}, n_{HCAL}, n_{HCOL}	Number of moles of COL, HCAL and HCOL.
N-MWCNTs	Nitrogen doped carbon nanotubes
N-CNFs	Nitrogen doped carbon nanofibers
t	Time spent

Table 1: Abbreviations used in this chapter

III-1-2-Selective hydrogenation of α,β-unsaturated aldehydes

Hydrogenation reactions have been intensively studied ever since Paul Sabatier discovered heterogeneous catalysts for the addition of dihydrogen to unsaturated bonds [1-8]. During the last decades, many academic investigations used the hydrogenation of α,β-unsaturated aldehydes as model reactions to establish relations between selectivity and catalyst structure. The allylic alcohols produced are valuable intermediates for the production of perfumes, flavoring additives, pharmaceuticals and agrochemicals [5-8].

The hydrogenation of cinnamaldehyde may proceed via different reaction pathways as shown in Figure 1. The 1,2-addition of hydrogen gives the unsaturated alcohol (COL). The 3,4-addition gives the saturated aldehyde (HCAL). The hydrogenation of the C=O and C=C bonds gives the saturated alcohol (HCOL). The two C=O or C=C bonds being in competition, the challenge is to selectively hydrogenate one of them, leaving the other bond intact. In this work we select the selective hydrogenation of cinnamaldehyde to cinnamyl alcohol to estimate the performances of our catalysts. The hydrogenation of the carbonyl group is difficult to achieve since thermodynamics favors the hydrogenation of the C=C over the C=O bond by about 35 kJ/mol [9], and due to kinetic reasons, the reactivity of the olefin bond is higher than that of the carbonyl.

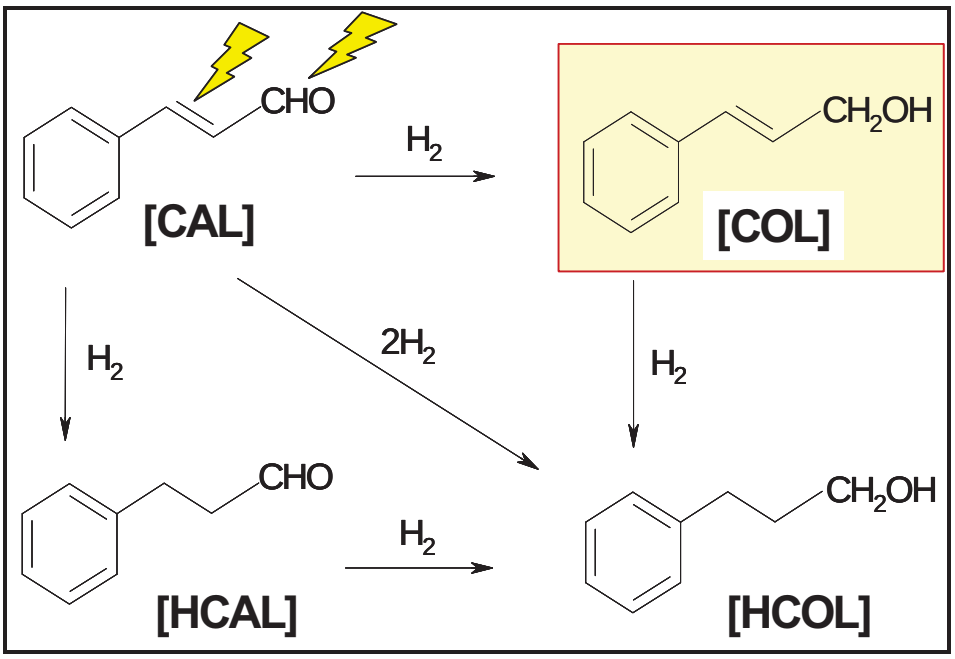

Figure 1: Scheme of hydrogenation of cinnamaldehyde [CAL] to cinnamyl alcohol [COL], hydrocinnamyl alcohol [HCOL] and hydrocinnamaldehyde [HCAL]

III-1-3-Side reactions

The reaction scheme given in Figure 1 can be further complicated considering side reactions occurring either on the metal or on the support. We note the decarbonylation, isomerization, and hydrogenolysis reactions leading to by-product formation. The hydrogenolysis of cinnamyl alcohol results in the formation of highly

reactive β-methylstyrene that is readily hydrogenated to 1-propylbenzene [10-12].

Decarbonylation of cinnamaldehyde yields styrene that is subsequently hydrogenated to ethylbenzene [10]. Isomerization reactions have been previously reported to occur during the hydrogenation of α,β-unsaturated aldehydes [13, 14]. However, little or no information has been given about the isomerization of cinnamylalcohol into hydrocinnamaldehyde using heterogeneous catalysts. The aromatic ring is the most stable element of the cinnamaldehyde molecule. Further hydrogenation of hydrocinnamyl alcohol produces the saturation of the aromatic ring and the formation of 3-cyclohexyl-1-propanol [12].

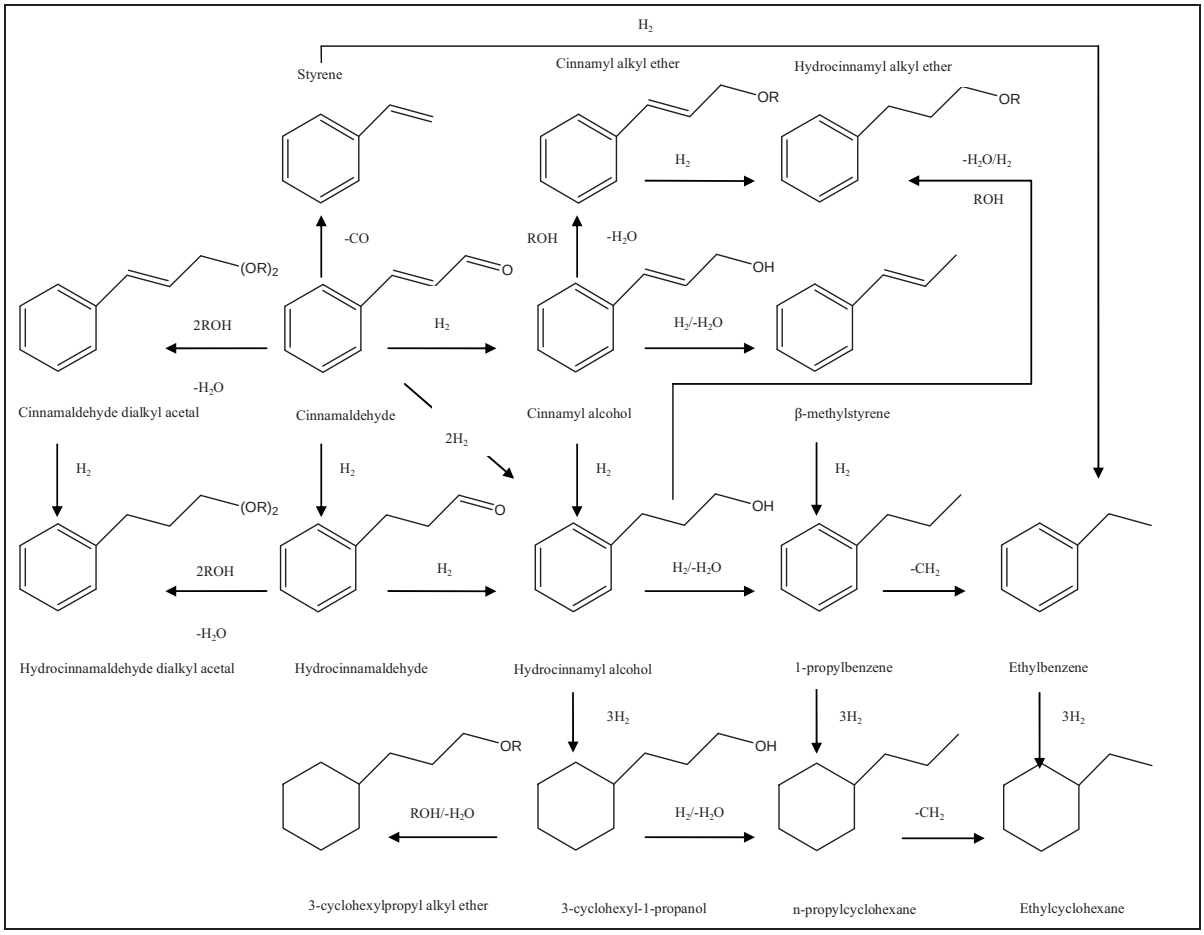

Figure 2: The complete pathway of cinnamaldehyde transformation

Alcoholic solvents may react with cinnamaldehyde or hydrocinnamaldehyde to form acetals, or with cinnamylalcohol or hydrocinnamyl alcohol to produce ethers and dehydration reactions may occur with formation of β-methylstyrene.

Condensation reactions may also occur mainly between COL and HCOL leading to cyclic products [15]. Those reactions are enhanced with the presence of acid/basic sites on the catalyst's surface. In Figure 2, a reaction scheme summarizes the complete pathway of reactions starting from cinnamaldehyde.

III-1-4-Mechanism of CAL selective hydrogenation

Hydrogenation reactions over a supported metal catalyst present several reactions steps: i) external diffusion, ii) internal pore diffusion, iii) adsorption of the reactants, iv) chemical reaction on the surface, v) desorption, vi) internal diffusion

and vii) external diffusion of the products [16]. Each of those steps could influence the reaction rate and selectivity.

Kinetics of competitive hydrogenation of C=O and C=C have been previously studied [17, 18]. Two main reaction mechanisms are usually considered in heterogeneous catalysis: Langmuir-Hinshelwood (LH) or Eley-Rideal (ER). In the LH mechanism the reaction occurs between species that are both adsorbed on the surface, whilst with the ER mechanism, the reaction occurs between a reactant molecule in the gas or liquid-phase and one that is adsorbed on the surface. For cinnamaldehyde hydrogenation kinetics, it is the LH mechanism that is considered as a good approximation [2, 10, 12, 19, 20]. The kinetic model may take into account either one or two different types of adsorption sites for CAL or H_2 and thus consider either competitive or non competitive adsorption steps as well as dissociative or non dissociative adsorption of H_2. Of course the model can grow in complexity if we include the by-product multiple reactions.

III-1-5-Requirements for the selective hydrogenation of cinnamaldehyde

Cinnamaldehyde selective hydrogenation was found dependent on many specifications related to the catalyst design, i.e the metal choice, size and surface state of the nanoparticles, the metal-support interaction, steric and electronic effects of the support, the effect of a second metal as promoter or to reaction conditions [21]. The issues related to the support will be detailed progressively during the interpretation of the experimental results.

Concerning the choice of the active phase for such reaction, it is reported that many un-promoted metals have specific selectivity to the unsaturated alcohol: Ir and Os are rather selective, platinum, ruthenium, and cobalt are moderately selective [22-24].

In summary the selectivity towards cinnamyl alcohol increased in the following order: Pd<Rh<Ru<Pt<Au<Ir<Os. This sequence was explained by theoretical calculations by Delbecq and Sautet [25] in terms of radial expansion of the d-band, since the larger the d-band, the stronger the four-electron repulsive interaction with the C=C bond and the lower the probability of its adsorption. Indeed, d-band width follows the same order as the selectivity towards cinnamyl alcohol (Pd<Pt<Ir,Os) [21]. Catalysts of monometallic and bimetallic nanoparticles of Pt and Ru are the most commonly used and were previously studied in our laboratory [26-

30]. In addition to the metal choice, Delbecq and Sautet also noted that there is a preferential adsorption mode (Fig. 3), which determines the selectivity, depending on the exposed crystal plane of the nanoparticle [25].

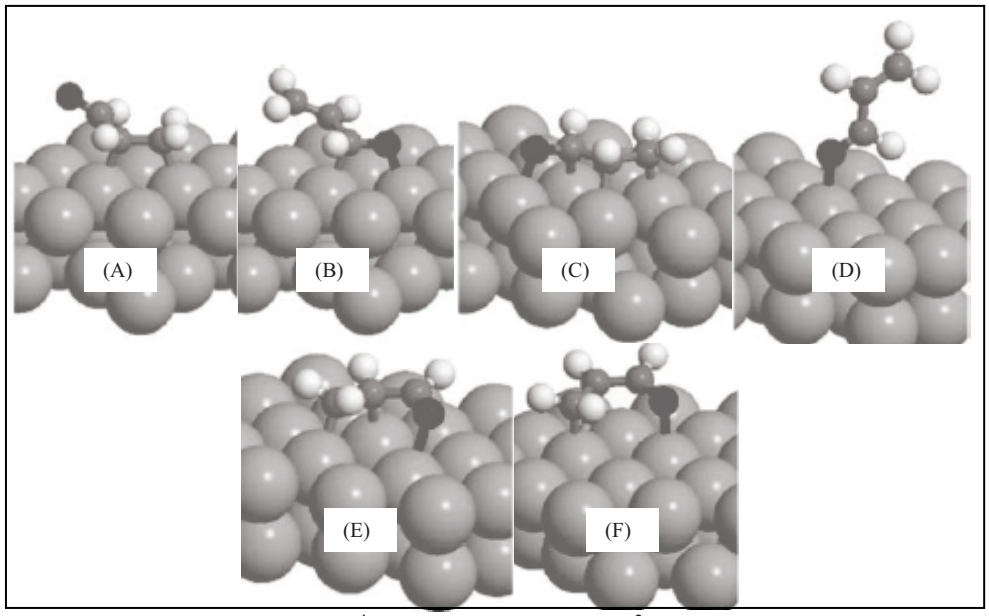

(A) di σCC, (B) di σCO, (C) η^4-trans, (D) top, (E) η^3-cis and (F) di σ-14 [25, 107]

Figure 3: Different adsorption modes of unsaturated aldehydes on a PtFe alloy

For exemple, the hydrogenation of CAL conducted on the Pt(111) plane, unlike the Pt(111) step, does not favor the coordination with the C=C bond and a higher selectivity to COL is observed.

In this work we will compare the carbonaceous nanostructures prepared in chapter II as supports for bimetallic nanoparticles of platinum and ruthenium catalysts, with classical supports like alumina, silica, MgO and ZnO. Later, we will show the advantages of using carbon supports, with a focuse on the multi-walled carbon nanotubes supported Pt-Ru bimetallic catalyst, by studying how can a thermal treatment, called the activation, affect the structure of the catalyst and thus improves the selectivity towards cinnamyl alcohol. Valuable insights on the pathway of hydrogenation of CAL, reaction kinetics and the elements behind the regioselectivity will be given.

In this chapter the catalytic activity was calculated by mean of the turn over frequency (TOF) expressed in moles of cinnamaldehyde transformed per moles of metal used per minute):

$$TOF = (n_{CAL}i - n_{CAL}t)/(n_{Pt} + n_{Ru}) / t \ (min^{-1}) \quad \text{Eq. 1}$$

Due to the possible presence of a high number of by products, the selectivity towards cinnamyl alcohol was calculated relative to the main hydrogenation products i.e COL, HCOL and HCAL.

$$\text{Selectivity: } S_{COL} = (n_{COL} * 100)/(n_{COL} + n_{HCAL} + n_{HCOL}) \ (\%) \quad \text{Eq. 2}$$

As more than 20 possible compounds may exist in the medium, the amount of by-products was calculated as what remains from the initial amount of CAL introduced in the reactor, and was not seen as COL, HCOL or HCAL or remaining CAL in the chromatograms.

$$\text{By-products} = (n_{CAL}i - (n_{COL} + n_{CAL}t + n_{HCOL} + n_{HCAL}))/(n_{CAL}i) * 100 \ (\%) \quad \text{Eq. 3}$$

III-2-Optimum condition determination

Catalysts of 2-2 wt % Pt-Ru/support were elaborated from the [Pt(COD)Me_2] and [Ru(COD)(COT)] organometallic precursors in hexane at 45 °C under Ar, and reduced at 350 °C under a 10 % H_2/Ar mass flow. The study is initiated using the 2-2 wt % Pt-Ru/MWCNT catalyst. After a brief study, we found as starting condition for hydrogenation: 2 g of cinnamaldehyde dissolved in 40 mL of isopropanol using 100 mg of catalysts at a pressure of 20 bars at 70 °C with a stirring velocity of 900 rpm. But before getting into further studies, two main parameters have been studied: the stirrer velocity and the choice of the solvent.

III-2-1-The stirrer velocity

The hydrogen in the autoclave is present in the gas phase or dissolved in the liquid phase. Diffusion of H_2 from the gas to the liquid phase could affect the reaction. Diffusion is controlled in particular by the stirring velocity inside the autoclave. Any reaction should be studied under what is called a chemical regime where the solution is saturated with H_2 and no diffusion limitation affects it [31].

Test	Stirring (rpm)	TOF (min^{-1})	Selectivity (%)			
			COL	HCOL	HCAL	By-products
C1	780	7.3	49.7	12.9	37.4	24.1
C2	900	8.1	49.6	11.0	39.4	31.3
C3	1000	8.2	48.6	10.2	41.8	25.2
C4	1200	8.2	54.2	11.4	34.3	19.7

Catalyst: 2-2 wt % Pt-Ru/MWCNT, $[CAL]_0 = 0.38$ Mol.L^{-1}, $m_{catalyst} = 100$ mg, $P(H_2) = 20$ bars, $T_{Catalysis} = 70$ °C, t = 1 h

Table 2: Effect of the stirring velocity on activity and selectivity

The stirrer velocity was varied between 780 and 1200 rpm and the activities and selectivity were calculated (Table 2). Above a stirring velocity of 900 rpm the catalytic activity is independent from the stirring speed (Figure 4).

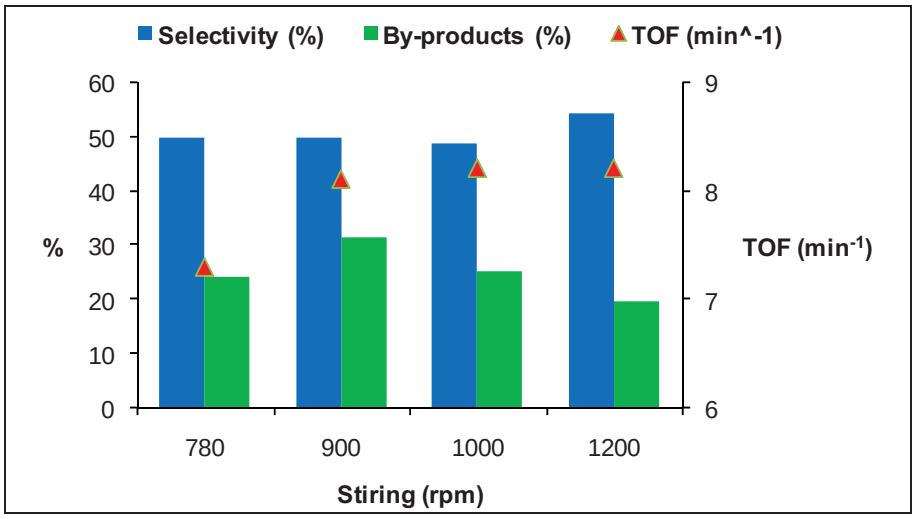

Figure 4: Chemical regime (plateau) of the autoclave reached above 900 rpm

III-2-2-Solvent choice

For the choice of the solvent many aspects has to be considered, like the solvent polarity, hydrogen solubility, interaction between the solvent and the catalyst as well as reactant and product solubility [17]. Adsorption and desorption of a reactant or product on the catalyst surface is commonly affected by competitive adsorption of the solvent. It has been found that a polar solvent enhances the adsorption of a non polar reactant and vice versa [32, 33]. Moreover, the solubility of the reactants in the solvent can change the availability of reactants and products for consecutive reaction on the catalyst surface. The use of both polar and non-polar solvents has been

reported for CAL hydrogenation [34-36], and the activity increased with the solvent polarity whereas selectivity decreased.

Cyclohexane and hexane are reported to yield the highest selectivity, but CAL was insoluble in such solvents at the concentrations of our tests. Propan-2-ol in association with acid surface catalysts like Ru/Y and Ru/MCM-41 yield 60-80 % of by-products, mainly acetals [37]. The supposed stable unsaturated cycle of toluene was reduced by our Pt-Ru/MWCNT catalyst at 100 °C and under 20 bars of H_2, mostly to methylcyclohexane during the 2 h in situ reduction step (Fig. 5). Over solvents like ionic liquids, supercritical CO_2, or multi-phase systems [38] could have been tried but this was not the aim of our study since what was important to us was the comparison of the catalytic performance as a function of the support.

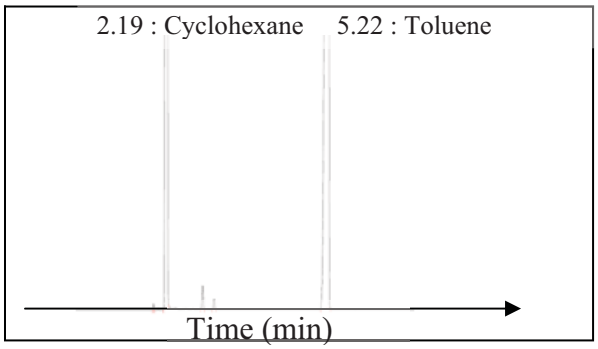

Figure 5: Chromatogram of the hydrogenation of toluene to methylcyclohexane

This limited our choice of solvent to propan-2-ol, a solvent often reported in literature for this reaction, yielding a good solubility of cinnamaldehyde and hydrogen, but giving rise to by-products.

III-3-Effect of the support on the catalytic performance

In this section we study the effect of the supporting material on the dispersion of the Pt-Ru bimetallic nanoparticles and on the catalytic performances. Before the Pt-Ru nanoparticles deposition by liquid impregnation, the single-, multi-walled carbon nanotubes and nanofibers were treated with nitric acid to create surface groups (mainly carboxylic acid) [39-41], acting as anchoring sites and enabling better dispersion [42]. They also improve the dispersibility of the catalyst in solvents [43-45]. As for the nitrogen doped carbonaceous material, we have discovered that there is no need for such treatment since surface nitrogen atoms would play this role.

Different metal binding sites (-COOH or –N) are expected to result in different electronic interactions and thus different activity and selectivity [46].

III-3-1-Catalyst characterization

Different metal-support interaction exist due to differences in the specific surface areas, nature of anchoring sites, graphene orientations and the amount of defects on the support. Thus, kinetic of nanoparticles formation was not the same on all the supports. The same deposing protocol was applied to various supporting materials resulting to variations in the metal loading. Since the catalytic activity was normalized relatively to the metal loadings and is presented in TOF this would not be so problematic. The TEM micrographs of the prepared catalysts are presented in Figure 6 and a summary of characteristics of the catalysts in Table 3.

			Catalyst residue					
Support	Pt (%)	Ru (%)	Metal (%)	Support	$d_{average}$ (nm)	BET (m^2 / g)	Vpores (cm^3/g)	dpore (nm)
MWCNTs	1.84	2.12	0.13 Fe	<100 ppm Al	2.70	224	1.6	29
CNFs	0.54	0.58	3.42 Ni	0.47 % Al	2.40	437	0.7	6
N-MWCNTs	0.11	0.50	2.23 Co	<0.30 % Si	1.60	119	0.6	19
N-CNFs	1.32	2.04	5.51 Fe	0.49 % Al	0.52	175	0.6	15
SWCNTs	0.41	1.73			1.21	72	0.4	24
AC	0.43	0.50			4.94	27	0.1	22
Alumina	1.94	2.04			2.70	147	0.2	6
Silica	1.46	1.68			6.16	245	1.7	28
MgO	0.41	0.17			5.15	0.07	$3x10^{-3}$	205
ZnO	1.92	1.92			2.90	14	0.1	35

Table 3: Characteristics of the prepared catalysts as a function of the nature of the support

In general, the nanoparticles size distribution was comparable and narrow, mainly between 1 and 6 nm (Figure 6, 7) and average diameters between 0.5 and 6 nm. This was advantageous since highly dispersed small metal particles are generally more active in activating organic molecules [47].

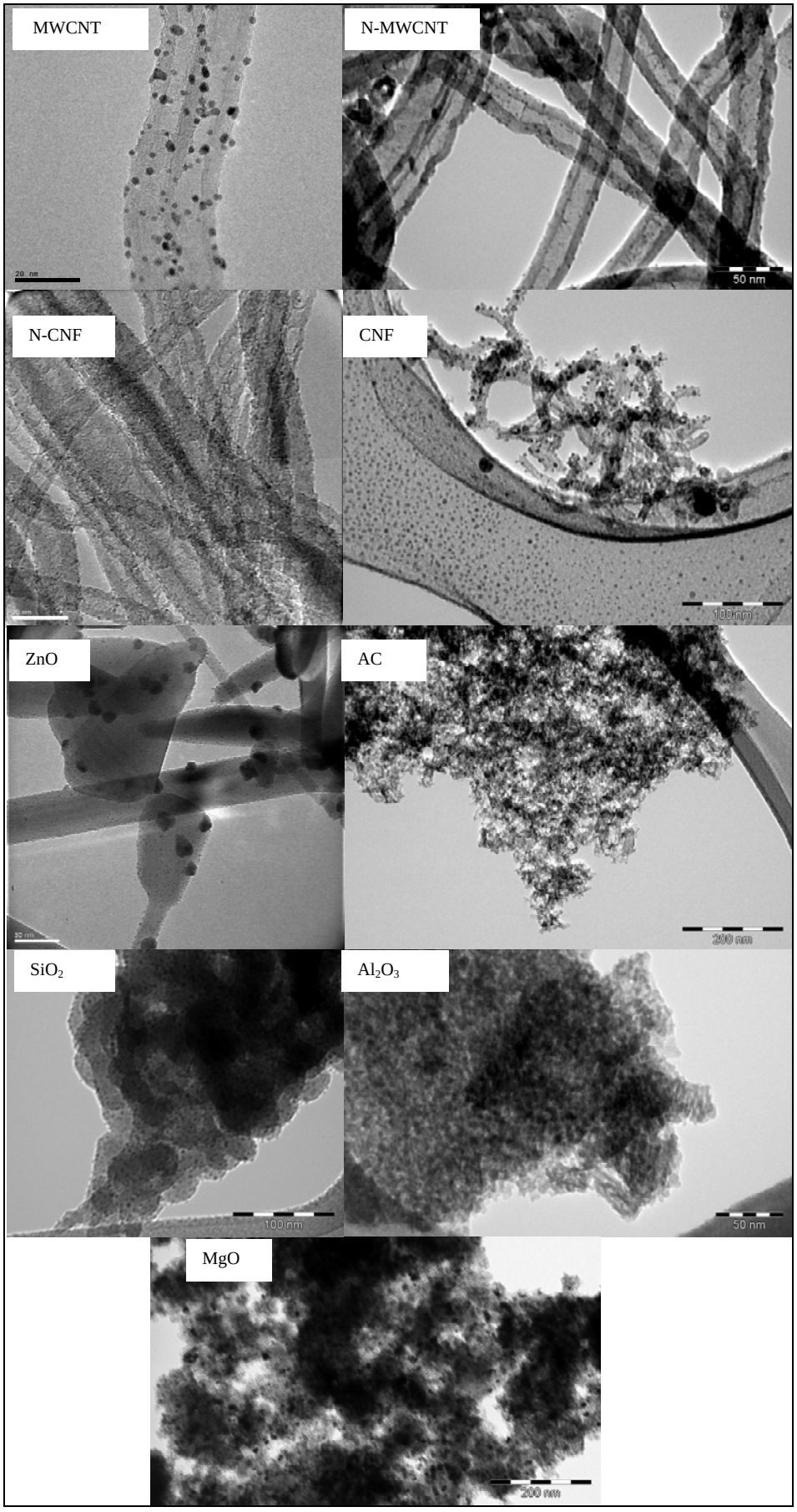

Figure 6: TEM micrographs of the different catalysts

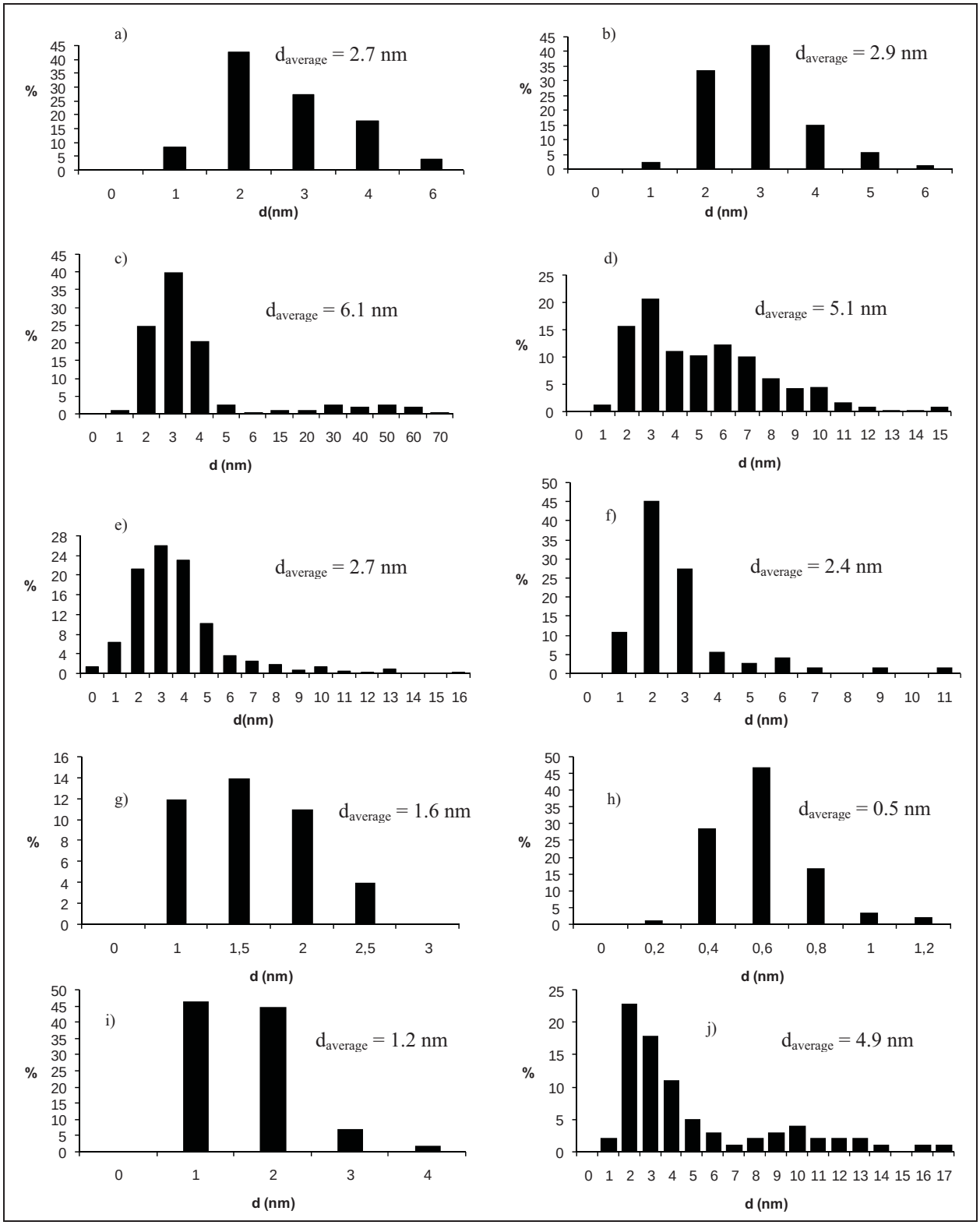

Figure 7: Pt-Ru nanoparticles size distribution as a function of the nature of the support: a) Al_2O_3, b) ZnO, c) SiO_2, d) MgO, e) MWCNTs, f) CNFs, g) N-MWCNTs, h) N-CNFs, i) SWCNTs, j) Activated carbon

We note that the dispersion of the nanoparticles on carbonaceous supports was better than that on classical alumina or silica supports. This must be related to their anchoring sites (N or COOH) and stronger metal-support interactions (SMSI).

III-3-2-Catalytic tests

In Table 4 are presented different 2-2 wt % Pt-Ru bimetallic catalysts supported on different supports and their catalytic performances. TOF were calculated according to the metal loadings found by the ICP-MS method (Table 3).

Test	Support	Conversion (%)	TOF (min^{-1})	Selectivity (%)			
				COL	HCOL	HCAL	By-products
C5	MWCNT	72	7	56	21	23	25
C6	CNF	91	27	19	20	61	51
C7	N-MWCNT	64	35	43	13	44	35
C8	N-CNF	53	5	57	10	33	16
C9	SWCNT	70	8	60	11	29	17
C10	AC	56	20/**6***	43	9	48	44/**30***
C11	Al_2O_3	24	2	57	7	36	11
C12	SiO_2	24	3	70	6	24	12
C13	MgO	6	4	78	5	16	0.6
C14	ZnO	3	0.2	69	6	25	0

$[CAL]_0 = 0.38$ Mol.L^{-1}, $m_{catalyst} = 100$ mg, $P(H_2) = 20$ bars, $T_{Catalysis} = 70$ °C, t = 1 h, Stirring = 900 rpm, ***Corrections made by adsorption contribution removal**

Table 4: Catalytic performance of the Pt-Ru catalysts as a function of the nature of the support

As we varied the nature of the support, the catalytic performances varied (Fig. 8), proving once again that the support in heterogeneous catalysis is not inert towards catalytic performance [1, 2], and its role is not limited to recycling and re-use of the active site.

III-3-2-1-Catalytic activity comparison

Nanostructured carbon catalysts present a dynamic structure so there would be no clogging and better diffusion on the pores. With the novel carbonaceous materials

there is a better dispersion of the Pt-Ru active phase, resulting to smaller nanoparticles. In addition, carbon nanostructures are reported to store significant amount of hydrogen by surface dissociative adsorption [48]. This phenomenon may induce high H_2 concentration around the active PtRu nanoparticles that could allow activity enhancement. This phenomenon does not exist when metal oxide supports are used. All these characteristics contribute to a much better catalytic activity (varying between 5-35 min^{-1}) when using carbonaceous nanostructures compared to the one of rigid structured metal oxides (2-3 min^{-1}) [26, 47].

Pt-Ru nanoparticles supported on MgO yield the highest catalytic activity among metal oxides. This might be related to its macroporous structure that eases accessibility and diffusion along its surface.

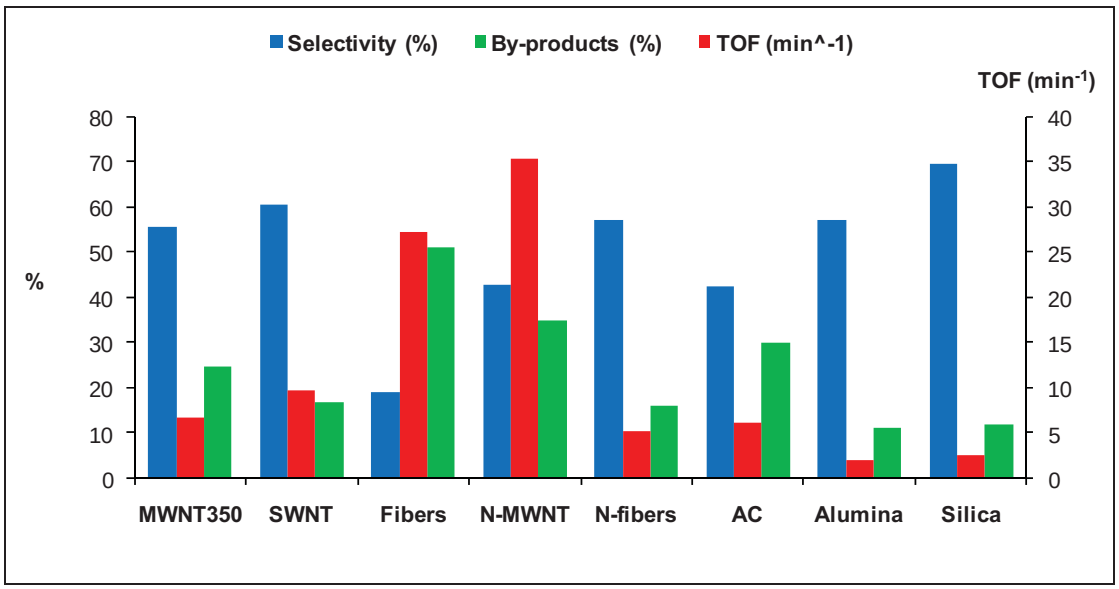

Figure 8: Catalytic performances of different catalysts as a function of the nature of the support

The highest catalytic activity was achieved with nitrogen doped carbon nanotubes supported catalyst with TOF value of 35 min^{-1}. Insertion of nitrogen atoms modifies the electronic structure of the nanostructure, and their surface chemistry. Compared to the MWCNT support, presenting –COOH groups on their surface, the use of N-MWCNT should impact the kinetics of CAL adsorption, diffusion on the surface and desorption of the hydrogenated products. Thus, catalytic activity increased 6 times (TOF of carboxylic MWCNT catalyst is 7 min^{-1}) as reported in [46, 49]. The decrease of number of walls from MWCNTs to SWCNTs permits an increase of the catalytic activity in accordance with what is reported in literature: the

increase in CNT diameter increases the concavity of the surface and a convex surface is reported to be more reactive towards addition reactions than the concave one [50].

The catalytic activity of the carbon nanofibers supported catalyst was also higher than that with MWCNTs and that was attributed to the increase in their specific surface area up to 437 m^2/g and the better dispersion (Fig. 7) due to the orientation of their graphene sheets making them more defective and thus more reactive. Surprisingly, nitrogen doping of the fibers decreases their catalytic activity as opposed to what was observed with the carbon nanotubes doping, making each support with unique property. Lower catalytic activity on Pt-Ru/N-CNF catalyst could also be explained by its very small nanoparticles (0.5 nm) making them very vulnerable to rapid poisoning.

In the case of activated carbon, the surface area dropped dramatically to 27 m^2/g after the Pt-Ru deposition, indicating that the nanoparticles have blocked the micropores. Stirring inside the reactor may break the Pt-Ru/AC catalyst grain making the micropores once again accessible and re-increase the specific surface area. High activity of 20 min^{-1} may be due to adsorbed cinnamaldehyde, an observation very common on AC, which did not react and could not be seen in the chromatogram. This is also confirmed by the highest amount of by-products calculated at 44 % with this support that is also overestimated and should comprise the adsorbed proportion. Mixing 2 g of CAL with 100 mg of AC in 40 mL of propan-2-ol at room temperature and atmospheric pressure for 1 h revealed an adsorption of 0.4 g of CAL. The correction of the catalytic activity revealed a TOF of 6 instead of 20 min^{-1} and by-products of 29 instead of 44 %.

As a conclusion, the activity of catalysts on carbonaceous supports was largely better than the one of catalyst supported on metal oxides, and further, was dependant on the orientation and number of the graphene layers and the nature of the surface anchoring sites (carboxylic *vs* nitrogen groups). However, high catalytic activity without selectivity is meaningless in catalysis. The most important factor in our research was selectivity to cinnamyl alcohol.

III-3-2-2-Selectivity comparison

III-3-2-2-a-Classical *vs* non classical supports

Selectivity to cinnamyl alcohol was affected by the nature of the support. At a first glance, we can say that the best selectivity towards cinnamyl alcohol was achieved with the oxide supports (MgO > SiO_2 > ZnO > SWCNTs > MWCNTs…) [51, 52].

It has been reported that the selectivity to cinnamyl alcohol increases as the particle size increases [21, 53, 54]. This was attributed to a steric effect whereby the planar cinnamaldehyde molecule cannot adsorb parallel to a flat metal surface because of the steric repulsion of the aromatic ring.

Indeed, theoretical calculations showed that aromatic rings that are chemisorbed on a metal surface must lie at a distance exceeding 0.3 nm because there is an energy barrier preventing a closer approach to the surface [54]. Because of this energy barrier, the C=C bond cannot approach the surface as closely as the C=O bond does (Fig. 9), the latter is then hydrogenated preferentially. This steric effect does not operate on small particles where both the C=C and the C=O bonds can approach the surface.

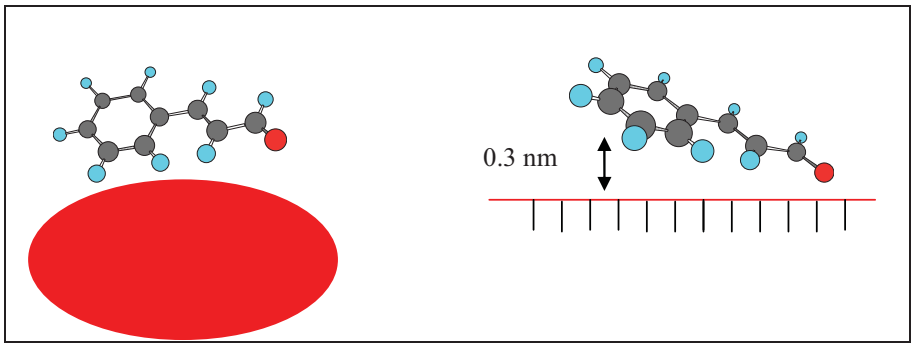

Figure 9: Scheme of CAL adsorption on a small metal particle and on a flat surface

As previously mentioned, carbon nanostructures enable better dispersion of the active phase resulting to smaller nanoparticles than in the case of metal oxides thus selectivity to COL is disfavored. In addition, MgO and SiO_2 present surface groups that act as electron-donor sites modifying the electronic properties of the nanoparticles and increasing selectivity (*vide infra*). ZnO is a semiconductor that can play a similar role.

Between carbonaceous supports, selectivity was also dependant on the orientation and number of the graphene layers and the nature of the surface anchoring sites (carboxylic *vs* nitrogen doped).

III-3-2-2-b-AC *vs* graphitic support

First, catalysts based on graphitic carbon nanomaterials are more selective towards COL than disordered carbon in activated carbon. This was in accordance with the work of Richard et al [55, 56] who interpreted this in terms of an electronic ligand effect. Metal particles are preferentially located on steps and edges of graphitic planes, the π-electrons of the graphitic planes can be easily extended to the metal particles, thus increasing the charge density of the metal. In fact, the graphitic support acts like a macro electron donating ligand. The increased charge density on the nanoparticles decreases the probability of adsorption via the C=C bond, so that the selectivity towards the COL increases.

III-3-2-2-c-Orientation of the graphene layers

Pt catalysts supported on tubular carbon nanostructures are rather selective (S_{COL} = 55-60 %) towards cinnamyl alcohol. Selectivity increased with the decrease of the number of graphene layers (S_{SWCNT}>S_{MWCNT} Table 4) [57]. A Pt catalyst supported on nanofibers is reported to be selective towards hydrocinnamaldehyde (HCAL) [2]. This was also true with our bimetallic Pt-Ru/CNF system (S_{HCAL} = 61 %).

The different hydrogenation behavior of Pt-Ru/MWCNT, Pt-Ru/SWCNT and Pt-Ru/CNF catalysts may result from the variations in the properties of the support. Changes in the graphene layer number or orientation changes the electronic and steric effects in addition to metal to support interactions. It is well known that a rehybridization of carbon orbital to a non-planar sp^2 configuration is necessary to form CNTs by rolling the graphene sheet up, leading to the modifications of the π–electron density of the graphene plane [58]. Consequently, when a metal is deposited on CNTs, electronic effects, i.e., transfer of π-electrons from the graphene sheet of CNTs to the metal particle and vice versa, may occur. The curvature of the most outside tube is expected to decrease with the increase of the tube diameter (number of walls), leading to a decrease for the non-planar degree of the rehybridized

sp^2 configuration of carbon orbital [57]. Since SWCNTs are more electrons donating, the nanoparticles are more charged in electronic density, and thus selectivity to COL is increased relative to MWCNTs. The metal-support interaction and the mobility of the delocalized π-electrons in the carbon nanofiber should be less than the one of the nanotube due to the orientation of the graphene plane (Fig. 7, 8 chapter I), explaining the selectivity difference. The lower metal-support interaction was evidenced in the case of CNFs by TEM observations. The nanoparticles detached from their surface, during sonication and got fixed on the carbon film of the cupper grid (Fig 6 d). In addition, in order to be hydrogenated selectively towards one or another of the molecules COL or HCAL, the CAL must gain a certain orientation and adsorption mode on the surface of the support or of the nanoparticle [2]. The bent graphene sheets of the nanofibers make there surface polar and the CAL adsorption on their surface is weak and oriented in a way to favor the C=C bond, whereas straight graphene sheets of the carbon nanotubes makes them non-polar, there is an optimal adsorption of CAL due to π- stacking interaction between the aromatic ring of CAL and that of the MWCNTs, that favors the C=O bond hydrogenation. A schematic representation of this hypothesis is presented in Figure 10.

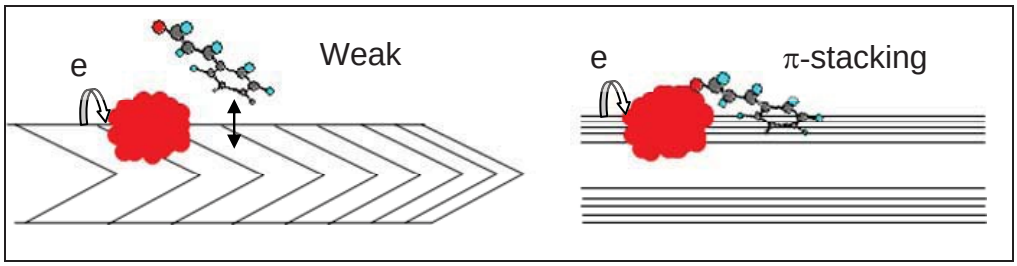

Figure 10: Role of the orientation of the graphene sheets in the adsorption of CAL and support-nanoparticles electronic transfer

III-3-2-2-d-Carboxylic *vs* nitrogen containing surface groups

Interestingly, the nitrogen doping of the surface of MWCNTs and CNFs inverts the observation in the previous section. Nitrogen doping of the carbon nanofibers largely increased the selectivity of the catalyst towards cinnamyl alcohol from 19 to 57 % and the doping of the multi-walled carbon nanotube decreases it slightly from 55 to 42 %. Addition of nitrogen containing organic surface species was expected to be beneficial to cinnamyl alcohol selectivity. It is reported that the selectivity of a Pt catalyst to COL was improved by the presence of basic molecules

like phosphine, arsines [59], amines [60] and KOH [61, 62]. Nitrogen is more electrons donating than the -COOH group and results in chemically active, localized areas of higher electron density on the nanoparticles [63]. In the doped nanostructure, nitrogen atoms entering the graphene sheets as substitute of carbon, and the absence of carboxylic groups could modify in a large extend the surface acido-basic properties and also adsorption on the nanotube due to changes in polarity and / or steric effects. The decrease in selectivity of the nitrogen doped carbon nanotubes catalyst in comparison with carboxylic nanotubes catalyst could be related to the large increase in the external tube diameter [57]: 24 nm for N-MCWNTs versus 6.5 nm for MWCNTs. Depending on the synthesis condition, various types of nitrogen doped carbon nanotubes can be synthesized (Chapter II-5) with different surface properties. Some nitrogen insertions are electronegative (N-oxides: N^{+}-O^{-}) explaining why some work announce that the N-MWCNTs are selective towards the C=C bond [46]. In our case, the N-CNFs had a dominant quaternary form of nitrogen insertion (Chapter II), which seems optimal for the C=O bond hydrogenation (S_{COL} = 57 %). As for N-MWCNTs, either the nitrogen type was not selective to any bond (S_{COL} = 43 % and S_{HCAL} = 44 %) maybe due to a mixture of types, or most probably due to the diameter increase since the doping was only 1.5 %. It is reported that nitrogen doped carbon nanotubes exhibit a 50 % selectivity towards COL when the external diameter is around 25 nm [49].

III-3-2-3-By-products

The acidic/basic sites of the supports exhibit isomerization and cyclization properties [15]. The CNF supported catalyst produced the higher amount of by-products, and that was expected since they should present the higher amount of defects that could act as Lewis acidic sites. The by-products were the same irrespective of the carbonaceous support, as almost the same unidentified peaks were seen in the GC chromatograms. The products were identified by mass spectrometry as products of cyclization and isopropanol condensation (Fig. 11). The major products were the (1) cinnamic acid ($C_9H_8O_2$), (2) isopropyl cinnamaldehyde ($C_{12}H_{14}O_2$), (3) cinnamyl propyl ether ($C_{12}H_{16}O$), (4) p-isobutylbenzaldehyde ($C_{11}H_{14}O$), (5) benzeneacetaldehyde (C_8H_8O), (6) 2-methyl benzofurane ($C_9H_{12}O$) and (7) 3-methyl-benzofuranone. For the majority of those products, it is the C=O bond that reacted and the C=C bond is untouched, confirming the selectivity. All the by-products could have

been generated from the cinnamic acid (Fig. 11), that was probably generated from the oxidation of CAL catalyzed by an acid site and a –OH surface group from the carbon nanostructure.

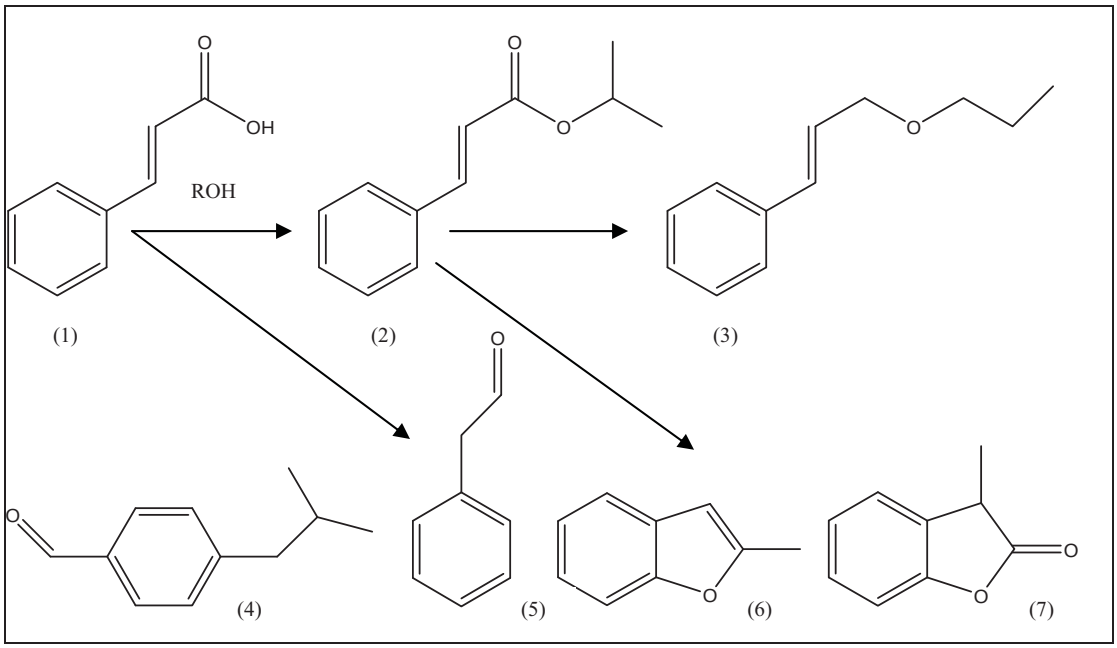

Figure 11: Chemical structure and evolution of the most frequently encountered by-products

III-3-3-Conclusion

The procedure of catalyst preparation is simplified by nitrogen doping of the carbon nanomaterials which no longer require prior functionalization. In addition to the peculiar structure of carbonaceous supports, i.e variation of the number and orientation of the graphene sheets, electronic properties and the resulting metal to support interaction, the doping with heteroatom's is an additional variable to master the selectively depending on its electron donating/up taking aptitude. With the novel carbonaceous supports, activity is largely superior compared to conventional oxide supports due to the dynamic structure, so there would be no mass transfer limitations and pore clogging. All these considerations make carbonaceous supports largely advantageous over classical supports of metal oxides for this liquid phase hydrogenation reaction. One last detail remains, could their selectivity be enhanced so it may overcome the one of the metal oxide classical support? This will be the subject of the next study.

III-4-Surface modification of the Pt-Ru/MWCNT catalyst by heat treatment

For α,β–unsaturated aldehydes hydrogenation, it has been reported that the removal of the surface groups by a heat treatment of monometallic catalytic active species supported on carbon nanofibers may increase their selectivity towards the saturated aldehyde [2, 39]. In the following study, we chose to work with the MWCNT support, which had an average selectivity towards cinnamyl alcohol of 55 %, and was easily produced in high quantity in our laboratory in comparison with SWCNT supported catalyst. The Pt-Ru/MWCNT was heated under nitrogen at different temperatures for 3 hours and this treatment was called the activation. The Pt-Ru/MWCNT catalysts resulting from the activation were tested under the same condition of section III-3 (Table 5).

Test	Catalyst	Conversion (%)	TOF (min^{-1})	Selectivity (%)			
				COL	HCOL	HCAL	By-products
C5	MWCNT350	72	6.7	56	21	23	25
C15	MWCNT700	67	7.9	81	10	9	35
C16	MWCNT850	82	4.6	84	11	4	30
C17	MWCNT1000	78	4.8	90	5	5	44

$[CAL]_0 = 0.38$ Mol.L^{-1}, $m_{catalyst}$ =100 mg, $P(H_2) = 20$ bars, $T_{Catalysis} = 70$ °C, t = 1 h, stirring = 900 rpm

Table 5: Hydrogenation of CAL on different activated catalysts

The selectivity towards cinnamyl alcohol increased linearly with the activation temperature to reach 90 % for the 1000 °C activated (Fig. 12). The turn over frequency was variable (Table 5) due to fluctuations in the metal loadings and particles size. More accurate TOF measurements could have been made by taking into account the active surface. Anyway catalytic activity was always better than that of metal oxide supported catalysts. By-products concentration also increased with the activation temperature from 25 to 44 %.

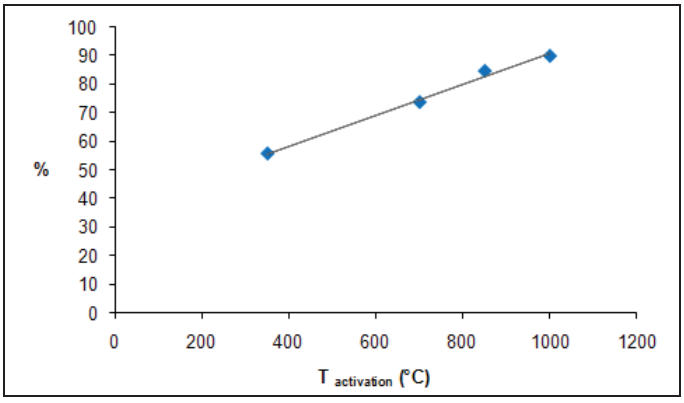

Figure 12: Selectivity towards COL as a function of $T_{activation}$

Now that we confirmed the feasibility of selectivity increase towards COL with thermal activation the next step was to understand how and why this selectivity increased. Kinetic studies are presently lacking, and are needed to evaluate the effect of reaction conditions on the activity and selectivity [21]. Thus, a parametric study has been performed on the catalysts activated at 350 and 700 °C. We evaluated the influence of the initial concentration of cinnamaldehyde, the initial pressure of hydrogen, the temperature of hydrogenation and the concentration of catalyst used. Then, a full analysis of the catalyst surface by specific surface measurement (BET), temperature programmed reduction; high resolution transmission electron microscopy (HREM) coupled to microanalysis (EDX) and finally extended X-ray absorption fine structure (EXAFS) and wide angle X-ray spectroscopy (WAXS) was also performed.

III-4-1-Parametric study on Pt-Ru/MWCNT350 and Pt-Ru/MWCNT700

III-4-1-1-MWCNT catalyst without noble metals (Blank tests)

The catalytic performances of virgin multi-walled carbon nanotubes were tested under the conditions of Table 6. First, we found no conversion of CAL to any product without the use of a catalyst. The catalytic activity of the 350 °C MWCNTs was low and doubled after activation at 700 °C under N_2. This is in accordance with the results related to the removal of the carboxylic groups, enabling better adsorption and faster surface diffusion [26, 33] that will be detailed below.

Test	Catalyst	Conversion (%)	Selectivity (%)			
			COL	HCOL	HCAL	By-products
C33	None	0	0	0	0	0

C43	MWCNT350	9.3	68.8	19.2	12	1.9
C44	MWCNT700	18.97	44.42	11.98	43.59	11

m_{Cal} =2 g; $m_{catalyst}$ = 100 mg, $P(H_2)$ = 20 bars, $T_{Catalysis}$ = 70 °C, t = 1 h; stirring = 900 rpm

Table 6: Catalytic performance of the MWCNTs as a function of surface COOH groups

As for selectivity towards COL, it was very high at 350 °C (68 %) and decreases after activation at 700 °C. In fact –COOH surface group act as electron donating ligand that favor the C=O bond activation [64] and their removal decreases the selectivity.

III-4-1-2-Initial concentration of cinnamaldehyde

The initial concentration of cinnamaldehyde was varied between 0.38 and 2.27 $Mol.L^{-1}$ for the 350 °C catalyst, and 0.38 and 3.21 $Mol.L^{-1}$ for the 700 °C catalyst. The hydrogenation reaction was performed under the conditions of Table 7.

Test	Catalyst	$[CAL]_0$ $Mol.L^{-1}$	Conversion (%)	TOF (min^{-1})	Selectivity (%)			
					COL	HCOL	HCAL	By-products
C18	MWCNT350	0.38	97	8	50	11	39	31
C19		1.13	48	12	59	7	33	33
C20		1.51	27	9	59	5	36	17
C21		2.27	10	5	56	4	40	2
C22	MWCNT700	0.38	66	8	81	10	9	35
C23		1.13	35	13	86	3	11	21
C24		1.51	34	16	87	2	11	18
C25		2.27	31	22	81	3	15	18
C26		3.21	20	19	86	0	14	15

$m_{catalyst}$ = 100 mg, $P(H_2)$ = 20 bars, $T_{Catalysis}$ = 70 °C, t = 1 h, stirring = 900 rpm

Table 7: Hydrogenation condition with variation of the $[CAL]_0$

For the 350 °C catalyst, at low CAL concentration [0.38-1.13] $Mol.L^{-1}$, increasing the $[CAL]_0$ increases the catalytic activity, an indication of a positive kinetic order dependence towards $[CAL]_0$. This kinetic order becomes negative at higher $[CAL]_0$ (Fig. 13).

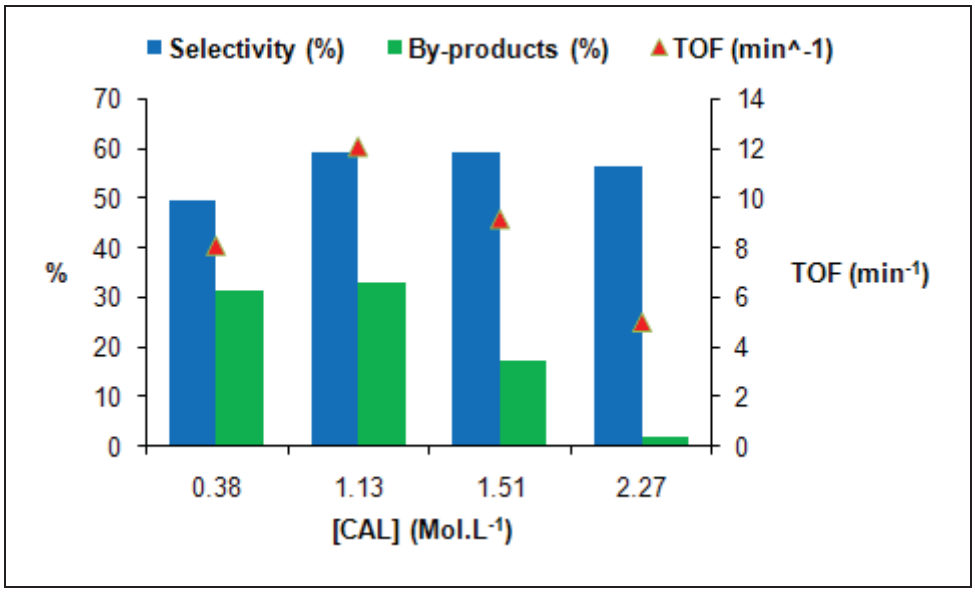

Figure 13: Catalytic performances of the Pt-Ru/MWCNT350 as a function of $[CAL]_0$

When activated at 700 °C, the behavior of the Pt-Ru/MWCNT catalyst followed different behavior from the one reduced at 350 °C. First, the maximum of catalytic activity was reached at higher CAL concentration (Fig. 14).

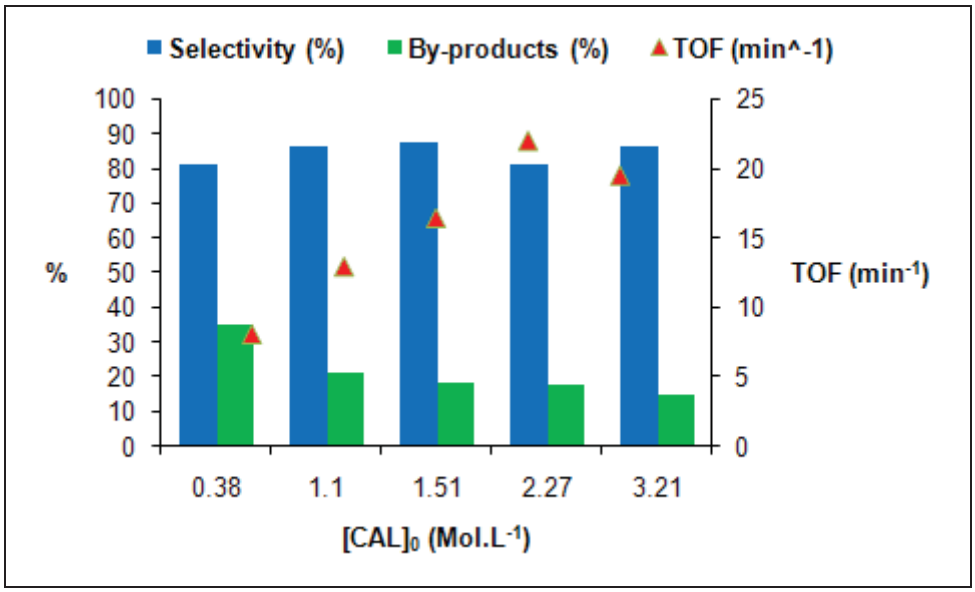

Figure 14: Catalytic performances of the Pt-Ru/MWCNT700 as a function of $[CAL]_0$

This must be related to the lost of carboxylic groups that were preventing adsorption on the surface of the MWCNT350 (see part III-4-2-2) [2, 26]. In fact, the catalytic activity increased with the increase of the initial CAL concentration, the

surface saturates at 2.27 Mol.L^{-1} in comparison with a 1.13 Mol.L^{-1} for the 350 °C catalyst. After 2.27 Mol.L^{-1} of CAL concentration, a competitive adsorption between H_2 and CAL could begin and the catalytic activity slightly decreases. A more extended adsorption of the catalysts activated at 700 °C (TOF = 22 min^{-1}) increased its activity 4 times in comparison with the one activated at 350 °C (TOF = 5 min^{-1}) for the same CAL concentration of 2.27 Mol.L^{-1} at 20 bars of hydrogen pression and 70 °C (Fig. 13, 14).

The increase in the initial reaction rate of CAL hydrogenation with the increase of the initial concentration of CAL is confirmed by the difference in the tangential angles of the hydrogen consumption evolution (Fig. 15) and the increase of the total hydrogen consumption after 60 minutes from 0.6 to 1.4 bars. The saturation starting at 2.27 Mol.L^{-1} is also proven by the decrease in the total hydrogen consumption and initial rate at 3.21 Mol.L^{-1}. The 3.21 and 1.51 Mol.L^{-1} become almost similar if the hydrogen pression is not increased.

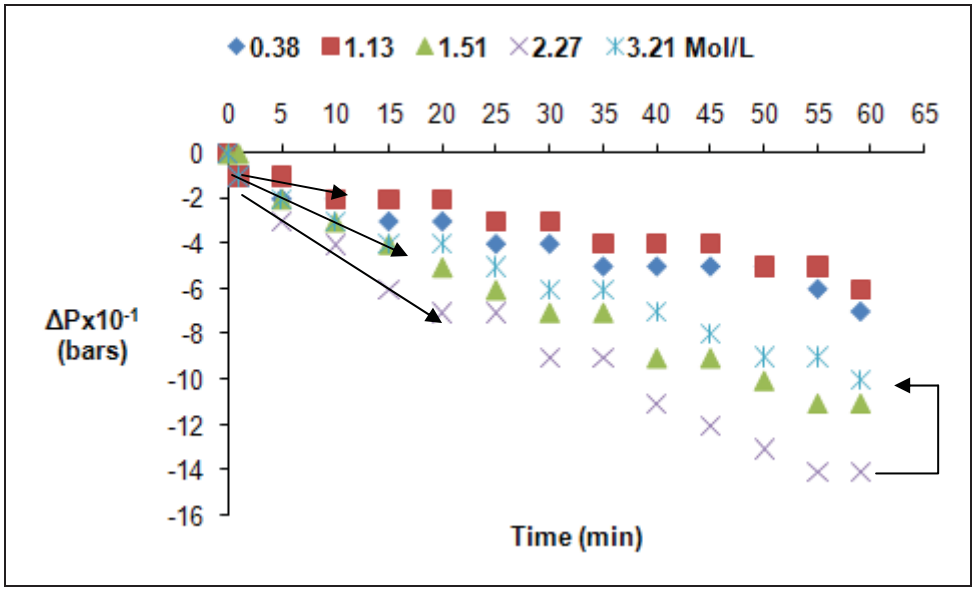

Figure 15: Hydrogen consumption as a function of time and $[CAL]_0$ on the 700 °C catalyst

This is in accordance with Langmuir-Hinshelwood adsorption kinetics for both 350 and 700 °C catalysts [2, 20, 21], for which at low reactant concentrations, the fractional occupancy of the catalyst surface increases linearly with the concentration in the solution, and with this the catalytic activity. At higher reactant concentrations, there is a saturation limit where the surface is almost fully occupied,

the increase in the $[CAL]_0$ became a limiting factor for catalytic activity due to a competitive adsorption between hydrogen and CAL. This proves that the hydrogenation of cinnamaldehyde requires the adsorption of both H_2 and CAL on the catalyst surface (LH). An increase in the pressure of hydrogen should re-increase the catalytic activity. This will be confirmed by the variation of the hydrogen pressure (*next section*).

Figure 13 and 14 shows that not only activity but also selectivity towards COL is a function of the initial concentration of CAL. For the 350 °C catalyst, it increased from 49 to 59 % by increasing the initial concentration of cinnamaldehyde from 0.38 to 1.13 $Mol.L^{-1}$, but later it decreases again to 56 % at 2.27 $Mol.L^{-1}$. As for the 700 °C catalyst, selectivity increased with the thermal activation whatever the CAL concentration was. But this latter followed the same variation as the one of the 350 °C catalyst: it increased from 81 to 87 % by increasing the initial concentration of cinnamaldehyde from 0.38 to 1.51 $Mol.L^{-1}$ but later it decreases again to 80 % at 2.27 $Mol.L^{-1}$.

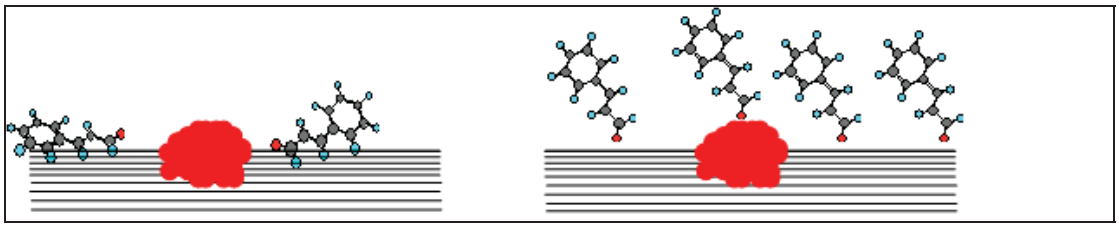

Figure 16: Adsorption modes of CAL as a function of its concentration: (left) flat at low concentration, vertically aligned (atop) in high concentrations (right)

Variations in the initial CAL concentration change its adsorption mode [2]. Delbeq and Sautet [25, 65] carried out a DFT study on the adsorption modes of unsaturated aldehydes and alcohols on Pt (1 1 1). They also considered the effect of surface coverage. They found that the adsorption mode that leads to the formation of unsaturated alcohols is the C=O atop geometry (Fig. 16). However, their calculations showed that this adsorption mode is slightly less favored than the planar C=C and that would explain why the C=C bond is easier to hydrogenate. An increase in the the surface coverage results in a promoting steric effect that leads to the hydrogenation of the C=O bond. But CAL concentration has a limit and should not affect hydrogen adsorption, otherwise selectivity decreases again.

In both the 350 and 700 °C catalysts, the selectivity increase was mainly at the expense of the complete hydrogenation to HCOL or the by-products formation. The by-product formation is inhibited with the increase of the initial CAL concentration. This must also be related to the competitive adsorption between CAL and the products. At low CAL concentration, the diffusion of the products from the surface of the MWCNTs to the external solution is slow, the local concentration of the intermediate products COL and HCAL is high, which increases the transformation to their complete hydrogenated product HCOL and by-products. High CAL concentrations enable their quick desorption, their local concentration is decreased [66] and selectivity increases.

III-4-1-3-Initial hydrogen pressure

The hydrogen pressure in the autoclave was varied between 10 and 33 bars (Table 8).

Test	Catalyst	$P(H_2)$ (Bars)	Conversion (%)	TOF (min^{-1})	Selectivity (%)			
					COL	HCOL	HCAL	By-products
C27	MWCNT350	10	9	4	53	4	43	4
C28		15	10	5	57	3	40	3
C29		20	10	5	56	4	40	2
C30		25	19	10	55	4	41	13
C31	MWCNT700	10	19	13	76	2	22	13
C25		20	31	22	81	3	15	18
C32		26	29	20	82	3	15	18
C33		33	39	28	77	4	19	26

$[CAL]_0 = 2.27$ Mol.L^{-1}, $m_{catalyst} = 100$ mg, $T_{Catalysis} = 70$ °C, t = 1 h, stirring = 900 rpm

Table 8: Hydrogenation condition with variation of the initial pressure of hydrogen

As expected, below 20 bars of initial hydrogen pressure the catalytic activity of the 350°C catalyst was constant. The increase of the initial hydrogen pressure to 25 bars re-increases the catalytic activity by equilibrating the competitive adsorption between CAL and H_2 (Fig. 17).

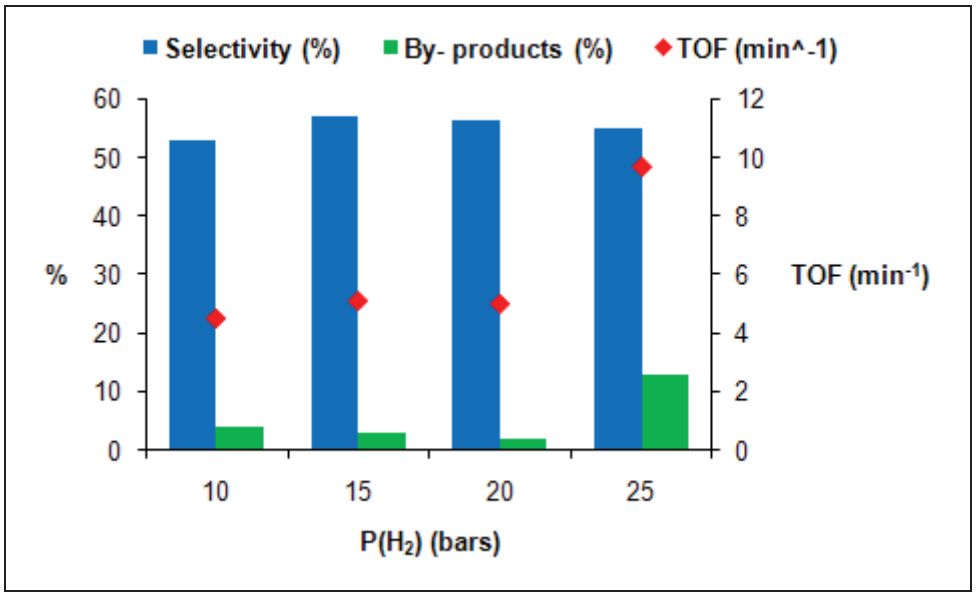

Figure 17: Catalytic performances of the Pt-Ru/MWCNT350 as a function of initial $P(H_2)$

For the 700 °C catalyst we chose to keep the $[CAL]_0$ at 2.27 $Mol.L^{-1}$ and varied the hydrogen pressure between 10 and 33 bars (Table 8). Catalytic activity increased more and more with the increase of the initial hydrogen pression (Fig. 18).

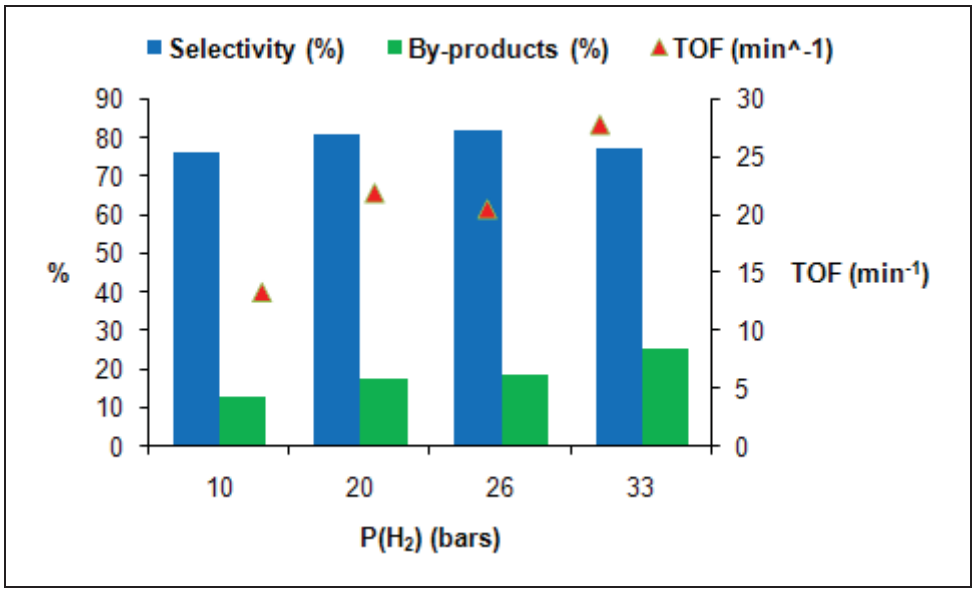

Figure 18: Catalytic performances of the Pt-Ru/MWCNT700 as a function of initial $P(H_2)$

This could be explained by the adsorption of H_2 on the catalyst surface in the form of active H-ad-species creating a micro-environment with higher concentration, thus increasing the rate of surface hydrogenation reactions. Indeed, dissociative

adsorbed hydrogen is frequently invoked for modeling hydrogenation reactions over Pt catalysts [17].

The dependence of the initial reaction rate on the initial pression of hydrogen was also evident by the increase of the initial reaction rate with the initial pression of hydrogen. The initial rate of the reaction is proportional to the tangential angle of the hydrogen consumption evolution (Fig. 19). The initial rate of the reaction at 10 bars was largely lower than the one at higher pressions. The hydrogen pressure evolution under 20, 26 and 33 bars of H_2 was almost the same, indicating that the variation under such condition was very local, at the surface of the catalyst as previously seen and was below the detection of our system.

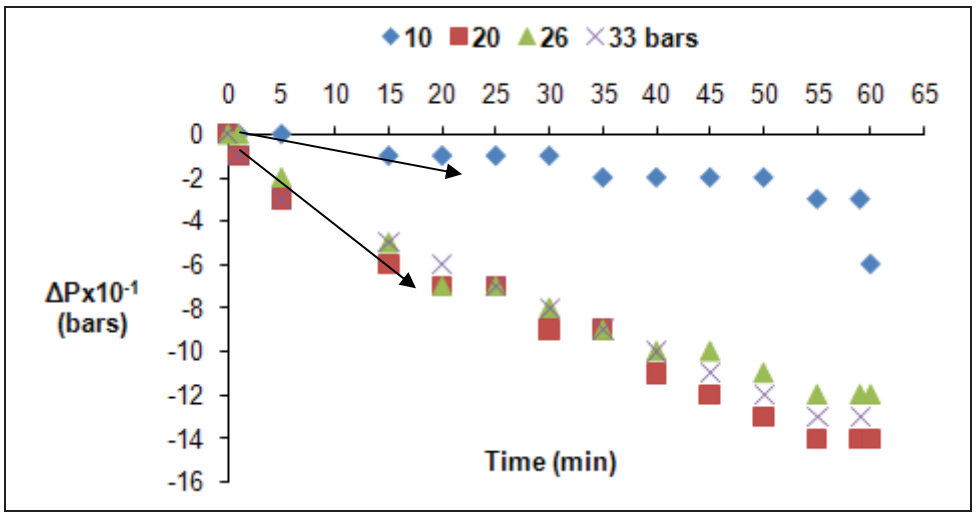

Figure 19: Consumption of hydrogen as a function of the time and initial H_2 pression on the 700 °C catalyst

The LH kinetic model was once again confirmed, both reactants must adsorb on the surface of the catalyst. We are not sure if H_2 and CAL adsorb on the same or different catalytic sites, but since there is a competition, the first hypothesis is more probable. Since catalytic activity was dependant on H_2 and CAL concentrations, the rate determining step should be the adsorption of CAL and H_2 on the surface of the catalyst.

The selectivity to unsaturated alcohols in chemoselective hydrogenations can either be constant [67, 68], decreases [69, 34], or passes through a maximum [70] with increasing hydrogen pressure. In our case, selectivity of the 350 °C and 700 °C

catalysts towards COL was almost constant whatever the H_2 pressure was (Fig. 17 and 18).

Since CAL and H_2 can get in competition, affecting the adsorption and orientation of one another, an optimum local concentration of CAL and H_2 adsorbed on the surface of the catalyst is a necessity for the increase of both catalytic activity and selectivity.

The by-products concentration increased with the increase of hydrogen pression, indicating that hydrogen plays a role in their formation as presented in Fig. 2 and 11.

III-4-1-4-Concentration of the catalyst

The concentration of active sites on the catalyst surface was varied by varying the weight of the catalyst introduced in the autoclave (Table 9).

Test	Catalyst	$m_{catalyst}$ (g)	Conversion (%)	TOF (min^{-1})	Selectivity (%)			
					COL	HCOL	HCAL	By-products
C34	MWCNT700	0.05	15	20	72	3	25	11
C25	MWCNT700	0.1	31	22	81	4	15	18
C35	MWCNT700	0.15	47	22	79	4	17	28
C36	MWCNT700	0.2	51	18	80	4	15	31

$[CAL]_0 = 2.27$ Mol.L^{-1}, $P(H_2) = 20$ bars, $T_{Catalysis} = 70$ °C, t = 1 h, stirring = 900 rpm

Table 9: Hydrogenation results with variation of the concentration of the catalyst

Catalytic activity and selectivity were independent from the concentration of active sites. Only the by-product concentration increased with this latter (Fig. 20). In fact the acidic/basic sites (Lewis defects, -OH) [15] of carbon nanotubes may enhance by-products formation by condensations with isopropanol and isomerizations.

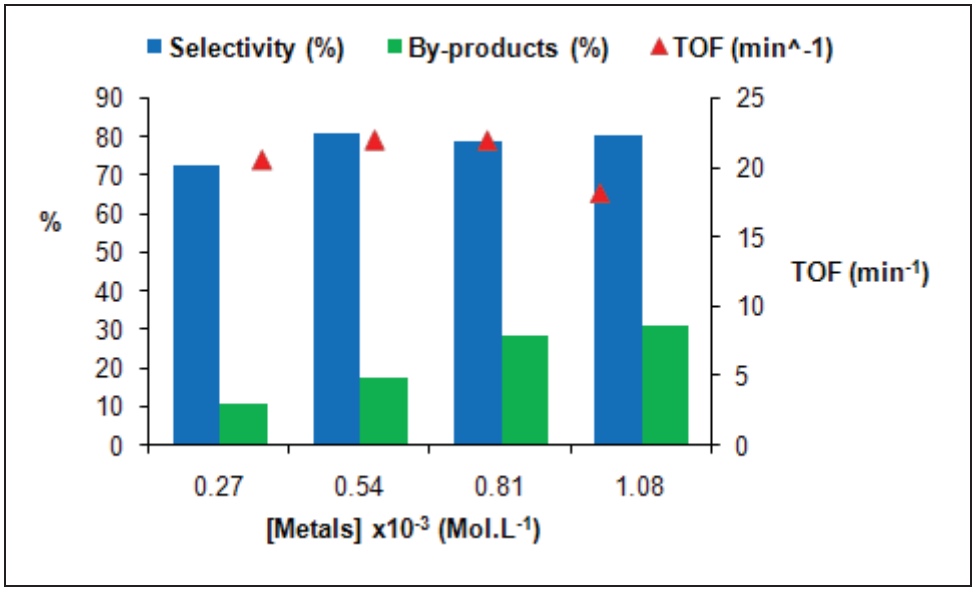

Figure 20: Catalytic performances of the Pt-Ru/MWCNT700 as a function of the catalyst concentration

Measuring the conversion of cinnamaldehyde over a range of different catalyst masses also enabled us to check again that mass transfer was not controlling the rate of the reaction. The absence of mass transfer limitations was confirmed [71] by a straight-line plot of conversion against catalyst mass (Fig. 21).

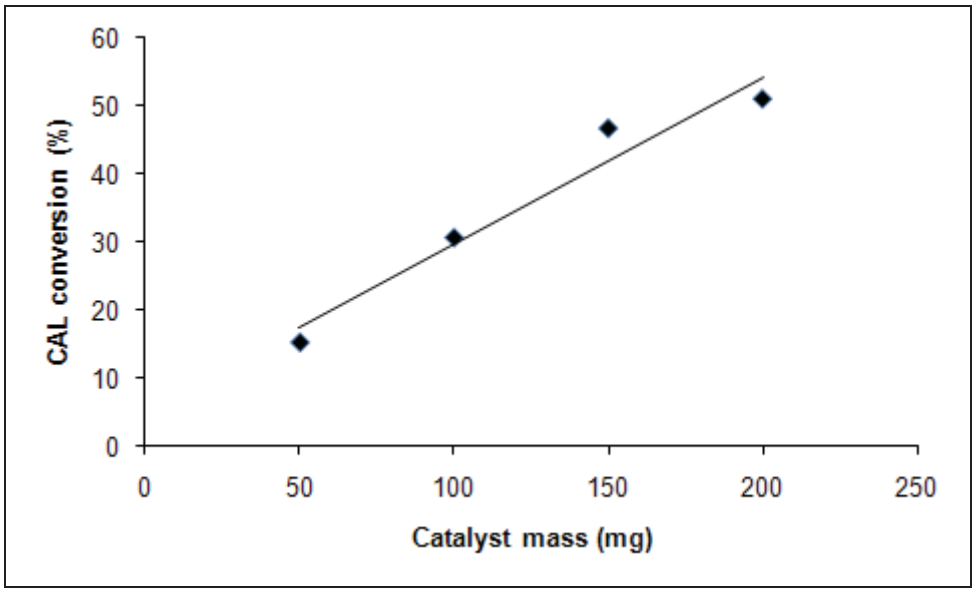

Figure 21: Cinnamaldehyde conversion as a function of catalyst mass

III-4-1-5-Initial selectivity

We have demonstrated that the Pt-Ru/MWCNT700 catalyst is more selective towards COL than the Pt-Ru/MWCNT350, but our measurements were done after 1 h

of reaction. In the current study we investigate what happens before and after that duration. First we have studied the evolution of each reactant as a function of time and then we have tried to determine a reaction favorable pathway by studying the reactivity of the products.

III-4-1-5-a-Run duration

The evolution of each product as a function of time was studied on the MWCNT700 catalyst under the conditions of Table 10.

Catalyst	t (min)	A $_{CAL}$	A $_{COL}$	A $_{HCAL}$	A $_{HCOL}$
MWCNT700	30	138	78	17	0
MWCNT700	50	136	115	18	22
MWCNT700	80	122	157	23	33
MWCNT700	140	101	284	29	65
MWCNT700	180	75	386	33	91
MWCNT700	200	75	389	32	93

$[CAL]_0 = 2.27$ Mol.L^{-1}, $P(H_2) = 20$ bars, $m_{catalyst} = 100$ mg, $T_{Catalysis} = 70$ °C, stirring = 900 rpm

Table 10: Hydrogenation products evolution as a function of time

Since microliter samples were withdrawn from the reactor at different reaction time, we could not do a precise titration, and we only obtained an evolution aspect by comparison of the peaks areas (Fig. 22).

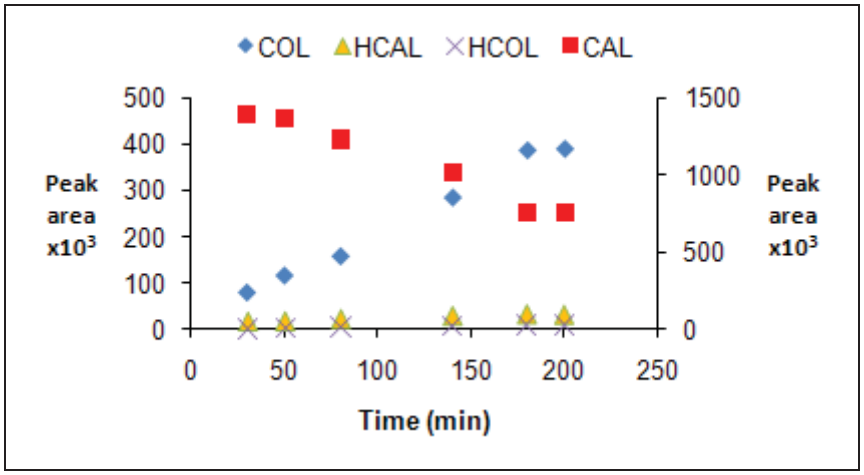

Figure 22: Evolution of each product as a function of the time of hydrogenation

We can say that as a function of time, the conversion increases linearly without deactivation even after 3 h. The selectivity towards COL increased also linearly. This is in accordance with previous reports [55] where graphitic supports were used and where selectivity to COL increased linearly as a function of conversion and the rest of the products concentrations remained constant. This behavior is specific to graphitic supports since it was different using activated carbon, i.e all products concentrations increased and HCAL was dominant [55].

It is apparent from the data in Figure 22 that most of the HCAL is formed in the initial stages of the reaction. Initially, the cinnamaldehyde can follow two reaction pathways, the majority undergoes C=O reduction to give COL but some undergo C=C reduction to give HCAL. Somehow during these first stages of reaction, the catalyst behavior is modified, and the production of HCAL is stopped. It has been reported that the presence of COL on the catalytic surface auto-enhanced the selectivity to COL [71, 35], the 3,4 addition to the C=C double bond becoming less significant as the conversion increased. In fact, Delbeq and Sautet [25, 65] also considered the adsorption of reaction products, unsaturated aldehydes and saturated alcohols, and found that adsorption of the unsaturated alcohol product occurs preferentially through a vertical atop geometry that competes with the adsorption of reactants, making an additional steric effect hindering its C=C bond and explaining the auto-selectivity enhancement. This hypothesis has been tested by deliberately adding COL to the CAL and observing that the initial selectivity to HCAL is greatly diminished [71] (Fig. 23).

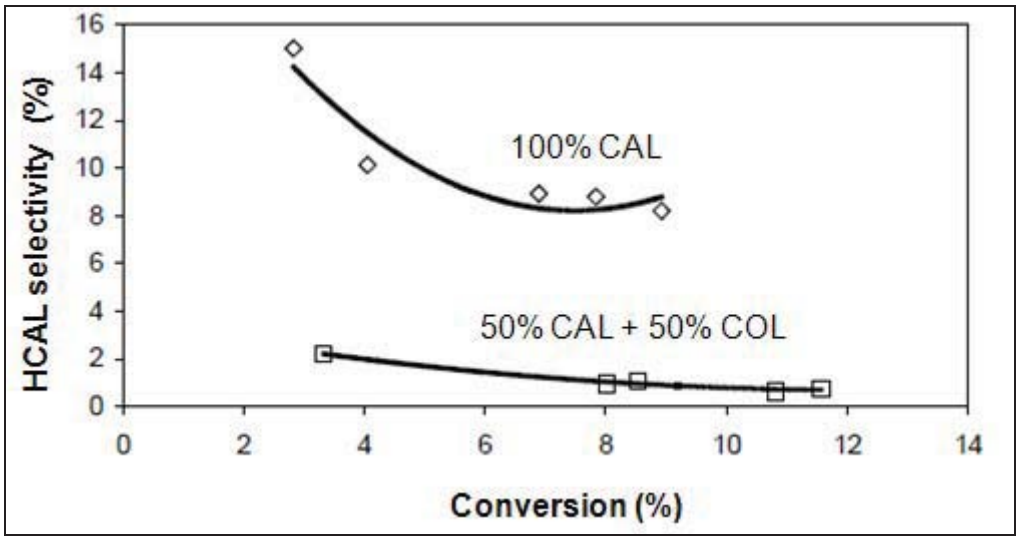

Figure 23: Selectivity towards HCAL as a function of COL concentration [71]

III-4-1-5-b-Hydrogenation of COL and HCAL

The scheme in Figure 1 indicates that HCOL can be produced by either the hydrogenation of HCAL or of COL. In order do define which mechanistic pathway of hydrogenation of CAL is the most favored at the initial stage by our catalyst, the separate hydrogenation of the two main products i.e cinnammyl alcohol and hydrocinnamaldehyde was studied. The results are grouped in Table 11.

Test	Catalyst	Substrate	Conversion (%)	TOF (min^{-1})	Selectivity (%)	
					HCOL	By-products
C37	MWCNT700	2 g COL	99.8	11	92	8
C38	MWCNT700	2 g HCAL	92.3	11	92	3
C39	MWCNT700	2 g HCAL + **2g COL**	75	13/**7**	86	14

$m_{catalyst}$ = 100 mg, P(H_2) = 20 bars, $T_{Catalysis}$ = 70 °C, t = 1 h, stirring = 900 rpm

Table 11: Hydrogenation of COL and HCAL

Both products i.e COL and HCAL could be hydrogenated to HCOL at 91 % of selectivity and same catalytic activity of 10 min^{-1}. Both COL and HCAL produces by-products but COL produces more than HCAL, the pathway to by products formation should have passed by the C=O bond hydrogenation. A more accurate test was to put a 50:50 mixture of COL and HCAL to be hydrogenated at the same time: the catalytic activity relative to COL was 7 min^{-1}, largely inferior to that of HCAL at 13 min^{-1}. So it is the HCAL who produces the majority of HCOL [71]. The C=O bond of HCAL is always favored over a C=C of HCOL even after C=C bond hydrogenation. The explanation could be associated with the role of Ru in activation of the carbonyl bond that will be detailed later in section III-4-4-7.

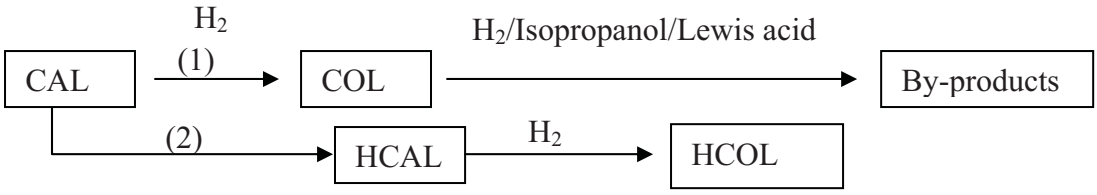

Figure 24: Favorable pathway for CAL transformation with the Pt-Ru/MWCNT700 catalyst

As seen previously the path (2) of Figure 24 is only limited to the early stage of the reaction and is quickly inhibited later, leading to selective production of COL via path (1). Since HCAL is only produced in very low amount at the beginning of the reaction, we can consider that in all the previous tests, the production of by-products is more associated to the carbonyl bond hydrogenation. The selectivity of our catalyst is once again verified.

III-4-1-6-Temperature of reaction

The reactivity of CAL hydrogenation was investigated between 25 and 100 °C (Table 12).

Test	Catalyst	$T_{Catalysis}$ (°C)	Conversion (%)	TOF (min^{-1})	Selectivity (%)			
					COL	HCOL	HCAL	By-products
C40	MWCNT700	25	8	6	80	5	15	0
C41	MWCNT700	50	21	15	76	5	19	13
C25	MWCNT700	70	31	22	81	4	15	18
C42	MWCNT700	100	57	41	81	4	15	36

$[CAL]_0 = 2.27$ Mol.L^{-1}, $m_{catalyst} = 100$ mg, $P(H_2) = 20$ bars, t = 1 h, stirring = 900 rpm

Table 12: Hydrogenation condition with variation of the reaction temperature

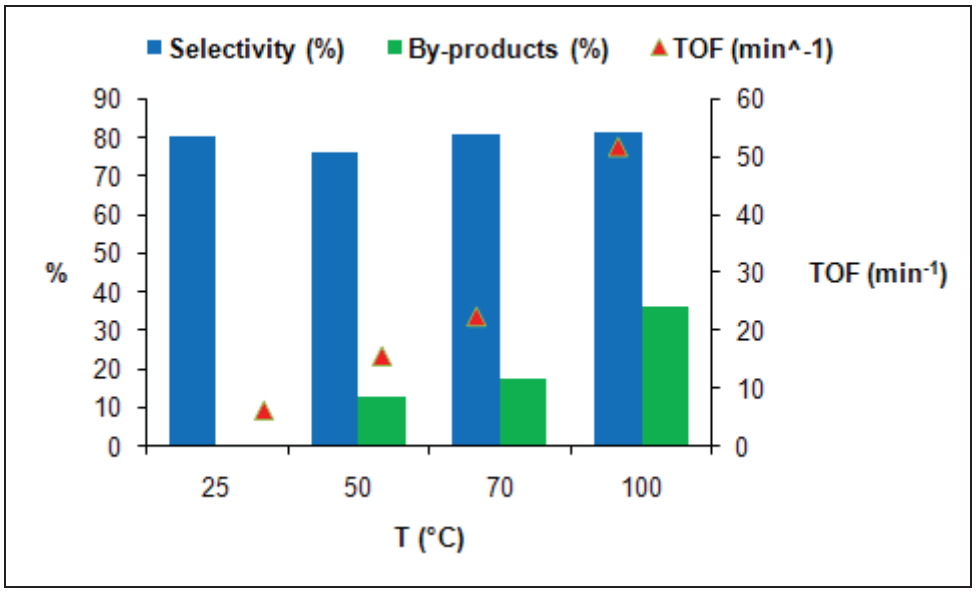

Figure 25: Catalytic performances of the Pt-Ru/MWCNT700 as a function of the reaction temperature

We found that our catalyst can hydrogenate selectively CAL to cinnamyl alcohol even at room temperature. Reaction temperature has a significant effect on the catalytic activity that increased linearly (Fig. 25). The CAL hydrogenation reaction showed conventional Arrhenius type behavior over the Pt-Ru/MWCNT700 catalyst (Fig. 26), giving an apparent activation energy of 25 kJ.Mol^{-1}.

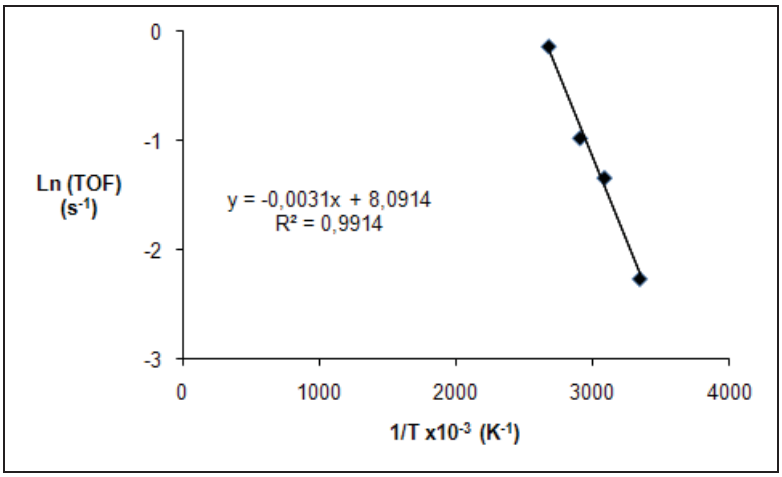

Figure 26: Ln (TOF) = f (1/T) for the Pt-Ru/MWCNT700 catalyst

There are no comparable studies of the effect of temperature on the hydrogenation of CAL over Pt-Ru bimetallic catalysts. Cobalt catalysts have been found to exhibit Arrhenius type behaviour for the hydrogenation of CAL with activation energies ranging from 18.0 kJ.mol^{-1} for a Co-B amorphous alloy catalyst to 35 kJ mol^{-1} for a Raney cobalt catalyst [72]. For the reaction of CO_2 hydrogenation to methanol on a Pd-ZnO supported on CNF-H, apparent activation energy (Ea) of 56.8 kJ mol^{-1} is reported [73]. For our catalyst with different transition metals and hydrogenating substrate, the E_a value was relatively low indicating that Pt-Ru/MWCNT provides a favorable kinetic pathway for CAL hydrogenation to COL.

A similar comparative study should be done in the future over the catalysts of Pt-Ru with the other carbonaceous and metal oxide supports to depict the role of the support in the decrease of the activation energy.

Selectivity to COL was independent from the hydrogenation temperature and remained around 80 %. On the other hand, at room temperature there was no by-product formation and their concentration increased with temperature.

III-4-1-7-Influence of the aromatic ring of CAL: hydrogenation of crotonaldehyde

The structure of the α,β-unsaturated aldehydes may play a role in the selectivity towards the unsaturated alcohol. Steric hindrance around the C=C bond enables a selective hydrogenation of the carbonyl group, whereas the absence of large substituent on the same bond directs the reaction towards the formation of the saturated aldehyde [74, 75].

To see if there was a certain role played by the aromatic ring of cinnamaldehyde, in selectivity determination by imposing any steric effect, we hydrogenated the crotonaldehyde molecule using 100 mg of the MWCNT700 supported Pt-Ru catalyst with an initial concentration of crotonaldehyde of 0.38 $Mol.L^{-1}$; H_2 pressure of 20 bar; temperature of catalysis at 70 °C and stirring velocity at 900 rpm.

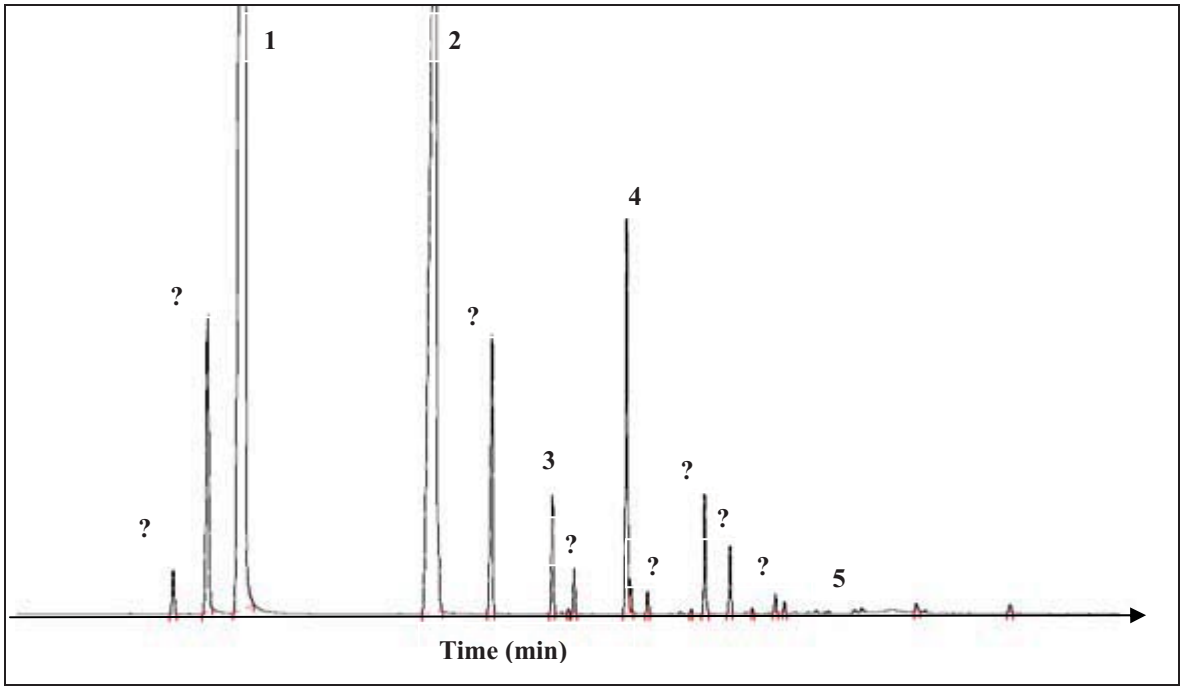

1) Propan-2-ol, 2) crotonaldehyde, 3) butanol, 4) crotyl alcohol, 5) Butyraldehyde, ?) By-products

Figure 27: Chromatogram of the hydrogenation products of Crotonaldehyde

As seen in Figure 27 the selectivity towards the unsaturated alcohol (peak 4) was evident in peak 4 when compared to peaks 3 of butanol and nearly non existing peak 5 of butyraldehyde. The selectivity towards the unsaturated alcohol is not

directly linked to the structure of the substrate since with the benzene cycle or a methyl substituent, the C=O bond was predominantly hydrogenated. There was also a production of large number of by-products that were identified by gas chromatography coupled to a mass spectrometer (Fig. 28). They were, as in the case of cinnamaldehyde, mainly cyclic and condensation products with isopropanol.

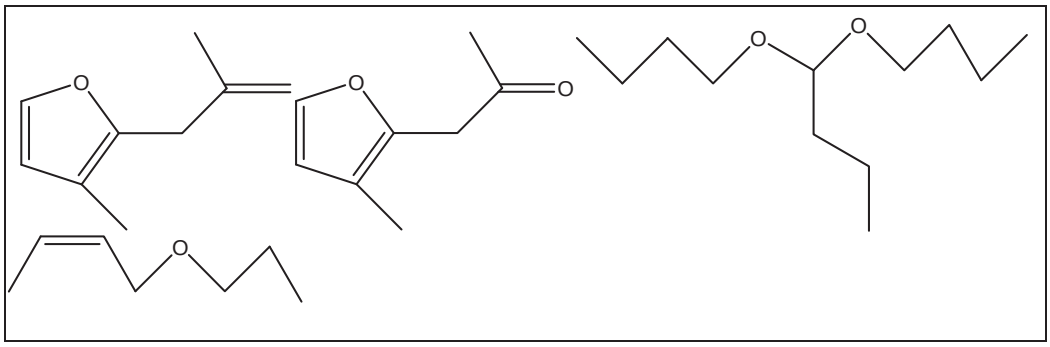

Figure 28: Main by-products formed during the hydrogenation of crotonaldehyde

III-4-1-8-Conclusions on the parametric study

Based on the theoretical calculations carried out by Delbecq and Sautet and our experimental observations, a hypothesis for the mechanism of selective hydrogenation of cinnamaldehyde can be proposed.

The catalytic performances of both Pt-Ru/MWCNT350 and Pt-Ru/MWCNT 700 catalysts towards cinnamyl alcohol were dependent on the association between their surface characteristic and hydrogenation conditions. The cinnamaldehyde can adsorb onto the surface via two competitive mechanisms. One is a planar geometry through the C=C double bond and the other through a vertical C=O atop geometry (Fig. 16).

Mainly high CAL concentrations allow the atop vertical arrangement that increase selectivity towards COL. Higher concentrations of CAL were needed with the MWCNT700 catalyst to obtain the maximum catalytic activity due to higher adsorption capability and CAL surface diffusion on this latter support. Increasing the CAL concentration, lowering the hydrogenation temperature and amount of catalyst used, decreased the by-products formation. For an optimum catalytic activity, H_2 should be able to enrich the surface of the catalyst with ad-hydrogen atoms, working as hydrogen source.

The competitive adsorption between H_2 and CAL should be mastered. Both molecules should adsorb on the catalytic surface to react, a Langmuir-Hinshelwood kinetic model is propose for this reaction [2, 21, 71].

The selectivity of the reaction towards COL is initially low and increases with conversion of CAL. HCAL and HCOL are almost exclusively formed during the early stages of the reaction. The production of COL as the reaction proceeds inhibits the further production of HCAL. This can be explained by means of a steric ligand effect, whereby the unsaturated alcohol adsorbs preferentially through a vertical atop geometry that competes with the adsorption of CAL. With increasing surface coverage of COL, the CAL becomes more constrained to adsorb through a vertical C=O geometry, thus preventing the hydrogenation of the more thermodynamically favored C=C bond.

Selectivity of the Pt-Ru/MWCNT700 catalyst was independent from the alkyl substituent (CH_3-, C_6H_5- …) and the reaction temperature. Arrhenius plot behavior was found in the range of temperatures studied, with an apparent activation energy of 25 $kJ.mol^{-1}$.

All the previous observations contribute to selectivity enhancement, but since the variation is relatively important, from 55 to 80% when activated at 700 °C in comparison to the parametric 10 % enhancement relative to the CAL concentration or hydrogen pressure, other phenomenon should be taken into account to explain the selectivity increase. Selectivity depends mainly on the catalyst itself. Thus, a more focused study on the state of the catalytic nanoparticles as a function of activation temperature was mandatory.

III-4-2-Characterization of the catalysts

In the next sections we will characterize the nanoparticles by HREM, EDX, EXAFS and WAXS as a function of the activation temperature. Additionally, the mobility of Pt and Ru atoms on the surface of MWCNTs will be studied by DFT calculations.

III-4-2-1-General characteristics

The characteristics of the catalysts as a function of the activation temperature are assembled in Table 13.

support	Pt (%)	Ru (%)	Fe (%)	Al (ppm)	$d_{average}$ (nm)	BET (m^2/g)	V_{pore} (cm^3/g)	d_{pore} (nm)
MWCNT350	1.84	2.12	0.13	<100	2.7	224	1.61	29.23
MWCNT700	1.77	2.22	0.46	310	2.9	246	2.38	39.33
MWCNT850	2.88	3.14	0.68	640	6.1	-	-	-
MWCNT1000	2.48	2.91	0.20	160	12.9	-	-	-

Table 13: Pt-Ru/MWCNT catalysts as a function of $T_{activation}$

The metal loading varied significantly as a function of the temperature of activation indicating a lost of carbon during the heat treatment possibly due to traces of O_2 in Ar or N_2. This was not problematic since activity is presented in TOF in which it is normalized towards the metal loadings. Iron and alumina contaminations were also variable. Alumina remained at the ppm scale but iron from MWCNT synthesis reached 0.68 %. Such iron is trapped inside the carbon nanotubes and should not be active. The specific surface area measured by the BET method and the pore volume increase when the catalyst is activated at 700 °C. All of this is in favor of the increase of the catalytic activity from 350 °C to the 700 °C activated catalyst. The nanoparticles size also increases particularly at 850 and 1000 °C.

III-4-2-2-Temperature programmed desorption (TPD)

Temperature programmed desorption was performed on the nitric acid treated multi-walled carbon nanotubes (Fig. 29).

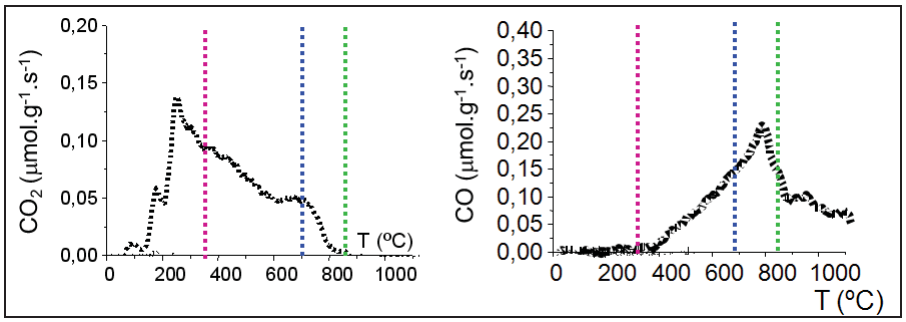

Figure 29: Temperature programmed desorption study on the nitric acid treated MWCNT

TPD showed a lost of the surface functions as a function of temperature, starting from the carboxylic groups in the form of CO_2 and CO, and that this lost is almost total at 800 °C [39].

III-4-2-3-HREM and EDX

HREM and EDX analysis were performed in collaboration with Dr Andrea Falqui from the Instituto Italiano di Technologia in Genova, Italy. As seen in the HREM micrographs of Figure 30 there is only very little change in the particle size between the catalysts activated at 350 °C and 700 °C.

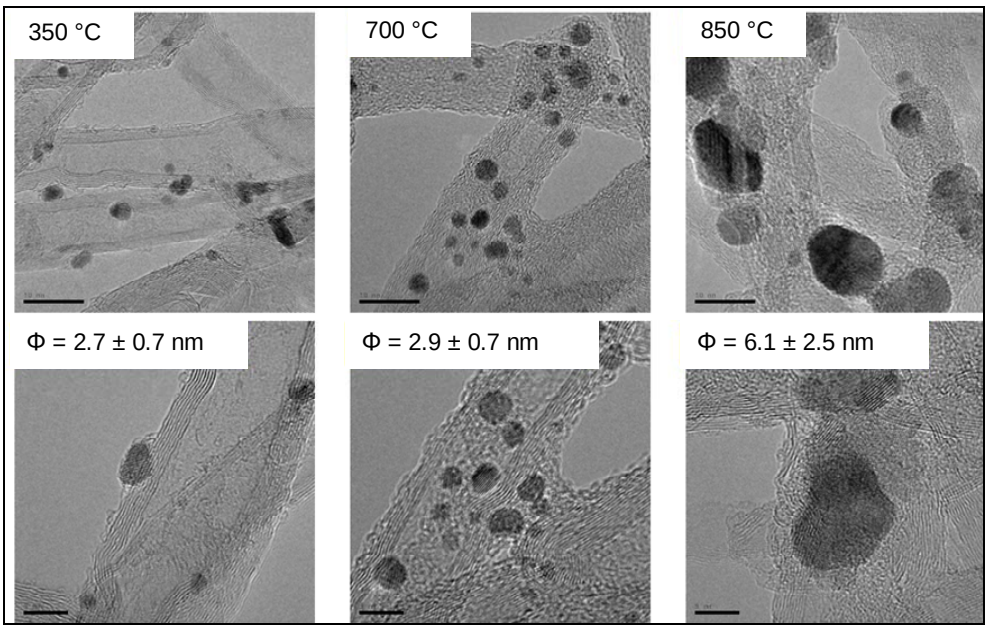

Figure 30: HREM micrographs of different catalysts activated at different temperatures

So, the increase in selectivity from 55 to 80 % could not be linked to the size modification of the nanoparticles but rather to a structural change (Fig. 31). On the other side, the particle size doubles to reach 6 nm for the activated catalyst at 850 °C and is 12 nm at 1000 °C (Fig. 30, 31). This size increase could be associated to the lost of the carboxylic anchoring sites as previously observed by TPD analysis, resulting to sintering of the nanoparticles, and once again confirms their role in the achievements of particle size control and their good dispersion on the surface of the MWCNTs.

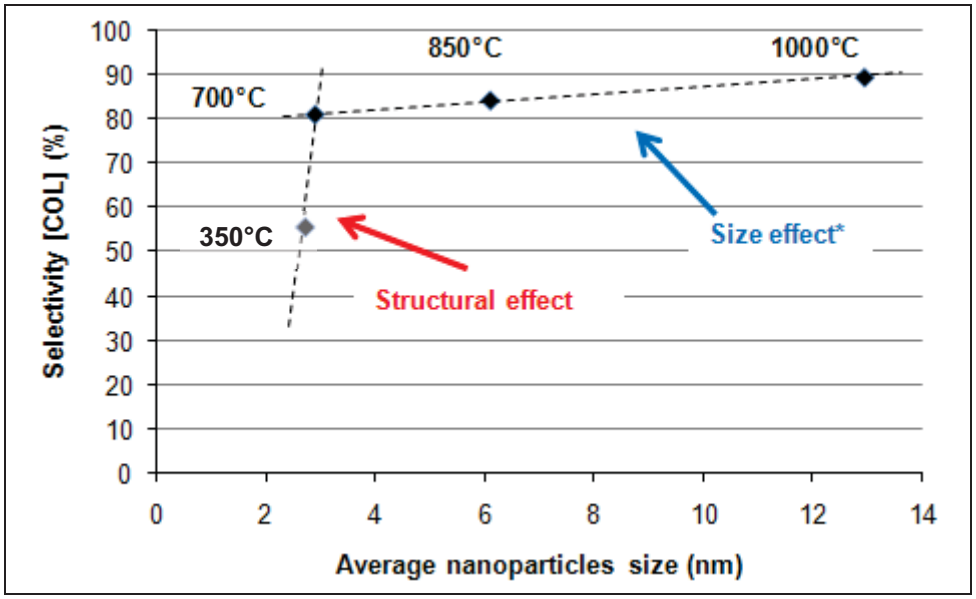

Figure 31: Selectivity evolution as a function of particle size

Starting from the catalyst activated at 700 °C the selectivity improvements may be also associated to the increase of the nanoparticles size (Fig. 9). The next study will focus on the nanoparticles themselves to study the structural changes induced by the heat treatment.

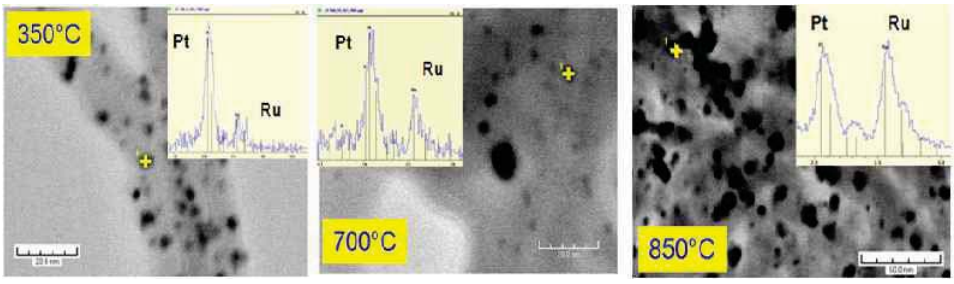

Figure 32: HREM micrograph and correspondant EDX analyses on some nanoparticles at different activatiozn temperatures

X ray microanalysis on the nanoparticles revealed that all the nanoparticles are bimetallic, since we always observed two characteristic peaks of the Ru and Pt elements (Fig. 32). As we increased the temperature of activation the Ru peak becomes more intense (see inset).

The quantification of each metal was done using the Cliff-Lorimer method. The atomic percents of each element C_A and C_B can be related to the measured intensities by the so called Cliff-Lorimer equation (Eq. 4).

$$\frac{C_A}{C_B} = k_{AB}\frac{I_A}{I_B} \qquad \text{Eq. 4}$$

where A is Pt and B is Ru. I_A and I_B are the heights of the corresponding Gaussians for the L_A peaks used in the fit. The background was approximated with an exponential function. k_{AB} is the calculated Cliff-Lorimer factor (=1.254 at 200 kV). For each sample, a sum of all the single particle's spectra was calculated to get a total spectrum (it approximates an average if the particles have similar sizes). The corresponding data are reported in Figure 33 and Table 14.

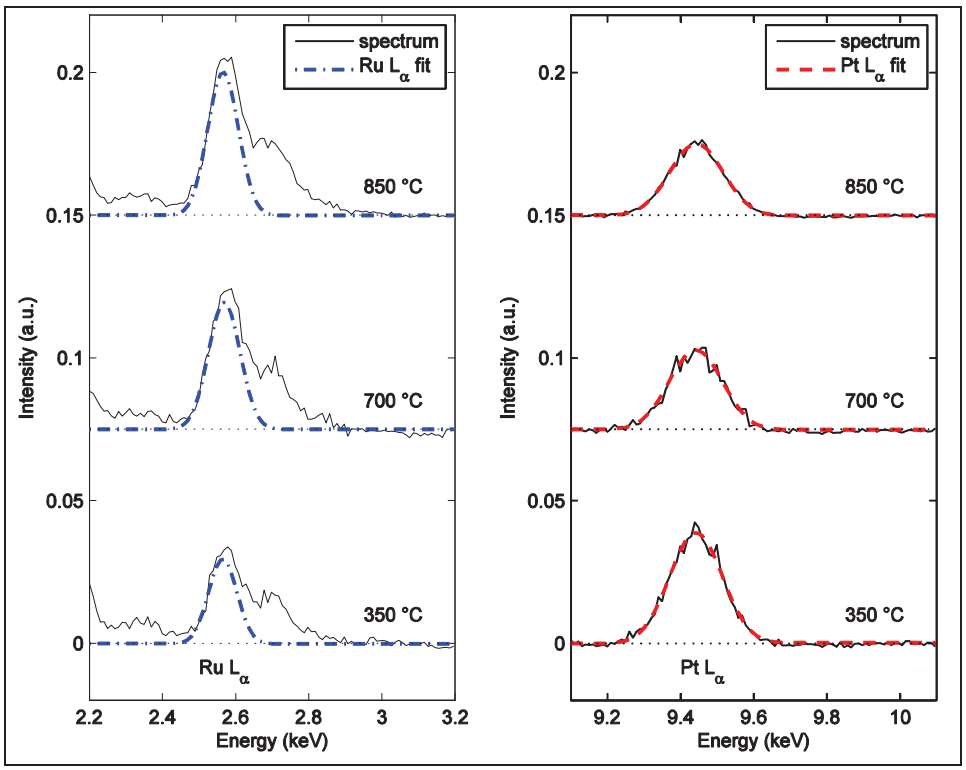

Figure 33: (Color online) Comparison of the resulting fits of the EDX spectra at different temperatures. (Full lines) the experimental spectra after background subtraction. (Blue dash dot lines) Resulting curves for Ru L_α peak. (Red dash lines) Resulting curves for Pt L_α peak. The spectra are normalized to the sum of counts under Ru and Pt L_α peaks.

T	Pt at. %	Ru at. %
350 °C	62 (±3)	38 (±2)
700 °C	44 (±2)	56 (±2)
850 °C	39 (±1)	61 (±1)

Table 14: Ru and Pt concentration as a function of temperature obtained from the fits of the EDX spectra. Such a trend is summarized in Figure 34.

There is a clear trend in Pt/Ru ratio variation with increasing the temperature of activation: Pt decreases and Ru increases in the nanoparticles (Fig. 34).

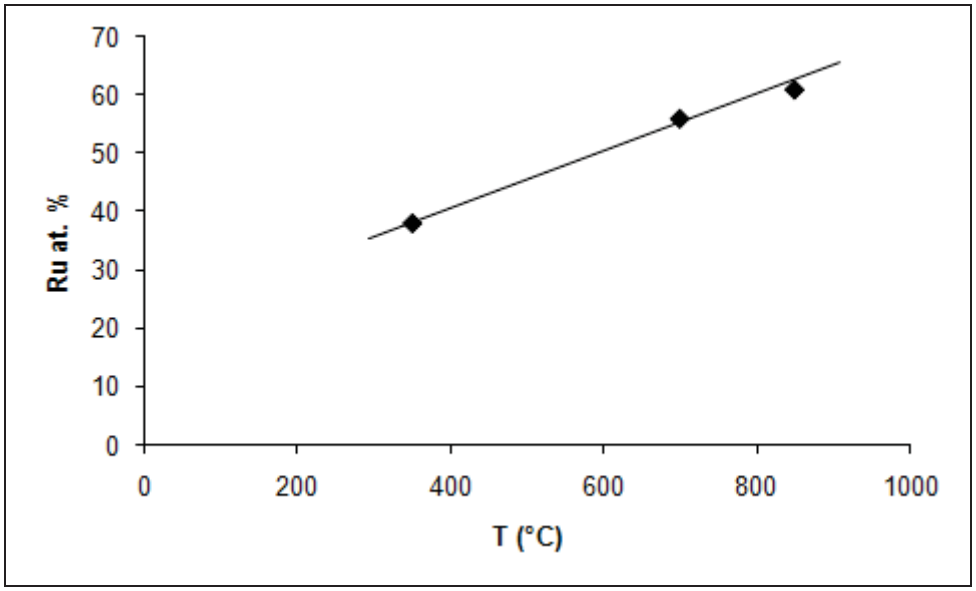

Figure 34: Ruthenium atomic concentration as a function of temperature obtained from the fits of the EDX spectra

The High Resolution Transmission Electron Microscopy (HREM) analysis of the 350 °C catalyst shows the coexistence of two separate crystalline phases (Fig. 36). The first one has a face centered cubic (fcc) structure while the second one has a hexagonal close packed (hcp) structure. Two distinct particles are here clearly visible, named (a) and (b), both oriented to show a structural projection. The insets show the numerical diffractogram of the two particles, obtained on the base of the two dimensional fast Fourier transform (2D-FFT) calculated over the square zones reported in the HRTEM image.

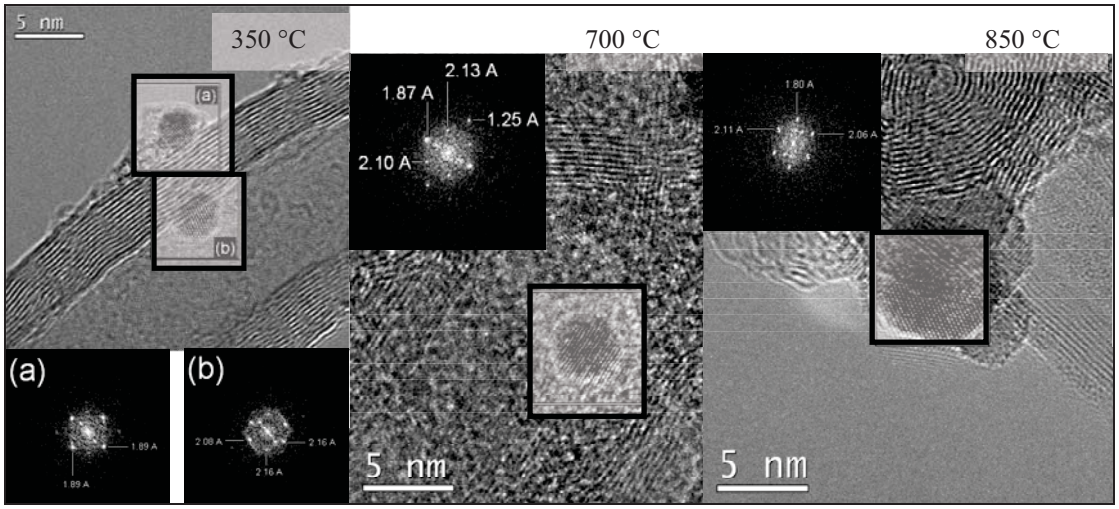

Figure 35: HREM images of nanoparticles of MWCNT350, MWCNT700 and MWCNT850 catalyst and corresponding diffraction patterns

The particle named (a) shows a structural projection that can be ascribed to a fcc lattice oriented along its [001] zone axis. The interplanar distances that are measured for the two perpendicular sets of lattice planes are both equal to 1.89 Å. The most probable explanation is that these distances were originally those corresponding to two (200) mutually perpendicular lattice sets of pure platinum, that should measure 1.96 Å. The measured distance indicates then a compressive strain (i. e., a contraction of the original lattice) of the platinum fcc structure, where a certain number of Ru atoms has been diffused in the Pt lattice. The cubic lattice observed appears thus contracted of -3.7 % with respect to that of the pure bulk platinum.

The particle named (b) shows a different structure. It seems not too far from that expected for an hcp lattice oriented along its [100] zone axis, with some differences in the interplanar distances with respect to those of the pure hcp Ru. More specifically, if one compares the structure measured with that of the hcp ruthenium it is possible to observe that:

a) All the interplanar distances are higher than those expected for the pure ruthenium, indicating a tensile strain of the original pure Ru lattice.
b) The tensile strain (i.e., a dilatation of the original lattice) is not the same for the different crystalline axis. In fact, the original Ru (002) distance of 2.14 Å has suffered a very low increase to 2.16 Å. On the contrary, the two other pairs of spots in the numerical diffractogram, corresponding to two d-equivalent (101) lattice sets (d=2.06 Å for the pure ruthenium), suffered a quite different increase in their own directions: 2.08 Å (+1 % with respect to pure ruthenium) for that are counterclockwise with respect to the (002) spots, and 2.16 Å (+4.8 %) for the one that appears clockwise.

Besides, the angles around the (002) direction are almost equal to those expected for and hcp structure in its [100] zone axis, being the small differences observed comprised in the intrinsic angular error due to a measure on a numerical diffractogram calculated by a small area in the HREM image. The basic hcp character seems then retained, but a lattice tensile strain is present. This could be probably ascribed to the fact that a certain number of Pt atoms have been diffused in the Ru lattice.

Finally, the HREM analysis has low statistically informative value and it was noted that in the 350 °C catalyst, the smaller particles have the tendency to retain the fcc structure while the bigger ones tend to maintain a hcp structure.

The HREM analysis of the 700 °C catalyst mainly shows crystalline particles with structure similar to that reported for the 350 °C (Fig. 35). Its diffractogram in the inset shows a structure that most likely can be ascribed to a fcc lattice oriented along its [011] zone axis. The interplanar distances that are measured for the four sets of lattice planes are respectively equal to 2.10 Å, 1.87 Å, 2.13 Å, 1.25 Å, and the angular distances between them are those expected for a fcc lattice in its [011] zone axis. These should then correspond to the (11-1), (200), (1-11) and (0-22) lattice sets, respectively. If one compares these d-values with those expected for the pure platinum fcc structure (d(111)=2.26 Å, d(200)=1.96 Å and d(022)=1.39 Å) it's interesting to note that again a compressive strain of the lattice is observed. However, in such a case, this contraction is much more pronounced than in the case of the 350 °C catalyst, and it has not the same value for the different fcc lattice planes. In fact, it is maximized along the (0-22) axis (-9.1% with respect to the corresponding axis of the pure platinum) and minimized along the (200) one (-4.8 %), perpendicular to the (0-22). Besides, a contraction is observed along the (11-1) and (1-11) axis, around -7 % in average, but not having exactly the same value for both. Even in this case the phenomenon is probably due to the diffusion of a certain number of Ru atoms in the Pt original lattice, but here it was more marked than in the 350 °C catalyst.

The HRTEM analysis of the 850 °C catalyst again shows a crystalline configuration similar to that reported for the 350 and 700 °C catalysts (Fig. 35). Its inset shows the numerical diffractogram of the particle. It shows a structure that most likely can be again ascribed to a fcc lattice oriented along its [011] zone axis. The interplanar distances that are measured for the three sets of lattice planes are respectively equal to 2.11 Å, 1.80 Å., and 2.06 Å, and the angular distances between them are those expected for a fcc lattice in its [011] zone axis. These should then correspond to the (11-1), (200), and (1-11) lattice sets, respectively. If one compares these d-values with those expected for the pure platinum fcc structure (d(111)=2.26 Å, d(200)=1.96 Å and d(022)=1.39 Å) again a compressive strain of the lattice is

observed. However, in such a case, this contraction further evolved with respect to the 700 °C catalyst. Here, the compressive strain is -8.8% with respect to the corresponding axis of the pure platinum along the (200) axis. Besides, a contraction is observed even along the (11-1) and (1-11) axis, -8.3% in average, but not having exactly the same value for both. Even in this case the phenomenon is probably due to the diffusion of a certain number of Ru atoms in the Pt original lattice.

As a conclusion on the consideration of the HREM analysis of the 350, 700 and 850 °C catalysts:
a) only the 350 °C catalyst seems to show the Ru in its hcp structure with distortions (compressive strain) probably due to the presence of Pt in its lattice; the majority of the particles retain a fcc structure that seems due to a compressive strain of the original one of Pt; in such a case this strain of the lattice is measured isotropic and of around -4% with respect to the pure Pt lattice.

b) in the 700 °C catalyst the Ru hcp structure seems to disappear and the particles show again a fcc structure with non isotropic compressive strain, around -9% along the (022) direction and -5% along the (200) one.

c) the 850 °C catalyst shows a situation further evolved with respect to the 700 °C catalyst: fcc lattice with non isotropic compressive strain of around -9% along the (200) lattice and of -8% in average on the two (111) axis.

The final consideration is that the particles mainly tend to retain the original fcc structure of the platinum, with a compressive strain that increases with the treatment temperature, that is with the amount of Ru atoms in the lattice confirming the EDS results.

III-4-2-4-Extended X-Ray Absorption Fine Structure (EXAFS)

The EXAFS analyses were performed in collaboration with Pr Anna Corrias from Triest, Italy.

III-4-2-4-a-Introduction to EXAFS

EXAFS is the oscillating part of the X-ray absorption spectrum (XAS) of atoms of a sample that extends to about 1000 eV above an absorption edge of a

particular element (Fig. 36). Electrons are knocked out of an atom when the energy value of incident X-rays, generated by a synchrotron surpasses the ionization threshold (the edge energy). The emitted photoelectrons, having both particle and wave character, are scattered back from neighboring atoms in a lattice.

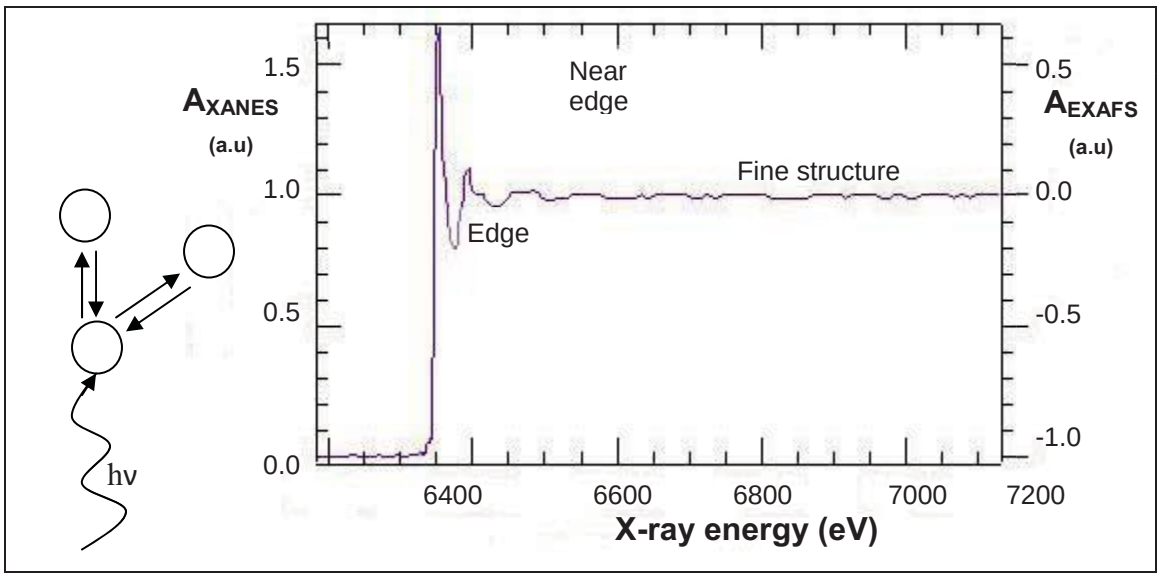

Figure 36: Principle of EXAFS and model spectrum

Interference phenomenon takes place between the outgoing and backscattering electron. Depending on the wavelength of the electron, the distance between emitting and scattering atom as well as the shift in phase caused by the scattering effect the two waves enhance or destroy each other giving rise to maxima and minima. As a result the X-ray absorption spectrum exhibits fine structure above the absorption edge (Fig. 36). This fine structure gives detailed local structure information on the distance, number and type of neighbors of the absorbing atom [76, 77]. The intensity of the wiggles goes up if the number of neighbors is increased; the number of oscillations depends inversely on the interatomic distance and the step height of the edge is proportional to the concentration of atoms in the sample. The EXAFS function is presented in Eq. 5.

$$\chi(k)=\Sigma_j A_j(k) \sin(2 k r_j + \phi_j(k)) \qquad \text{Eq. 5}$$

k is the wave number of the photoelectron

$\chi(k)$ is the EXAFS function

j_j is the label of the coordination shells around the electron-emitting atom

$A_j(k)$ is the amplitude, the scattering intensity due to the j^{th} coordination shell

r_j is the distance between the central atom and atoms in the j^{th} shell

$\phi_j(k)$ is the total phase shift, equal to the phase shift of the backscattering atom plus twice that of the absorbing atom

When the X-Ray energy range is limited to few hundred eV above the edge the technique is called XANES.

The EXAFS function becomes more understandable if we look at its Fourier transform, which resembles a radial distribution function.

III-4-2-4-b-EXAFS observation

The EXAFS interference functions $k^3\chi(k)$ at the Ru K-edge and Pt LIII-edge of the 350 °C and 700 °C activated catalysts and their corresponding Fourier Transforms along with the reference samples are shown in Figure 37 and 38.

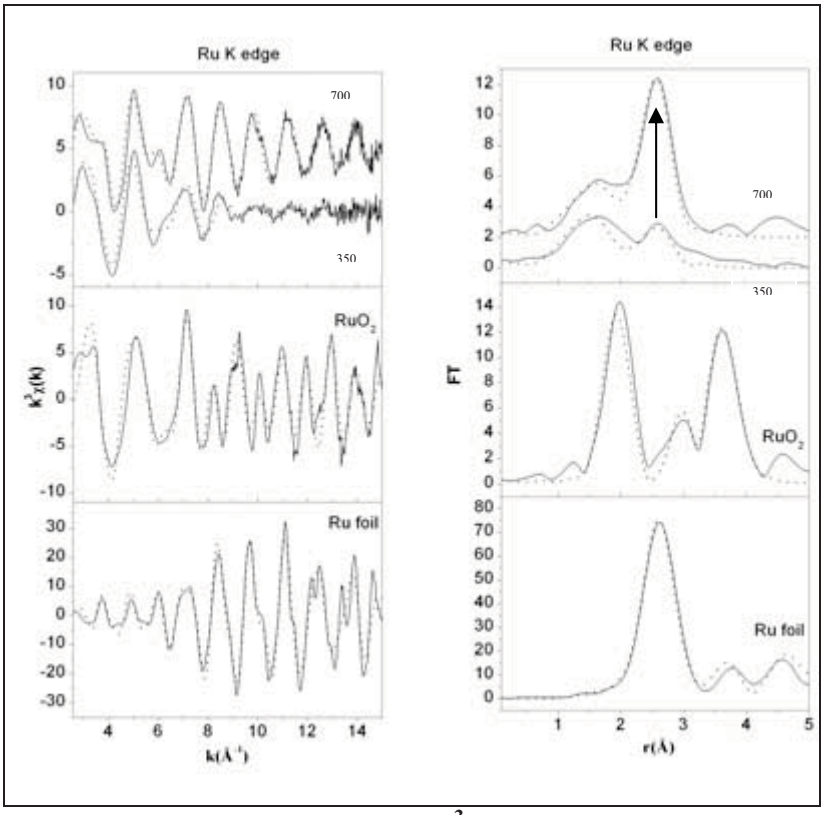

Figure 37*:* EXAFS interference functions $k^3\chi(k)$ (Left)) at the Ru K-edge and its corresponding FT (right) of the 350 and 700 °C catalysts and some reference samples

At the Ru K-edge (Fig. 37) the EXAFS interference functions $k^3\chi(k)$ of the 350 °C and 700 °C catalysts show significant differences. In particular $k^3\chi(k)$ of the 350 °C is significantly noisier compared to the 700 °C, due to much weaker oscillations, indicating a much more disordered and/or less symmetric structure. The differences are also evident in the corresponding Fourier transforms (FTs); in particular, the comparison with the FTs of the reference compounds clearly indicates that the peak around 2.5-3 Å, which is due to Ru bonded either to Ru or Pt, is increasing significantly. In both samples evidence of a contribution of Ru bonded to a light element (O or C) at about 2 Å is also observed. No peak beyond 3 Å is evident.

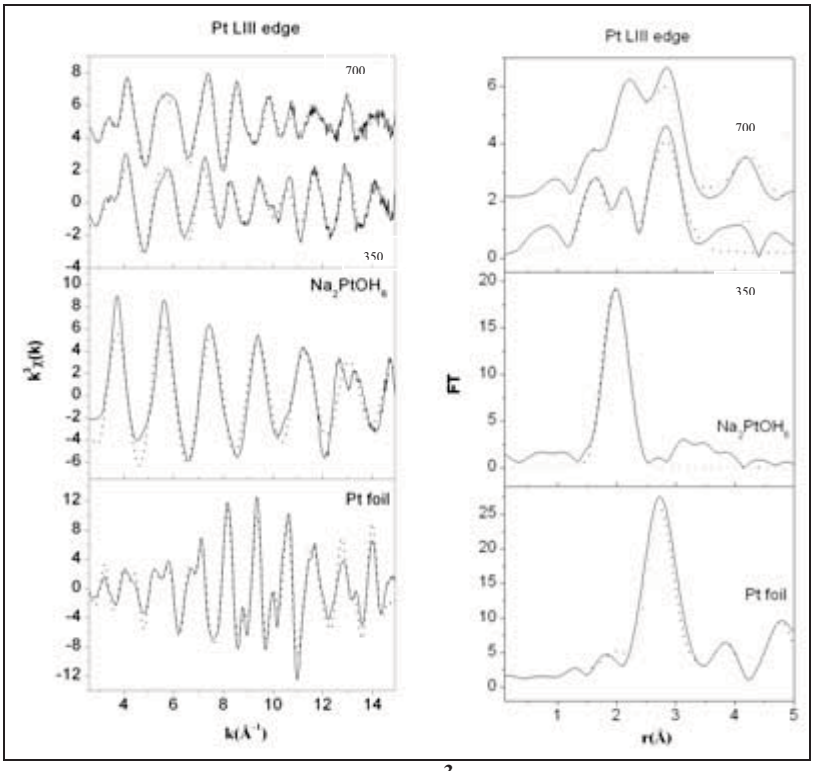

Figure 38: EXAFS interference functions $k^3\chi(k)$ (left)) at the Pt LIII-edge and its corresponding FT considering Pt-O (right) of the 350 and 700 °C catalysts and some reference samples

At the Pt L_{III}-edge (Fig. 38) the EXAFS interference functions $k^3\chi(k)$ of the 350 and 700 °C catalysts are much more similar, showing oscillations with similar amplitudes. The comparison of the FTs indicates also in this case a contribution from Pt bonded to a light element (O or C) and a contribution from Pt bonded to a heavy element (Ru or Pt). In the 700 °C catalyst a peak beyond 3 Å is also evident.

III-4-2-4-c-EXAFS data fitting

The qualitative analysis of the EXAFS interference functions and corresponding FTs indicates that fitting will require at least one shell involving a light element and one involving a heavy element. Due to the stronger backscattering of heavy elements it is more difficult to distinguish between O or C neighbours than to distinguish between Ru or Pt neighbours. Even if some contributions from Ru-C interactions cannot be ruled out, the fitting of the two samples at the Ru edge was performed considering only O in the first shell, since Ru is easily oxidized and in fact XANES data (Fig. 39) indicate that Ru is partly oxidized in both samples and that the 350 °C catalyst is more oxidized than the 700 °C.

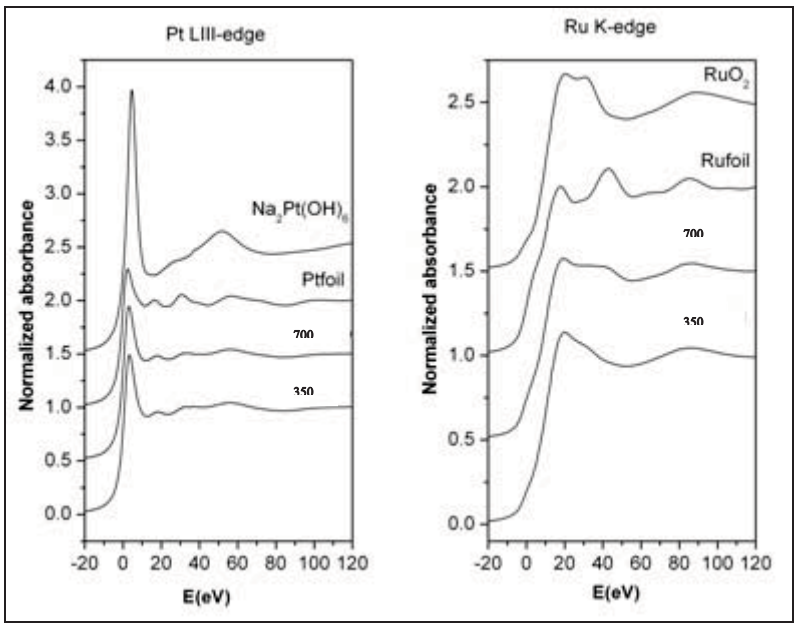

Figure 39: Comparison of the XANES spectra of the 350 °C and 700 °C catalysts with the reference samples

At the Pt L_{III} edge the presence of Pt-O interactions is more questionable and in fact XANES data indicate very little oxidation in both samples, with the 350 °C catalyst slightly more oxidized than the 700 °C. In this case the fitting of the first shell was done considering either only Pt-O interactions or only Pt-C interactions, obtaining quite similar results (Table 15).

The ab-initio phase shifts and amplitudes calculated in DL_EXCURV were first used to fit the data of the standards. A good fit was obtained for all standards (shown in Figures 37 and 38, and parameters reported in the Tables 15 and 16), considering only single scattering contributions for RuO_2 and Na_2PtOH_6 while also

multiple scattering was taken into account for Pt and Ru, were some multiple scattering path are expected to be strong due to a forward-scattering (also called the focusing or shadowing effect) consisting of collinear arrangements of neighboring atoms. Coordination numbers were kept fixed to the values of the known crystal structures, while distances and Debye-Waller factors were fitted, together with EF which is a correction to the beginning of the absorption edge, E_o. In the fitting of the samples also coordination numbers were free to vary.

Pt foil Pt LIII edge				Na_2PtOH_6 Pt LIII edge			
	R(Å)	N	$2\sigma^2$		R(Å)	N	$2\sigma^2$
Pt-Pt	2.77(1)	12	0.016(1)	Pt-O	2.01(1)	6	0.005(1)
Pt-Pt	3.91(1)	6	0.016(1)	**R=33**	EF = -13.2(4)		
Pt-Pt	4.81(1)	24	0.018(1)				
Pt-Pt	5.56(1)	12	0.019(1)				
R=33	EF = -12.8(3)						
350 °C Pt LIII edge				350 °C Pt LIII edge			
	R(Å)	N	$2\sigma^2$		R(Å)	N	$2\sigma^2$
Pt-O	2.00(1)	1.4(1)	0.015(2)	Pt-C	2.06(1)	1.8(2)	0.013(2)
Pt-Ru	2.69(1)	1.2(3)	0.018(2)	Pt-Ru	2.68(1)	1.2(2)	0.017(2)
Pt-Pt	2.74(1)	4.3(3)	0.018(1)	Pt-Pt	2.73(1)	4.6(3)	0.018(1)
R=32	EF = -11.0(3)			**R=33**	EF = -9.6(3)		
700 °C Pt LIII edge				700 °C Pt LIII edge			
	R(Å)	N	$2\sigma^2$		R(Å)	N	$2\sigma^2$
Pt-O	2.00(1)	1.2(1)	0.024(4)	Pt-C	2.06(1)	1.5(2)	0.019(3)
Pt-Ru	2.69(1)	1.8(2)	0.016(1)	Pt-Ru	2.68(1)	1.5(2)	0.015(1)
Pt-Pt	2.70(1)	4.3(3)	0.019(1)	Pt-Pt	2.69(1)	4.6(3)	0.020(1)
Pt-Ru	4.33(1)	2.1(1)	0.019(3)	Pt-Ru	4.33(1)	2.1(5)	0.019(3)
R=29	EF = -9.8(3)			**R=30**	EF = -8.9(3)		

Table 15: Parameters of the data fit of the standards and the catalysts at the Pt LIII edge

Best fit of the 350 °C catalyst at the Ru K-edge (shown in Figure 37, best fit parameters reported in Table 16) was performed with one Ru-O shell and one Ru-Ru

shell. The fit does not improve adding another shell Ru-Pt, making the use of a larger number of free parameters meaningless. The R-factor is high, due to very noisy data.

A good fit of the same sample at the Pt L_{III} edge was obtained with a first shell of either Pt-O (fit shown in Figure 38, best fit parameters reported in Table 15) or Pt-C (fit shown in Figure 40, best fit parameters reported in Table 15), as already discussed, and a second shell involving both Ru-Ru and Ru-Pt interactions. Both heavy atoms had to be introduced in order to get a good fit, suggesting the formation of an alloy.

Ru Foil Ru K-edge				RuO_2 Ru K-edge			
	R(Å)	N	$2\sigma^2$		R(Å)	N	$2\sigma^2$
Ru-Ru	2.67(1)	12	0.011(1)	Ru-O	1.97(1)	6	0.015(1)
Ru-Ru	3.78(1)	6	0.011(1)	Ru-Ru	3.07(1)	2	0.011(1)
Ru-Ru	4.27(1)	2	0.014(2)	Ru-O	3.42(3)	4	0.018(3)
Ru-Ru	4.67(1)	18	0.014(1)	Ru-Ru	3.54(1)	8	0.014(1)
Ru-Ru	5.33(1)	12	0.015(1)	Ru-O	3.85(2)	12	0.020(2)
R=33	EF = -5.6(3)			**R=35**	EF =0.28(4)		
350 °C Ru K-edge				700 °C Ru K-edge			
	R(Å)	N	$2\sigma^2$		R(Å)	N	$2\sigma^2$
Ru-O	2.00(1)	4.3(3)	0.033(3)	Ru-O	1.97(2)	2.5(2)	0.025(3)
Ru-Ru	2.65(1)	3.0(7)	0.036(5)	Ru-Ru	2.65(1)	3.5(3)	0.017(1)
R=45	EF = 3.6(3)			Ru-Pt	2.67(1)	1.5(6)	0.018(4)
				R=29	EF = 1.2(3)		

Table 16: Parameters of the data fit of the standards and the catalysts at the Ru K-edge

Best fit of the 700 °C catalyst at the Ru K-edge (shown in Figure 37, best fit parameters reported in Table 16) was performed with one Ru-O shell and one shell with both Ru-Ru and Ru-Pt. In this case the presence of additional Ru-Pt interactions improved the fit significantly enough to justify the use of additional free parameters.

The best fit of the 700 °C catalyst at the Pt L_{III} edge, similarly to the 350 °C catalyst, was obtained with a first shell of either Pt-O (fit shown in Figure 38, best fit parameters reported in Table 15) or Pt-C (fit shown in Figure 40, best fit parameters

reported in Table 15), a second shell involving both Ru-Ru and Ru-Pt interactions and an additional shell involving Pt-Ru. Since also in this case there is clear evidence of the formation of an alloy, this shell at longer distances should include both Ru-Ru and Ru-Pt interactions. However, only one contribution was considered in order to limit the number of free parameters.

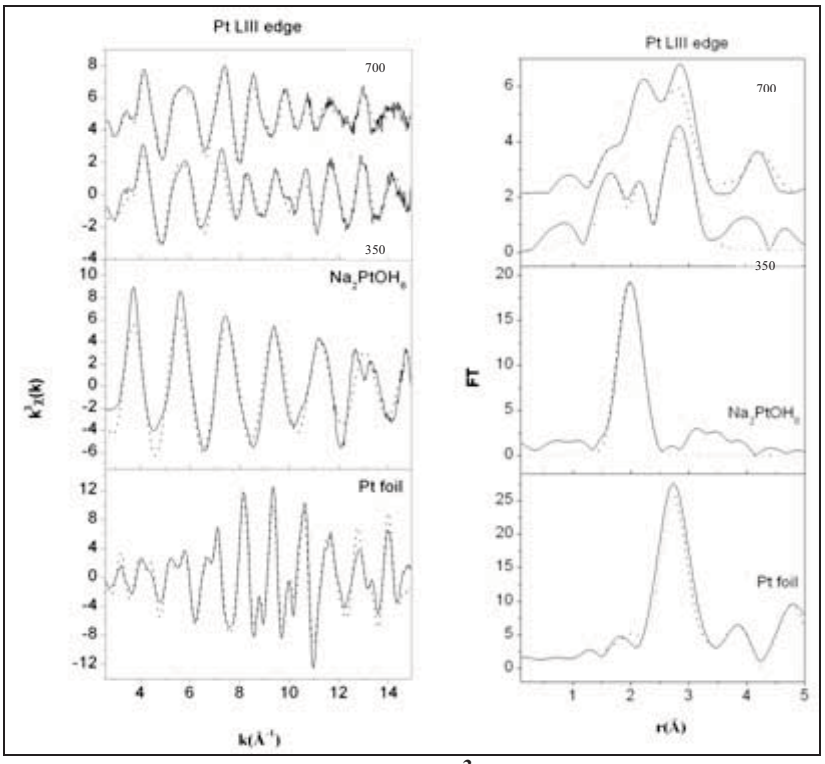

Figure 40: EXAFS interference functions $k^3\chi(k)$ (Left)) at the Pt LIII-edge and its corresponding FT considering Pt-C (right) of the 350 and 700 °C catalysts and some reference samples

The results of the fitting clearly indicate the structural evolution of the Ru with thermal treatment temperature, since the differences between the 350 and 700 °C catalysts at the Ru K-edge are much more evident than those at the Pt L_{III} edge. The results also indicate that the alloying process is progressing with thermal treatment temperature.

The coordination number for Ru-Ru(Pt) and Pt-Pt(Ru) in the samples are significantly smaller than the value of 12 found in the pure metals. The reduction in coordination number is due to two concomitant effects, the fact that some Ru and, in a much minor extent some Pt, is oxidized and to the dimension of the nanoparticles. A reduction of coordination numbers is expected for nanoparticles smaller than 5 nm,

and become progressively more significant as the crystallite size decreases [78]. The effect of the reduced nanocrystal size is also detectable from the absence of shells beyond 3 Å in the 350 catalyst and 4 Å in the 700 °C.

III-4-2-4-d-EXAFS conclusion

From the EXAFS results we can conclude that our nanoparticles are composed of an alloy at 350 °C and the alloying process is enhanced at 700 °C. The platinum characteristics encounter little change upon activation. As for ruthenium, there is a significant difference between the catalyst at 350 °C and 700 °C as marked with an arrow in Figure 37. We had a disordered Ru at 350 °C with a strong contribution of the Ru-O, that became much more ordered at 700 °C due to the appearance of the Pt-Ru bond with more Ru-Ru or Ru-Pt contributions than Ru-O.

III-4-2-5-Wide Angle X-Ray Scattering (WAXS)

WAXS measurements were performed in collaboration with Pierre Lecante in the CEMES-Toulouse.

III-4-2-5-a-WAXS overview

Very small nanoparticles (<6 nm) could be treated as amorphous materials since at this size, the crystalline order disappears at long distance: at small sizes the X-Ray diffraction pattern is no longer exploitable (very large peaks, drowned in the noise signal) but the diffusion signal contains all the structural information. In fact, the irradiation of a sample with an X-ray of a wave length small enough (Mo, λ = 0.071069 nm) leads to the emission in all the space directions of a secondary radiation which intensity at a certain diffusion angle depends on the structure of the sample [79]. To get the interatomic distances by measuring I(S), S the vector of diffusion S= $4\pi\sin\theta/\lambda$, we have to make some corrections; like getting over the adsorption phenomena and the polarization of the incident radiation, getting off the air contribution and the one of the matrix in which the nanoparticles are dispersed like the nanotubes, polymers, capillary tube; then normalize the corrected intensity. I_{corr} contains different structural contributions: some due to the intraparticular diffusion

(I_{intra} (S)); or interparticular (I_{inter} (S)) and the signal of diffusion associated to the chemical nature of the material (I_{indept} (S), that can be calculated). In the case of isolated nanoparticles we can neglect the I_{inter}(S). In this approximation, I_{intra}(S) is named reduced intensity i(S): i(S) = I(S)-I_{indept}(S). The passage to the real space to obtain the function of radial distribution (FDR), or the matrix of interatomic distances inside the nanoparticles is done by a simple Fourrier transformation of i(S). The comparison of the experimental FDR and i(S) diagrams with model arrangements permits the structural identification of the nanoparticles [74, 75]. Even though those structural studies bring statistical data very complementary to the studies done by high resolution transmission electronic microscopy, the WAXS technique is not yet familiar to the scientific community of catalysis. In this study we also try to promote such technique, becoming of high importance, replacing the classical X-Ray diffraction technique when studying very small nanoparticles.

III-4-2-5-b-WAXS results

The wide angle X-ray spectroscopy was performed over all the catalysts treated at different temperatures. The spectrums of pure nanotubes were identical whatever the applied temperature was. Their signature is highly present, in particular the strong peak at 10° that do not belong neither to Pt (fcc) nor to Ru (hcp) (Fig. 41). This peak could serve as correction criteria. Classic polarization and absorption corrections were applied.

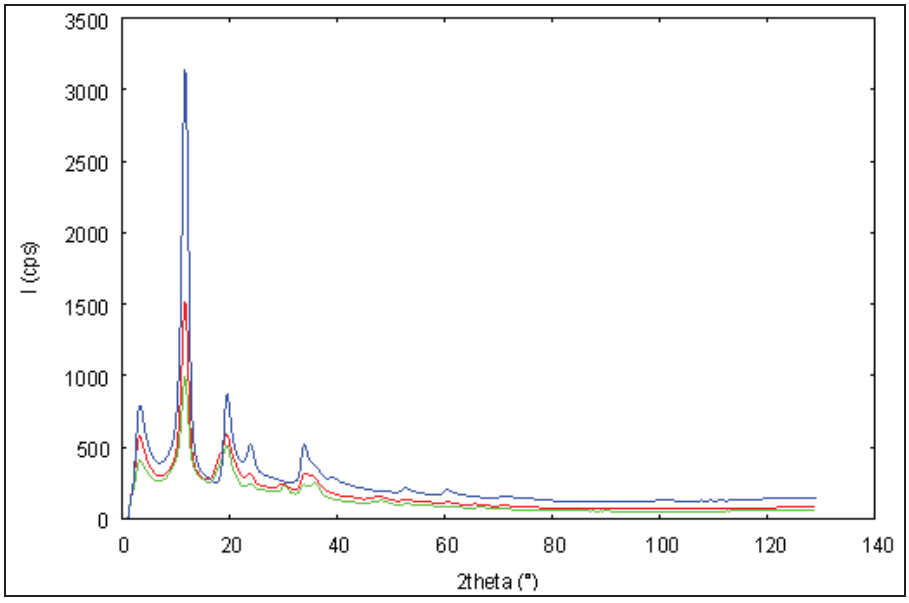

Figure 41: non-corrected diffractograms of 350°C (red) and 700 °C (green) Pt-Ru/MWCNT catalysts. Diffractograms of the 350 °C and 700 °C carbon nanotubes are identical (blue).

A critical step in data reduction was the accurate determination of the amount of matrix (pure nanotube) to subtract: very small changes in capillary diameter or sample density have strong influence, thus exclude a priori correction. A simple criterion was used: the cancellation, in reciprocal space, of peaks characteristic of carbon nanotubes (e.g. peak at 10° 2theta); an additional criterion was the cancellation, in real space, of the characteristic C-C distance.

After subtraction of the contribution of pure nanotubes, the data were normalized then Fourier transformed in order to obtain the Radial Distribution Function (RDF, also called Pair Distribution Function). The RDF displays a series of peaks pointing to distances between atoms, up to the coherence length. For well ordered objects, the complete damping of the function is related to the size of the particles. However, because of the limited resolution of the instrument, the function is terminated for distances between 4 and 5 nm. Peaks amplitude is related to both multiplicity of the distance, that is related to the average number of atoms, thus to size of the particles and the static disorder in the structure.

The corrected diffractograms of the 350, 700, 850 and 1000 °C catalysts as well as references of Pt and Ru are presented in Figure 42.

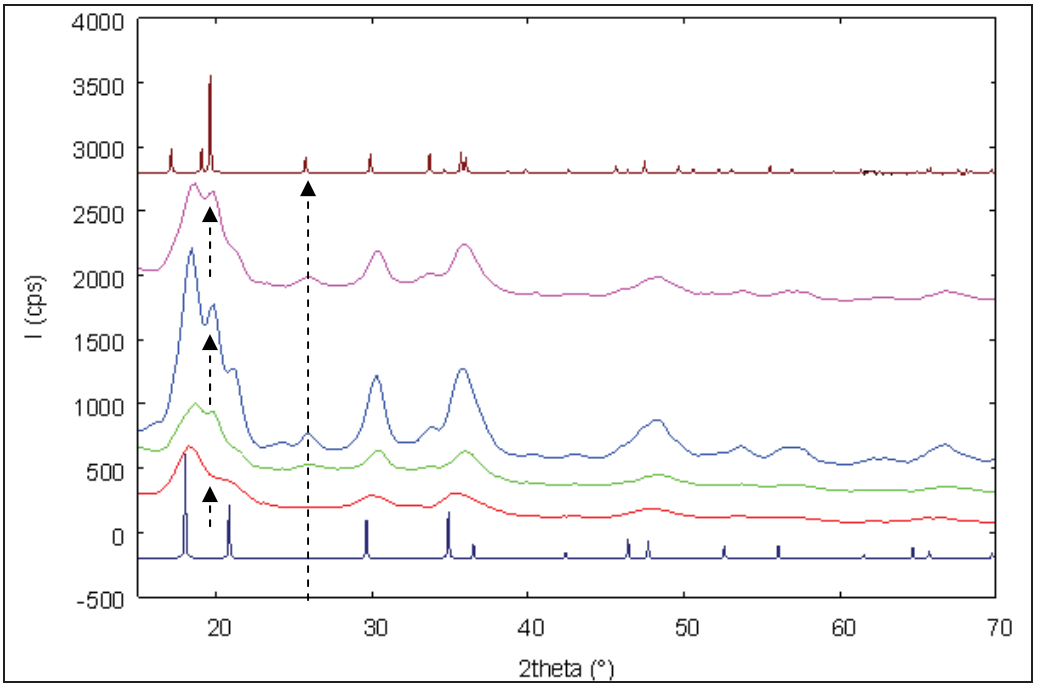

Figure 42: Corrected diffractograms of the 350 (red), 700 (green), 850 (blue) and 1000 °C (purple) catalysts , with hcp ruthenium (brown) and fcc platinum (deep blue) references.

Platinum is known to crystallize in a fcc crystal phase whereas ruthenium crystallizes in a hcp structure [82-84]. The Pt-Ru/MWNT350 catalyst present small and broad peaks in good agreement with the fcc pattern and indicating small objects. But these peaks present a cumulative shift towards larger angles, indicating a cell parameter smaller than in pure Pt, probably due to Ru insertion. After annealing at 700 °C, peaks are not higher nor sharper, but the pattern includes both fcc and hcp features. The situation is the same in the 850 °C catalyst, but with much higher and sharper peaks, indicating much larger and/or less disordered particles. For the 1000 °C catalyst, a pattern similar to the 850 °C catalyst is observed, however significantly less sharp.

After Fourier transformation, similar observations can be concluded in the real space presented in Figure 43.

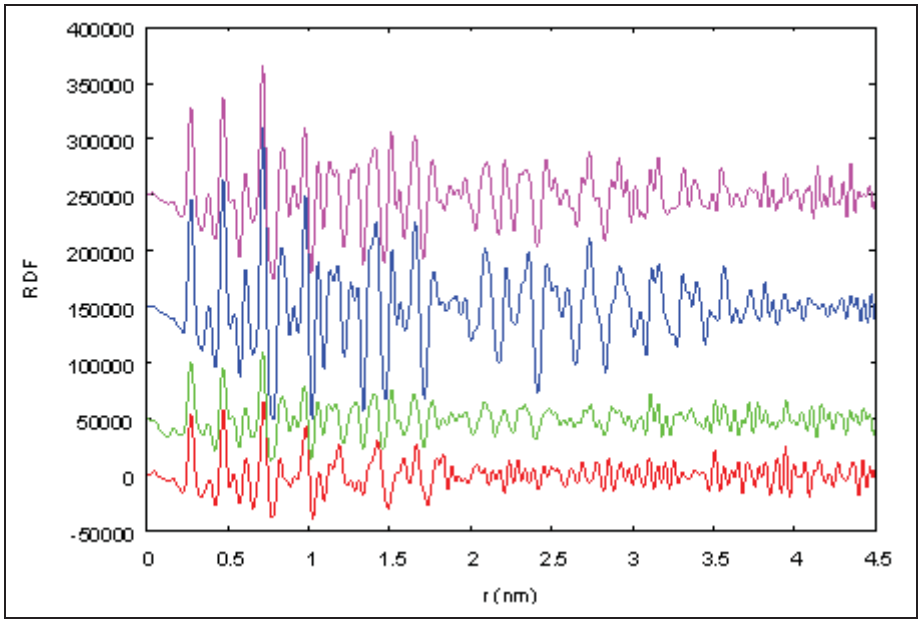

Figure 43: exact (non-scaled) RDFs for the 350 (red), 700 (green), 850 (blue) and 1000 °C (purple) catalysts

RDFs amplitude are similar for the 350 and 700 °C catalysts, indicating similar sizes. A dramatic increase in size occurs for the 850 °C catalyst, with a small reduction for the 1000 °C one. Coherence length can be evaluated to 2.5 nm for the 350 °C, and 3.0 nm for the 700 °C catalyst in accordance with TEM data. This indicates an ordering generated by the thermal treatment, in accordance with what was seen in the EXAFS spectroscopy. However, a similar estimation can not be done for the 850 °C and 1000 °C catalysts: the extinction of the functions above 4 nm only indicates that their size is at least equal to 4 nm. As the nanoparticles could have sintered under the electron beam of the high resolution microscopy, we calculated once again the nanoparticles size using the Sherrer formula: $D=k\,\lambda / \beta\,\mathrm{Cos}\theta$ [96, 97] and found similar results to those with the HREM observations. The nanoparticles size was 2.5 nm at 350 °C, 3nm at 700 °C and beyond 5 nm for the 850 °C and 1000 °C.

To identify the crystal phase (fcc or hcp), it is interesting to focus on the 0.8-1.0 nm range (Fig. 44) which is very different for the two structures. The 350 °C catalyst is nearly purely fcc, whereas both characters appear for the 700, 850 and 1000 °C catalysts.

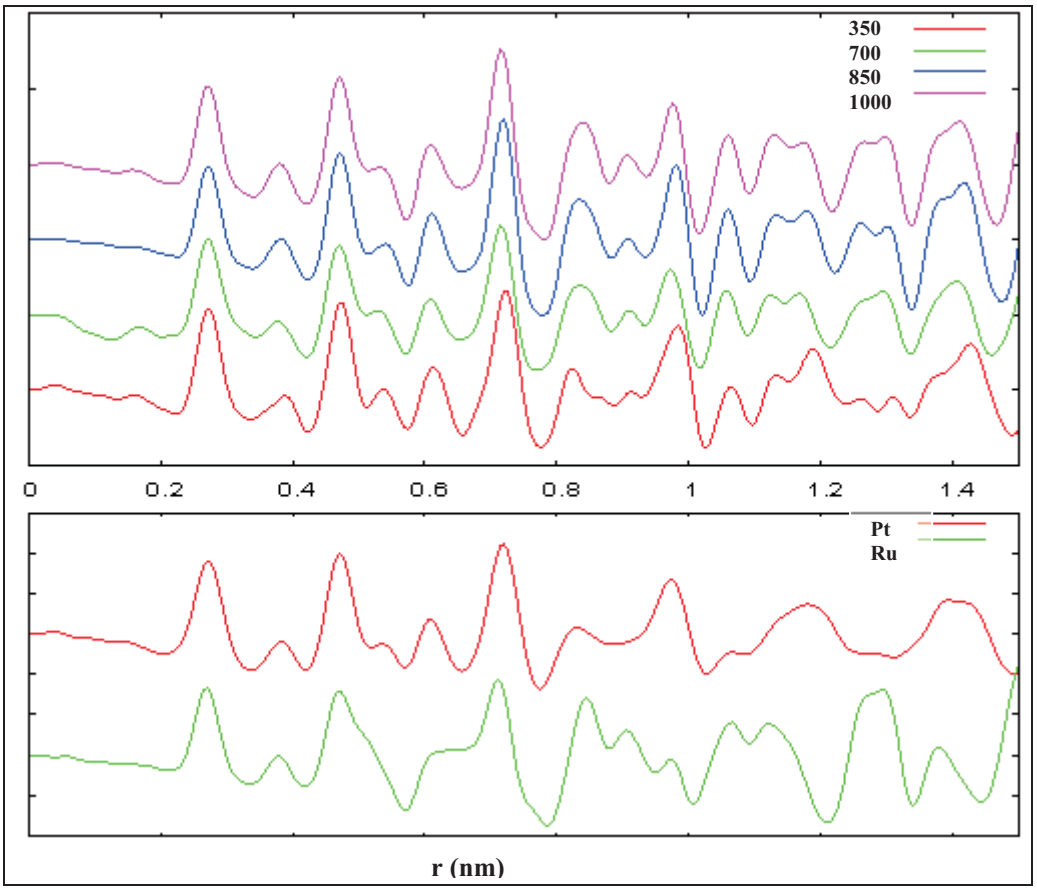

Figure 44: short distances section of the RDFs (scaled for better comparison) for the samples (top) and bulk fcc and hcp references (bottom)

Because the 350 °C catalyst is very close to the perfect fcc structure, comparison with an adjusted fcc model is possible: a good agreement is obtained for a 2.4 nm particle, applying to the pure Pt parameter a 1.5% shrinking factor (Fig. 45).

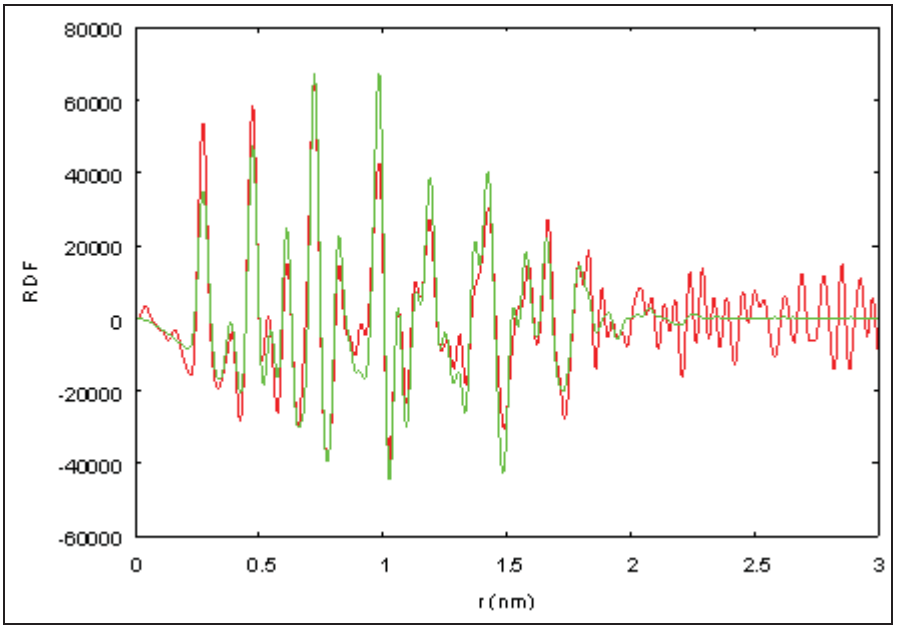

Figure 45: comparison of the experimental RDF of the 350 °C catalyst (red) with a theoretical one (green) computed from a spherical fcc model (diameter: 2.4nm, metal-metal bonding distance: 0.2733 nm)

This result to a parameter for the cubic cell equals to 0.3865 nm, which points to a Ru content slightly smaller than 50 % (Fig. 46) [84]. This interatomic distance was in accordance with the literature value of 0.2735 nm (Table 17) corresponding to a 3 Pt/1 Ru ratio [85]. The 350 °C catalyst can be described in a fcc model contracted of 1.5 %.

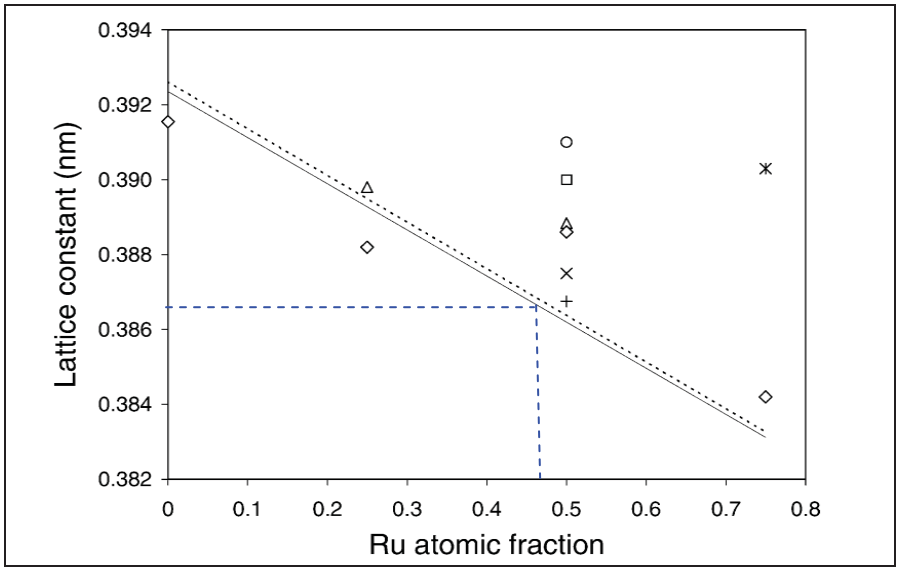

Figure 46: The fcc lattice parameter of carbon-supported PtRu alloys vs. nominal PtRu in the sample. (◊) [86]; (Δ) [87]; (○, ×) [88]; (+) [89]; (□) [90]. Full line: unsupported PtRu bulk alloy obtained by data from [91, 92]; dashed line: unsupported PtRu bulk alloy from [93]

The blue dashed bar in Fig. 46 is set for the 0.3865 nm value derived for the cubic cell parameter from WAXS studies on the 350 °C catalyst.

Composition	Size (nm)	Structure (major)	Interatomic distance (Å)	CO stretch (cm^{-1})
Pt	1.5	fcc	2.740	2040
Pt3Ru1	1.5	fcc	2.735	2040, 1840
Pt1Ru1	1.5	fcc	2.715	2032
Pt1Ru3	1.1	Twinned fcc	2.704	2024
Pt1Ru5	1.4	hcp	2.690	2017
Pt1Ru9	1.5	hcp	2.680	2017
Ru	1.2	hcp	2.660	2013

Table 17: Some physical characteristics of mono- and bimetallic nanoparticles [85]

In fact the preparation of practical catalysts, i.e. supported bimetallic alloys, presents some problems with respect to model catalysts, i.e. unsupported bulk alloys. It is to be distinguished supported alloy from supported bimetallic, being in this case two metals present on the same support and not being alloyed [94]. In many supported

catalysts reported in literature, the metals were only partially alloyed (supported bimetallic alloy). Moreover, in the presence of alloy it is to be distinguished supported solid solution (disordered alloy) from supported intermetallic compound (ordered alloy) [84].

To summarize, all measurements point to the following structural evolution:

- Initially, nanoparticles of the 350 °C catalyst are small, strongly fcc, with a parameter pointing to a PtRu alloy.
- When heated at 700 °C, from coherence length we can conclude that particles are probably similar in size, but both fcc and hcp characters are present due to pronounced Ru enrichment.
- The alloying is at its maximum at 850 °C and the nanoparticles increased in size, but with a similar structure than the 700 °C catalyst.
- At 1000 °C, particles are slightly smaller and/or more disordered than in the 850 °C catalyst.

This was in accordance with previous works (Fig. 47) were the percentage of alloyed Ru progressed exponentially as a function of the activation temperature [88].

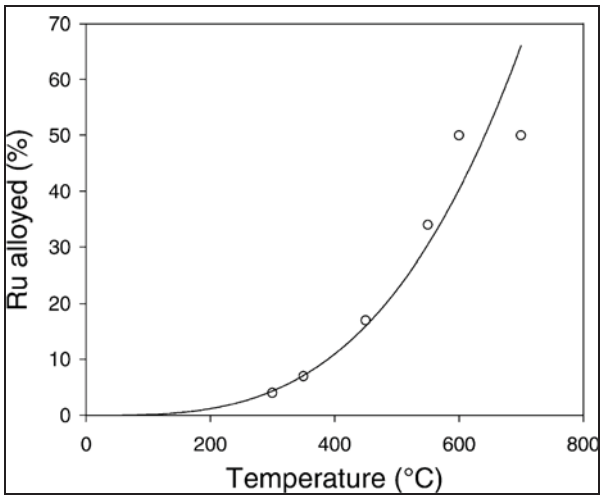

Figure 47: Proportion of Ru alloying to Pt as a function of temperature [88]

III-4-2-5-c-WAXS study of oxidized samples

In order to verify the alloying between Pt and Ru, the four samples were left exposed to air in open glass capillaries and re-measured after short (one hour, using a fast measurement) and long (approximately one month) exposure to air.

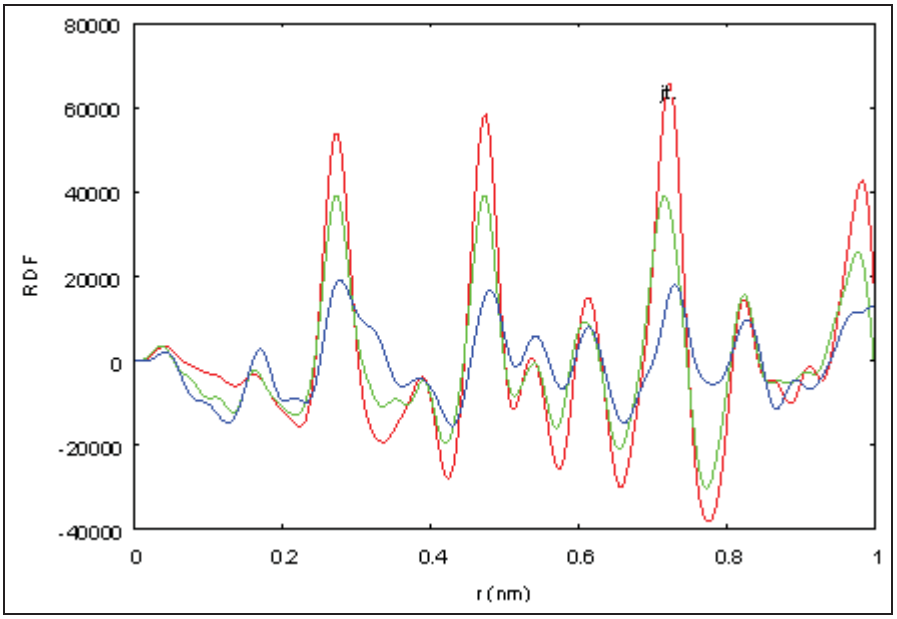

Figure 48: the 350 °C catalyst before exposure (red), after one hour (green), after one month (blue).

The main result is that the 700, 850 and 1000 °C catalysts displayed nearly no evolution from the diffraction point of view, even after one month exposed to air.

Quite differently, the 350 °C catalyst presents obvious indications of oxidations just after one hour, and a very strong alteration after one month (Fig. 48).

The reduction of the amplitude for the peak pointing to the metallic bond (0.26 nm) and the growth of peaks for a shorter distance (approx. 0.18 nm, metal-oxygen bond) and a longer one (approx. 0.3 nm, metal-metal non-bonding distance, bridged by oxygen) are evidences of sample oxidation.

This result is consistent with a very different exposition of the Ru atoms, more sensitive to oxidation, in the 350 °C catalyst, compared to the three other samples. This is a clear evidence of the alloying starting at 700 °C where the neighboring Pt atoms protect the Ru from oxidation [95].

III-4-2-5-d-X-ray fluorescence study

A crude fluorescence study was also performed using the energy discrimination capabilities of the solid state detector used for the WAXS measurements.

In Figure 49, the three well marked peaks between 10 and 15 keV are L emissions lines from Pt and thus are indications of the Pt concentration in the samples.

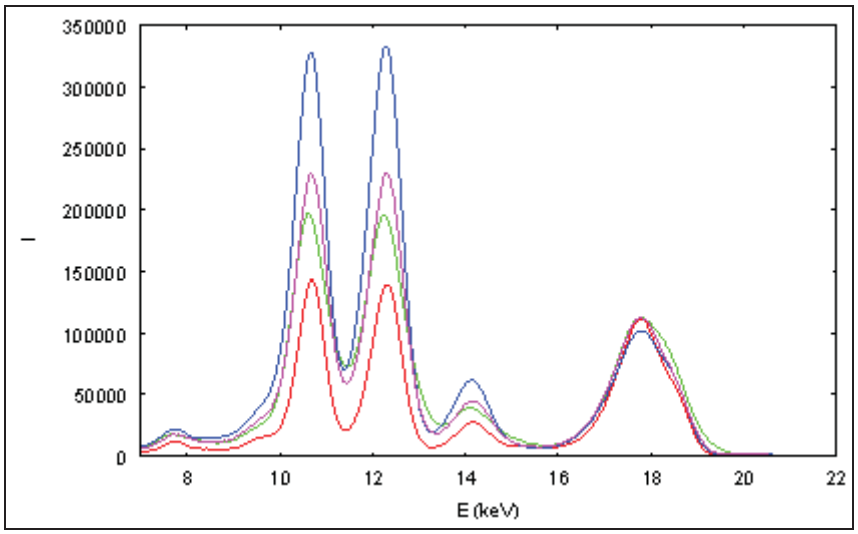

Figure 49: Fluorescence in the Pt range of the 350 °C (red), 700 °C (green),850 °C (blue), 1000 °C (purple) catalysts

The broad peak at 18 keV comes from elastic and inelastic scattering of the primary beam (Molybdenum K emission line), and integrates contributions from all the species present in the sample.

In Figure 50, the peak at 22.5 keV is the Ru K beta emission line, the broad peak between 30 and 34 keV comes from elastic scattering by all atoms of the white radiation produced by the source.

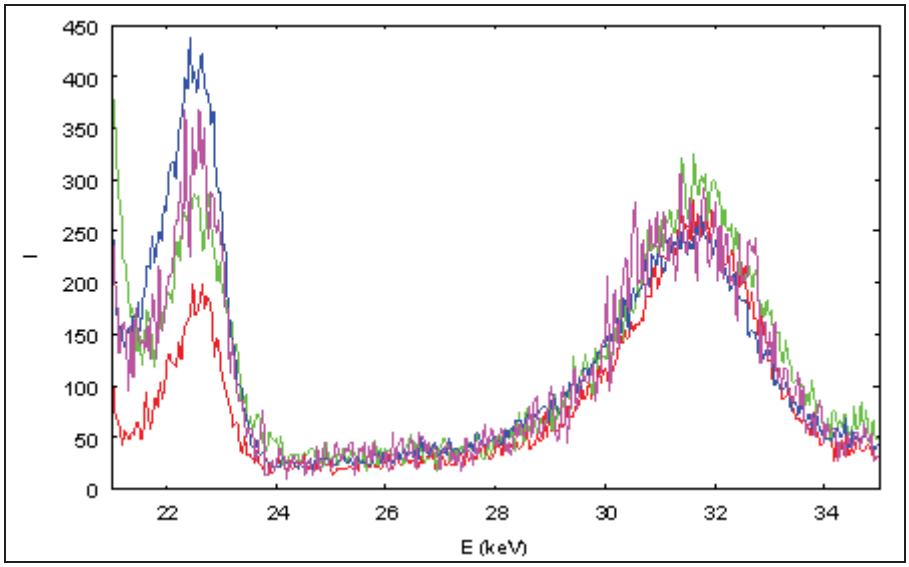

Figure 50: Fluorescence in the Ru range 350 °C (red), 700 °C (green),850 °C (blue), 1000 °C (purple)

The intensity of the fluorescence radiation produced follows the same evolution for Pt and Ru atoms: significant increase from the 350 °C to the 700 °C catalyst, then much stronger from the 700 °C to the 850 °C catalyst, then decrease in the 1000 °C catalyst. Those observations were in accordance with the loadings found by the ICP-MS method (Table 13).

Several effects may alter the amount of fluorescence effectively collected, and in the case of large segregated particles, the relative arrangement of species may induce differential absorption of radiation. Not taking into account such (unknown) effects, these results should be consistent with a regular increase of the metal / nanotube ratio with the level of annealing, excepted for the 1000 °C catalyst which points to a small decrease compared to the 850 °C one. Since such trend is observed for both elements, this crude analysis doesn't indicate a significant change in the Pt/Ru ratio.

III-4-2-6-DFT theoretical calculations

The mobility of Pt and Ru on the MWCNT surface was studied by DFT in order to understand its impact on the nucleation of the nanoparticles, its related final structure, in addition to sintering upon thermal activation) and structure evolution.

Those calculations were performed in collaboration with Iann Gerber in the LPCNO Toulouse.

III-4-2-6-a-Computational details

DFT calculations were carried out using the Vienna ab initio simulation package VASP [98, 99]. The code uses the full-potential Projector Augmented Waves (PAW) framework [100, 101]. Exchange-correlation effects have been approximated using the PBE [102] functional and applied in spin-polarized calculations. A kinetic energy cutoff of 400 eV was found to be sufficient to achieve a total energy convergence within several meV considering k-point sampling. All atoms were fully relaxed to forces on individual atoms smaller than 0.02 eV/ Å. Diffusion barriers were estimated by the climbing image nudge elastic band (CI-NEB) method [103], with a force tolerance of 0.02 eV/Å and five intermediate geometries for the transition state search. To get insights of the mobility of the metallic atoms on the graphenic surfaces of nanotubes, we have used two models. One consists in a repetition of five primitive cells of a small metallic tubes, namely (6,6) nanotubes and the second one is a graphene plane that is supposed to be a reasonable model of large diameter CNTs, modelled by a 7x7 primitive cells. Considering these two models, it allows for the observation of curvature effects at a reasonable concentration of defects (around one metallic atom for one hundred C atoms).

III-4-2-6-b-Results adsorption enrgy (eV) of Pt adatom

To obtain diffusion barriers of metallic atoms, it is necessary to find the most stable configurations (geometries) of the adsorbed species. After complete geometry's relaxation, it appears that in the case of Pt adatom, on the planar model, the most stable configuration is a bridging position above a C-C bond. This adsorption's site is more stable by 0.2 eV (4.6 kcal/mol) over the hollow (in the middle of a hexagone) and on-top positions. The calculations performed on the small tube, show that curvature's effect in one hand, tends to reduce energy differences between the different adsorption sites (on-top and bridge sites have almost the same energy), on the other hand, enhances globally the adsorption energy (by 0.4 eV), which results from a stronger binding. Same general trends are obtained for Ru adatoms, with only one main difference: the hollow site is more favored. The identification of the most

stable sites done, we can estimate diffusion barriers on the planar model more representative of the experimental conditions. In the case of Pt adatom, with a minimum energy path from one bridge to the nearest bridge position, the diffusion barrier is about 0.16 eV (3.7 kcal/mol). For the Ru adsorbed, the path is evidently from one hollow to the nearest hollow site, the diffusion barrier is now 0.65 eV. From those two estimates, it is clear that the hopping process that controls the diffusion of Pt or Ru adatoms, is much more easier in the case of Pt than Ru. In other words, Pt adatoms are more mobile than Ru ones.

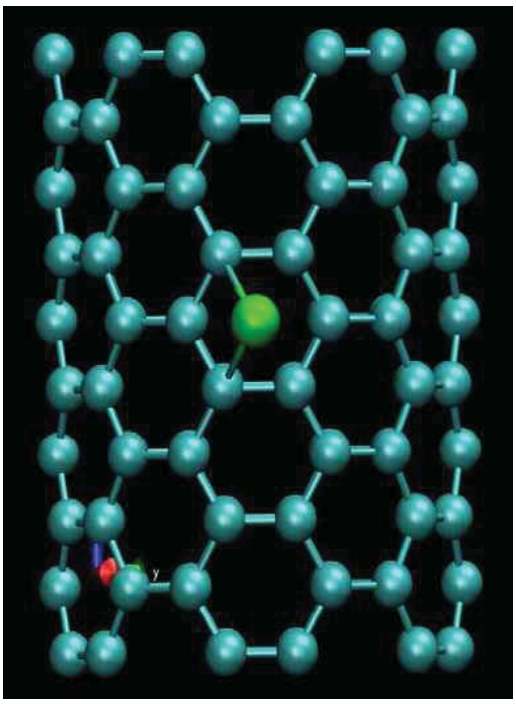

Figure 51: Different modes of adsorption of atom on a MWCNT surface

III-4-2-7-Interpretation

It is known that the decomposition kinetic of the [Ru(COD)(COT)] complex is more rapid than the [Pt(COD)Me_2] one [26], and Ru atoms [104, 105] interact more strongly than Pt with the graphene layers of CNTs. This was in accordance with the DFT calculations. Thus in the liquid phase impregnation of the multi-walled carbon nanotubes, it is the Ru atoms that nucleate first on the carboxylic groups at 45 °C.

After the reduction phase at 350 °C, a layer composed of disordered ruthenium is generated (Fig. 52). This was verified by EXAFS were we observed more Ru-O

bonds than Metal-Metal bonds. Over this Ru layer, which should act as a catalyst for Pt precursor decomposition, some nanoparticles are formed witch are rich in platinum atoms and present some Ru insertion. The nanoparticles are composed of 62 % Pt and 38 % of Ru as seen by HREM/EDX. This explains the fcc crystal phase dominance in the WAXS spectroscopy. The non alloyed ruthenium, once exposed to air is rapidly oxidized. The measured nanoparticles size was 2.7 nm as seen in HREM and verified by WAXS.

The activation of the catalyst at 700 °C under nitrogen does not largely affect the nanoparticles size (2.9 nm) even if we start loosing some carboxylic groups in the form of CO_2 and CO (TPD). There is a structural evolution of the nanoparticles to the hcp crystal phase provoked by this activation that enriched them with ruthenium originating from the Ru layer. The nanoparticles are composed of 44 % of Pt and 56 % of Ru (EDX). There is a Ru-Pt alloying verified by the stability against oxidation of the Ru (WAXS) and the ordering seen in the EXAFS spectra: appearance of the Pt-Ru bond with more Ru-Ru or Ru-Pt contributions than Ru-O. Both hcp and fcc phases are present (WAXS).

At 850 °C and 1000 °C, as all the carboxylic groups are removed from the surface, the sintering phenomena takes place, that doubles the nanoparticles size to 6 nm and then to 12 nm and the crystal structure remains mainly hcp. The alloying effect continues, the Ru is always stable against oxidation, a maximum is obtained at 850 °C with nanoparticles composed of 39 % of Pt and 61 % of Ru. A schematic representation of the entire phenomenon encountered during the thermal activation of the catalyst is presented in Figure 52.

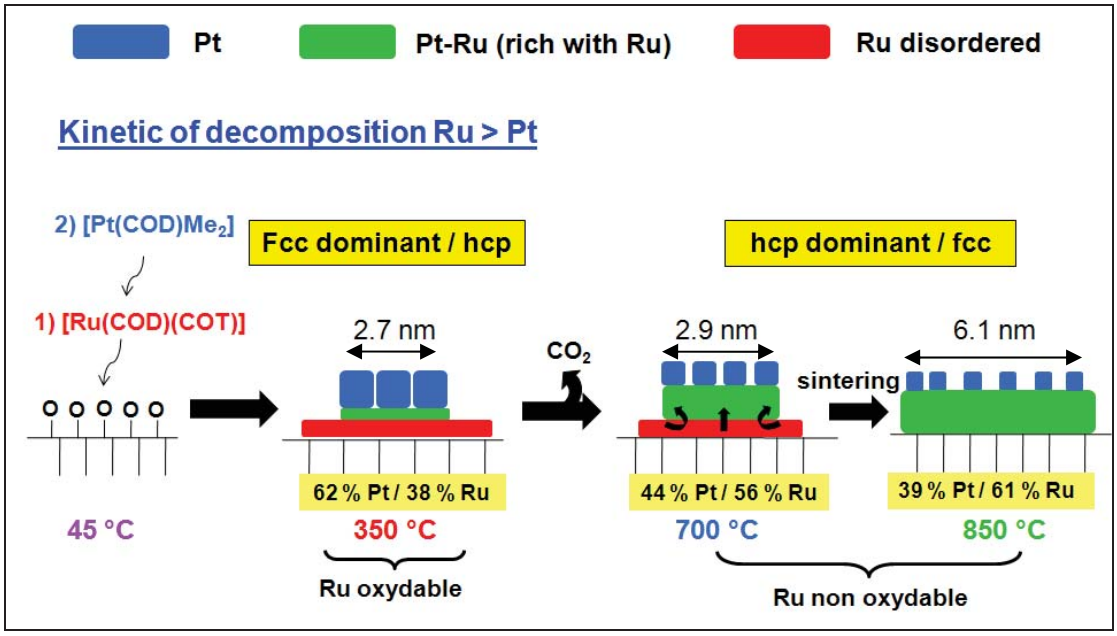

Figure 52: Proposed model for the thermal activation effect on the Pt-Ru/MWNT catalyst (disordered Ru (red); Pt: (blue); Pt-Ru rich in Ru:(green))

Now that we know the structural evolution of the catalyst as a function of the temperature of activation, the explanation of the increase of selectivity with activation temperature is more clear.

The Ru enrichment of the nanoparticle should enhance the selectivity of the catalyst, and the promoting role of Ru can be explained via two mechanisms:

1) the Ru can act like an electropositive metal that increase the electron density on the Pt, thus decreasing the binding energies, particularly that of the C=C bond (inhibiting the adsorption via the C=C), and favors the hydrogenation of the C=O with respect to the C=C bond. This effect has been studied in detail by Delbecq and Sautet [106, 107] by theoretical calculations. In fact, this electronic effect caused by Ru is similar to that of the electron donating carbonaceous support discussed before.

2) The electropositive Ru, on the surface of Pt act as electrophilic or Lewis sites for the adsorption and activation of the C=O bond via the lone electron pair of the oxygen atoms as schematically described in Figure 53. This second mechanism referred to as the ‘’electrophilic C=O activation’’ was the most frequently invoked to account for the promoting effect of electropositive species [71, 108].

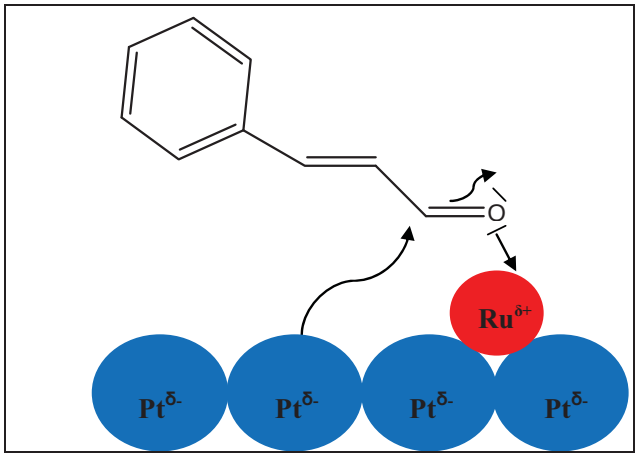

Figure 53: Scheme of C=O bond activation by electropositive Ru atoms on platinum surface [95]

Both mechanism should favor selectivity enhancement, the first by decreasing the activation of the C=C bond, and the second one by increasing the activation of the C=O bond. However, the effect of mechanism 2 should be predominant because significant increase of the rate of the C=O bond hydrogenation was observed in almost all the metal-promoted catalytic systems.

In a global summary many phenomena have occurred during the thermal activation and they all contribute to selectivity enhancement. In addition to the main Ru promoting effect previously discussed (structural evolution), the carboxylic group removal from the surface of the catalyst, changes the surface polarity [2], enables better CAL and H_2 adsorption [26, 39], and increased the nanoparticles size. All this parameters contribute to better electronic transfer effect and CAL orientation that favors the C=O bond hydrogenation. The CAL and H_2 concentration should be equilibrated in a way to overcome the competitive adsorption of reactant and in a same way vertically orient the CAL molecules to favor the C=O bond hydrogenation. The optimum CAL and H_2 concentration was also dependent on the carboxylic group concentration on the surface.

III-5-Conclusion

The hydrogenation of cinnamaldehyde over heterogeneous catalysts follows a Langmuir-Hinshelwood kinetic model. On a supported Pt-Ru alloyed nanoparticles on multiwalled carbon nanotubes activated at 700 °C the actictivation energy of such reaction was 25 kJ/Mol.

In this work we have evidenced the promising advantages of the carbonaceous supports over classical supports. To increase the selectivity of carbon supports, a thermal activation was needed. Thus, we got a performant system with better catalytic performances than the ones supported on classical supports, i.e better activity and selectivity. We also evidenced the important role of the catalyst structure that is the structure of the support, that of the nanoparticles and their association.

III-6-References

1) A.B. da Silva, E. Jordao, M.J. Mendes, P. Fouilloux, Braz. J. Chem. Eng. 15 (1998) 2

2) M.L. Toebes, T.A. Nijhuis, J. Hajek, J.H. Bitter, A.J.V. Dillen, D.Y. Murzin, K.P. de Jong, Chem. Eng. Sci. 60 (2005) 5682

3) J. Zhang, X. Liu, R. Blume, A. Zhang, R. Schlogl, D.S. Su, Science 322 (2008) 73

4) D. Begin, G. Ulrich, J. Amadou, D.S. Su, C. Pham-Huu, R. Ziessel, J. Mol. Catal. A: Chem. 302 (2009) 119

5) H. Knözinger, k. Kochloefl, Heterogeneous catalysis and solid catalysts, in Ullman's Encyclopedia of industrial chemistry (2008) John Willey Sons Inc: Weinheim.

6) B. Chen, U. Dingerdissen, J.G.E. Krauter, H.G.J. Lansink Rotgerink, K. Möbus, Appl. Catal. A: Gen. 280 (2005) 17

7) H.U. Blazer, C. Malan, B. Pugin, F. Spindler, H. Steiner, M. Studer, Adv. Synth. Catal. 345 (2003) 103

8) P.L. Mills, R.V. Chaudhari, Catal. Today 37 (1997) 367

9) C. Mohr, P. Claus, Science Progress 84 (2001) 311

10) G. Neri, L. Bonaccorsi, L. Mercadante, S. Galvagno, Ind. Eng. Chem. Res. 36 (1997) 3554

11) M. Lashdaf, A. Hase, E. Kauppinen, A.O.I. Krause, Catal. Lett. 52 (1998) 199

12) T. Vergunst, F. Kapteijn, J.A. Moulijin, Catal. Today 66 (2001) 381

13) B. Coq, F. Figueras, P. Geneste, C. Moreau, P. Moreau, M. Warawdekar, J. Mol. Catal. 78 (1993) 211

14) J. Simonik, L. Beranek, J. Catal. 24 (1972) 348

15) J. Barrault, A. Derouault, G. Courtois, J.M. Maissant, J.C. Dupin, C. Guimonb, H. Martinez, E. Dumitriu, Appl. Catal. A: Gen. 262 (2004) 43
16) E. Santacesaria, Catal. Today 34 (1997) 393
17) U.K. Singh, M.A. Vannice, Appl. Catal. A: Gen. 213 (2001) 1
18) D. Loffreda, F. Delbecq, F. Vigne, P. Sautet, J. Am. Chem. Soc. 128 (2006) 1316
19) A. Hammoudeh, S. Mahmoud, React. Kin. Catal. Lett. 91 (2007) 131
20) A.J. Marchi, J.F. Paris, N.M. Bertero, C.R. Apestegua, Ind. Eng. Chem. Res., 46 (2007) 7657
21) P. Gallezot, D. Richard, Catal. Rev. Sci. Eng., 40 (1998) 81
22) P.N. Rylander, in Catalytic hydrogenation in Organic Synthesis, Academic Press, New York, (1979) 72
23) G. Gordier, Y. Colleuille, P. Fouilloux, in Catalyse par les Métaux (B. Imelik et al., eds.), Editions du CNRS, Paris, (1994) 349
24) G. Gordier, French patent F2,329,628 (1975), to Rhône-Poulene S. A., Chem. Abstr., 87, 38862s (1977)
25) F. Delbecq, P. Sautet, J. Catal., 152 (1995) 217
26) H. Vu, F. Goncalves, R. Philippe, E. Lamouroux, M. Corrias, Y. Khin, D. Plee, P. Kalck, P. Serp, J. Catal. 240 (2006) 18
27) W. Koo-amornpattana, J.M. Winterbottom, Catal. Today 66 (2001) 277
28) M. Chatterjee, Y. Ikushima, F. Zhao, New J. Chem., 27 (2002) 510
29) J. Hajek, N. Kumar, V. nieminen, P. Maki-Arvela, T. Salmi, D. Y. Murzin, L. Cerveny, Chem. Eng. J. 103 (2004) 35
30) M. Lashdaf, J. Lahtinen, M. Lindblad, T. Venalainen, A.O.I. Krause, Appl. Catal. A: Gen. 276 (2004) 129
31) A. Jung, A. Jess, T. Schubert, W. Schütz, Appl. Catal. A: Gen. 362 (2009) 95
32) R. L. Augustine, Catal. Today 37 (1997) 419
33) Y.Z. Chen, S.W. Wei, K.J. Wu, Appl. Catal. A: Gen. 99 (1993) 85
34) M. Shirai, T. Tanaka, M. Arai, J. Mol. Catal. A: Chem. 168 (2001) 99
35) J. Hajek, N. Kumar, P. Maki-Arvela, T. Salmi, D.Y. Murzin, I. Paseka, E. Laine, P. Laukkanen, J. Vayrynen, Appl. Catal. A: Gen. 251 (2003) 385
36) J. Hajek, N. Kumar, P. Maki-Arvela, T. Salmi, D.Y. Murzin, J. Mol. Catal. A: Chem. 217 (2004) 145
37) C. Milone, M.C. Trapani, S. Galvagno, Appl. Catal. A: Gen. 337 (2008) 163
38) H. Yamada, H. Urano, S. Goto, Chem. Eng. Sci. 54 (1999) 5231

39) A. Solhy, B.F. Machado, Y. Kihn, F. Goncalves, M.F.R. Pereira, J.J.M. Orfao, J.L. Faria, P. Serp, Carbon 46 (2008) 1194

40) V. Datsyuk, M. Kalyva, K. Papagelis, D. Tasis, A. Siokou, C. Galiotis, Carbon 46 (2008) 833

41) G. Zhang, S. Sun, D. Yang, J.-P. Dodelet, E. Sacher, Carbon 46 (2008) 196

42) R. Giordano, P. Serp, P. Kalck, Y. Khin, J. Schreiber, C. Marhic, J.-L. Duvail, Eur. J. Inorg. Chem. 2003 (2003) 610

43) S.D. Kim, S.J. Park, Y.S. Lee, J. Dispersion Sci. Techn. 29 (2008) 426

44) B.A. Kakade, V.K. Pillai, J. Phys. Chem. C 112 (2008) 3183

45) A. Cabiac, G. Delahay, R. Durand, P. Trens, B. Coq, D. Plée, Carbon 45 (2007) 3

46) J. Amadou, k. Chizari, M. Houllé, I. Janowska, O. Ersen, D. Bégin, C. Pham-Huu, Catal. Today 138 (2008) 62

47) P. Mäki-Arvela, J. Hajek, T. Salmi, D.Y. Murzin, Appl. Catal. A: Gen. 292 (2005) 1

48) C.-H. Chen, C.- C. Huang, Intern. J. Hydrogen Energy 32 (2007) 237

49) X. Lepró, E. Terrés, Y. Vega-Cantú, F. J. Rodríguez-Macías, H. Muramatsu, Y. Ahm Kim, T. Hayahsi, M. Endo, M. Torres, M. Terrones, Chem. Phys. Lett. 463 (2008) 124

50) Z. Chen, W. Thiel, A. Hirsch, Chem. Phys. Chem. 4 (2003) 93

51) P. Gallezot, A. Giroir-Fendler, D. Richard, Catal. Lett. 4 (1990) 169

52) D. G. Blackmond, R. Oukaci, B. Blanc, P. Gallezot, J. Catal. 131 (1991) 401

53) A. Giroir-Fendler, D. Richard, P. Gallezot, Catal. Lett., 5 (1990) 175

54) C. Minot, P. Gallezot, J. Catal., 123 (1990) 341

55)A. Giroir-Fendler, D. Richard, P. Gallezot, Studies Surf. Sci. Catal. Vol 4&, Elsivier, Amsterdam, (1988) p.171

56) D. Richard, P. Fouilloux, P. Gallezot, in Proceeding of the 9th International Congress on Catalysis (M.J.Phillips and M. Ternan, eds.), Calgary, Canada, 1988, p.1074

57) Z-T Liu, C-X Wang, Z-W Liu, J. Lu, Appl. Catal. A: Gen. 344 (2008) 114

58) P. Serp, M. Corrias, P. Kalck, Appl. Catal. A 253 (2003) 337

59) M.L. Khidekel, E.N. Bakhanova, A.S. Astakhova, K.A. Brikenshtein, V.I. Savchenko, USSR Patent 264,352 (1968), to Institute of Chemical Physics, Accademy of Sciences of the U.S.S.R , Chem.Abstr., 73, 14992u (1970)

60) T. Mizoroki, K. Seki, S. Meguro, A. Ozaki, Bull. Chem. Soc. Jpn., 50 (1977) 2148
61) C. G.M. Van de Moesdijk, M.A.R. Bosma, European Patent 219,905 (1986), to Stamicarbon B.V., Chem. Abstr. 107, 98593w (1987)
62) V. Satagopan, S.B. Chandalia, J. Chem. Tech. Biotechnol. 59 (1994) 257
63) AH. Nevidomskyy, G. Csanyi, MC. Payne, Phys. Rev. Lett., 9 (2003) 1055021
64) V. Satagopan, S.B. Chandalia, J. Chem. Tech. Biotechnol., 60 (1994) 17
65) F. Delbecq, P. Sautet, J. Catal. 211 (2002) 398
66) T.A. Nijhuis, G. Van Koten, F. Kapteijn, Catal. Today 79-80 (2003) 315
67) E. Ronzon, G. Del Angel, J. Mol. Catal. A: Chem. 148 (1999) 105
68) W. Koo-amornpattana, J.M. Winterbottom, Catal. Today 66 (2001) 277
69) M. Englisch, V.S. Ranabe, J.A. Lercher, Appl. Catal. A 163 (1997) 111
70) I. Kun, G. Szöllö si, M. Bartok, J. Mol. Catal. A: Chem. 169 (2001) 235
71) J.P. Breen, R. Burch, J. Gomez-Lopez, K. Griffin, M. Hayes Appl. Catal. A: Gen. 268 (2004) 267
72) H. Li, X. Chen, M. Wang, Y. Xu, Appl. Catal. A 225 (2002) 117
73) X. Liang, X. Dong, G. Lin, H. Zhang, Appl. Catal. B: Environ. 88 (2009) 315
74) R.L. Augustine, L. Meng, in Catalysis of Organic Reactions, R.E.M. Jr, Editor. 1996, Marcel Dekker, Inc: New York. P.15-30
75) T.B.L.W. Marinelli, S. Naburs, V. Ponec, J. Catal. 195 (1995) 431
76) A. Bianconi, L. Incoccia and S. Stipcich (Eds), EXAFS and Near edge structure, Springer, Berlin,1983.
77) D.C Koningsberger and R. Prins (Eds), X-ray absorption, Wiley, New York, 1987
78) J.W. Niemantsverdriet, in Spectroscopy in Catalysis: an introduction, New York, Basel, Cambridge, Tokyo: VCH, 1993
79) P. Lecante, A. Mosset, J. Galy, J. Appl. Crystallogr. 18 (1985) 214
80) O. Margeat, C. Amiens, B. Chaudret, P. Lecante, R.E. Benfield, Chem. Mater. 17 (2005) 107
81) O. Margeat, F. Dumestre, C. Amiens, B. Chaudret, P. Lecante, M. Respaud, Progress in Solid State Chemistry, in press
82) W.B. Pearson, A. Handbook, of Lattice Spacings and Structures of Metals and Alloys, Pergammon Press, Oxford, 1958
83) C.A. Angelucci, M. D. Silva, F.C. Nart, Electrochimi. Acta 52 (2007) 7293
84) E. Antolini, Mater. Chem. and Phys. 78 (2003) 563

85) C. Pan, F. Dassenoy, M.J. Casanove, K. Philippot, C. Amiens, P. Lecante, A. Mosset, B. Chaudret, J. Phys. Chem. B 103 (1999) 10098

86) E. Antolini, L. Giorgi, F. Cardellini, E. Passalacqua, J. Solid State Electrochem. 5 (2001) 131

87) V. Radmilovic, H.A. Gasteiger, P.N. Ross, J. Catal. 154 (1995) 98

88) E. Antolini, F. Cardellini, J. Alloy Comp. 315 (2001) 118

89) E. Antolini, F. Cardellini, L. Giorni, E. Passalacqua, J. Mater. Sci. Lett. 19 (2000) 2099

90) C. He, H.R. Kunz, J.M. Fenton, J. Electrochem. Soc. 144 (1997) 970

91) D. Chu, S. Gilman, J. Electrochem. Soc. 143 (1996) 1685

92) P. Villars, L.D. Calvert (Eds.), Pearson's Handbook of Crystallographic Data for Intermetallic Phases, American Society for Metals, Metals Park, OH, 1985, p. 3046

93) H.A. Gasteiger, P.N. Ross, E.J. Cairns, Surf. Sci. 293 (1993) 67

94) J. Sinfelt, Bimetallic Catalysts: Discoveries, Concepts and Applications, Wiley, New York, 1983, p. 1

95) F. Cao, T.K. Nandy, D. Stobbe, T.M. Pollock, Intermetallics 15 (2007) 34

96) B.D. Cullity, Elements of X-Ray Diffraction, first ed. Addison Wesley (1967)

97) G. Arnaud, PhD thesis, Université Toulouse III–Paul Sabatier, (2007)

98) G. Kresse, J. Furthmüller, Comput. Mater. Sci. 6 (1996) 15

99) G. Kresse, J. Furthmüller, Phys. Rev. B 54 (1996) 11169

100) P. E. Blöchl, Phys. Rev. B 50 (1994) 17953

101) G. Kresse, D. Joubert, Phys. Rev. B 59 (1999) 1758

102) J.P. Perdew, K. Burke, M. Ernzerhof, Phys. Rev. Lett., 77 (1996) 3865

103) G. Henkelman, B.P. Uberuaga, H. Jonsson, J. Chem. Phys. 113 (2000) 9901

104) Y.V. Naidich, V.M. Perevertailo, O.B. Loginova, Izvestia Akad. Nauk. SSSR. Metally 4 (1979) 37

105) Y. Okamoto, Chem. Phys. Lett. 407 (2005) 354

106) F. Delbecq, P. Sautet, J. Catal., 165 (1996) 152

107) R. Hirschl, F. Delbecq, P. Sautet, J. Hafner, J. Catal. 217 (2003) 354

108) D. Richard, J. Ockelford, A. Giroir-Fendler, P. Gallezot, Catal. Lett., 3 (1989) 53

IV-Application of carbonaceous supports for fuel cells electrocatalysts

Chapter IV: Application of carbonaceous supports for fuel cells electrocatalysts

IV-1-Introduction

IV-1-1-General

Fuel cells are electrochemical devices that convert the chemical energy of a reaction directly into electrical energy. The electrical current is generated thanks to the oxidation of a reducing combustible on an anode coupled to the reduction of an oxidant on a cathode. The difference relative to other traditional methods of energy production is the non dependence of the yield on the Carnot cycle. Sir William Grove is considered as the inventor of the fuel cell in 1839, by using the reverse electrolyses of water to produce water and a current (Fig. 1).

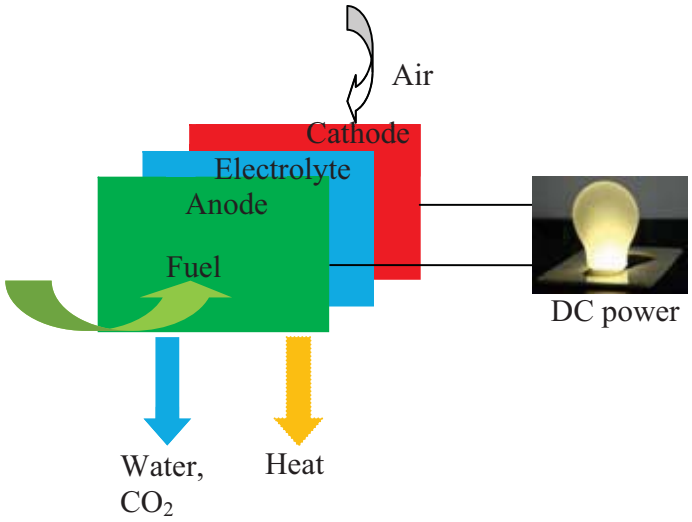

Figure 1: Simplified scheme of a fuel cell

If hydrogen and oxygen molecules are brought into direct contact, they interact spontaneously producing water (Eq. 1), because of the negative value of the Gibbs energy of reaction ΔG, which for liquid water equals -228.6 kJ.mol^{-1} at 25 °C [1]. If the reaction is carried out at a constant pressure, the liberated heat is $-\Delta H$ and equals 285.8 kJ.mol^{-1}. Alternatively, the reaction may be carried out in a fuel cell, with hydrogen and oxygen fed into two separate

compartments: the anode and the cathode, respectively. Hydrogen is ionized at the anode to produce protons and electrons (Eq. 2 and Fig. 2). These flow to the cathode: the electrons through the external electric circuit, while the protons through a proton conducting membrane, separating the anode and the cathode compartments (Fig. 1). At the cathode they interact with oxygen, producing water (Eq. 3). This allows transformation of the Gibbs energy of reaction into the electrical energy.

$$O_2 + 2\,H_2 \longrightarrow 2\,H_2O \quad (1)$$

$$H_2 \longrightarrow 2\,H^+ + 2e^- \quad (2)$$

$$O_2 + 4\,e^- + 4\,H^+ \longrightarrow 2\,H_2O \quad (3)$$

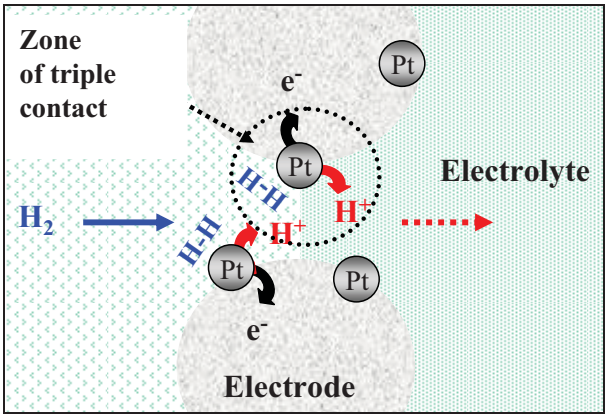

Figure 2: Reaction on the catalyst surface

Even though very promising, the fuel cell progress remained stagnant until the beginning of 1990 when it gain high interest due to the rise of the oil price and its depletion, global warming, technological progress of membranes with higher performances and novel catalysts discovery. At that time, hybrid prototype cars start to appear on the market.

IV-1-2-Different types of fuel cells

In addition to H_2, many fuels can be oxidized and according to the nature of the electrolyte used, temperature of run, nature of the catalyst, their architectures and application domains, a variety of fuel cells are in different stages of development. They are classified in

polymer electrolyte membrane fuel cells (PEMFC), alkaline fuel cells (AFC), phosphoric acid fuel cells (PAFC), molten carbonate fuel cells (MCFC), and solid oxide fuel cells (SOFC) [2]. The specification related to each type of cell is summarized in Table 1.

	PEMFC	AFC	PAFC	MCFC	SOFC
Electrolyte	Ion exchange membranes	Mobilized or immobilized potassium hydroxide	Immobilized liquid phosphoric acid	Immobilized liquid molten carbonate	Ceramic
Operating temperature	80 °C	65–220 °C	205 °C	650 °C	600-1000 °C
Charge carrier	H^+	OH^-	H^+	CO_3^{2-}	O^{2-}
External reformer for CH_4	Yes	Yes	Yes	No	No
Prime cell components	Carbon based	Carbon based	Graphite based	Graphite based	Ceramic
Catalyst	Platinum	Platinum	Platinum	Nickel	Perovskites

Table 1: Different types of fuel cells and related characteristics

IV-1-3-PEMFC and DAFC

Polymer electrolyte membrane fuel cells (PEMFCs ≤ 100 °C at ambient pressure) have recently attracted much attention as promising power sources for small stationary, mobile and portable applications [3]. The heart of such fuel cell is the membrane electrode assembly (MEA, Fig. 3). This is a multi-layer sandwich composed of catalytic layers (CL), where electrochemical reactions occur; gas-diffusion layers (GDL), providing access of the fuel and the oxidant to the catalytic layers and a proton exchange membrane (PEM), such as Nafion® (acid media) or an anion exchange membrane (alkaline media). The structure and the composition of the MEAs have undergone decisive changes during the last 20 - 30 years. The CLs of fuel cells are multi-component media comprising a catalyst (often platinum on carbon), accelerating the rates of

electrochemical reactions; ionomer, providing flow of protons through the MEA; and gas- and liquid-filled pores, providing access of the reagents to and the products from the catalyst surface.

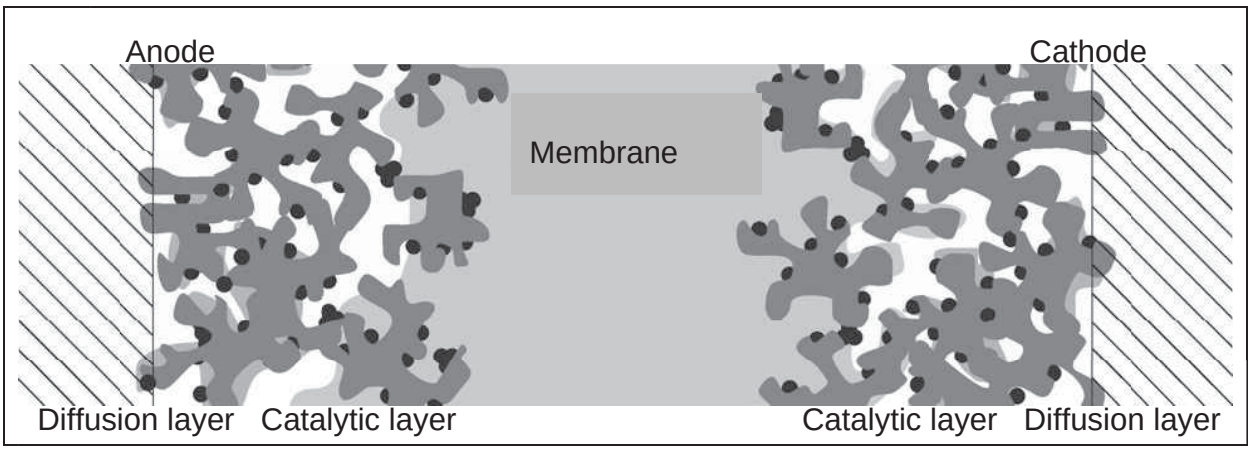

Figure 3: Schematic representation of a membrane-electrode assembly of a PEMFC. Platinum particles and carbon agglomerates are colored in black and gray, respectively

Practically, preparation of the CLs is performed by brushing or spraying the "catalyst ink" (suspension of the catalyst particles in water and/or organic solvent with addition of ionomer, e.g. Nafion®) either onto diffusion media (carbon paper or carbon cloth, also referred to as substrates), resulting in the so-called catalyst-coated substrate, or directly onto PEM, resulting in the so-called catalyst-coated membrane [4].

The maximum equilibrium voltage ΔE_{eq} between the electrodes in a fuel cell is determined by the Gibbs energy of the overall reaction and the number of electrons *n* transferred in the cell reaction, and is given by Equation 4, where F is the Faraday constant:

$$\Delta E_{eq} = E_{cathode} - E_{anode} = -nF\Delta G \tag{4}$$

This maximum voltage requires that equilibrium is established at both electrodes. In reality the cell voltage is given by Equation 5.

$$\Delta E_{cell} = \Delta E_{eq} - |\eta_{cathode}| - |\eta_{anode}| - \Delta E_{Ohmic} \tag{5}$$

Here $\eta_{cathode}$ and η_{anode} stand for overpotentials at the cathode and the anode, respectively.

For example, in a fuel cell fed with pure hydrogen, η_{anode} is small due to the fast kinetics of the hydrogen oxidation reaction (2) on Pt catalysts, and is often neglected [5]. An overpotential may be separated into the reaction overpotential η_R and the concentration overpotential η_{conc} (mass-transport). The former is the consequence of the sluggish reaction kinetics, while the latter arises from the mass transport limitations in the CL. ΔE_{ohmic} comprises the following contributions: (i) the contact resistance between the flow-field plates, (ii) the membrane resistance and (iii) the resistance of the CLs and GDLs. Figure 4 represents the so-called polarization curve, which is the main characteristic of a fuel cell.

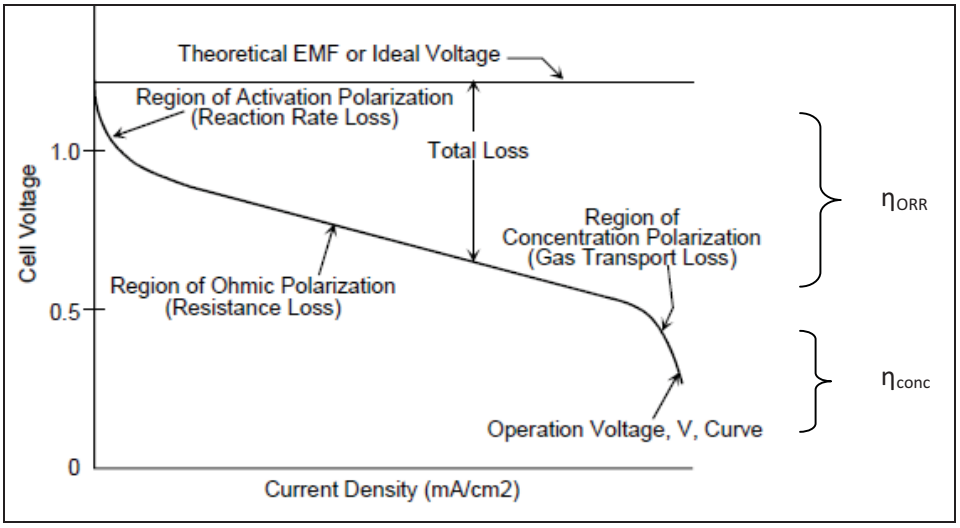

Figure 4: Ideal and actual fuel cell voltage/current characteristic

Since the electrochemical fuel cell efficiency is given by the ratio between ΔE_{cell} and ΔE_{eq}, Equation 5 and Figure 4 give a guidance on which contributions must be minimized in order to improve the fuel cell efficiency. At low current densities the difference between the actual cell voltage and the thermodynamic equilibrium value is dominated by the cathode overpotential (η_{ORR}) due to the sluggish kinetics of the oxygen reduction reaction (3). At high current densities, mass transport of oxygen in the cathode CL and in the GDL give significant contribution to the overall losses. The concentration overpotential η_{conc} strongly depends on the architecture of the catalytic layers and the porosities of catalytic supports used. Ohmic losses in the membrane, CLs and bipolar plates may also significantly limit the cell performance and thus have to be controlled.

IV-1-4-Fuels choice and related active metal

Primary alcohols, with a higher molecular weight than methanol, and polyalcohols are arousing major interest as fuels in direct alcohol fuel cells (DAFC) for various reasons, among which: their low toxicity, high boiling point, high specific energy and the capacity of some of them to be renewable [6–9]. Included in this group are ethanol and glycerol. The former can be massively produced from biomass feedstocks originating from agriculture (first-generation bio-

ethanol), or forestry and urban residues (second-generation bio-ethanol). The latter is a by-product of biodiesel production and, as such, is inexpensive and largely available.

Both alcohols, however, are difficult to oxidize on platinum or platinum alloys supported on carbon blacks that constitute the most common catalysts used as anodes for DAFCs [6–10]. In particular, no known anode catalyst based on platinum has demonstrated the capacity to produce acceptable power densities in either a direct ethanol fuel cell (DEFC) or a direct glycerol fuel cell (DGFC) even at high metal loading [6–9, 11]. The overall efficiency of Pt-based electrocatalysts suffers the consequences of effective catalyst poisoning by CO that is an intermediate of the oxidation of any alcohol [6–9, 12]. Notable efforts are therefore being carried out to design new catalytic structures for DAFC anodes that do not contain platinum or contain tiny amounts of this too rare metal and, most of all, are able to oxidize primary and secondary alcohols with fast kinetics and tolerable deactivation.

Palladium has recently aroused notable interest in electrocatalysis as it is more abundant than platinum, hence less expensive, and has the capacity to promote the oxidation of several alcohols, including ethanol and glycerol in alkaline media, with remarkable electrochemical stability [8, 13–16]. Another advantage of working in alkaline media is the increase in the oxidation potential from $E°_a = 0.084$ in acid media to $E°_a = -0.743$ V, and the direct production of carbonate instead of CO_2 that could be reused as a fertilizer to produce crops that may reproduce alcohols.

$$C_2H_5OH + 3\ H_2O \longrightarrow 2\ CO_2 + 12\ H^+ + 12\ e^- \qquad E°_a = 0.084\ V \qquad (6)$$

$$C_2H_5OH + 16\ OH^- \longrightarrow 2\ CO_3^{2-} + 11\ H_2O + 12\ e^- \qquad E°_a = -0.743\ V \qquad (7)$$

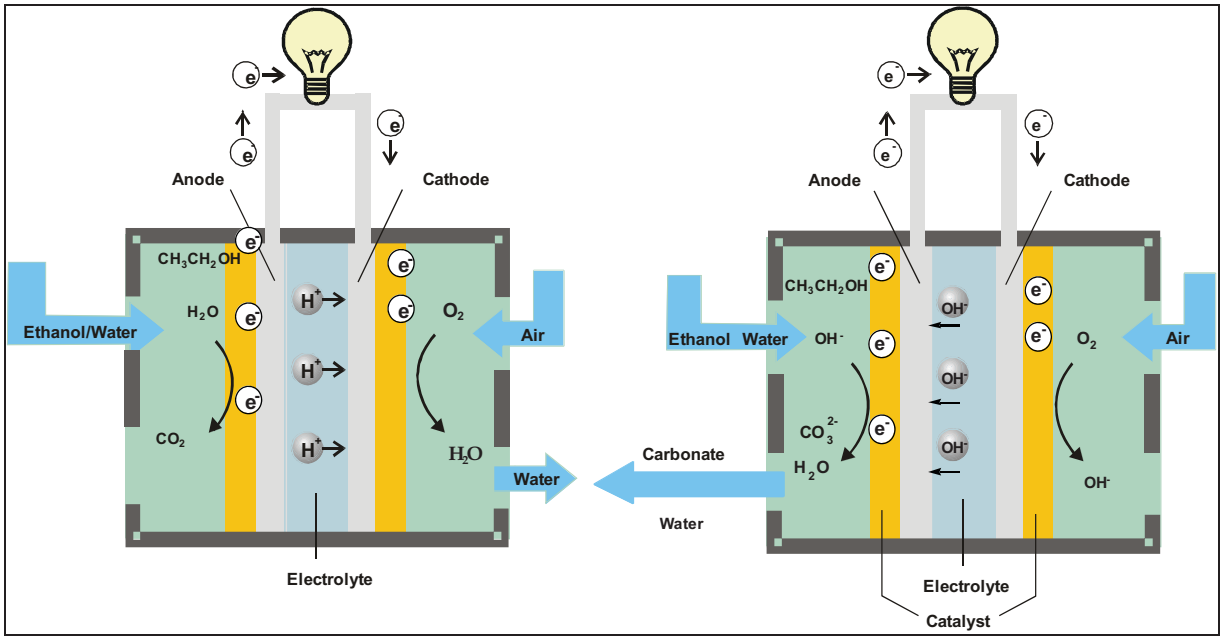

Figure 5: Representation of the DEFC used in our work: acidic media (left) and alkaline media (right)

IV-1-5-Role of carbonaceous materials

The CLs of the early PEMFCs were prepared from the noble metal blacks and thus contained very high metal loadings per geometric MEA area. Later, it became apparent that precious metals in these CLs were not efficiently utilized and the new generation of PEMFCs emerged, based on carbon supported precious metal nanoparticles catalysts (usually Pt or Pt-based alloy) [2]. The right choice of a carbon support greatly affects the cell performance and durability. In order that a fuel cell operates efficiently, carbon materials must satisfy the following requirements:

a) provide high dispersion of metal nanoparticles and protect them from agglomeration;

b) be chemically inert and pure in order that impurities do not inhibit electrochemical reactions;

c) have high electron conductance in order to minimize Ohmic losses associated with the electron transport;

d) possess adequate porosity in order to ensure efficient mass transport of reactants to and products from the CLs;

e) be compatible with the proton or anion conducting polymers, so that composites containing a catalyst and a proton or anion conductor provide efficient proton or anion transport through the CLs;

f) provide optimum water or product management; and

g) be corrosion resistant.

In addition to platinum-free metal catalysts, increasing research efforts are being directed to develop conductive supports, alternative to carbon black, in an attempt of improving the dispersion, activation and stability of the metal particles on the carbon surface as well as increasing the electroconductivity [17]. A large variety of conductive materials has been used to support Pd nanoparticles for use in electrocatalysis, these include carbon blacks like Vulcan XC-72, alone [18] or in combination with either nanocrystalline metal oxides (NiO, CeO_2, Co_3O_4, Mn_3O_4) [13–16,19] or tungsten carbide nanocrystals [20], carbon microspheres [21], coin-like hollow carbons [22], ultrahigh-surface hollow carbon spheres [23], carbonized porous anodic alumina [14], carbonized TiO_2 nanotubes [24], multi-walled carbon nanotubes [25] and activated carbon nanofibers [25]. To the best of our knowledge, however, no report has ever appeared in the relevant literature where a Pd catalyst is used in a real DAFC, all the known studies being limited to alcohol oxidation in half cells [13–16, 18–25].

In that context, we were interested, in collaboration with Dr C. Bianchini from the ICCOM-CNR in Italy where all electrocatalytic tests have been performed, to prepare and characterize new Pd electrocatalysts supported on the carbonaceous supports prepared in chapter II i.e MWCNTs, CNFs, N-MWCNTs, N-CNFs and to use them to manufacture anodes for the oxidation of methanol, ethanol or glycerol in either passive or active DAFCs equipped with an anion-exchange membrane (Fig. 5). For comparative purposes, we have also prepared and characterized Pt-Ru catalysts supported on MWCNTs and used them in a direct methanol fuel

cell (DMFC) in conjunction with a proton-exchange membrane. The purpose of this study is to analyze how structure and properties of carbon materials influence the performance of supported noble metal catalysts in the CLs of the PEMFCs.

IV-2-Catalyst characterization

Prior metal nanoparticle deposition, carboxylic groups were generated on MWCNTs and CNFs supports by a nitric acid treatment. Pd catalysts were prepared by liquid impregnation from $[Pd_2(dba)_3]$ in THF. Pt-Ru/MWCNT catalyst was prepared from [Ru(COD)(COT)] and $[Pt(COD)(CH_3)_2]$ precursors in toluene. All catalysts were reduced in a mixture of H_2/Ar at 350 °C.

IV-2-1-TEM micrographs

The TEM analysis of the Pd/MWCNT catalyst showed a rather narrow distribution of the metal particle size, with an overall mean diameter of 4.3 nm. As shown by a selected micrograph (Fig. 6), the Pd nanoparticles were well dispersed on the surface of the MWCNTs with a few large particles (8–12 nm) on some tubes, which may be due to the aggregate effect caused by a lower amount of carboxylic acid groups on their surface [25, 26]. The rest of the supports gave comparable characteristics, the average diameters are presented in Table 2, TEM micrographs in Figures 6 and corresponding nanoparticle size distributions in Figure 7.

Catalyst	Support	$d_{average}$	Pd %	Pt%	Ru%	BET (m^2/g
PH1	MWCNT (COOH)	4.3	3.8	0	0	214
PH2	N-MWCNT	2.7	3	0	0	119
PH3	CNF (COOH)	6.1	3	0	0	560
PH4	N-CNF	1.9	3	0	0	204

PH5	MWCNT (COOH)	5.9	0	4.5	2.5	214

Table 2: General characteristics of the catalysts

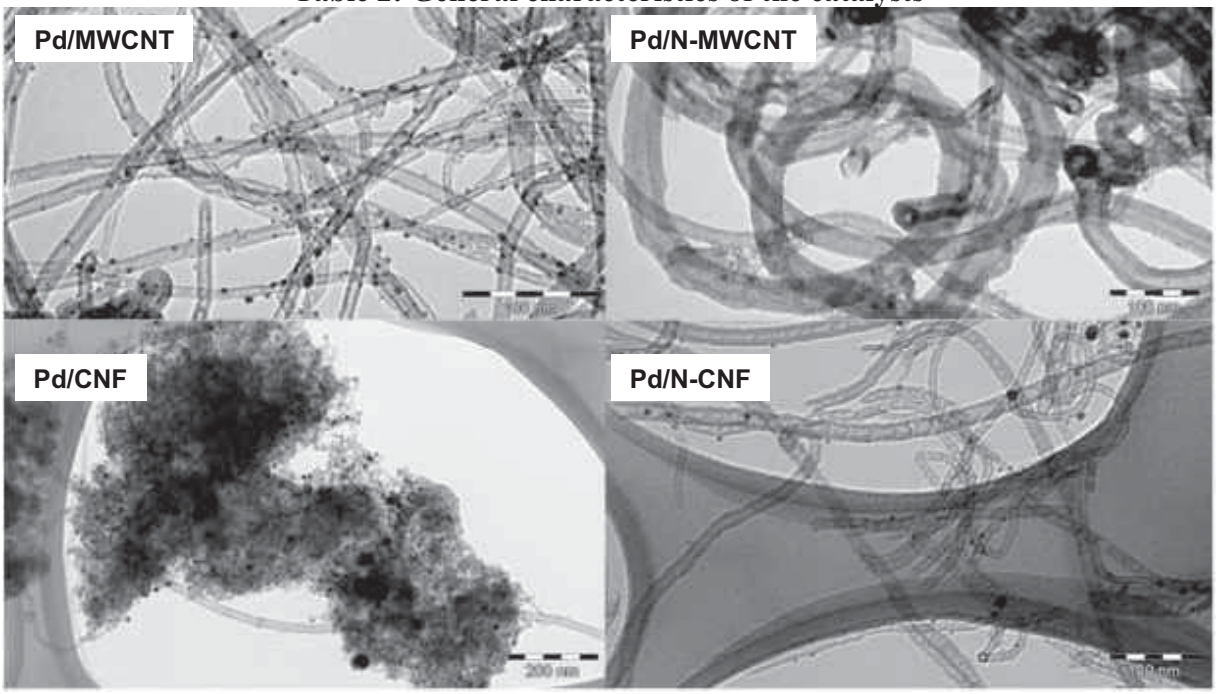

Figure 6: TEM micrographs of Pd/Carbon nanostructures electrocatalysts

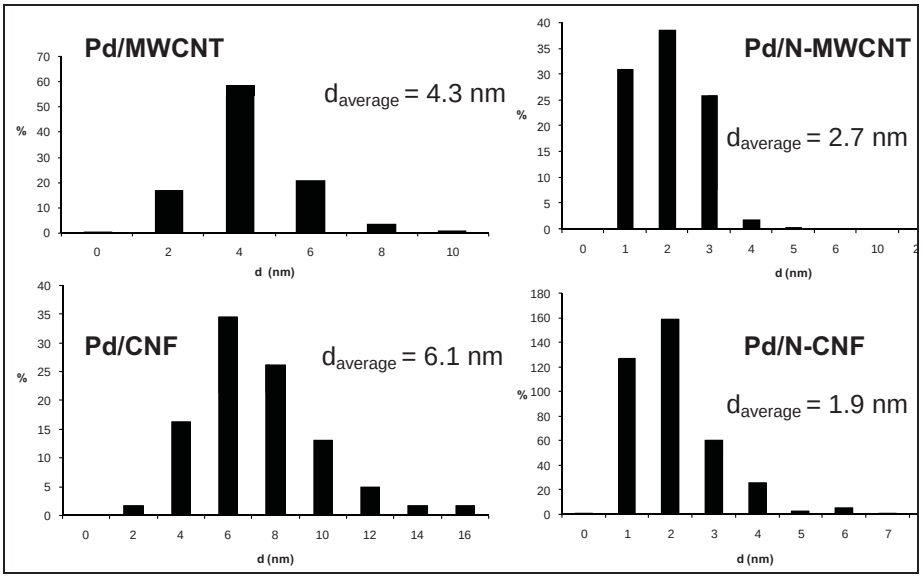

Figure 7: Histograms of Pd nanoparticles diameter distribution on different carbon nanostructures

The metal particles in the Pt–Ru/MWCNT catalyst were larger (5.9 nm average size), and less dispersed on the MWCNT surface than in the Pd/MWCNT one (Fig. 8). In particular, one may notice an accentuated concentration of metal particles, which may be due to the higher metal loading in the Pt–Ru/MWCNT.

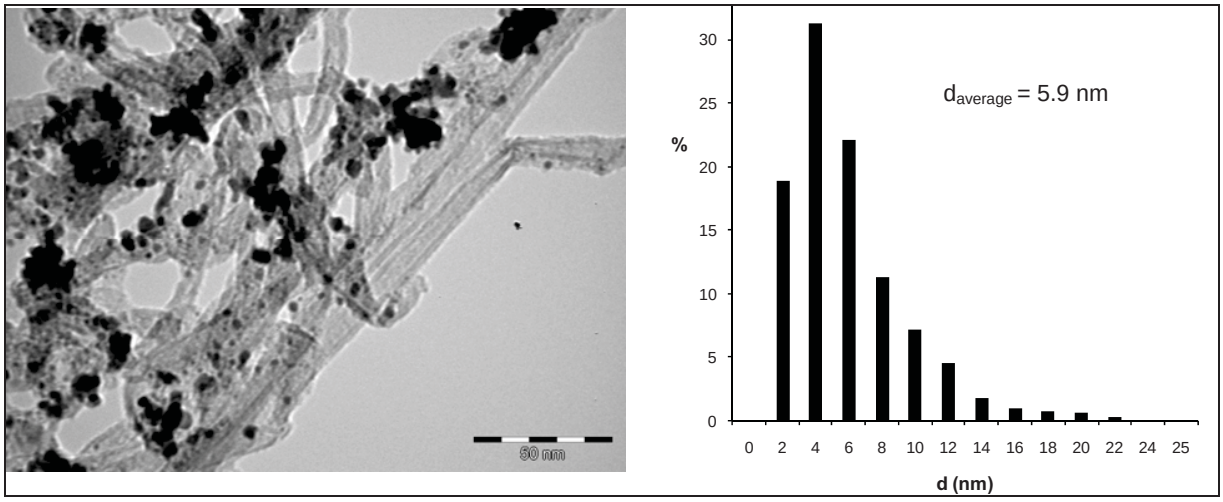

Figure 8: TEM micrographs of Pt–Ru/MWCNT and histogram of diameters distribution of particles

IV-2-2-XRD analysis

The structure of the Pd/MWCNT catalyst was investigated by XRD. Figure 9 shows the corresponding pattern where the diffraction peaks at the Bragg angles of 40.1°, 46.4° and 68.1° can be readily attributed to the (1 1 1), (2 0 0) and (2 2 0) facets of fcc Pd crystals [28, 29], while the peaks at ca. 25° and 44° are typical of the hexagonal graphite structure of the support [25].

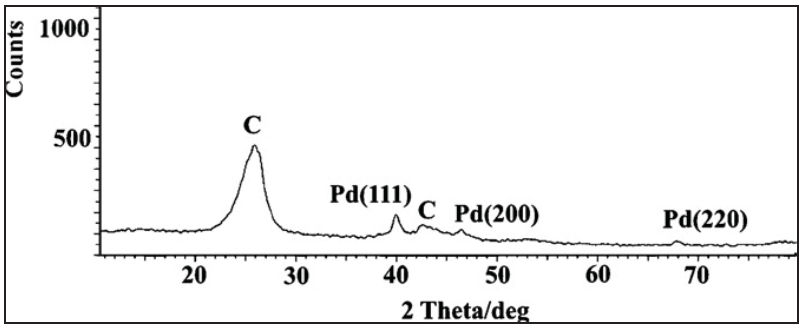

Figure 9: XRD pattern of Pd/MWCNT

The low intensity and broadness of the Pd peaks are consistent with the low metal loading as well as the high dispersion of the metal particles. Similar Pd diffraction peaks were observed with the Pd catalysts supported on N-MWCNTs and N-CNFs, but with the Pd/CNF catalyst the peaks were more intense in accordance with the lower dispertion previously observed in Figure 7 and Table 2.

The XRD diagram of Pt–Ru/MWCNT is shown in Figure 10. In addition to the peaks of the carbon support, the diagram displays the characteristic patterns of Pt–Ru aggregates with a relatively high Ru content [30–34]. In particular, diffraction peaks could be indexed to the (1 1 1) (40.1°), (2 0 0) (46.6°), (2 2 0) (67.9°), (3 1 1) (82.1°), (2 2 2) (86.5°) planes of a Pt-rich fcc phase. For Ru nanoparticles (hexagonal), the diffraction peaks could be indexed to the (1 0 0) (38.6°), (1 0 1) (43.9°), (1 1 0) (68.5°) and (1 0 3) (78.0°) planes. Since all peaks were slightly shifted to higher 2θ values as compared to the separated elements, one cannot disregard the presence of a Pt–Ru alloy [30–32].

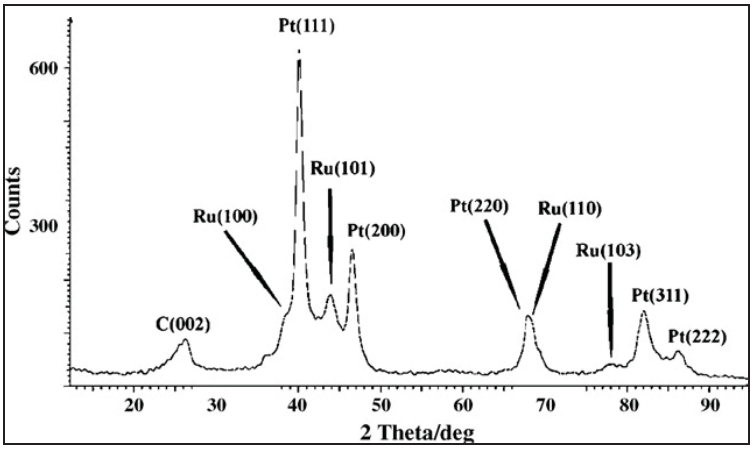

Figure 10: XRD pattern of Pt–Ru/MWCNT

IV-3-Electrochemical studies

IV-3-1-Electrochemical characterization of Pd/MWCNT in KOH solution

Before getting it in contact with any alcoholic fuel, the cyclic voltametry (CV) behavior of the Pd/MWCNT catalyst was preliminarily investigated in 2 M KOH solution. The corresponding cyclic voltammogram after the fifth cycle is reported in Figure 11.

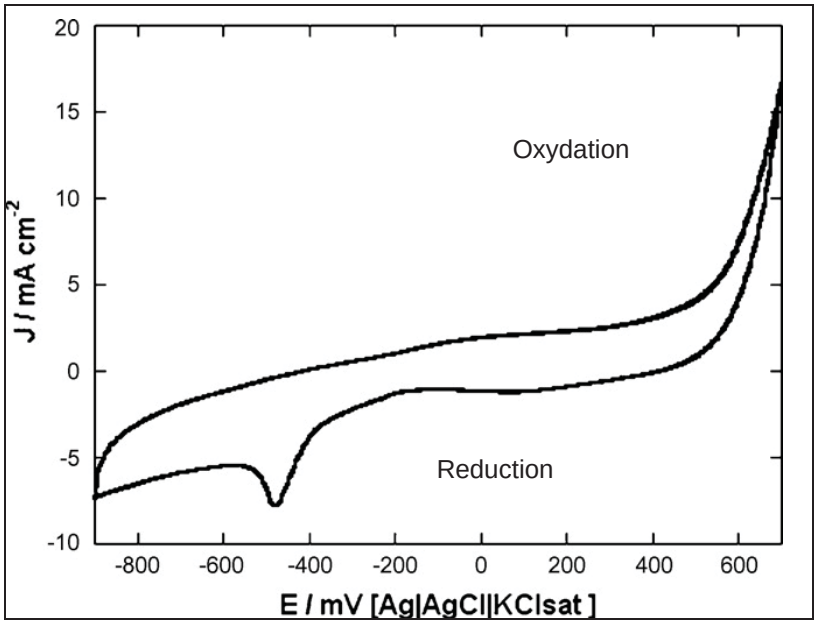

Figure 11: Cyclic voltammogram of Pd/MWCNT (at the fifth cycle) in 2 M KOH solution. Pd loading: 17 μg.cm^{-2}. Scan rate: 50 mV.s^{-1}.

The forward scan showed a very broad oxidation wave starting at ca. −200 mV, while a much narrower and more intense reduction peak was observed in the reverse scan with an onset potential of ca. −250 mV with a peak at -470 mV. The position and shape of this reduction wave are consistent with the reduction of nanostructured Pd^{II} species, either PdO or $Pd(OH)_2$. Indeed, in the range of potential investigated, the formation of Pd^{IV} species is to be ruled out [35–38]. Previous CV studies of electrodes coated with either PdO or nanostructured Pd in NaOH solution agree to consider the redox chemistry of these species as a quite complex process due to the number of possible oxide/hydrous or oxide/hydroxyl surface species [35, 39], which would explain the broad shape of the reduction wave.

IV-3-2-Electrochemical oxidation of methanol, ethanol and glycerol on Pd/MWCNT in half cells

The electrochemical activity of the Pd/MWCNT catalyst for methanol, ethanol and glycerol oxidation was investigated by cyclic voltametry at room temperature in deoxygenated 2 M KOH solutions. A series of cyclic voltammograms recorded at KOH concentrations spanning from 0.5 to 4 M showed the generation of the highest current densities in the range of 1–1.5 M of KOH. However all the following electrochemical studies, either in half cells or in monoplanar cells, were carried out using a 2 M KOH solution to keep the OH^- concentration as constant as

possible all over the experiment. Indeed, the oxidation of alcohols in alkaline media consumes OH^- groups (Eq. 8), irrespective of the oxidation level of the substrate [11, 40, 41].

$$R\text{-}CH_2\text{-}OH + 5\ OH^- \longrightarrow R\text{-}COO^- + 4\ H_2O + 4\ e^- \quad (8)$$

All the CV measurements were performed at a sweep rate of 50 $mV.s^{-1}$ on solutions containing 10 wt.% methanol, 10 wt.% ethanol or 5 wt.% glycerol using glassy carbon electrodes with a Pd loading between 16 and 17 $\mu g.cm^{-2}$ (Fig. 12).

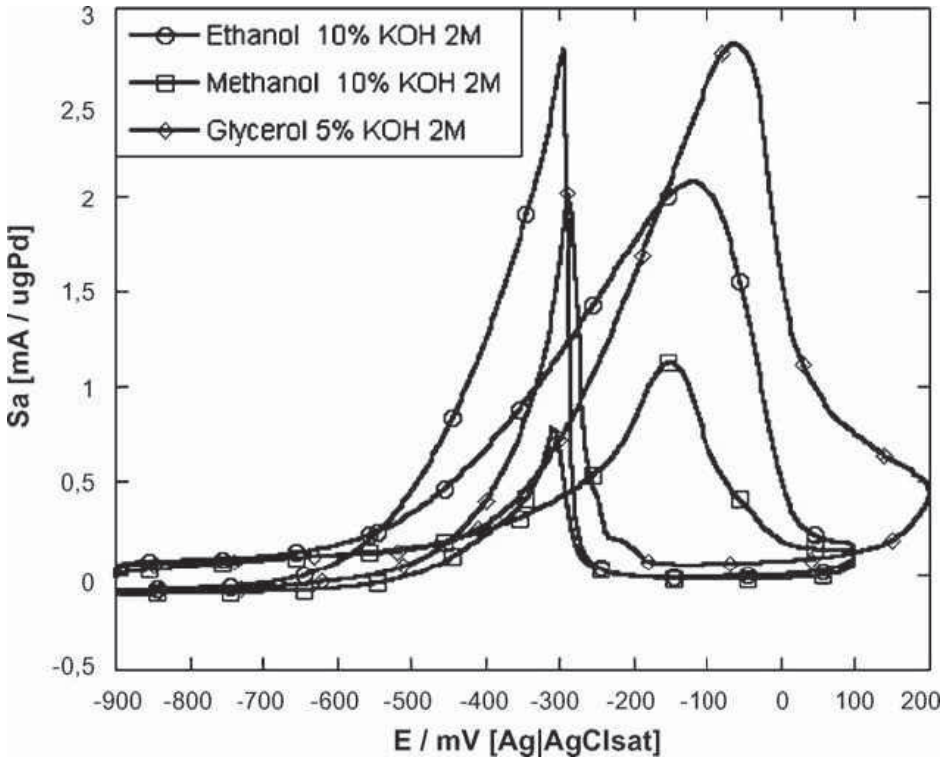

Figure 12: Cyclic voltammograms (at the fifth cycle) of methanol, ethanol and glycerol oxidation on a Pd/MWCNT electrode in 2 M KOH solution Pd loading: 17 μg.cm^{-2}. Scan rate: 50 mV.s^{-1}.

Depending on their characteristics, polyelectrolyte membranes have an alcohol permeability threshold relative to alcohol concentration. Beyond such threshold, the cross-over phenomenon occurs in the DAFCs: alcohol passage from anodic to the cathodic compartment via the membrane. Thus, higher alcohol concentrations, although yielding higher current densities, were not considered. Indeed, it is generally found that at concentrations higher than 10 wt.%, the alcohol cross-over may become relevant for most polymer ion-exchange membranes [39, 40]. This would result in increased cell overvoltage and also in decreased efficiency due to fuel loss by evaporation from the cathode compartment.

Relevant electrochemical parameters such as peak current density (J_p), specific peak current density (Sa_p), forward anodic peak potential (V_p) and Tafel slopes, together with the electronic transfer coefficient α, are given in Table 3 for all fuels investigated.

Substrate	Jp (mA.cm^{-2})	Sa_p(mA.μg.Pd^{-1})	V_p[b] (V)	V_{onset} (V)	Tafel slope (mV dec^{-1})
Methanol	19.4	1.1	-0.15	-0.55	282 (α 0.21)
Ethanol	35.1	2.1	-0.12	-0.75	249 (α 0.24)
Glycerol	53.7	2.8	-0.08	-0.60	-

[a]Average values for at least 3 measurements; [b]versus Ag/AgCl/KCl_{sat}

Table 3: Relevant electrochemical parameters for the methanol, ethanol and glycerol oxidation reactions on a Pd/MWCNT electrode[a]

The catalyst was active for the oxidation reaction of all alcohols investigated. In terms of peak current density, glycerol provided the best performance out of the three alcohols investigated in spite of its lower concentration, yet ethanol showed the lowest onset potential (-0.75 V vs. > -0.60 V for glycerol). The worst results were obtained with methanol, especially in terms of current density and oxidation overpotential. Since the peak back current decreased with increasing the anodic limit (from -0.1 to 0.6 V) for all alcohols, one may reasonably conclude that the backward scan peaks are compatible with the oxidation of both freshly chemisorbed substrate and residual adsorbed species [31]. The less marked decrease of the backward scan peak observed for ethanol suggests the formation of more weakly adsorbed species as compared to those originated by methanol and glycerol.

From a perusal of the literature and considering the very low Pd loading used (16–17 μg.cm^{-2}), one may readily realize that Pd/MWCNT can be classified among the most active electrocatalysts ever reported for the oxidation of alcohols in half cells, especially for ethanol and glycerol. Analogous results, in terms of onset potential and J_p for the oxidation of the present alcohols, have been reported by Shen et al. for a family of nanostructured Pd electrocatalysts, which includes Pd/C (C = Vulcan XC-72 [15]), oxide-promoted Pd/C (oxide = CeO_2, NiO, Co_3O_4, Mn_3O_4 [11], and Pd/CPAA (CPAA= carbonized and pulverized anodic alumina) [14]. However, the Pd loading on the Shen's anodes, being significantly higher than that in the present Pd/MWCNT catalyst (300 vs. 17 μg.cm^{-2}), ultimately yields Sa_p values lower by ca. an order of magnitude, irrespective of the alcohol, even for the best oxide supported Pd/C catalyst [14].

The better dispersion of the metal particles in Pd/MWCNT than in Pd/C, oxide-promoted Pd/C or Pd/CPAA (average 3.8 vs. 7–10 nm [14, 15]) and the intrinsic properties of the

MWCNT support (different macro- and meso-structure and higher electroconductivity and alcohol permeability as compared to carbon black) may well account for the remarkable activity of the present catalyst. The effect of the carbon support on the activity of Pd-electrocatalysts for ethanol oxidation in alkaline media has been previously investigated by Shen et al. for Vulcan XC-72, MWCNTs and activated carbon fibers [25]. It was found that, at comparable metal loading, the MWCNT-supported catalyst gives improved performance in terms of both peak current density and electrochemical stability. On the other hand, a reliable comparison between the MWCNT supported Pd catalyst described by Shen [14] and the present one is again precluded by the largely different Pd loadings (200 $\mu g.cm^{-2}$ in the former for a J_p of 25 $mA.cm^{-2}$; 17 $\mu g.cm^{-2}$ in the latter for a J_p of 35.1 $mA.cm^{-2}$), which apparently makes our Pd/MWCNT system twenty times more active for ethanol oxidation in terms of specific current density.

Tafel plots for methanol and ethanol oxidation reactions on the Pd/MWCNT electrode were obtained at a scan rate of $5mV.s^{-1}$ in the potential interval from -0.5 to -0.4 V. The usual form of the Tafel equation is expressed in Eq. 9.

$$\eta_{act} = (R\ T / \alpha\ n\ F)\ \ln (i / i_0) \qquad (9)$$

$\eta_{act} = a + b \ln I$ and $b = RT/ \alpha\ n\ F$

The term b is called the Tafel slope, and is obtained from the slope of a plot of η_{act} as a function of ln i, and α is the electron transfer coefficient of the reaction at the electrode being addressed, and i_0 is the exchange current density.

The two values of the Tafel slopes and α coefficients are quite comparable with each other (Table 1), yet they are significantly higher than those generally observed for nanostructured Pd catalysts supported on carbon black (ca. 190 $mV.dec^{-1}$) [13, 15]. The almost identical Tafel slopes for the oxidation of methanol and ethanol indicate the same reaction mechanism, while

the α parameters of 0.21 and 0.24 are consistent with an electrochemical rate limiting step for the oxidation reaction of both alcohols. As for the absolute values of the Tafel slopes, the high values observed are in line with porous high surface area electrodes [13, 42]. On such electrodes the charge transfer region is very narrow and mass transport interferences may be very important. Moreover, the oxidation of alcohols, especially of polyalcohols, can be mechanistically complicated by the occurrence of parallel steps (Fig. 13).

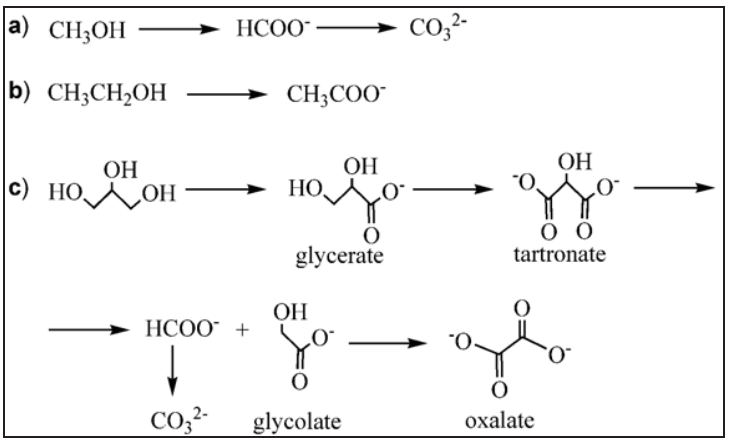

Figure 13: Products obtained by electro-oxidation of (a) methanol; (b) ethanol; and (c) glycerol on Pd/MWCNT

This is certainly the case of the glycerol oxidation reaction on the Pd/MWCNT electrode for which no linear dependence of log J vs. overpotential was actually observed.

The performance stability of the Pd/MWCNT electrocatalyst for methanol, ethanol and glycerol oxidation was investigated by chronopotentiometry. Steady state measurements were carried out by a constant current density polarization of 3.46 $mA.cm^{-2}$ (Fig. 14). As shown by the chronopotentiometric traces, the steady-state oxidation of ethanol was quite stable with negligible potential oscillation, indicative of no strongly adsorbed species on the catalyst surface.

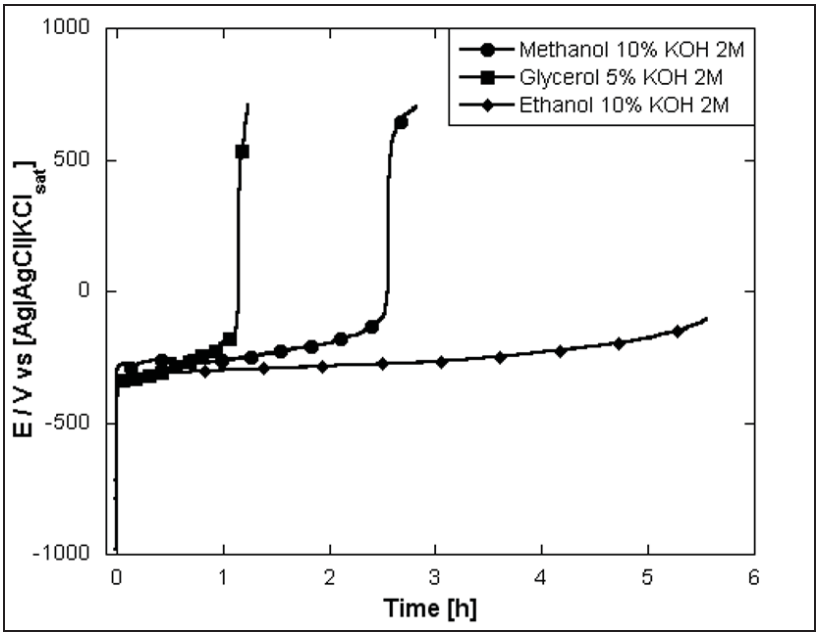

Figure 14: Chronopotentiometric traces of methanol (10 wt. %), ethanol (10 wt.%) and glycerol (5 wt.%) oxidation on a Pd/MWCNT electrode at 3.46 mA.cm^{-2} in 2 M KOH solution

As put in evidence by the ionic chromatography analysis of the chronopotentiometric solutions after 5 h and by the NMR analysis of the exhausts of passive and active DEFCs, it has been possible to establish that the oxidation of ethanol on Pd/MWCNT yields selectively acetic acid, transformed into acetate ion in the alkaline media of the reaction (10).

$$C_2H_5OH + 5\ OH^- \longrightarrow CH_3COO^- + 4\ H_2O + 4\ e^- \qquad E°=-0.743V \quad (10)$$

The increase in the response potential after 3 h might be due to several factors, which include the increasing viscosity of the solution at the electrode interphase, resulting in a slower diffusion rate of ethanol, the decreasing concentration of OH^- anions due to their consumption, and the increasing coverage of the catalyst surface with Pd-acetyl species whose reaction with OH_{ads} is believed to generate acetic acid [7]. Unlike ethanol, the potentials of glycerol and methanol oxidation increased rapidly with time, reaching the value of the oxygen evolution reaction only after 1 and 2 h, respectively, which is consistent with an effective electrode deterioration under the static half cell conditions.

For a rationalization of the chronopotentiometric tests, it may be useful to anticipate the results obtained from galvanostatic experiments with passive DAFCs (alcohol = methanol, ethanol, glycerol) (*vide infra)*. Ionic chromatography and NMR analysis of the cell exhausts showed unequivocally that ethanol was selectively converted on the Pd/MWCNT anode to acetate with no detection of intermediate species, while methanol gave carbonate via formate. In contrast, glycerol was converted to a plethora of species among which the C-C bond cleavage products glycolate, oxalate, formate and CO_3^{2-} (Fig. 13). The lower electrochemical stability of the Pd/MWCNT electrode for the methanol oxidation as compared to ethanol oxidation can be accounted for by the formation of CO as intermediate species in the former reaction. Indeed, unlike ethanol which is selectively converted to acetate, the oxidation of methanol on Pd/MWCNT occurs with formation of CO, successively oxidized to CO_2 (detected as CO_3^{2-} in the alkaline media of the present electrochemical reactions). The oxidation of CO adsorbed on noble metals such as Pt or Pd is rather difficult to achieve at low potential due to the strong binding of this molecule to metal centers [6–9, 11, 43]. As a matter of fact, the poisoning of Pt-based electrocatalysts by CO is an issue of extreme relevance for the development of both DAFCs in either acidic and alkaline conditions [6–9, 11, 43, 44] as well as PEMFCs using reformate hydrogen. Numerous papers on this subject have appeared in the literature [45]. A method commonly used to alleviate the dramatic overpotentials caused by the electro-oxidation of CO_{ads} is to alloy Pt with other metals such as Ru or Sn, yet all reported Pt-based catalysts undergo deactivation with time, which requires high metal loading to ensure an acceptable durability of the corresponding DMFCs. The formation of CO_{ads} may contribute to increase the polarization of the Pd/MWCNT electrode during glycerol oxidation, but it alone can hardly account for its much faster deactivation as compared to methanol oxidation (Fig. 14). In fact, the products derived from C–C bond cleavage paths, leading to CO_{ads} constitute a minor fraction (30–40%) of the overall transformation of glycerol. Besides, current studies of glycerol oxidation with nanostructured Pd catalysts supported on Vulcan XC-72 [46], showed an inverse trend with glycerol being a much better fuel than methanol in terms of both electrode polarization and power density produced. Therefore, other factors than CO poisoning of the Pd sites must

contribute to decrease the electrochemical stability of the Pd/MWCNT electrode for glycerol oxidation. It is likely that a major contribution to the observed polarization is provided just by the MWCNT support that, under the experimental conditions of the chronopotentiometric tests (room temperature), might disfavor either the access of glycerol to the active Pd sites or the desorption of the hydroxycarboxylate products (glycerate, tartronate and glycolate). It is worth recalling, in fact, that the MWCNTs used in this work contain a significant amount of surface carboxylic acid groups; therefore the different acidity of the alcohols employed as well as the different propensity of the intermediate products to form H bonds may well affect both the mass transfer through the catalytic layer and the product desorption. In the future, tests should be conducted after carboxylic group removal with a heat treatment similar to the one used in Chapter III.

The importance of substrate diffusion/product desorption in controlling the electro-oxidation of glycerol on the Pd/MWCNT electrode was confirmed by the plot of the anodic peak current density against the square-root of the scan rate as well as the performance of the relative active DAFC. Indeed, above 50 °C, the power density produced by the DGFC was higher than that of the DEFC and only slightly inferior to that of the DMFC (*vide infra*).

For all electrodes, the anodic peak current density for alcohol oxidation was plotted against the square-root of the scan rate (Fig. 15). As shown in Figure 15A, a linear relationship, typical of an electrochemical reaction under diffusion control, was found for the oxidation of ethanol at scan rates lower than 350 $mV.s^{-1}$. Above this scan rate, the slope decreased tending to a plateau, as if the peak current density were independent of the voltage scanning frequency. Apparently, at scan rates higher than 350 $mV.s^{-1}$, the ethanol oxidation reaction on Pd/MWCNT is limited by other factors than substrate diffusion, for example the very low density of catalytic centers due to the extremely low Pd loading (17 $\mu g.cm^{-2}$) as well as the desorption rate of the acetate product. A much narrower window of diffusion-controlled kinetics was observed for the oxidation of glycerol (Fig. 15B), the independence of the peak current density on the voltage scanning frequency being attained already at scan rates above 50 $mV.s^{-1}$.

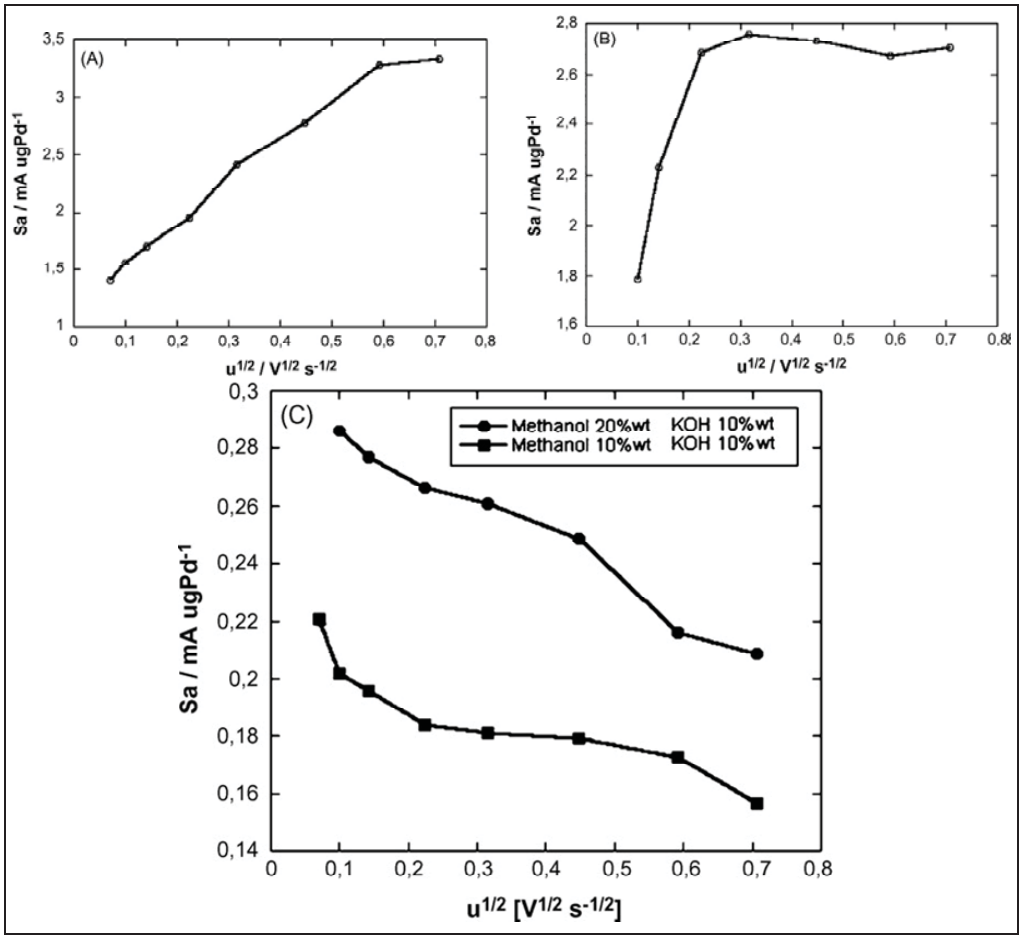

Figure 15: Plots of the anodic peak current density against the square-root of the scan rate for the oxidation on the Pd/MWCNT electrode of (A) ethanol; (B) glycerol; and (C) methanol (10 wt.% MeOH and 2M KOH; 20 wt.% MeOH and 2 M KOH)

The Sa_p / ($V^{½}.s^{-1/2}$) profile acquired for the oxidation of methanol was quite surprising (Fig. 15 C), since the peak current density was found to decrease with the scan rate, even by increasing the concentration of MeOH from 10 to 20 wt. %, in an attempt of magnifying the diffusion effects. Apparently, the diffusion of MeOH across the MWCNT support is very fast but the electrocatalyst is not sufficiently active and the peak current density decreases by increasing the scan rate. As an indirect confirmation of the role of the carbon support in controlling the substrate diffusion, it has been reported that the oxidation of methanol on an electrode catalyzed by nanostructured Pd particles supported on Vulcan XC-72 (same metal loading as in Pd/MWCNT) is diffusion-controlled in the range of scan rates from 50 to 500 $mV.s^{-1}$ [47].

IV-3-3-Electrochemical oxidation of ethanol and glycerol on 3 % Pd/N-CNF in half cells

There was a huge modification when using N-CNFs in comparison with the MWCNT support. In both ethanol and glycerol fuels, the peak current density were lower using the N-CNF support (Fig. 16) and the Tafel slope in the case of ethanol was a little bit higher (Table 4).

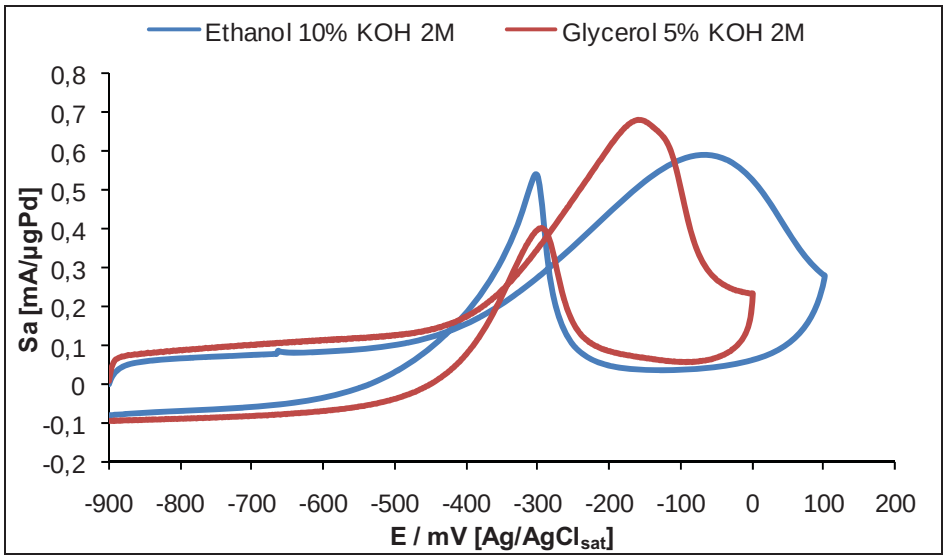

Figure 16: Cyclic voltammograms (at the fifth cycle) of ethanol and glycerol oxidation on a Pd/N-CNF electrode in 2 M KOH solution. Pd loading: 27 µg.cm^{-2}. Scan rate: 50 mV.s^{-1}

The change in the mechanism of reactant diffusion related to the changes of the carbon support structure was relevant from the plot of the anodic peak current density against the square-root of the scan rate (Fig. 17). In fact, what was observed with MWCNTs was exactly the opposite with N-CNF. Ethanol diffusion from the solution to the catalyst surface was controlled by the scan rate until 360 mV.s^{-1} for MWCNTs and was shorter at 120 mV.s^{-1} for N-CNFs. This meant that diffusion of ethanol on the N-CNFs surface was better. After 120 mV.s^{-1} the Pd suported on N-CNFs becomes less active to ethanol oxidation due either to poisoning or sluggish kinetic.

Substrate	Jp (mA.Cm^{-2})	Sa$_p$(mA.µg.Pd^{-1})	V$_p^b$ (V)	V$_{onset}$ (V)	Tafel slope (mV.dec^{-1})

Ethanol	15.6	0.58	-0.08	-0.75	259
Glycerol	18.1	0.67	-0.17	-0.61	-

[a]Average values for at least 3 measurements, [b]Versus $Ag/AgCl/KCl_{sat}$

Table 4: Relevant electrochemical parameters for the ethanol and glycerol oxidation reactions on a Pd/N-CNF electrode[a]

On the opposite the diffusion-controlled kinetics window of glycerol oxidation was unlimited between 10 and 640 $mV.s^{-1}$ at the Pd/N-CNF catalytic surface in comparison to the very narrow for the Pd/MWCNT one (Fig. 17).

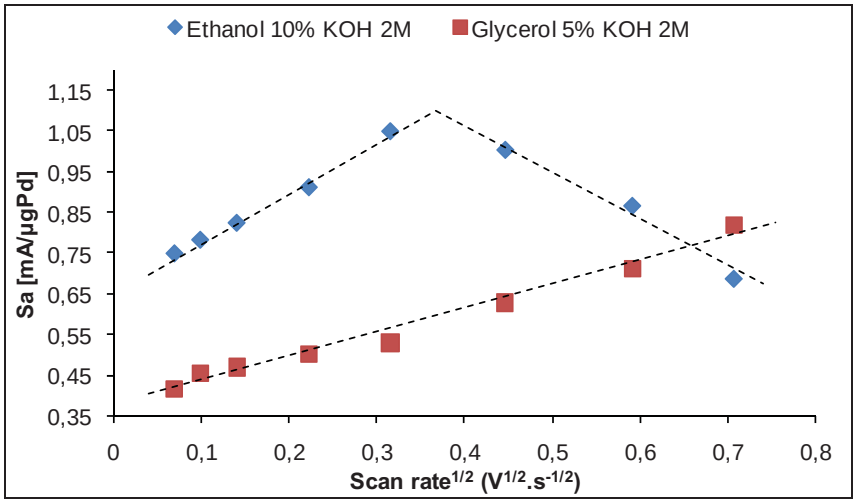

Figure 17: Plots of the anodic peak current density against the square-root of the scan rate for the oxidation on the Pd/N-CNF electrode of ethanol and glycerol

An exact explanation for the difference between MWCNTs and N-CNFs is difficult: the orientation of the graphene layer and thus polarity and electron conductance has changed; nitrogen atomic insertion replaced the carboxylic surface groups that were lowering reactant/product diffusion. All this contribute that adsorption of glycerol on the N-CNFs is weaker than on MWCNTs. Ethanol adsorption on MWCNTs should also be weaker than on N-CNFs.

The steady-state oxidation of ethanol with MWCNTs disappeared with the Pd/N-CNF catalyst that deteriorated only after 20 minutes (Fig. 18). In the case of glycerol the life time of the electrode was prolonged with the Pd/N-CNF catalyst, 2 h in comparison with 1 h with the

Pd/MWCNT catalyst (Fig. 14 and 18). All these findings are complementary to the previous observations, ethanol diffuse very fast onto the N-CNF surface, and the electrode blocking is fast, glycerol diffusion is slow, and the blocking is slower. Even though yielding disappointing results, the comparison between the Pd supported on MWCNTs and N-CNFs enabled us to conclude the importance of the catalyst carbonaceous support structure and the surface composition (nitrogen insertion, carboxylic function) in the diffusion control and thus oxidation control of alcohols.

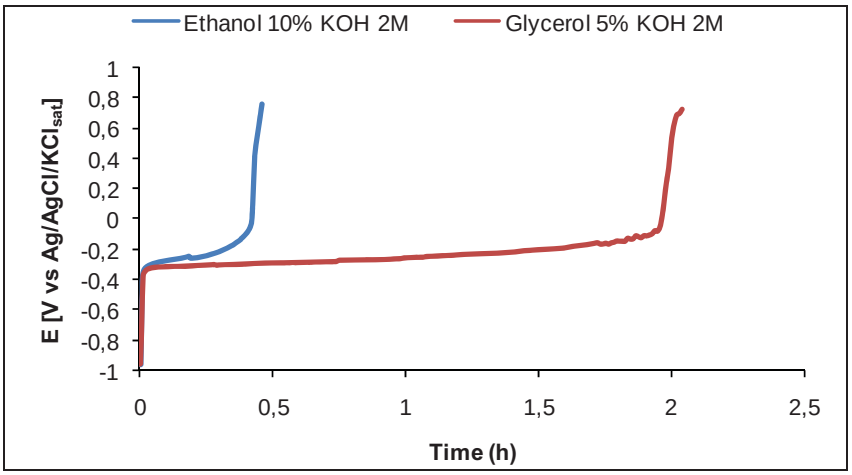

Figure 18: Constant current chronopotentiometry of the Pd/N-CNF catalyst (Pd 3 % w/w), I = 3 mA (J = 3.46 mA), fuel1: ethanol 10% KOH 2 M, catalyst loading: 27.7 µgPd/cm^{-2}, fuel2: glycerol 5% KOH 2 M, catalyst loading: 28.6 µgPd/cm^{-2}.

IV-4-DAFCs fuelled with methanol, ethanol or glycerol containing Pd/MWCNT-catalyzed anodes

The prepared electrocatalysts were tested in both passive (batch process) and active (continuous fuel feed) modes of direct alkaline fuel cells (DAFC).

IV-4-1-Passive (oxygen-breathing) systems

IV-4-1-a-Multiwalled carbon nanotubes supported Pd

The MEAs for the passive monoplanar DAFCs were realized as described in chapter V, with the anode catalyzed by Pd/MWCNT (0.7mg.cm^{-2} Pd), a Fe-Co HypermecTM K-14 cathode

and a Tokuyama A-006 membrane. The polarization and power density curves obtained with methanol, ethanol and glycerol in 2M KOH solution at room temperature are reported in Figure 19.

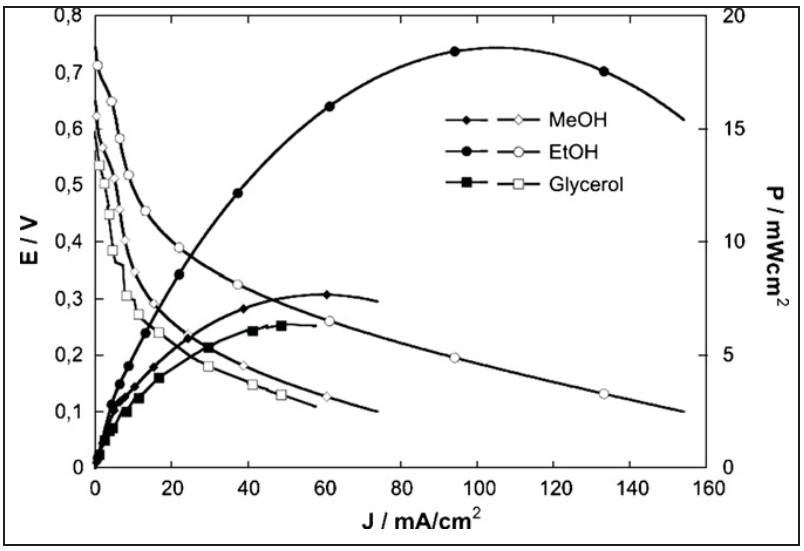

Figure 19: Polarization and power density curves provided by oxygen-breathing DAFCs fuelled with 2 M KOH solutions of methanol (10 wt. %), ethanol (10 wt. %) and glycerol (5 wt. %) at 20-22 °C

From a perusal of this figure, one may readily realize that the cell fuelled with ethanol shows the highest open circuit current (OCV) (0.74 V) and peak power density (18.4 mW.cm^{-2} at 0.2 V). To the best of our knowledge, no report has ever appeared in the relevant literature describing a passive DEFC equipped with an anion-exchange membrane. Just to better appreciate the result obtained with the present DEFC, a comparable power density (27 mW.cm^{-2} at 20 °C) has been recently obtained with an alkaline fuel cell (AFC) with a 3 M KOH solution as electrolyte and an anode catalyzed with 1 mg.cm^{-2} of Pt-black [48]. By the way, this AFC was reported to be selective for the transformation of ethanol into acetaldehyde. The lower performances of the DMFC and DGFC as compared to the DEFC are in line with the corresponding chronopotentiometric experiments (Fig. 14) for which a tentative explanation has been given above. The formation of carbonate upon oxidation of MeOH and to a lesser extent of glycerol, which may lead to membrane carbonatation, does not seem to account for the lower

performances of the DMFC and DGFC. In fact, the power densities obtained with the three fuels investigated did not appreciably vary by using MEAs where the membrane was either in the OH^--form or in the CO_3^{2-}-form.

While no comparison can be made with other DGFCs for the lack of known examples, the power density provided by the DMFC (8 $mW.cm^{-2}$) matches well the value reported by Coutanceau et al. for a DMFC fuelled with MeOH in 1 M NaOH, and equipped with an ADP-type membrane from Solvay and an anode catalyzed with 2 $mg.cm^{-2}$ of Pt–Pd nanoparticles supported on Vulcan XC-72 [11].

Galvanostatic experiments were carried out with the present DMFC, DEFC and DGFC charging the anode compartment with 40.7 mmol of MeOH, 28.3 mmol of EtOH or 6.8 mmol of glycerol, respectively (Fig. 20).

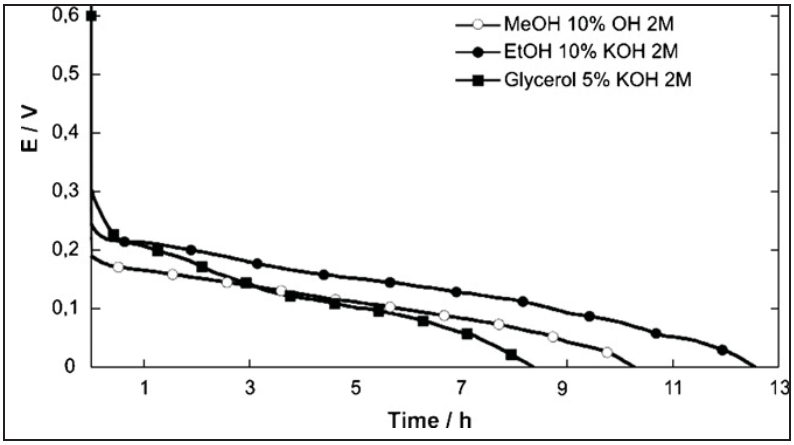

Figure 20: Galvanostatic traces of DAFCs fuelled with methanol, ethanol or glycerol oxidation at 102 mA

After a conditioning time of 1 h at the OCV, the circuit was closed and a constant current of 102 mA was allowed to flow until zero voltage.The DEFC continued to deliver constantly 102 mA for 12.5 h yielding 12 mmol of acetate and leaving 12 mmol of unreacted EtOH, as determined by $^{13}C\{^1H\}$ NMR spectroscopy on the cell exhausts (Fig. 21A).

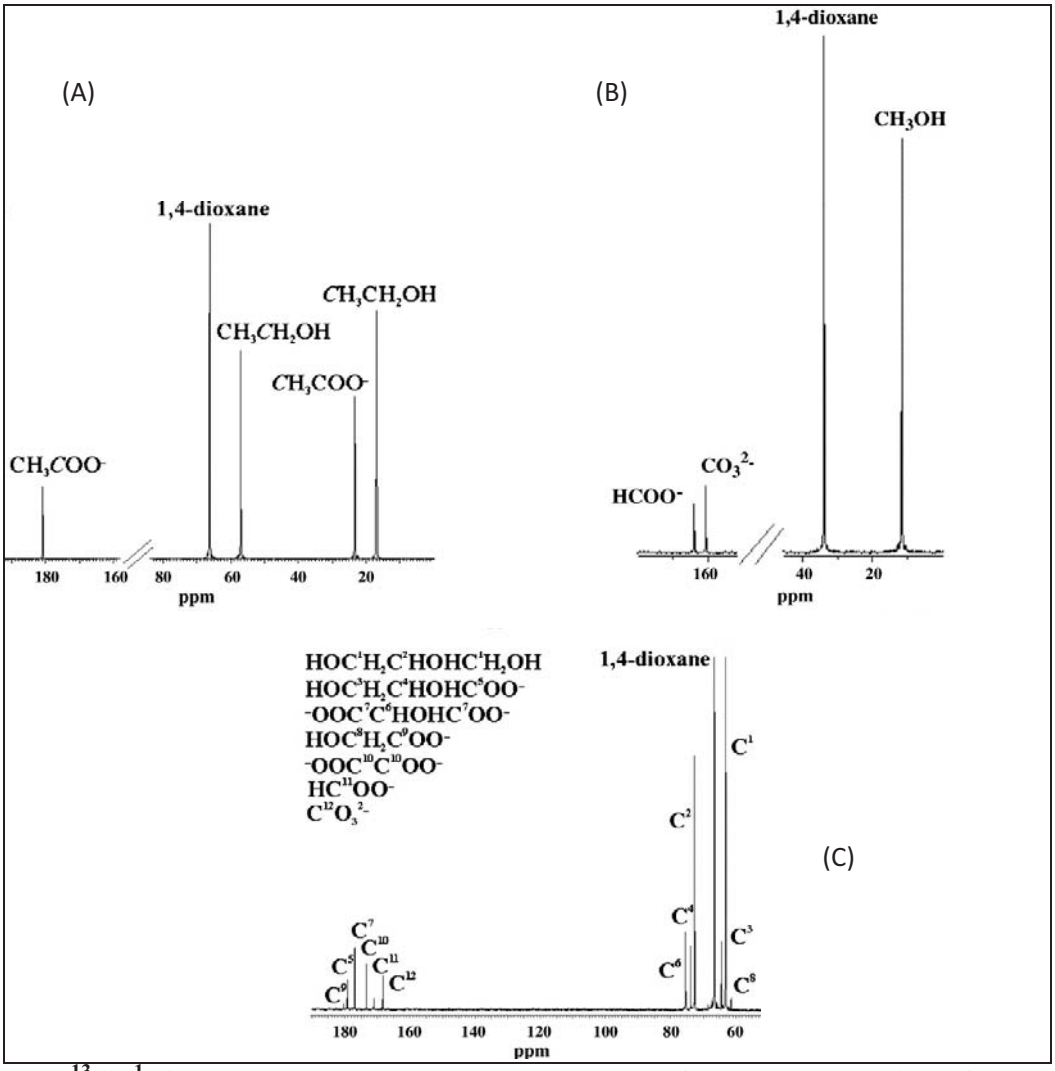

Figure 21: ^{13}C {^{1}H} NMR spectra at room temperature of the anode solution after 12.5 h at 102 mA of (A) DEFC; (B) DMFC; and (C) DGFC

Accordingly, ca. 4 mmol of EtOH were lost by evaporation, likely from the cathode side as cross-over alcohol. The overall DEFC reaction can be illustrated as in Eq. (11).

$$C_2H_5OH + O_2 + OH^- \longrightarrow CH_3COO^- + 2\,H_2O \quad (11)$$

$$CH_3OH + O_2 + OH^- \longrightarrow HCOO^- + 2\,H_2O \quad (12)$$

$$HCOO^- + 1/2\,O_2 + OH^- \longrightarrow CO_3^{2-} + H_2O \quad (13)$$

Under comparable conditions, the DMFC lasted 10.3 h yielding 3 mmol of formate and 7 mmol of carbonate, according to Eqs. (12) and (13), with 22 mmol of unreacted MeOH (Fig. 21B). The loss of substrate was therefore of ca. 8 mmol, in line with the lower boiling point of methanol and its easier permeation through the membrane as compared to ethanol.

The qualitative and quantitative analysis of the DGFC exhausts was complicated by the variety of products obtained (Fig. 13 and 21C). Overall, the cell continued to provide current for 8.4 h producing 3070 coulomb and leaving 10 mmol of unreacted glycerol. In line with the high boiling point and size of the latter molecule, no appreciable loss of fuel occurred, as the products obtained accounted for the 3.8 mmol of glycerol consumed. The following product distribution was determined by NMR and ionic chromatography: glycolate (4%), glycerate (27%), tartronate (23%), oxalate (15%), formate (9%) and carbonate (22%).

Most importantly, all the DAFCs described above were fully regenerated (same OCV and galvanostatic performance) upon replacement of the cell exhausts with fresh 2 M KOH solutions of methanol (10 wt. %), ethanol (10 wt. %) or glycerol (5 wt. %). This procedure was repeated four times with no apparent performance decay. Therefore, we are inclined to ascribe the severe polarizations shown in Figure 20 to the increasing viscosity of the solutions and the competitive adsorption of substrate/partial oxidation product on the catalyst surface rather than to catalyst or electrode poisoning.

IV-4-1-b-Other carbonaceous supports

None of the other carbon nanostructures supported Pd catalysts yield any better results in alkaline media than MWCNTs (Table 5).

Fuel	MWCNTs		N-MWCNTs		CNFs		N-CNFs	
	OCV (V)	Peak power density ($mW.cm^{-2}$)	OCV (V)	Peak power density ($mW.cm^{-2}$)	OCV (V)	Peak power density ($mW.cm^{-2}$)	OCV (V)	Peak power density ($mW.cm^{-2}$)
MeOH	0.65	8	0.60	1.2	0.54	1.7	-	-
EtOH	0.74	18.4	0.58	4	0.62	4.1	0.67	6
Glycerol	0.60	5	0.58	1.4	0.56	1.8	0.64	4.5

Table 5: DAFCs results with methanol, ethanol or glycerol containing Pd/carbonaceous supports-catalyzed anodes

Once again, the role played by the carbonaceous support in the catalytic activity is evidenced. Under our conditions, MWCNTs were largely better than N-MWCNTs, CNFs and N-CNFs as support for the Pd active electrocatalyst on the anodic electrode for alcohol oxidation.

IV-4-2-Active DAFCs

The MEAs for the active monoplanar DAFCs were realized as described in chapter V, with Pd/MWCNT (1 mg.cm^{-2} Pd) as anode catalyst, a Fe-Co HypermecTM K-14 cathode and a Tokuyama A-006 membrane. The fuel (water solutions containing 10 wt. % methanol, 10 wt. % ethanol or 5 wt. % glycerol) was delivered to the anode at 4 mL.min^{-1}, while the oxygen flow was regulated at 200 mL.min^{-1}. Each cell temperature was regulated at 25, 40, 60 or 80 °C.

Fig. 22 shows the polarization and power density curves for all the DAFC investigated. In the temperature interval from 25 to 40 °C, the performance trend exhibited by the three DAFCs was analogous to that found for the passive cells, with the DEFC being superior to both the DMFC and the DGFC.

Unexpectedly, however, increasing the cell temperature to 60 °C led to a reverse order of activity with the highest power density provided by the DMFC (peak power density of 95 mW.cm^{-2} at 80 °C) and the lowest peak power density provided by the DEFC (73 mW.cm^{-2} at 80 °C). In particular, the latter cell was featured by a sudden drop of voltage after 300 mA.cm^{-2}, which is consistent with a strong contribution of the concentration polarization to the overall cell polarization. Below 300 mA.cm^{-2} at 80 °C, the DEFC was competitive with the other cells. In the absence of further data, it would be hazardous to put forward any clear-cut explanation for these results. On the other hand, it is reasonable to think of a specific role of the functionalized MWCNT support in differentiating the diffusion of each substrate at high temperature. Indeed, recent studies in the ICCOM-CNR laboratory of Dr Bianchini have shown that ethanol is a better fuel than methanol or glycerol at any temperature from 20 to 80 °C in DAFCs identical with

those described in our work, except for having the anode catalyzed by nano-sized Pd particles supported on Vulcan XC-72 instead of MWCNTs [47].

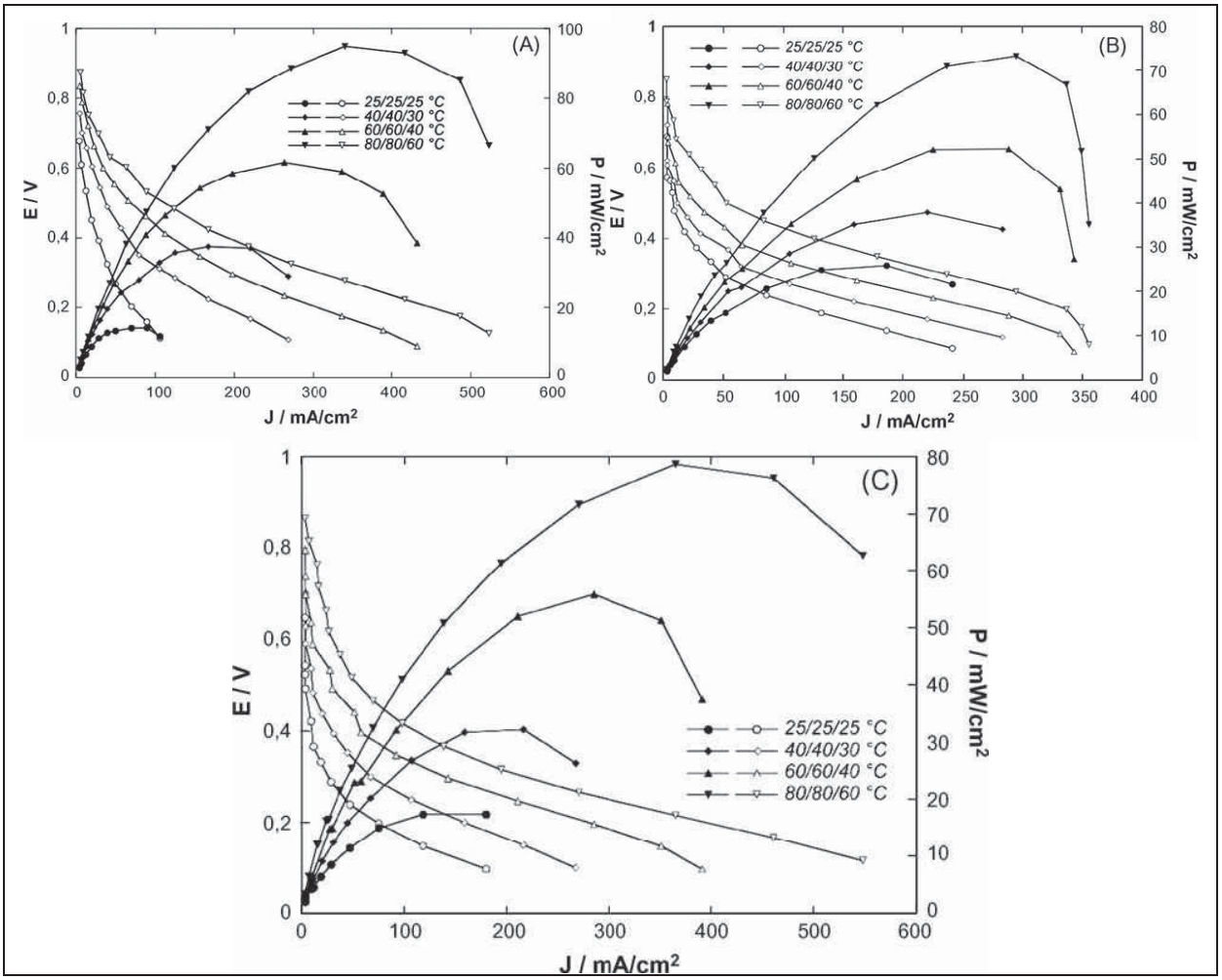

Figure 22: Polarization and power density curves at different temperatures of active DAFC with a Pd/MWCNT anode (metal loading 1 mg.cm^{-2}), fuelled with an aqueous 2 M KOH solution of (A) methanol (10 wt. %); (B) ethanol (10 wt. %); (C) glycerol (5 wt. %). Inset report the temperatures of fuel (left), cell (central), oxygen gas (right)

Unlike the case of the passive DAFCs for which the absence of reports in the literature has not allowed us to make a comparative study, some examples of active devices with anion-exchange membranes have been already described. Ogumi et al. have reported on active DAFCs fed with 1 M KOH solutions of various alcohols and polyalcohols, including methanol and glycerol, but not ethanol [41]. The anode and cathode catalyst were Pt–Ru/C (4 mg.cm^{-2}) and

Pt/C (1 mg.cm^{-2}) (C = Vulcan XC-72) from E-TEK (USA), respectively, and the solid electrolyte was a Tokuyama AHA membrane. At 45 °C, the peak power densities with methanol and glycerol were 8 mW.cm^{-2} at 28 mA.cm^{-2} and 6 mW.cm^{-2} at 27 mA.cm^{-2}, respectively. Scott et al. have investigated the performance of an active DMFC using a Morgane®-ADP membrane from Solvay using Pt–Ru/C (1 mg.cm^{-2}) as anode catalyst and Pt/C as cathode catalyst (both from E-TEK) [40]. At 60 °C using an oxygen flow, the highest power density was ca. 11 mW.cm^{-2} at ca. 40 mA.cm^{-2}. An active alkaline DEFC has been described by Hou et al. where the anode and cathode were catalyzed by commercial (Johnson-Matthey) Pt–Ru/C (2 mg.cm^{-2}) and Pt/C (1 mg.cm^{-2}) catalysts, respectively and the solid electrolyte was a polybenzylimidazole membrane doped with KOH, which is not a real anion-exchange membrane, however [49]. At 75 °C, a peak power density of 49 mW.cm^{-2} was obtained that increased to 61 mW.cm^{-2} by increasing the cell temperature to 90 °C. Since the peak power densities provided by the present DAFCs at 80 °C range from 95 mW.cm^{-2} with MeOH to 73 mW.cm^{-2} with EtOH at Pd loadings of ca. 1 mg.cm^{-2}, one may readily conclude that Pd/MWCNT exhibits unrivalled activity as anode electro-catalyst for alcohol oxidation.

IV-5-Electrochemical oxidation of methanol on Pt-Ru/MWCNT in half cells and in an active DMFC with a proton-exchange membrane

IV-5-1-Half cell

Since most of the known anode electrocatalysts for DAFCs are still based on nano-sized Pt, alone or in combination with other metals, especially Pt–Ru alloys, supported on carbon blacks or CNTs [6–9, 30-32, 50–53], Pt–Ru/MWCNT electrodes were prepared and tested in both half cell and active DMFC. Preliminary tests with ethanol and glycerol gave quite poor results and were not considered further. The study reported below was carried out to compare the performance of the Pd/MWCNT electrocatalyst in alkaline media with that of the Pt–Ru/MWCNT electrocatalyst in acidic media.

Figure 23 shows the cyclic voltammogram of the methanol oxidation on a Pt–Ru/MWCNT electrode (Pt 24 μg.cm^{-2}, Ru 13 μg.cm^{-2}) in 0.5M H_2SO_4 at a scan rate of 50 mV.s^{-1}.

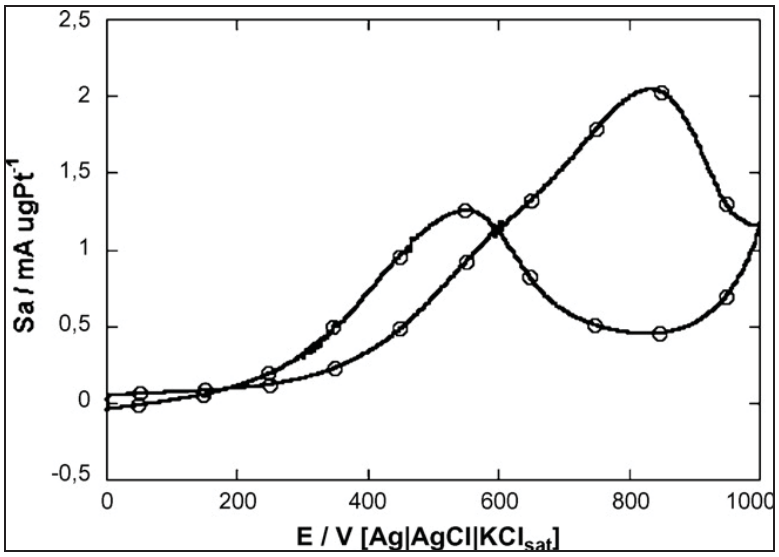

Figure 23: Cyclic voltammograms (at the fifth cycle) of methanol oxidation on a Pt–Ru/MWCNT electrode in 0.5M H_2SO_4 solution. Metal loading: 37μg. Scan rate: 50mV.s^{-1}.

A peak current density (J_p) of 38 mA.cm^{-2} was observed at a forward anodic peak potential of 0.83 V. The onset potential of MeOH oxidation was at 0.2 V and the specific peak current density (Sa_p), relative to Pt, was 2 mA (μg Pt)$^{-1}$. The $J_{forward}/J_{backward}$ ratio of 1.4 is consistent with a modest tolerance to CO poisoning as expected for a Pt–Ru catalyst where the two metals are in a 1:1 atomic ratio [6, 31]. Overall, these CV characteristics are in line with those reported in the literature for a number of Pt–Ru nanoparticles supported on carbon nanotubes [30-32, 51].

The performance stability of the Pt–Ru/MWCNT electrocatalyst for methanol oxidation was investigated by chronopotentiometry. Steady state measurements were carried out by a constant current density polarization of 3.46 mA.cm^{-2}. The potential of methanol oxidation increased rapidly with time, reaching the value of the oxygen evolution reaction only after 40 minutes, which is consistent with an effective electrode deterioration.

IV-5-2-Active DMFC

The MEA for the active monoplanar DMFC was realized as described in chapter V with Pt–Ru/MWCNT (metal loading: 0.70 mg cm^{-2}) at the anode, a commercial Pt/C (30 wt. % metal) catalyst (E-TEK) (2 $mg.cm^{-2}$) at the cathode and a Nafion® 117 membrane. Methanol was delivered at 1.5 $mL.min^{-1}$, while the oxygen flow was 200 $mL.min^{-1}$. The cell temperature was regulated at 60, 70 and 80 °C. Figure 24 shows the polarization and power density curves for a cell working at 60, 70 or 80 °C.

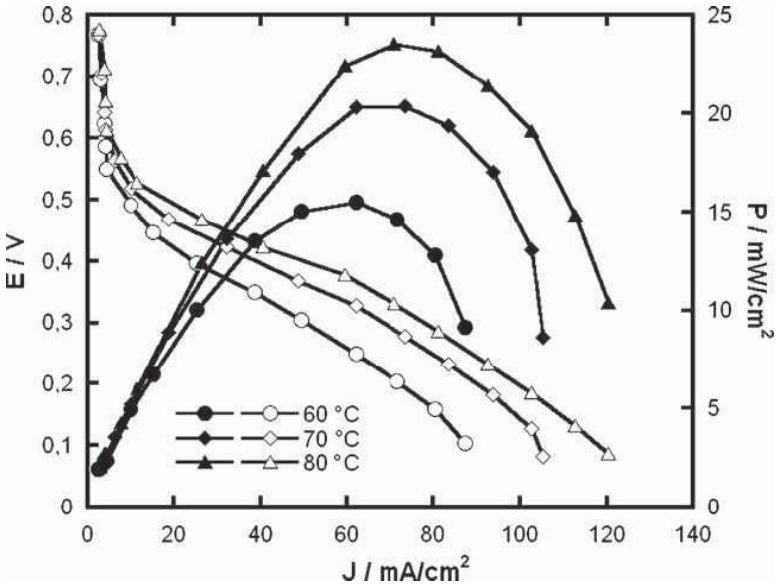

Figure 24: Polarization and power density curves at different temperatures of an active DMFC with a Pt–Ru/MWCNT anode fuelled with an aqueous 0.5 M H_2SO_4 solution of methanol (10 wt. %)

Considering the low Pt loading of the MEA in the present DMFC (0.43 $mg.cm^{-2}$ at the anode), the performance of the latter matches well those reported in the literature (from 55 to 100 $mW.cm^{-2}$ at Pt–Ru loadings of 3–4 $mg.cm^{-2}$) for a number of DMFCs containing Pt–Ru nanoparticles supported on CNTs [50-52]. On the other hand, it is also apparent that the alkaline DMFC with the anode catalyzed with Pd/MWCNT (Fig. 22A) provides much better results in terms of both electrochemical activity and stability.

IV-6- Cathode oxygen reduction reaction (ORR)

Nitrogen doped carbon nanotubes and nanofibers did not act as optimum supports at the anodic side. This seems in accordance with literature, since all the reports on such materials are directed towards their use in the cathode fabrication for the oxygen reduction reaction [54-56]. There are even speculations about their use without supported noble metals [57, 58]. Thus, pure carbon nanotubes and carbon nanofibers doped with nitrogen as well as the Pd/N-CNF catalyst were tested for the ORR reaction at the cathode side.

Figure 25 shows a typical linear sweep voltammogram at 5 mV/s using a rotating ring-disk electrode (RRDE), made with various materials in oxygen bubbling (10 mL/min) solutions of 0.1 M KOH.

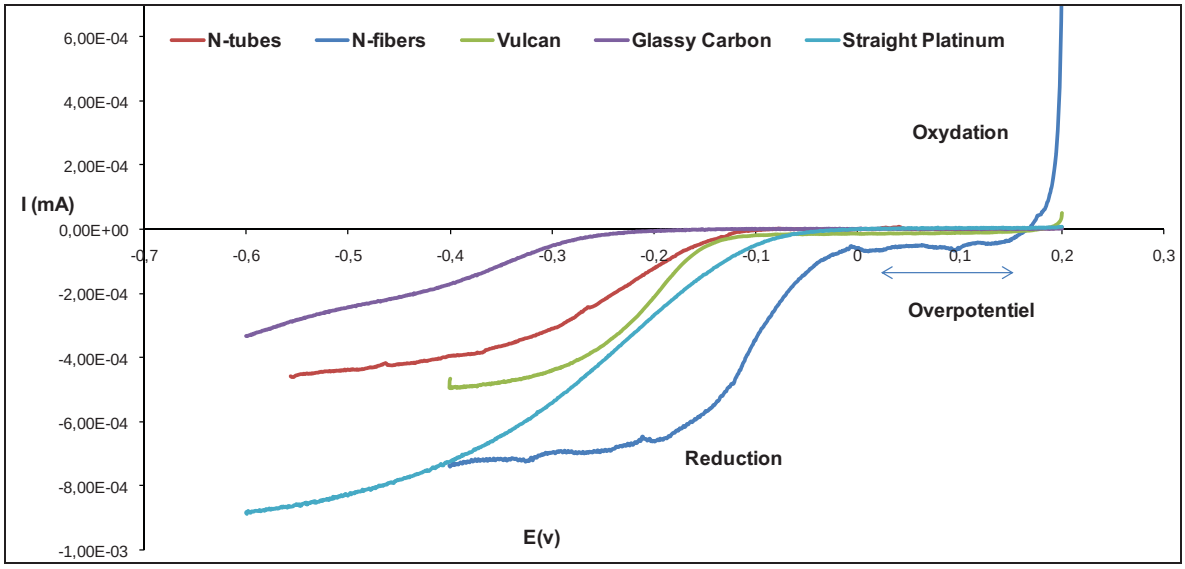

Figure 25: Current–potential curves of on a variety of supports

The pure N-CNFs present the best performance towards the ORR reaction in term of overpotential (the lowest) and stationary current (the highest). It is almost similar to pure platinum electrodes. It is followed by Vulcan and nitrogen doped carbon nanotubes.

But all the pure materials had low activity of current production in comparison with the Pd modified one (0.8 mA in comparison with only $7x10^{-4}$ mA) (Fig. 26).

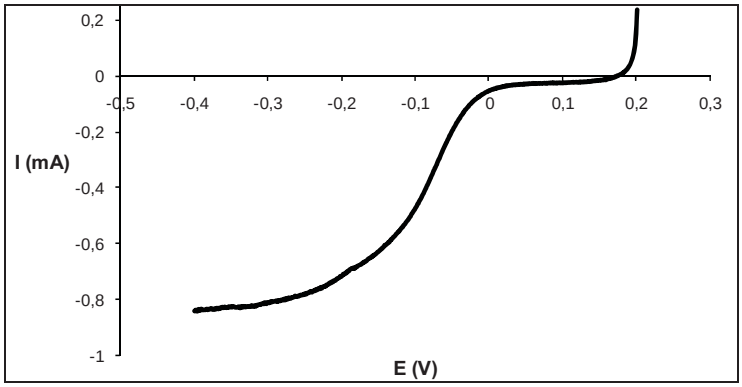

Figure 26: Current–potential curves of the 3% Pd/N-CNF catalyst

ORR can proceed by two pathways in alkaline media: a four-electron pathway (14) leading directly to OH^-, or a two-electron pathway (15) with hydrogen peroxide (HO_2^- in alkaline media) as an intermediate or final product [59, 60]:

$$O_2 + 2H_2O + 4e^- \longrightarrow 4OH^- \quad \text{(four-electron pathway)} \quad (14)$$

$$O_2 + H_2O + 2e^- \longrightarrow HO_2^- + OH^- \quad \text{(two-electron pathway)} \quad (15)$$

By varying the rotation speed of the disk, and measuring the stationary current we plot the Levic equation (16) and obtained the mechanism of oxygen reduction.

$$\mathbf{i_L = (0.620\ n\ F\ A\ D^{2/3}\ v^{-1/6}\ C)\ w^{1/2}} \quad (16)$$

w is the electrode rotation rate (rpm), n is the number of the transferred electrons in the overall reduction process, F is the Faraday (96500 C), A is the electrode area (1 cm^2), D is the diffusion coefficient of oxygen across the stagnant layer (0,0000197 cm^2/s), v is the kinematic viscosity of the electrolyte (1,0788x$10^{-2}cm^2/s$), C is the concentration of oxygen (1,03 x 10^{-3}M).

For pure and Pd decorated N-CNF we found n = 1.95 and 1.92, respectively (Fig. 26), indicating a 2 electron pathway of reduction leading to the formation of HO_2^- (Equation 16).

Electron-accepting nitrogen atoms on the surface of CNFs impart a relatively high positive charge density on adjacent carbon atoms or superposed Pd nanoparticles. Thus, on Pd nanoparticles oxygen tends to form a complex $Pd^{\delta+}(O_2)^{\delta-}$ on their surface [60], with very

negatively charged oxygen atoms interacting with OH^- to form surface HO_2^-. The HO_2^- ion is highly corrosive for the cell, but it is reported that on a Pd/MWCNT electrocatalyst in acidic media, H_2O_2 will be reduced further to OH^- by a successive reduction mechanism. As a result, the oxygen reduction reaction proceeded through two-step two-electron processes [60]. We are not sure if a second reduction (17) occur in alkaline media.

$$HO_2^- + H_2O + 2e^- \longrightarrow 3\ OH^-\qquad \text{(two-electron pathway)} \qquad (17)$$

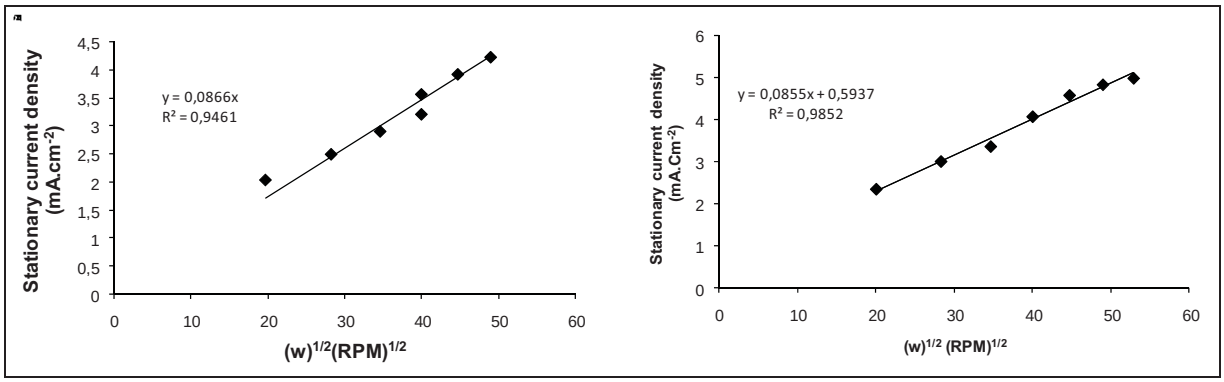

Figure 27: Plot of the electrocatalytic oxygen reduction stationary currents as a function of the square root of scan rates: using the N-CNF catalyst without any noble metal (left), and the 3% Pd/N-CNF catalyst (right)

IV-7- Conclusion

The MWCNT-supported palladium catalysts prepared and characterized in this work are effective for the electrooxidation in alkaline environment of methanol as well as renewable alcohols like ethanol and glycerol. The oxidation of these alcohols has been primarily investigated in half cells by a variety of electrochemical techniques, using glassy carbon electrodes. The results obtained have highlighted the excellent electrocatalytic activity of Pd/MWCNT in terms of both peak current density, as high as 2800 A.(g Pd)$^{-1}$ with glycerol, and onset oxidation potential, as low as -0.75 V *vs* $Ag/AgCl/KCl_{sat}$ with ethanol. Such a remarkable electrocatalytic activity of Pd/MWCNT can be associated both to the high dispersion of the metal particles and to the intrinsic properties of MWCNTs. Membrane-electrode assemblies (MEA) containing a Pd/MWCNT anode, a commercial Fe-Co Hypermec^{TM} cathode and a Tokuyama A

006 anion-exchange membrane have provided excellent results in monoplanar fuel cells. The MEA performance has been evaluated in either passive and active DAFCs fed with aqueous solutions of 10 wt. % methanol, 10 wt.% ethanol or 5 wt.% glycerol. In view of the peak power densities obtained in the temperature range from 20 to 80 °C, at Pd loadings at the anode as low as 1 $mg.cm^{-2}$, one can safely conclude that Pd/MWCNT exhibits unrivalled activity as anode electrocatalyst for DAFCs. Ionic chromatography and $^{13}C\{^{1}H\}$ NMR spectroscopy have been employed to analyze the anode exhausts of galvanostatic experiments showing that ethanol is selectively oxidized on Pd/MWCNT to acetic acid, converted to acetate ion in the alkaline media of the reaction, while methanol yields carbonate and formate. A much wider product distribution, including glycolate, glycerate, tartronate, oxalate, formate and carbonate, was obtained from the oxidation of glycerol. A comparison with a DMFC containing a Pt–Ru/MWCNT anode catalyst has fully confirmed the superior performance of Pd/MWCNT in alkaline media. Among the fuels investigated, ethanol is giving rise to the major interest as the relative DEFCs, either passive or active, combine excellent power outputs with superior stability with time. The oxidation of ethanol to acetic acid, isolable as potassium acetate, presages the use of Pd/MWCNT to realize alkaline direct fuel cells capable of producing selective chemicals from alcohols with concomitant release of energy.

In contrast, CNFs, N-CNFs and N-MWCNTs supported palladium did not yield satisfactory results. Reports claim that electric conductivity of such supports could be enhanced by high temperature treatments, removal of diffusion blocking carboxylic groups, better purification (Fe and Al total removal)[61].

IV-8- References

1) D.R. Lide, editor. 2003-2004. CRC Handbook of Chemistry and Physics. CRC Press

2) Fuel cells Handbook (sixth edition), EG&G Technical Services, Inc. Science Applications International Corporation (2002) p.1-5

3) W. Vielstich, A. Lamm, H.A. Gasteiger, editors. 2003. Handbook of Fuel Cells. Fundamentals, Technology and Applications. John Wiley & Sons, Chichester

4) P. Costanaga, S. Srinivasan, J. Power Sources 102 (2001) 242

5) H.A. Gasteiger, S.S. Kocha, B. Sompalli, F.T. Wagner, Appl. Catal. B 56 (2005) 9
6) C. Lamy, A. Lima, V. LeRhun, F. Delime, C. Coutanceau, J.-M. Leger, J. Power Sources 105 (2002) 283
7) F. Viguer, S. Rousseau, C. Coutanceau, J.-M. Leger, C. Lamy, Top. Catal. 40 (2006) 111
8) E. Antolini, J. Power Sources 170 (2007) 1
9) J.S. Spendelow, A. Wieckowski, Phys. Chem. Chem. Phys. 9 (2007) 2654
10) K.Y. Chan, J. Ding, J. Ren, S. Cheng, K.Y. Tsang, J. Mater. Chem. 14 (2004) 505
11) C. Coutenceau, L. Demarconnay, C. Lamy, J.-M. Leger, J. Power Sources 156 (2005) 14
12) H. Igarashi, T. Fujino, Y. Zhu, H. Uchida, M. Watanabe, Phys. Chem. Chem. Phys. 3 (2001) 306
13) P.K. Shen, C. Xu, Electrochem. Commun. 8 (2006) 184
14) Z.Wang, F. Hu, P.K. Shen, Electrochem. Commun. 8 (2006) 1764
15) C. Xu, Z. Tian, P. Shen, S.P. Jiang, Electrochim. Acta 53 (2008) 2610
16) C. Xu, P.K. Shen, Y. Liu, J. Power Sources 164 (2007) 527
17) S.-H. Hong, M.-S. Jun, I. Mochida, S.-H. Yoon, in: P. Barbaro, C. Bianchini (Eds.), Catalysis for Sustainable Energy Production, Wiley, 2009
18) R. Pattabiraman, Appl. Catal. A: Gen. 153 (1997) 9
19) F. Hu, C. Chen, Z. Wang, G. Wei, P.K. Shen, Electrochim. Acta 52 (2006) 1087
20) M. Nie, H. Tang, Z. Wei, S.P. Jiang, P.K. Shen, Electrochem. Commun. 9 (2007) 2375
21) C. Xu, L. Cheng, P. Shen, Y. Liu, Electrochem. Commun. 9 (2007) 997
22) D. Yuan, C. Xu, Y. Liu, S. Tan, X. Wang, Z. Wei, P.K. Shen, Electrochem. Commun. 9 (2007) 2473
23) F.P. Hu, Z. Wang, Y. Li, C. Li, X. Zhang, P.K. Shen, J. Power Sources 177 (2008) 61
24) F. Hu, F. Ding, S. Song, P.K. Shen, J. Power Sources 163 (2006) 415
25) H.T. Zheng, Y. Li, S. Chen, P.K. Shen, J. Power Sources 163 (2006) 371
26) A. Solhy, B.F. Machado, J. Beausoleil, Y. Kihn, F. Goncalves, M.F.R. Pereira, J.J.M. Orfao, J.L. Figueiredo, J.L. Faria, P. Serp, Carbon 46 (2008) 1194
27) J.-C. Hierso, PhD thesis, Université Paul Sabatier, Toulouse, 1997
28) Y. Sudong, Z. Xiaogang, M. Hongyu, X. Ye, J. Power Sources 175 (2008)

29) JCPDS Card No. 00-046-1043, International Centre for Diffraction Data, Newton Square, PA, 1993
30) G. An, P. Yu, L. Mao, Z. Sun, Z. Liu, S. Miao, Z. Miao, K. Ding, Carbon 45 (2007) 536
31) J. Huang, Z. Liu, C. He, L.M. Gan, J. Phys. Chem. B 109 (2005) 16644
32) C. Yang, D. Wang, X. Hu, C. Dai, L. Zhang, J. Alloys Compd. 448 (2008) 109
33) F. Colmati, W.H. Lizcano-Valbuena, G.A. Camara, E.A. Ticianelli, E.R. Gonzalez, J. Braz. Chem. Soc. 13 (2002) 474
34) A. Caillard, C. Coutanceau, P. Brault, J. Mathias, J.-M. Leger, J. Power Sources 162 (2006) 66
35) C.-C. Hu, T.-C. Wen, Electrochim. Acta 41 (1996) 1505
36) C.-C. Hu, T.-C. Wen, Electrochim. Acta 40 (1995) 495
37) M. Grden, M. Łukaszewski, G. Jerkiewicz, A. Czerwinski, Electrochim. Acta 53 (2008) 7583
38) J.P. Singh, X.G. Zhang, Hu-lin Li, A. Singh, R.N. Singh, Int. J. Electrochem. Sci. 3 (2008) 416
39) V.M. Barragan, A. Heinzel, J. Power Sources 104 (2002) 66
40) K. Scott, E. Yu, G. Vlachogiannopoulos, M. Shivare, N. Duteanu, J. Power Sources 175 (2008) 452
41) K. Matsuoka, Y. Iriyama, T. Abe, M. Matsuoka, Z. Ogumi, J. Power Sources 150 (2005) 27
42) A.E. Bolzan, A.J. Arvia, J. Electroanal. Chem. 157 (1992) 247
43) L. Demarconnay, S. Brimaud, C. Coutanceau, J.-M. Leger, J. Electroanal. Chem. 601 (2007) 169
44) K. Matsuoka, Y. Iriyama, T. Abe, M. Matsuoka, Z. Ogumi, Electrochim. Acta 51 (2005) 1085
45) R. Borup, J. Meyers, B. Pivovar, Y.S. Kim, R. Mukundan, N. Garland, D. Myers, M. Wilson, F. Garzon, D. Wood, P. Zelenay, K. More, K. Stroh, T. Zawodzinski, J. Boncella, J.E. McGrath, M. Inaba, K. Miyatake, M. Hori, K. Ota, Z. Ogumi, S. Miyata, A. Nishikata, Z. Siroma, Y. Uchimoto, K. Yasuda, K.-C. Kimijima, N. Iwashita, Chem. Rev. 107 (2007) 3904

46) V. Bambagioni, C. Bianchini, J. Filippi, W. Oberhauser, A. Marchionni, F. Vizza, R. Psaro, L. Sordelli, M.L. Foresti, M. Innocenti, ChemSusChem 2 (2009) 99
47) C. Bianchini, F. Vizza, unpublished results
48) A. Verma, S. Basu, J. Power Sources 145 (2005) 282
49) H. Hou, G. Sun, R. He, Z. Wu, B. Sun, J. Power Sources 182 (2008) 95
50) K.-T. Jeng, C.-C. Chien, N.-Y. Hsu, S.-C. Yen, S.-D. Chiou, S.-H. Lin, W.-M. Huang, J. Power Sources 160 (2006) 97
51) Z. Liu, X.Y. Ling, B. Guo, L. Hong, J.Y. Lee, J. Power Sources 167 (2007) 272
52) K.-T. Jeng, C.-C. Chien, N.-Y. Hsu, W.-M. Huang, S.-D. Chiou, S.-H. Lin, J. Power Sources 164 (2007) 33
53) C.-C. Chien, K.-T. Jeng, Mat. Chem. Phys. 99 (2006) 80
54) B. Yue, Y. Ma, H. Tao, L. Yu, G. Jian, X. Wang, X. Wang, Y. Lu, Z. Hu, J. Mater. Chem. 18 (2008) 1713
55) T. Schilling, M. Bron, Electrochimica acta 53 (2008) 5379
56) K. Prehn, A. Warburg, T. Schilling, M. Bron, K. Schulte, composite science and technology 69 (2009) 1570
57) http://www.greenoptimistic.com/2009/02/07/nitrogen-doped-carbon-nanotube/
58) **Erreur ! Référence de lien hypertexte non valide.**
59) L. Genies, Y. Bultel, R. Faure, R. Durand, Electrochimica acta 48 (2003) 3879
60) Y. Lin, X. Cui, X. Ye, Electrochemistry Communications 7 (2005) 267
61) E. Antolini, Applied Catalysis B: Environmental 88 (2009) 1

V-Experimental details

Chapter V: Experimental details

V-1-List of main chemicals used

V-1-1-Organnometallic precursors

[Ni(Cp)$_2$] (Cp = η^5-C$_5$H$_5$): Nickelocene was purchased from Alfa Aesar GmbH & Co. KG.

[Fe(CO)$_5$]: Iron pentacarbonyl was purchased from Sigma-Aldrich. Purety: 99.999 %, M = 195.90 g. Mol^{-1}, d = 1.49 g.mL^{-1} at 25 °C, $T_{decomposition}$ = 103 °C, Vapor pressure = 35 mmHg at 25 °C.

[Pd$_2$(dba)$_3$] (dba = C$_{17}$H$_{14}$) tris-dibenzylideneacetone **[Ru(COD)(COT)] (COD = C$_8$H$_{12}$, COT = C$_8$H$_{10}$)**: Those two precursors were purchased from NanoMePS (Toulouse, France)

[Pt(COD)Me$_2$]: was prepared from [PtI$_2$] according to the modification of a reported procedure [1].

In this synthesis, all solvents were dried over $MgSO_4$ and degassed with a 10 min Ar bubbling step. All the material was well dried in an autoclave before usage.

The [Pt(COD)Me$_2$] synthesis was done in two steps, [Pt(COD)I$_2$] then [Pt(COD)Me$_2$] synthesis.

Pt(COD)I$_2$ synthesis

$$PtI_2 + COD \longrightarrow [Pt(COD)I_2] \qquad (1)$$

In a 250 mL flask, under Ar, 1 g of PtI$_2$ was dissolved in 50 mL of acetone. Under magnetic stirring, 12 mL of 1,5-cyclooctadiene (COD) were added. After 12 h, a yellow dirty precipitate appears. This later is recovered by filtration, then washed with a 50/50 v/v % water/propanol solution to remove the COD excess and the dark powder that could originate from PtI$_2$ decomposition to I$_2$ and Pt^0. After 24 h drying under vacuum, the yield was 60 %.

Pt(COD)Me_2 synthesis

$$[Pt(COD)I_2] + 2\ MeLi + 2\ NH_4Cl \longrightarrow [Pt(COD)Me_2] + 2\ LiCl + 2\ NH_4I \quad (2)$$

In a 500 mL flask maintained at 1 °C by an ice bath, 6 g (14.6 mmol) of the well dried [Pt(COD)I_2] were dissolved in 130 mL of well dried and Ar degassed ether. Using syringes and septums, to stay under Ar, 0.7 g (32 mmol) of MeLi were introduced drop by drop, under vigorous stiring. The mixture turns progressively to green then to dark. After 2 h, the mixture is hydrolyzed with a solution of 35 g of NH_4Cl in 100 mL of water. The two phases are separated by decantation; the dark-green ether phase was recovered and dried by adding $MgSO_4$. The ether is evaporated and the [Pt(COD)Me_2] complex was purified by sublimation. White brilliant [Pt(COD)Me_2] needles were recovered with a 40 % yield.

V-1-2-Supports

Al_2O_3: activated neutral, Brockmann I, particles size: 100-120 μm, BET specific surface area = 155 m^2/g, d= 3.97, mean pore diameter = 5.8 nm purchased from Aldrich.

SiO_2: Silice EP10X provided by Crossfield Limited.

ZnO: Prepared by CVD in our laboratory [2].

SWCNTs: SWCNT (NTX11) with COOH functional groups were purchased from Nanothinx.

Activated carbon: Darco G-60, -100 Mesh powder purchased from Sigma-Aldrich.

V-1-3-Solvents

Ethanol, Toluene, Propan-2-ol and Hexane were purchased from Sigma-Aldrich.

V-1-4-Acids

H_2SO_4 (95 %), HNO_3 (68 %), HCl (37 %) and HF (40 %) were purchased from Accros Organics.

V-1-5-Gas

All gases were purchased from Air liquid and were used without any purification step.

Methane N35: 99.95 % CH_4 , 5 ppm H_2O, 10 ppm O_2, 200 ppm C_2H_6, 10 ppm CO_2, 20 ppm H_2, 200 ppm N_2, and 50 ppm hydrocarbons.

Ethylene N35: 99.95 % C_2H_4, 5 ppm H_2O, 10 ppm O_2, 5 ppm CO_2, 40 ppm N_2, 430 ppm hydrocarbons, 10 ppm H_2.

Hydrogen alpha gas 2: 99.9999 % H_2, 0.5 ppm H_2O, 0.1 ppm O_2, 0.1 ppm CO, 0.1 ppm CO_2, 0.1 ppm hydrocarbons, and 0.1 ppm N_2.

Argon alphagas 1: 99.995 Ar, 3 ppm H_2O, 2 ppm O_2 and 0.5 ppm hydrocarbons.

Azote alphgas 1: 99.9999 % N_2, 3 ppm H_2O, 2 ppm O_2, 0.5 ppm hydrocarbons.

V-2-OM-CVD synthesis of catalyst for carbon nanostructure synthesis

Our apparatus (Fig. 1) consists of 3 major parts: the sublimation chamber (A), the deposition column (B), the upper closing part (C) and some annexed parts like by-passes (D), a vacuum pomp, mass flow regulators (E), liquid bubblers (F), and a thermostat bath for liquid heating and circulation (G).

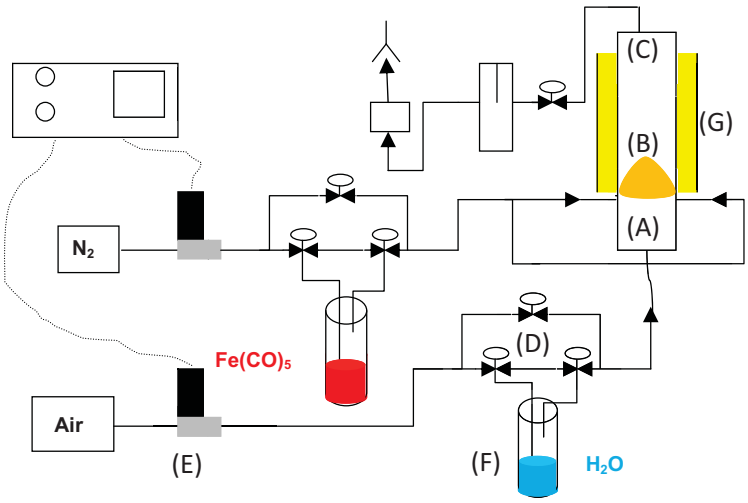

Figure 1: FB-CVD apparatus for the catalyst elaboration

The reactor was designed to operate under low pressure due to the low volatility of many organometallic precursors. The support powder is fluidized thanks to gas flow that passes

through an inox grid called the distributor intercalated between the sublimation chamber and the deposition column. The deposition column is the place where the thermal decomposition of the organometallic complexes occurs on the fluidized support, leading to the formation of supported metal catalyst. Bringing the vapor of the organometallic precursor to the deposition column depends on its physical state. In the case of a liquid compound like iron pentacarbonyl, a classical bubbler is intercalated in the nitrogen pass way (Fig. 3, chapter II), the sublimation chamber being empty. For solid compounds like nickelocene, it is done by thermal sublimation in the sublimation chamber and nitrogen flow carrying (Fig. 40, chapter II). The three OM-CVD parts are assembled using two silicon junction and two inox clips. In this setup, reactive gases such as O_2, H_2O, or H_2, can be introduced to assist precursor decomposition. These reactants are preferably introduced in the vicinity of the distributor in order to avoid a premature decomposition of the precursor in the sublimation chamber. The sublimation chamber and the deposition column are heated by two different heating glass jackets containing a circulation of thermal conducting fluid heated by two thermostat baths. This allows fine tuning of both precursor and deposition temperature. The temperature range of such process was between 25 and 250 °C.

1, 2, 4 and 6 w/w % of iron supported on alumina OM-CVD catalysts were prepared according to the conditions of Table 1.

% w/w Fe	$m_{alumina}$ (g)	$V_{[Fe(CO)5]}$ (mL)	T_s (°C)	T_C (°C)	Air (sccm)	N_2 (sccm)	P (mbars)	t (min)
1	50	1.5	25	220	125	125	1	15
2	50	3	25	220	125	125	1	15
4	50	6	25	220	125	125	1	30
6	50	8	25	220	125	125	1	30

Table 1: Conditions for iron oxide deposition on alumina

50 g of γ-alumina (100 <d<120 μm, $U_{m,f}$ = 1.75 cm/s) were introduced in the deposition column and a 1 mbars pressure was imposed by the pump. The powder was fluidized under 125 sccm of air, 125 sccm of N_2 and heated to 220 °C. At this temperature the nitrogen was allowed to circulate inside the bubbler of [$Fe(CO)_5$] and air inside the water bubbler. After the requested volume of [$Fe(CO)_5$] is deposited, the heating and the pump are switched-off and the column is cooled to room temperature. The as prepared catalyst was stored in a vessel under N_2.

A 6 % Ni^0/Al_2O_3 catalyst was prepared by OM-CVD deposition using the reactor presented in Figure 40 of Chapter II. Nine grams of [$Ni(Cp)_2$] were introduced in the sublimation chamber. This later was connected to the deposition column via the distribution grid using a silicon junction and an inox clips. 50 g of γ-Al_2O_3 were introduced in the deposition chamber and the upper closing part was connected. A 0.5 mbars pressure was imposed by the pump. A mass flow of 300 sccm of N_2 fluidized the powder. The column was heated to 220 °C by a circulation of the thermal conducting fluid. At 220 °C the sublimation chamber was heated to 135 °C by the same way. At 135 °C, a 350 sccm H_2 flow was sent to the column. After 5 h, the column, the sublimation chamber, and the deposition chamber were cooled progressively, then the H_2 flow cut-off. The as prepared catalyst was stored in a vessel under N_2.

V-3-Carbon nanostructure synthesis

V-3-1-SWCNT synthesis

The appropriate weight of catalyst was placed in an alumina boat in the middle of a horizontal quartz tube. This later was heated by an oven at a ramp of 30 °C / min until 900°C under air. The tube was connected to the gas arrival, and an appropriate mixture of Ar, H_2 and CH_4 was sent in the reactor via mass flows. After 30 minutes the oven was switched of, and the reactor cooled under Ar. The process is represented in Figure 4 of chapter II. An example is given in Table 2.

Test	Product	% Fe	$m_{catalyst}$	t_2	T	CH_4	Ar	H_2

			(mg)	(min)	(°C)	(sccm)	(sccm)	(sccm)
7	SWCNTs	2	100	30	900	200	100	0

Table 2: An example of SWCNT synthesis conditions

V-3-2-MWCNT, N-MCWNT, CNF and N-CNF synthesis

The MWCNT, N-MWCNT, CNF and N-CNF syntheses were performed in a fluidized bed CVD apparatus represented in Figure 2.

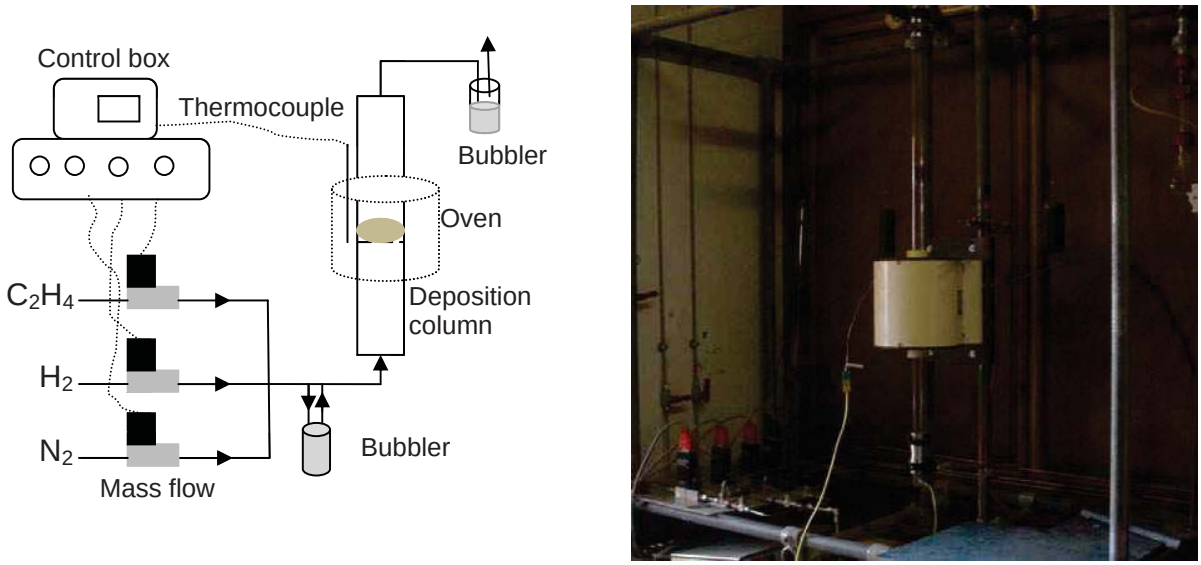

Figure 1: Vertical reactor for carbonaceous nanomaterials synthesis

Since the physico-chemical parameters of such deposition were not the same as for catalyst elaboration, some technical modifications were done in the design of the reactor. A vertical quartz tube with quartz porous grid in the center serving as gas distributor is heated by a vertical oven because much higher temperatures are needed (600-900 °C). The carbon deposition occurred at atmospheric pressure, using hydrocarbons as carbon source. The catalyst was fluidized with a mixture of C_2H_4, H_2, and N_2 using mass flow meters. In the case of nitrogen

doped structures, a bubbler containing the nitrogen and carbon sources was intercalated between the mass flowmeters and the reactor by a by-pass.

A mass of catalyst was introduced on the porous quartz distributor of the vertical tube. The entry and exit of the tube were connected, and the tube was heated to the desired temperature under a flow of H_2 and N_2.

For MWCNT synthesis, for example in the case of test MW8, 0.5 g of the 4 w/w % Fe/Al_2O_3 catalyst were introduced in the column, heated to 700 °C under 120/160 sccm of H_2/N_2. At 700 °C, 200/100 sccm of C_2H_4/H_2 were introduced, and the N_2 flow was cut-off. After 30 minutes the reactor was cooled under N_2.

For CNF synthesis, taking test F2 as an example, 4 g of the 6 w/w % Ni/Al_2O_3 were introduced in the column, and heated to 700 °C under 120/160 sccm H_2/N_2. At 700 °C, 105 sccm of C_2H_4 were added in the reactor for 60 minutes. The reactor was later cooled under N_2.

For N-CNF and N-MWCNT synthesis, the bubbler was filled with acetonitrile and heated to 30 °C. Taking respectively test AN2 and MW2 as examples, 2 g of the 2 % w/w Fe/Al_2O_3 (N-CNF) or 2 g of the 2 w/w % Co/SiO_2 (N-MWCNT) catalysts were introduced in the reactor. After heating to 700 °C under 120/160 sccm of H_2/N_2, the gas is allowed to pass via the bubbler for 1 h. The gas was switched back to by-pass the bubbler and the reactor cooled under N_2.

V-4-Carbon nanostructure post synthesis treatments

V-4-1-Catalyst removal

In the case of MWCNT, CNF and N-CNF carbon nanostructure-catalyst composite, the catalyst was removed according to the following procedure: 10 g of the as prepared material were introduced in a 2 liters tricol flask. 500 mL of water were added and a rotor was allowed stirring to enable dispersion. Under vigorous stirring 500 mL of H_2SO_4 were introduced drop wise (Caution: very exothermic). The flask was heated by a sand bath until 120 °C (boiling point

of H_2SO_4) and left for 2 h. The whole solution was filtered at 120 °C, to avoid the precipitation of any salt (Eq. 3), and the substrate washed with permuted water until a pH of 6 was reached.

$$Al_2O_3 + 3\ H_2SO_4 \longrightarrow Al_2(SO_4)_3 + 3\ H_2O \quad (3)$$

In the case of N-MWCNT-catalyst composite, the catalyst was removed by NaOH. 4 g of the as prepared composite were introduced in a 500 mL tricol flask and 200 mL of a 1 M solution of NaOH were added. The flask was connected to a condenser, the solution was magnetically stirred and heated to 70 °C. After 3 h the heating was cut of and the solution was filtered at 70 °C, and then washed with permuted water until a pH of 6 was reached. The reaction is represented in Eq. 4.

$$SiO_2 + 2\ NaOH \longrightarrow Na_2SiO_3 + H_2O \quad (4)$$

For the SWCNT-catalyst composite, the catalyst was removed with a 20 % solution of HF and SWCNTs separated by decantation. A Teflon material was used in all the process since HF dissolves silica.

V-4-2-Surface functionnalization

10 g of the purified carbon nanomaterial were introduced in a 2 liters tricol flask and a motor stirrer was connected. 500 mL of HNO_3 were added drop wise (very exothermic and toxic), A vigorous stirring was allowed and the flask was heated to 120 °C. After 8 h the hot solution was filtered and washed with permuted water. The atomic oxygen percentage as determined by XPS after nitric acid treatment was ca. 7 %.

V-5-Pt–Ru/supported catalysts for cinnamaldehyde hydrogenation

In a 250 mL flask, N_2 was bubbled into 60 mL of hexane for 10 minutes. Under N_2, 2 g of the supporting material were added and well dispersed by 15 min of sonication. Magnetic stirring was allowed and 0.13 g of [Ru(COD)(COT)] and 0.071g of [$Pt(COD)Me_2$], (COD = 1,5-C_8H_{12} and COT = C_8H_8) were added simultaneously. The mixture was kept at 45 °C overnight.

Finally, the solid catalytic material was obtained by filtration, vacuum drying and reduction in a fixed bed at 350 °C under 15 sccm of hydrogen and 160 sccm of argon.

V-6-Pt-Ru/supported catalysts for PEMFC application

V-6-1-Pd/Carbon nanostructure

To a suspension of 1 g of MWCNTs in a 250 mL flask containing 50 mL of THF, was added a solution of $[Pd_2(dba)_3]$ (0.25 g) in 50 mL of THF. A condenser was connected to the flask and the resulting mixture was magnetically stirred at room temperature for 3 days. The solid product was filtered-off and dried under vacuum, grounded and treated in an oven under 100 sccm of hydrogen flow for 4 h at 200 °C. The final material was collected and stored under argon.

V-6-2-Pt–Ru/Carbon nanostructure

Into a 250 mL flask, equipped with a reflux condenser, containing 65 mL of toluene de-aerated with argon 2 g of MWCNTs were introduced. After sonication under argon for 1 h 1.0 g of [Ru(COD)(COT)] and 0.7 g of $[Pt(CH_3)_2(COD)]$ were added. Hydrogen gas was bubbled into this solution at 110 °C for 1 day. After cooling to room temperature, toluene was evaporated from the resulting yellow solution under vacuum. The solid residue was calcined at 300 °C under air for 3 h and later treated with a hydrogen flow (100 sccm) at 300 °C for 2 h.

V-7-Hydrogenation of cinnamaldehyde

A desired amount of catalyst (typically 100 mg) was introduced in a 100 mL autoclave (Top Industry) and 20 mL of propan-2-ol were added. The autoclave was closed; the stirring was fixed at 900 rpm and the reactor was purged five consecutive times with H_2 at 3 bars. The reactor was heated to 100 °C and kept 2 h under 20 bar of H_2. Later, it was quickly cooled to 10 °C, depressurized and the stirring cut off. The autoclave was opened and the referred amount of CAL

was quickly added and the reactor was closed. The total liquid volume in the autoclave was 40 mL. The autoclave was purged again with H_2 under 900 rpm and heated to the desired temperature. A desired pression of hydrogen was imposed, and its evolution was followed by a Log100 program. After the desired time, the autoclave was quickly cooled to room temperature, depressurized, the stirring cut off and the solution recovered. This latter was injected in a gas chromatography apparatus with anisole as internal standard.

V-8-Caracterization techniques

V-8-1- Termogravimetric analysis (TGA)

A SETARAM 92-12 apparatus was used. 5 to 15 mg of the material to analyze were deposited in a platinum crucible. This latter was deposited on a microbalance placed in a thermoregulated and tight chamber enabling a gas flow throw. The analysis was made under air, with a heating ramp of 10 °C.min^{-1} starting from room temperature to 1000 °C followed by a 30 minutes isotherm.

V-8-2-Raman spectroscopy

The Raman spectroscopy was performed with a Una Labram HR800 de Jobin and Yvon spectrometer and an incident wave length of 632.82 cm^{-1}. Few milligrams of the products were spread and crushed between two plexiglas lamella that are fixed directly on the sample holder under the incident beam. The analysis were made by Corine Routaboul in the 'Service commun de Spectroscopie Infra-Rouge et Raman' of the Paul Sabatier University in Toulouse.

V-8-3-TEM/HREM

The SWCNT HREM micrographs were obtained with a Philips CM-20 microscope of the CEMES-Toulouse, but operating at 120 kV to avoid their burning. The SWCNT samples were grounded in an agate mortar, dispersed in ethanol, and a drop of the suspension was deposited on a cupper grid covered with a carbon film with holes.

TEM micrographs of the nanoparticles deposited on various supports have been recorded with a JEOL JEM 1011 microscope operating at 100 kV. HREM and EDX analysis were performed in collaboration with Andrea Falqui from the Instituto Italiano di tecnologia, Electron Microscopy Laboratory, Via Morengo, 30, Genova, Italy. The grid preparation was the same as for the SWCNTs but without grounding.

V-8-4-Field emission gun scaning electron microscopy (FE-SEM)

FE-SEM analysis were performed by Mr Vincent Collière in the 'Service Commun de Micoscopie Electronique' of the 'Université Paul Sabatier' of Toulouse. A HITACHI S 4500 I apparatus was used. SWCNT samples were glued on a metallic cylinder and a metallisation step was performed by deposition of a thin layer of gold under vaccum in order to enable better observation.

V-8-5- Mossbauer spectroscopy

The Mossbauer spectra were recorded on a constant acceleration spectrometer with a 25 mCi ^{57}Co source in a rhodium matrix at constant temperatures of 25 or -268 °C. The sample was grounded to a fine powder and fixed on a double facet scotch glued on a plexiglas pellet. The Mossbauer parameters were obtained by fitting the experimental spectra. The Mossbauer analyses were performed by Mr Jean-Francois Meunier at the ''Service de Mesures Magnétiques'' of the LCC-Toulouse.

V-8-6-Temperature programmed reduction (TPR)

The TPR analysis were performed in the ''Laboratoire des Materiaux, Surface et Procédés pour la Catalyse'' de l'Ecole Européenne de Chimie Polymères et Matériaux in Strasbourg. Analysis were performed with a 15 °C/min ramp of heating from 20 to 900 °C under 3.6 mL.min^{-1} of hydrogen and 45 mL.min^{-1} of argon.

V-8-7-ICP-MS

The metal loading of some supported metal nanoparticles was determined by plasma chemical ionization coupled to mass spectroscopy (ICP-MS) after a dissolution step according to sample matrix. This analysis was performed by 'Antellis géochimie et environnement' in Toulouse. A Perkin Elmer Elan 6000 apparatus was used. Another part of analysis was determined by inductively coupled plasma atomic emission spectroscopy (ICP-AES) with a Intrepid Iris instrument (Thermo Elemental) in collaboration with the ICCOM-CNR (Sesto-Fiorentino, Italy).

V-8-8-Elemantal analysis

Micro-analyses of C, H, and N elements were performed in the 'service d'analyse chimiques'of the LCC-Toulouse. A PERKIN ELMER 2400 II apparatus consisting of a gas Chromatography coupled to mass spectrometry was used.

V-8-9-XPS/ESCA

XPS analysis were performed on a VG Escalab model MKII spectrophotometer with a pass energy of 20 eV and with Al Kα (1486.6 eV, 300 W) photons as an excitation source.
Few mg of the sample are spread on a double facet gluing scotch fixed on a sample holder. ESCA analyses were performed by Mr Gérard Châtaigner at the ESCA service of the CIRIMAT at the ENSIACET of Toulouse.

V-8-10-XRD

Part of this analysis was made in the 'service de diffraction X' of the LCC-Toulouse using a Panalytical MPDPro powder diffractometer with Cu Kα radiation (λ = 0.15406 nm). Another part was made in collaboration with Pr Claudio Bianchini at the ICCOM-CNR (Sesto-Fiorentino, Italy) at room temperature with a Bruker D8- Advance diffractometer, employing Cu

Kα radiation (λ = 1.5418 Å) in the range between 2.5 and 80.0° and using an acquisition step of 0.030° per second.

V-8-11-Gas chromatography

A GC Clarus 500 Perkin Elmer apparatus was used to analyze the products of CAL hydrogenation equipped with a FID detector (260 °C) and a Stabilawax®-DA Restek column serie 852382 (Stationnary phase: Nitroterephthalic acid modified polyethylene glycol with high polarity (l = 30 m, $d_{internal}$ = 0.25 mm, film thickness = 0.25 μm). The gas vector was argon (14 psig) and the method used: 3 minutes isotherm at 60 °C, 10 °C.min^{-1} ramp until 220 °C and an isotherm of 15 minutes at this later.

Standard curves of CAL, COL, HCAL, HCOL (Chapter III) concentration vs peak area were ploted using the internal standard method (Fig. 3). In a 20 mL volumetric flask, a certain volume from the autoclave solution is filtered, (sometimes diluted) and 0.05g of anisole are added as an internal standard. 2 μl of this sample are injected.

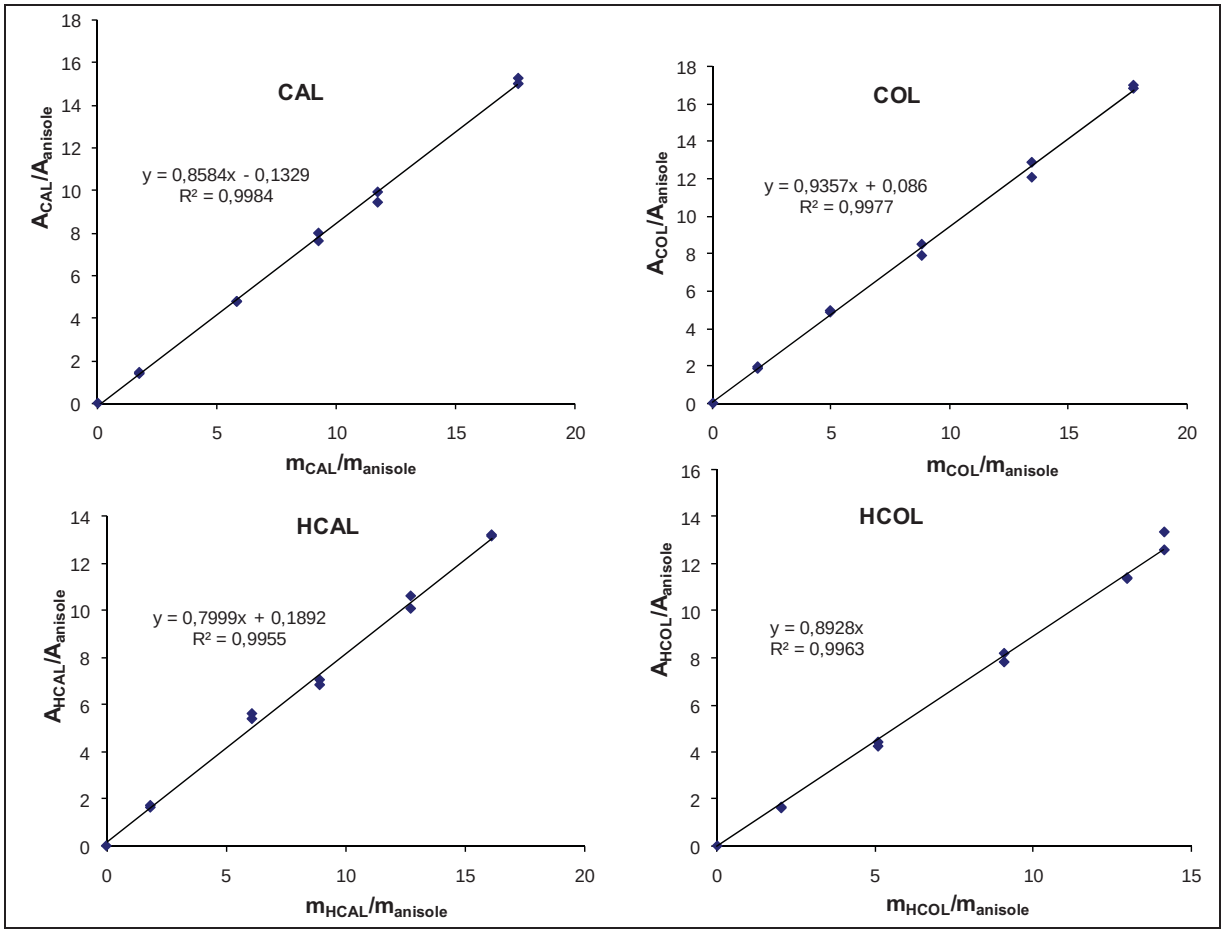

Figure 2: Standart curves for CAL, COL, HCAL and HCOL

V-8-12-Gas chromatography coupled to Mass spectrometry (GC-MS)

The GC-MS analyses was performed in the ‘’service commun de spectroscopie de masse’’ of the Paul Sabatier University of Toulouse. A GC autosystem coupled to a turbo mass MS was used, in association with a non polar column named DB5-n5. The stationary phase was 5% diphenyl and 95 % dimethyl arylene siloxane (L=30m, $d_{internal}$ = 0.25 mm, film thickness= 0.25 μm) with temperatures between -60 and 325 °C and He as vector gas.

V-8-13-EXAFS

EXAFS analyses were performed in Trieste (Italy), in collaboration with Pr Anna Corrias at the Università di Cagliari, Dipartimento di Scienze Chimiche.

V-8-14-WAXS

WAXS spectroscopy was performed on a home made apparatus by Dr Pierre Lecante at the ‘’Centre d’élaboration des matériaux et d'études structurales’’ of Toulouse. The samples were kept under Ar after reduction in the oven, and filled into capillary tubes (L=5 cm, d=1 mm) using a glove box.

V-8-15-NMR

The quantitative analysis of the fuel cell exhausts was obtained by ^{13}C $\{^{1}H\}$ NMR spectroscopy using a Bruker Avance DRX-400 instrument with the chemical shifts relative to external TMS. The calibration curves for the quantitative analysis were obtained using authentic samples of the various products in the appropriate range of concentrations, using 1,4-dioxane as internal standard.

V-8-16-Ionic chromatography

Ionic chromatography (IC) was used to identify the oxidation products in the fuel cells exaust. A Metrohm 761 Compact instrument equipped with a Metrosep Organic Acids column was used.

V-9-Fuel cell application

This work was in collaboration with Dr Claudio Bianchini from the Iccom-CNR in Italy.

V-9-1-Materials and product analysis

All manipulations, except stated otherwise, were routinely performed under argon or nitrogen atmosphere using standard airless technique. Aqueous solutions were freshly prepared with doubly distilled-deionized water.

The alkaline solid electrolyte used in both passive and active DAFCs was a Tokuyama anion-exchange membrane A-006 (OH-type) obtained from Tokuyama Corporation. The cation-exchange membrane was a Nafion® 117 (Du Pont) material purchased from Aldrich. The cathodes were provided by ACTA S.p.A. (Fe-Co-based Hypermec^{TM} K-14).

V-9-2-Electrochemical measurements

V-9-2-1-Ink preparation for the CV study

V-9-2-1-a-Pd/MWCNT

A portion of Pd/MWCNT (about 45 mg) was introduced into a 5 mL high-density polyethylene container together with 1.01 g of water, 65 mg of KOH (99.99% Sigma–Aldrich), 0.50 g of absolute ethanol (99.8% Fluka) and 0.37 g of 5% Nafion® ion-exchange resin in alcohol solution (Sigma–Aldrich). The resulting suspension was sonicated for 30 min with a Branson 3200 bath. Each suspension was freshly prepared just before carrying out the experiment scheduled. The metal loading on each glassy carbon electrode was determined by weighting the amount of ink deposited on the glassy carbon disk.

V-9-2-1-b-Pt–Ru/MWCNT

The procedure was analogous to that described above except for the absence of KOH.

V-9-2-2-Apparatus for cyclic voltammetry studies

The cell used for the cyclic voltammetry (CV) experiments was a Kelef cylinder with a 7.2 mm inner diameter and a 50 mm outer diameter. The inner volume of the cell was about 1 mL. The working electrode, Glassy Carbon (Sigradur® G) (0.867 cm^2), covered by the catalyst, was housed in a cavity at the top end of the cylinder, and the counter electrode was a gold disc placed at the bottom end. The solution contained in a Pyrex flask was previously de-aerated by bubbling N_2, and then flushed into the cell by a pressure as low as 0.3 bar of N_2. The miniaturized reference electrode, $Ag/AgCl/KCl_{sat}$, was placed on the outlet tubing. This allocation allows one to avoid contamination and at the same time is sufficiently close to the

working electrode to reduce the uncompensated resistance. All CV studies were carried out using a Parstat 2277 potentiostatgalvanostat (Princeton Applied Research).

V-9-2-3-Passive DAFC

The home-made, oxygen-breathing DAFC used to evaluate the electrochemical performance of the Pd/MWCNT anodes, in conjunction with the Tokuyama A-006 anion-exchange membrane and Fe-Co Hypermec^{TM} cathodes, is shown in Fig. 4.

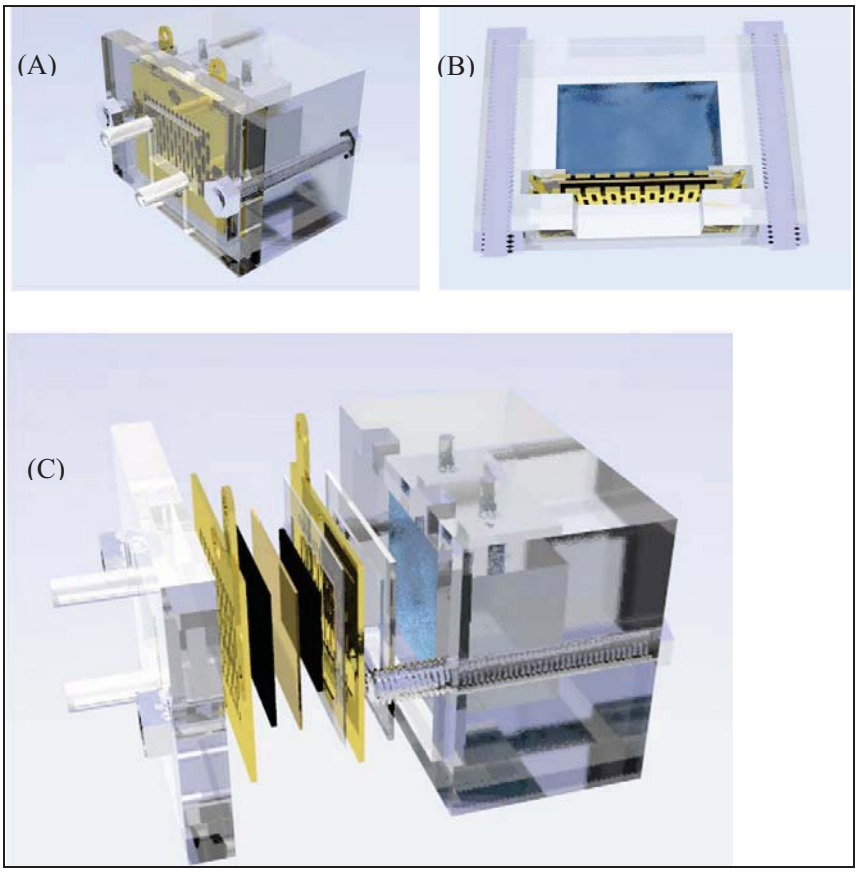

Figure 4: The home-made oxygen-breathing DAFC used in this work. (A) Complete view. (B) Top view showing the anode compartment. (C) Exploded view showing the MEA

The device was realized with plexiglas and the electricity collectors were plated with gold. The volume of the anode compartment was ca. 20–25 mL for an actual fuel solution of 13–15 mL. The anode was realized with a 5.13 cm^2 nickel foam plate onto which was deposited the

appropriate amount of a dense catalytic ink. This was prepared by dispersing the solid catalyst (Pd/MWCNT) in the minimum amount of water with no need of a binder. The cathode (catalyzed carbon cloth) was provided by ACTA S.p.A. The membrane-electrode assembly (MEA) was obtained by mechanically pressing anode, cathode and membrane, while silicone–rubber gaskets were employed to seal the system. In order to avoid any possible contamination of the alkaline anode solution by carbonate ions formed upon reaction with atmospheric CO_2, the DAFCs were positioned inside a home-made plexiglass dry box where the anode compartment was maintained all the way under a static nitrogen atmosphere, while the cathode was exposed to either air or an oxygen flow.

The cell performance was evaluated with an ARBIN BT-2000 5A-4 channels instrument.

V-9-2-4-Active DAFC

The active DAFC were purchased from Scribner-Associates (USA) (25 cm^2 fuel cell fixture) and were modified in our laboratory with gold-plated current collectors and titanium end plates to tolerate the alkaline conditions used in this work to evaluate the performance of the Pd/MWCNT catalyzed anode. The MEA was fabricated by mechanically pressing anode, Hypermec^{TM} cathode and Tokuyama A006 membrane. A dense anode ink was prepared by mixing the powdered catalyst with a 5–10 wt. % aqueous dispersion of PTFE. As a general procedure, an identical amount of the resulting paste was spread onto two identical Ni-foam plates. One of these was used almost immediately to fabricate the MEA, the other was dried until constant weight for the quantitative determination of the Pd loading that was, in all cases, ca. 1 $mg.cm^{-2}$. The effective electrode area was 5 cm^2. The fuel (water solutions containing 10 wt. % methanol, 10 wt. % ethanol or 5wt. % glycerol in 2 M KOH) was delivered to the anode at 4 $mL.min^{-1}$ by a micropump, while the oxygen flow was regulated at 200 $mL.min^{-1}$. The entry temperatures of the fuel and of the oxygen gas were regulated at the desired temperature and the effective cell temperature under working conditions was determined by an appropriate sensor positioned inside the end plate at the cathode side.

Except for the use of aluminum end plates, the DMFC employed to study the performance of the Pt–Ru/MWCNT-catalyzed anode was identical with that used in alkaline

media. The MEA for this cell was made by hot-pressing a Nafion® 117 membrane together with an anode sheet and a cathode sheet. The anode sheet was carbon cloth (5 cm^2) painted with an ink made by dispersing the catalyst in a 25 wt. % Nafion® solution in alcohol. The cathode sheet was carbon cloth with a commercial Pt/C (30 wt. % metal) catalyst (E-TEK) dispersed in the same Nafion® binder. The catalyst loading at the anode and cathode was 0.7 and 2 $mg.cm^{-2}$, respectively. Methanol was delivered at 1.5 $mL.min^{-1}$, while the oxygen flow was 200 $mL.min^{-1}$. All electrochemical measurements were carried out using an 850e Integrated PEM Fuel cell Station by Scribner- Associates (USA).

V-10-References

1) J.C. Hierso, PhD thesis, Université Paul Sabatier, Toulouse, 1997

2) R. Bacsa, J. Dexpert-Ghys, M. Verelst, A. Falqui, B. Machado, W. Bacsa, P. Chen, S. Zakeeruddin, M. Graetzel, P. Serp, Adv. Funct. Mater. 19 (2009) 819

General conclusion and perspective

In this work, iron, nickel and cobalt based catalysts were elaborated by fluidized bed CVD, and tested for carbon nanostructures synthesis.

Optimum conditions for single-walled carbon nanotubes were fixed; permitting yields around 0.05 g of carbon per gram of catalyst, and good selectivity as shown by an I_G/I_D ratio of 3. A key element in SWCNTs synthesis was the nature of the iron species supported on alumina: Mössbauer spectroscopy revealed the nature of iron on alumina and that iron oxide crystallites may yield carbon nanofibers whereas a submonolayer of a solid solution of Fe^{3+} could be the active phase for the selective growth of SWCNTs. Mössbauer spectroscopic analysis should be performed on the composite powder resulting from the conditions under argon, to see if the reduction of iron is slower and if the iron species are the same as in the case of the hydrogen conditions. Indeed, it would be necessary to check whether H_2 plays a role in the iron oxide reduction, on the methane decomposition or on both.

An optimum catalyst responding to selective SWCNTs synthesis demands was the 4% Fe/Al_2O_3 iron oxide activated at 900 °C for 10 hours, with or without the presence of H_2 in the gas mixture of synthesis. But the presence of H_2 reduces dramatically the yield and thus was avoided. Those conditions are meant to be further developed to push higher the selectivity and catalytic activity. Scaling up studies under such conditions should be performed. We note that a major part of methane destiny in such synthesis remains unknown since upon 200 sccm of methane sent in the reactor at 900 °C only low amounts of carbon are deposited. Gas chromatographic analysis of the gas mixture at the exit of the reactor should indicate whether the methane does not react, is transformed to other gases like C_2H_4, C_2H_6 or is totally decomposed at 900 °C in contact with the catalyst but later on regenerated in the H_2 rich atmosphere.

Multi-walled carbon nanotubes, carbon nanofibers and nitrogen doped carbon nanotubes and nanofibers were also elaborated. Nanostructures with specific properties like high surface specific surface areas; high electrical conductivity could be aimed. In the future other elemental

doping like sulfur, bore or oxygen should be performed to see their effect on the structure, the catalytic activity and physical property. A more adequate purification and standardization method of such nanomaterials could be required.

The performance of such nanomaterials as catalyst supports was investigated in the selective hydrogenation reaction of cinnamaldehyde. A parametric study, as well as an in-depth characterization of the catalyst, focusing on the effect of a heat treatment on the performance of the 2:2 w/w % Pt-Ru nanoparticles supported on MWCNTs were performed. The use of various techniques like HREM, EDX, EXAFS and WAXS enabled us to propose an explanation for the increase in activity and selectivity. Indeed, the high temperature treatment permits to eliminate carboxylic surface groups, which should affect surface diffusion of cinnamaldehyde, and induce a lower catalytic activity. Additionally, the high temperature activation induces a reconstruction of the PtRu nanoparticles, these latter becoming ruthenium rich and more selective towards the hydrogenation of the carbonyl group. In the future, the same work should be performed on CNFs, N-CNFs or N-MWCNTs to see if the results would vary according to the type of the carbonaceous support. After annealing, the 2:2 w/w % Pt-Ru bimetallic catalysts supported on MWCNTs gave better performances than classical supports like alumina and silica in term of selectivity and activity.

Finally the carbonaceous nanomaterials were also tested as electrocatalytic supports for polyelectrolyte membrane fuel cells application. This work was performed in collaboration with the ICCOM-CNR Laboratory in Italy. Only Pd/MWCNTs revealed very encouraging results. In the future, further treatments like high temperature annealing, nanoparticles supporting without surface carboxylic group generation (known to decrease electrical conductivity) should increase their electrochemical performances. Nitrogen doped carbon nanostructures were found particularly promising for the ORR reaction. Work is under process to replace Pd/N-CNF catalysts with Fe-Co/N-CNF ones, to enable one direct 4 e pathway of oxygen reduction. It is

also reported that a heat treatment of the Fe-Co/N-Carbon catalyst resulted in activity enhancement as well as a mechanism change from a two-electron dominant to a four-electron dominant reduction process, when compared to that of the unpyrolyzed catalyst [1]. This performance behavior was linked to the change of the nitrogen type. This heat treatment effect should be tested in the future.

In conclusion, this work has highlighted the high flexibility of carbon nanostructure in terms of structure, properties and chemical composition, and revealed their potential as support in catalysis, particularly for hydrogenation reaction and for electrocatalysis. Among others, parameters such as the orientation of the graphenes and the surface chemistry of the support should be carefully mastered to produce well-defined and highly effective catalysts.

1) K. Lee, L. Zhang, H. Lui, R. Hui, Z. Shi, J. Zhang, Electrochimica Acta 54 (2009) 4704

Résumé

Dans ce travail, nous décrivons la méthode de synthèse, la structure, les propriétés et quelques applications en catalyse de différentes formes du carbone, en particulier les nanostructures carbonées (Chapitre I). La technique de dépôt chimique en phase vapeur en réacteur à lit fluidisé a été utilisée pour le dépôt de métaux ou d'oxydes de métaux sur des supports comme l'alumine ou la silice. Le matériau résultant est utilisé comme catalyseur pour la synthèse de diverses nanostructures carbonés par dépôt chimique en phase vapeur catalytique : nanotubes de carbone mono- et multi-feuillets (SWCNTs, MWCNTs), nanofibres de carbone (CNFs), et des nanotubes de carbone (N-MWCNTs) ou nanofibres (N-CNFs) dopés en azote (Chapitre II). Après dissolution du catalyseur par un traitement à l'acide sulfurique ou par la soude, suivit dans le cas des MWCNTs et CNFs, par un traitement à l'acide nitrique pour générer des fonctions carboxyliques de surface, les nanostructures carbonées ont été utilisées comme supports de catalyseurs. L'hydrogénation du cinnamaldehyde a été choisit comme réaction modèle pour comparer les performances de différents catalyseurs bimétalliques de Pt-Ru en fonction de la nature du support. Une étude paramétrique détaillée ainsi que l'étude de l'effet d'un traitement thermique sur l'amélioration des performances du catalyseur de Pt-Ru/MWCNT sont présentés. Une explication de l'augmentation des performances catalytiques sera proposée après analyses du catalyseur par HREM, EDX, EXAFS et WAXS (Chapitre III). Les nanostructures carbonées préparées seront également testées comme supports conducteurs d'électrocatalyseurs pour l'élaboration d'électrodes de ''polyelectrolyte membrane fuel cells'' (PEMFC).

Mots clés

Dépôt chimique en phase vapeur, nanoparticules, catalyse, nanotubes de carbone mono-multi-feuillets, nanofibres, hydrogénation sélective, cinnamaldehyde, pile à combustible.

ChI-Nanostructures carbonées pour la catalyse

En 1959 Richard Feynman déclara: ‘’There's Plenty of Room at the Bottom [1]! L’avancement des recherches technologiques depuis 1959 ont rendu la manipulation de la matière à l’échelle atomique possible. Le domaine de la Nanotechnology est né. Une nanostructure est quelque chose ou une structure atomique qui a une dimension physique inférieure à 100 nanomètres, allant de clusters d’atomes ou molécules (1 nm) à la dimension de couches.

I-1-Différentes structures de carbone

Le carbone est l’un des éléments les plus abondants de la nature. Il forme différent allotropes, selon son hybridation spécifique, et ses liaisons avec les atomes voisins. Le carbone à hybridation sp^3 forme une maille tétraédrique, donnant du diamant. Le carbone à hybridation sp^2 va former ou bien du graphite (arrangé en feuillet hexagonaux), buckminsterfullerene (60 atomes de carbone formant une sphère), ou des nanotubes de carbone selon les conditions de leurs formations.

Certains allotropes de carbone, comme le graphite et le diamant, sont formé naturellement et sont connues depuis longtemps; d’autres comme les fullerènes et les nanotubes, ont été découvert récemment [2]. L’abondance du carbone et sa versatilité fait qu’il soit le plus étudié en nanotechnologie. Le carbone amorphe et le graphite sont les deux allotropes les plus connues, et font la majorité du carbone naturel.

Dans le paragraphe suivant nous décrivons chacun de ces allotropes de carbone ainsi que leurs propriétés essentielles.

I-1-1- Carbone amorphous

Le carbone amorphe ne présente pas de structure cristalline particulière (Fig. 1). Cette forme de carbone est très distordue et manque d’intégrité. Le désordre lui permet d’avoir plusieurs liaisons disponibles. Le carbone amorphe se forme sur les bords ou dans les résidus d’autres composés élémentaires.

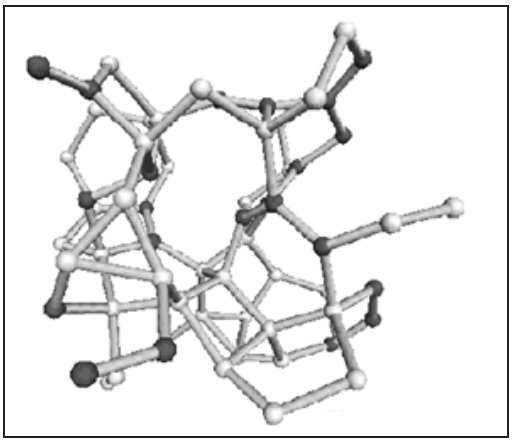

Figure 1: Coke (carbone désordonné)

I-1-2-Le Graphite

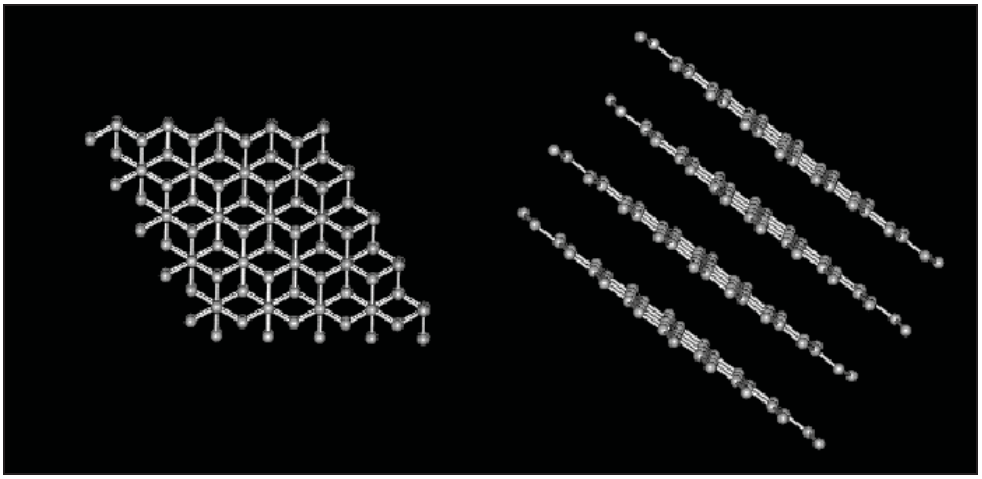

Figure 2: Structure du graphite

En 1924, J. D. Bernal a identifié la structure cristalline du graphite: atomes de carbone arrangés en couches (Fig. 2), chaque atome a une liaison forte avec son voisin dans la même couche, la maintenant ensemble, mais les couches ne sont pas liés fortement, et peuvent facilement être détachés l'une de l'autre [3].Le graphite présente une hybridation sp^2. La longueur de la liaison C–C sp^2 est de 0.142 nm et l'espace entre les couches de carbone est de 0.335 nm.

Le graphite est un matériau très résistant à la chaleur, utilisé dans des environnements atroces.

La graphitisation est le processus que la coke, ou d'autres structures carbonées irrégulières subissent pour devenir plus ordonnées en graphite. Ceci pourrait être fait par des traitements thermiques et de pression [5].

I-1-3-Le diamant

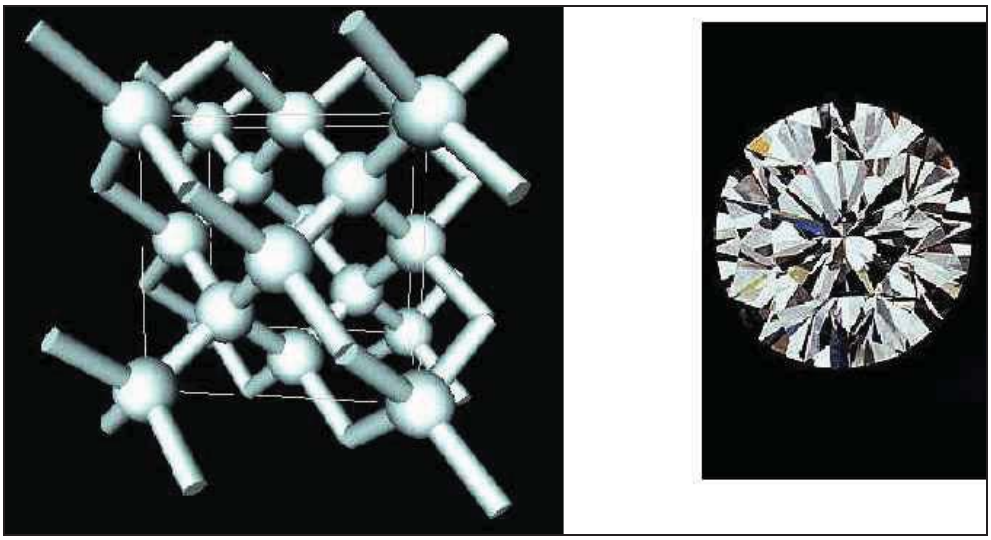

Figure 3: Cristallographie du diamant

Le diamant est un autre allotrope naturel du carbone [6]. Sa structure est triangulairement dense, ce qui lui donne la propriété d'être la substance la plus dure de toutes les substances naturelles [7]. Dans son état naturelle, le diamant possède une structure dérivé de la structure cubique face centré (fcc), nommé type diamant où en plus des atomes aux sommets, et au centre de chaque facette, quatre des huit sites tétraédriques sont occupés, ce qui donne finalement huit atomes par maille élémentaire (4 dans le cas de structure fcc classique), et fait que chaque atome soit entouré par quatre voisins (Fig. 3). Le diamant a été synthétisé avec succès depuis 1955 par dépôt chimique en phase vapeur [8].

I-1-4-Le charbon actif

Le charbon actif est une forme différente du graphite par sa structure imparfaite, aléatoire et très poreuse. La structure graphitique donne à cette forme sa haute surface spécifique supérieure à 1000 m^2/g: 3 g de charbon actif développe la surface d'un terrain de football. Ceci donne au charbon actif la propriété physique d'adsorption la plus forte de tous les matériaux connus par les Hommes.

I-1-5-Buckminsterfullerene ou C60

En 1985 trois chercheurs R. Smalley, R. Curl (Université de Rice, Houston, USA) et H. Kroto (Université de Sussex, UK) découvrirent une forme nouvelle de carbone: Buckminsterfullerene ou C60 [10-11]. Le nom est attribué pour honorifier Richard

Buckminster Fuller, qui a popularisé le dôme géodésique. C'est une molécule avec 60 atomes de carbone distribués aux sommets d'un polyèdre régulier constitué de facettes hexagonales et pentagonaux (Fig. 4). Ensuite, d'autres types de fullerènes ont été découverts: C70, C80, et autres.

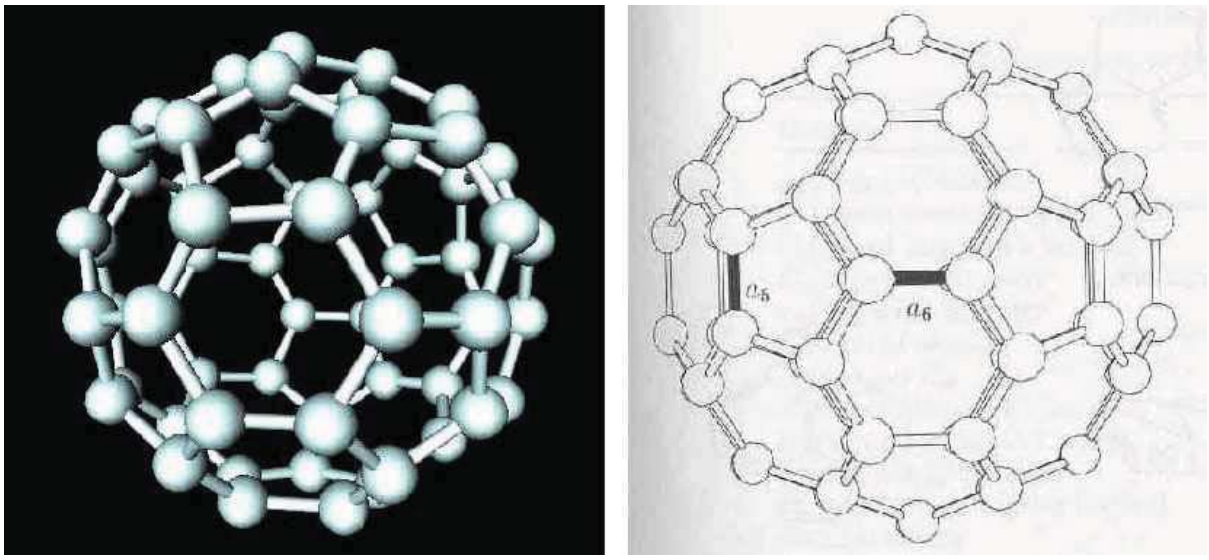

Figure 4: Structure du fullerène

I-1-6- Onions de graphite

Sumio Iijima est le premier à prouver l'existence de multi-cages de carbone, maintenant connu sous le nom d'onions de graphite, observés par HREM [12]. Après huit années, H. Kroto et K. McKay ont proposes aussi, pour la première fois, le modèle d'onions de graphite formé de icosaèdre superposés de fullerène. (C60, C240, C540, C960, …) Aujourd'hui, les onions de graphite sont produites par différentes méthodes et conditions [14-15] et leurs applications principales sont des nanocapsule pour la délivrance de médicaments ou la fabrication d'engins électroniques.

I-1-7-Carbon nanofibres

Les nanofibres consiste de feuillets de graphite arranges parfaitement dans différentes orientations par rapport à l'axe de la fibre, donnant différentes conformations. Dans ce travail, on va se focalisé sur trois types de CNF : CNF rubans (CNF-R) où les couches de graphène sont parallèles à l'axe de croissance, les CNP en palettes (CNF-P) présentant des couches de graphène perpendiculaires à l'axe de la fibre, et finalement les nanofibres en arrêtes de poisson, présentant des couches oblique par rapport à l'axe de croissance [16] (Fig. 5). Le

diamètre des CNF est généralement large et pourrait atteindre facilement 500 nm. La production de fibres de graphite date depuis longtemps, et les recherches avaient pour but d'inhiber leurs croissances dans des procédés commerciaux comme le reformage à la vapeur [18].

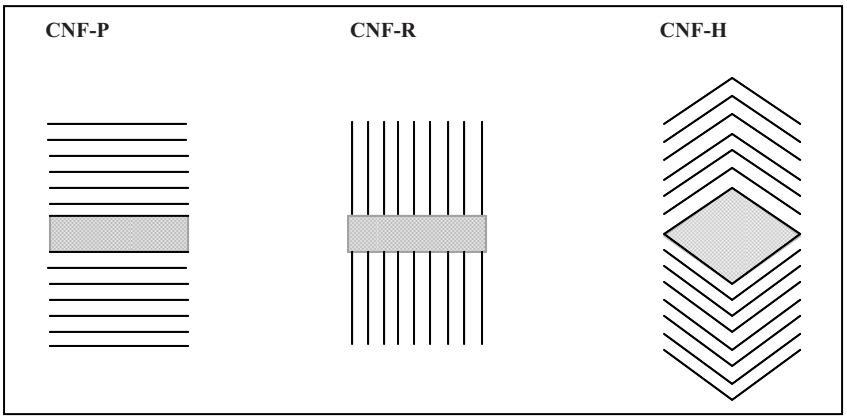

Figure 5: Différents types de nanofibres de carbone

I-1-8- Nanotubes de carbone (CNT)

Les nanotubes de carbone peuvent être considérés comme des fullerènes étirés. Un des premières preuves que les nanofilaments produites auraient pu être des nanotubes, présentant une cavité interne, peut être trouvé dans les micrographes de microscopie électronique à transmission publiés par Hillert et Lange en 1958 [19]. Les premier micrographes de hautes résolution de MET de CNT on été publiés par Sumio Iijima [20-21].

La différence majeure entre CNT et CNF consiste en l'absence de la cavité vide dans ce dernier. Les nanotubes de carbone peuvent être divisés en deux catégories: mono-feuillets (SWCNT) et multi-feuillets (MWCNT).

Idéalement, les nanotubes de carbone mono-feuillet sont faits d'un feuillet de graphène parfait, i.e. une couche monoatomique polyaromatique faite d'atomes de carbone à hybridation sp^2 et à structure hexagonale, comparable à celle d'un graphite original, qui est enroulé à un cylindre et fermé par deux semi-fullerènes (Fig. 6). La façon dont le feuillet de graphène est enroulé est représenté par le vecteur d'élicite (C_h) qui est modulé par une paire d'indices n et m. Les intégrateurs n et m représentent le nombre d'unités de vecteurs selon deux directions de la maille cristalline du graphène. Si m=0, les nanotubes sont nommés zigzag. Si n=m, les nanotubes sont nommés armchair. Dans d'autres cas, ils sont nommés

chiral (Fig. 6). Le diamètre des SWCNT peut varier entre 0.4 et 2.5 nm et leur longueur de quelques microns à plusieurs millimètres. Dû à la très haute énergie de surface de ces macromolécules monodimensionnelles, les SWCNTs sont arrangés en faisceaux.

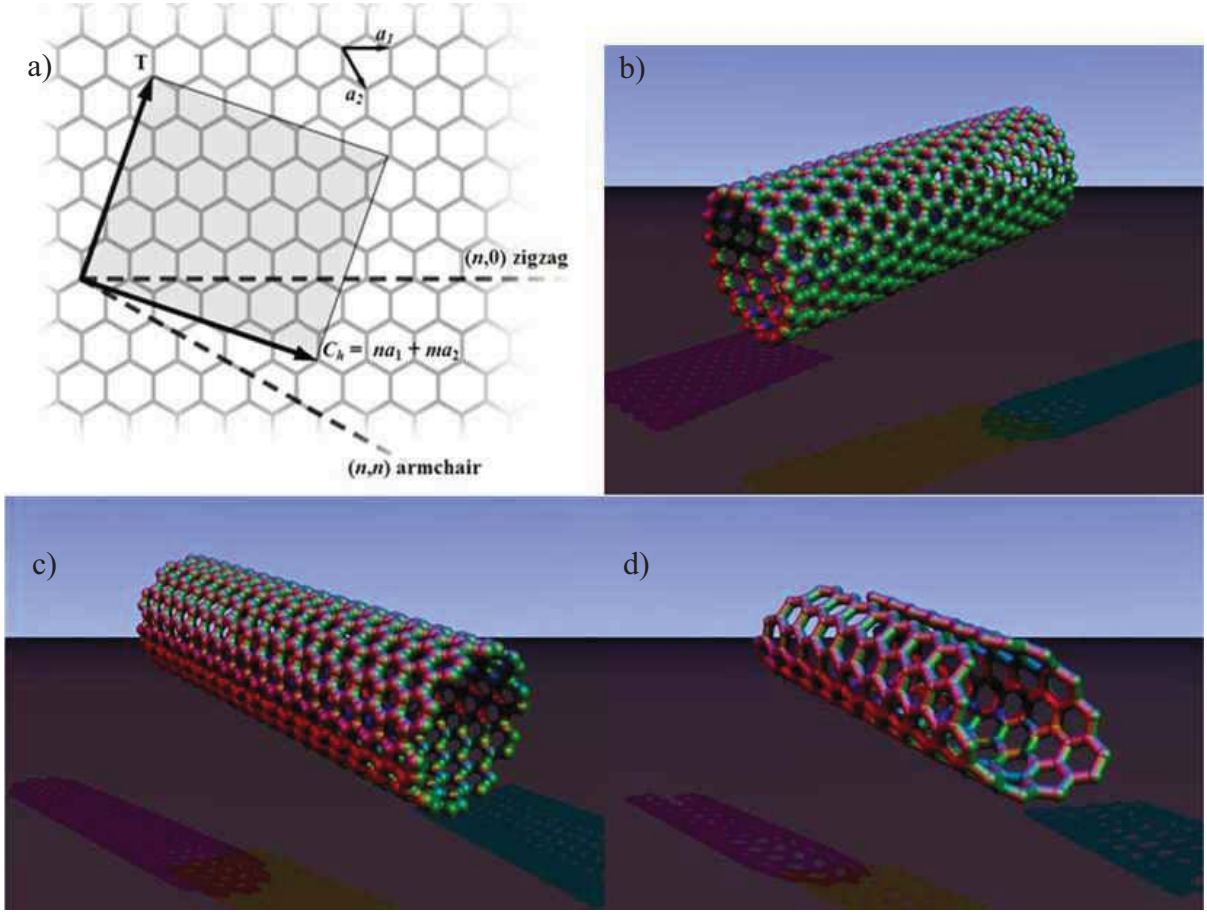

Figure 6: (a) Structure schématique honeycomb d'une feuille de graphène. Nanotubes de carbone mono-feuillet peuvent se former en enroulant la feuille selon le vecteur de maille. Les deux vecteurs de base a_1 et a_2 sont présentés. Enroulement des vecteurs (n, 0), (n,n) and (n,m) vecteurs engendre des tubes (b) zigzag (c) armchair, et (d) chiral, respectivement.

Les MWCNT peuvent être considérés comme des SWCNT concentriques, avec une incrémentation du diamètre et une disposition coaxiale. Le nombre de parois peut varier de deux (DWCNT) à quelques dizaines, alors le diamètre extérieur peut atteindre 100 nm. Les parois concentriques sont éspacés réguliairement de 0.34 nm. Des particules métalliques résiduelles venant du procédé de leurs productions peuvent être trouvées dans la cavité interne des MWCNT. Il est aussi important de noter que la plupart des MWCNT obtenu par CVD, la cavité interne est rarement accessible dû à des compartiments à structure bamboo avec des couches de graphène perpendiculaires aux parois du tube.

Les nanotubes de carbone sont l'un des plus domaines actives de la nanoscience à cause de leurs structures exceptionnel et leurs propriétés électroniques, thermiques, d'adsorption et mécaniques, ce qui les rend intéressants pour plusieurs applications : renforcent de polymères, stockage d'énergie, l'électronique et la catalyse. Cette dernière sera le sujet de notre étude.

ChII-Synthèse de nanostructures carbonées par C-CVD

II-1-Synthèse de SWCNT sur des catalyseur de Fe2O3/Al2O3

Des catalyseurs de 2 et 4 w/w % de Fe/Al_2O_3 ont été préparés par MO-CVD à partir du fer pentacarbonyle en présence d'une pression partiel faible en oxygène et en eau. Le réacteur MO-CVD est présenté dans la figure 7.

Figure 7: Procédé FB-CVD pour l'élaboration de catalyseurs

Les catalyseurs MO-CVD ont été testés sous différentes conditions de mélanges gazeux de CH4, H2 et Ar dans un réacteur à lit fixe. Le réacteur est présenté dans la figure 8.

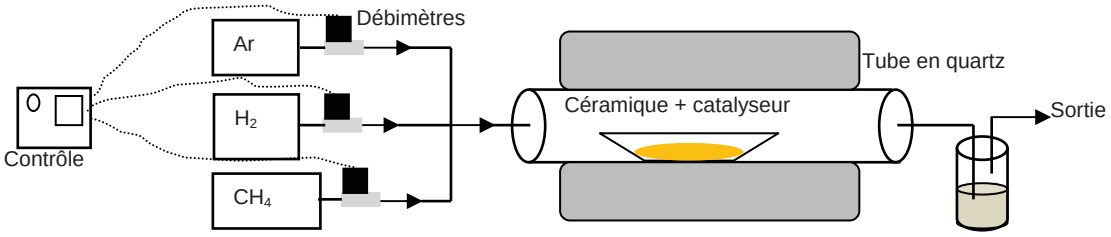

Figure 8: Procédé à lit fixe pour la synthèse de SWCNTs

Test	CH_4 sccm	Ar sccm	H_2 sccm	I_G/I_D	RBM
1	100	200	0	0.76	*
2	100	190	10	0.86	**
3	100	180	20	0.86	**
4	100	150	50	0.90	None
5	100	100	100	0.86	None
6	200	0	100	0.76	None
7	200	100	0	1.08	***

T_d=900°C; $t_{déposition}$=30min; *un peu **moyen ***beaucoup

Table 1: Différentes conditions pour la synthèse de SWCNTs

L'identification des structures carbonées à été effectué par spectroscopie RAMAN et microscopie électronique.

Dans les micrographes MET de tout les échantillons on observe différent types de structures carbonées, i.e, fibres denses, nanoparticules encapsulé et nanotubes de carbone monoparois (Fig. 9).

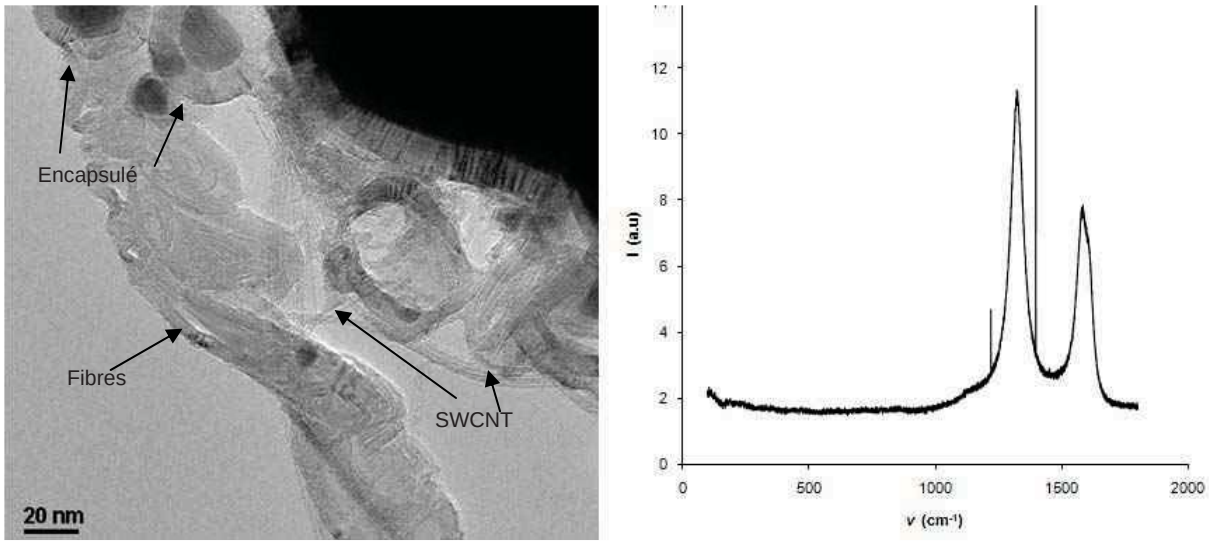

Figure 9: micrographe MET (gauche) et spectroscopie Raman (droite) de l'échantillon 7

Ceci est en accord avec la spectroscopie RAMAN où l'on observe un I_G/I_D inférieur à 1 et une absence de RBMs.

On augmente le chargement métallique à 4 % et on active le catalyseur pendant 10 heures à 900 °C et on le soumet à la condition de 200 sccm de méthane et 100 sccm d'argon. Le résultat est présenté dans la figure 10.

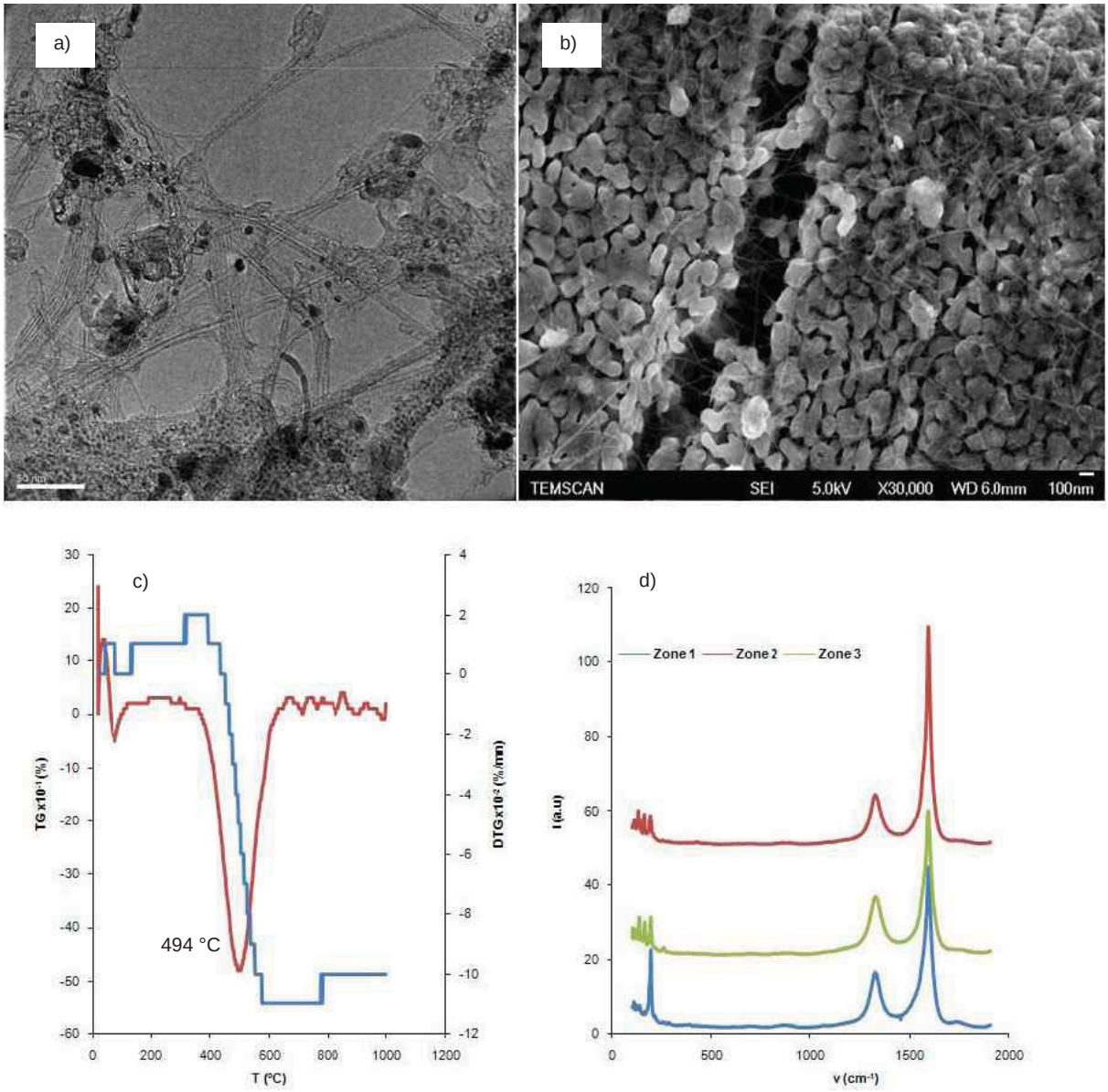

Figure 10 : a) METmicrographes, b) MEB micrographes, c) ATG, d) Spectroscopie Raman de l'échantillon après activation.

La sélectivité à augmenté nettement. On a un rapport de piques RAMAN I_G/I_D de l'ordre de 2,7. De nombreux piques RBMs apparaissent aussi entre 100 et 300 cm^{-1}. Par ATG on observe une température d'oxydation de 494 °C pouvant être attribué à des SWCNTs.

La sélectivité à été vérifié par observations de microscopie électronique à transmission, où l'on observe une majorité de nanotubes de carbone monoparois, quelques particules encapsulés et des structures mal définis.

Pour expliquer la variation de la sélectivité des catalyseurs avant et après activation, ces derniers ont été étudié par spectroscopie Mössbauer, analyses de réductions à température contrôlé, analyses élémentaires, mesures de surfaces spécifique par la méthode BET, et finalement par diffraction des rayons X.

Après le dépôt chimique en phase vapeur, on trouve deux phases de fer sur alumine. Une première phase est constituée d'une monocouche de solution solide d'ions de fer (III) dans les défauts de structure de l'alumine et une seconde phase de nanoparticules d'hématite de diamètres inférieur à 10 nm superposés la dessus.

L'activation thermique à 900 °C pendant 10 h engendre la redistribution des atomes de fer de l'hématite dans la matrice de l'alumine sous forme de solution solide. C'est ainsi que l'on passe de deux espèces de fer présentent à la surface de l'alumine, et présentant différentes réactivités envers le mélange réactif à une espèce, ce qui augmente la sélectivité.

II-2-Synthèse de MWCNT sur des catalyseur de Fe2O3/Al2O3

Le même catalyseur de 4 w/w % de Fe2O3/Al2O3 utilisé pour la synthèse de SWCNT à été utilisé pour la synthèse de MWCNT, sous un mélange de 200 sccm d'éthylène, 120 sccm d'hydrogène et 160 sccm d'argon. L'activité catalytique du catalyseur sous nos conditions à été de 14 h^{-1}. Le diamètre moyen de ces MWCNT est de 6,5 nm.

II-3-Synthèse de CNF sur des catalyseurs de Ni/Al2O3

Un catalyseur de 5 % de Ni/Al2O3 à été préparé par OM-CVD à partir de Nickélocène. Après avoir subit une activation thermique à 700 °C pendant 3h, le catalyseur à été testé sous les conditions de 100 sccm d'éthylène, 120 sccm d'hydrogène et 160 sccm d'azote à 700 °C.

L'activité catalytique à été de 7,1 h^{-1} et le diamètre moyen de 7,8 nm. On obtient sélectivement de nanofibres de carbones du type arrêtes de poisson.

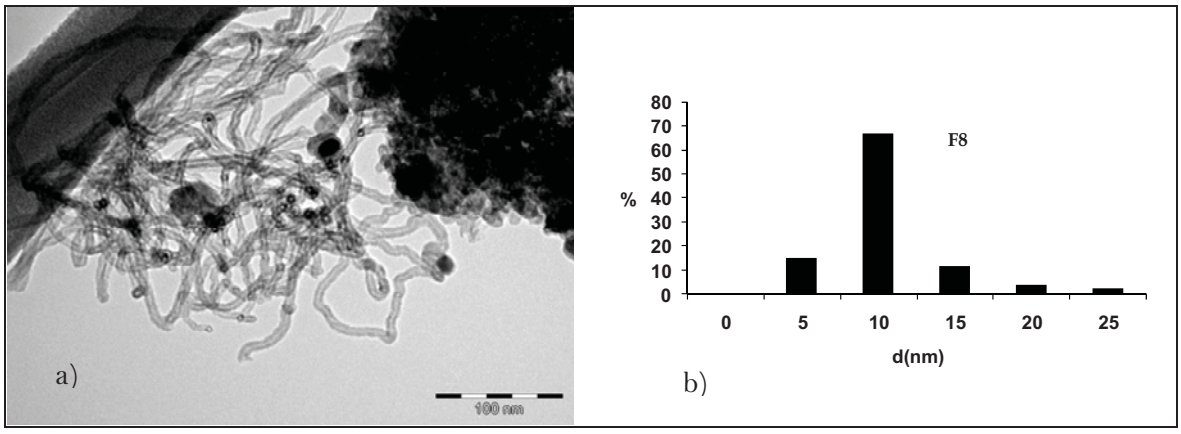

Figure 11 : Micrographe TEM et distribution de diamètre des nanofibres

II-3-Synthèse de N-CNF sur des catalyseurs de Fe/Al2O3

Un catalyseur de Fe/Al2O3 à été préparé par OMCVD et sous 120 sccm d'hydrogène et 160 sccm d'azote envoyés dans un bulleur d'acétonitrile aboutissent à la formation de nanofibres de carbone types arrêtes de poisson dopés en azoté. Le dopage en azote à été vérifié par XPS et analyses élémentaires, 3,8 et 6,4 respectivement.

Différents types d'insertion de l'azote peuvent exister. On distingue le type pyridinique, pyrrollique, N-oxyde et le type quaternaire. Dans le cas de nos échantillon, les types pyridiniques et quaternaires sont dominants.

II-4-Synthèse de N-MWCNT sur des catalyseurs de Co/SiO2

Pour la synthèse de nanotubes de carbone dopés en azote un catalyseur de Cobalt supporté sur un support de silice à été élaboré par imprégnation liquide. Après activation à 350 °C sous air pendant 3 heures et sous 120 sccm d'hydrogène et 160 sccm d'azote envoyés dans un bulleur d'acétonitrile, et avec une température de colonne de déposition de 700 °C, des nanotubes de carbone dopés en azote se forment. Le dopage en azote à été vérifié par XPS et analyses élémentaires de 0,6 et 1,3 respectivement.

II-5-Purification des supports carbonés :

Support	ATG		Analyse élementaire		ICP-MS		MET	Surface Spécifique (BET)			Raman
	T_{ox} (°C)	%	C	N	% M	% S	d (nm)	BET (m^2/g)	Vp cm^3/g	dp (average)	I_G/I_D

										(nm)	
MWCNT	582	95	95	0	0.94	0.02	6.5	180	2.05	46	0.77
MWCNT-COOH	655	98	94	0.08	0.44	0.02		214	2.16	54	0.56
N-MWCNT	486	97	95	1.6	2.23	<0.3	24	119	0.56	18.7	0.83
CNF	609	92	91	0.02	4.56	0.05	7.8	437	0.70	6.44	0.97
CNF -COOH	637	93	87	0.6	3.42	0.47		560	0.78	5.6	0.84
N-CNF	502	88	81	6.4	5.43	0.46	14.6	204	0.74	14.5	0.86

Table 2 : Caractéristiques des différents supports carbonées après purification

Les divers catalyseurs sont séparés du support carboné par traitements à l'acide sulfurique à 140 °C pendant 2h ou à la soude caustique à 70°C pendant 2 h. Ensuite les nanostructures purifiés sont récupérés par filtration et lavé jusqu'à pH neutre. A l'exception des supports carbonés dopés en azote, un traitement à l'acide nitrique à 120 °C pendant 8 h pour les MWCNT et à froid pour les CNF est ajouté pour créer des groupements acides de surface, principalement de type carboxyliques. Ceux-ci seront responsables de la bonne dispersion des nanoparticules sur la surface des nanostructures carbonées. Dans le cas des nanostructures dopés en azote, c'est ce dernier qui jouera ce rôle. Les différent supports obtenues on été caractérisés par ATG, analyses élémentaires, chromatographie ionique couplé à la spectroscopie de masse (ICP-MS), microscopie électronique à transmission, spectroscopie RAMAN, et mesures de surface spécifiques (BET). Les différentes caractéristiques sont regroupées dans le tableau 2.

On trouve que les différents supports présentent une pureté entre 88 et 97 % permettant leurs utilisations en tant que supports en catalyse. Leurs surfaces spécifiques est variables de 119 à 560 m^2/g.

ChIII-Hydrogénation sélective du cinnamaldehyde en cinnamylalcool

III-1-Effet du support sur la performance catalytique :

Support	Pt (%)	Ru (%)	Catalyst residue					
			Metal	Support	$d_{average}$	BET	Vpores	dpore

			(%)		(nm)	(m^2 / g)	(cm^3/g)	(nm)
MWCNTs	1.84	2.12	0.13 Fe	<100 ppm Al	2.70	224	1.6	29
CNFs	0.54	0.58	3.42 Ni	0.47 % Al	2.40	437	0.7	6
N-MWCNTs	0.11	0.50	2.23 Co	<0.30 % Si	1.60	119	0.6	19
N-CNFs	1.32	2.04	5.51 Fe	0.49 % Al	0.52	175	0.6	15
SWCNTs	0.41	1.73			1.21	72	0.4	24
AC	0.43	0.50			4.94	27	0.1	22
Alumina	1.94	2.04			2.70	147	0.2	6
Silica	1.46	1.68			6.16	245	1.7	28
MgO	0.41	0.17			5.15	0.07	$3x10^{-3}$	205
ZnO	1.92	1.92			2.90	14	0.1	35

Table 3: Caractéristiques des catalyseurs préparés en fonction de la nature du support

Différents catalyseurs bimétalliques de 2-2 w/w% Pt-Ru supportés sur différents supports carbonés et oxydes métalliques ont été préparés. Leurs caractéristiques sont présentées dans le tableau 3.

Ces catalyseurs ont été testés dans l'hydrogénation sélective du cinnamaldéhyde en cinnamylalcool (Fig. 12). Les catalyseurs supportés sur du carbone se sont avérés les plus actifs. Ceci pourra être lié à leur mésoporosité, leurs structures dynamique et ouverte qui empêche les limitations de transfère de masse et le blocage des pores rencontré dans le cas des supports classiques. Les nanostructures carbonées assurent une meilleure dispersion de la phase active, donc des nanoparticules plus petites sont créées. Les petites nanoparticules sont plus actives que les grosses.

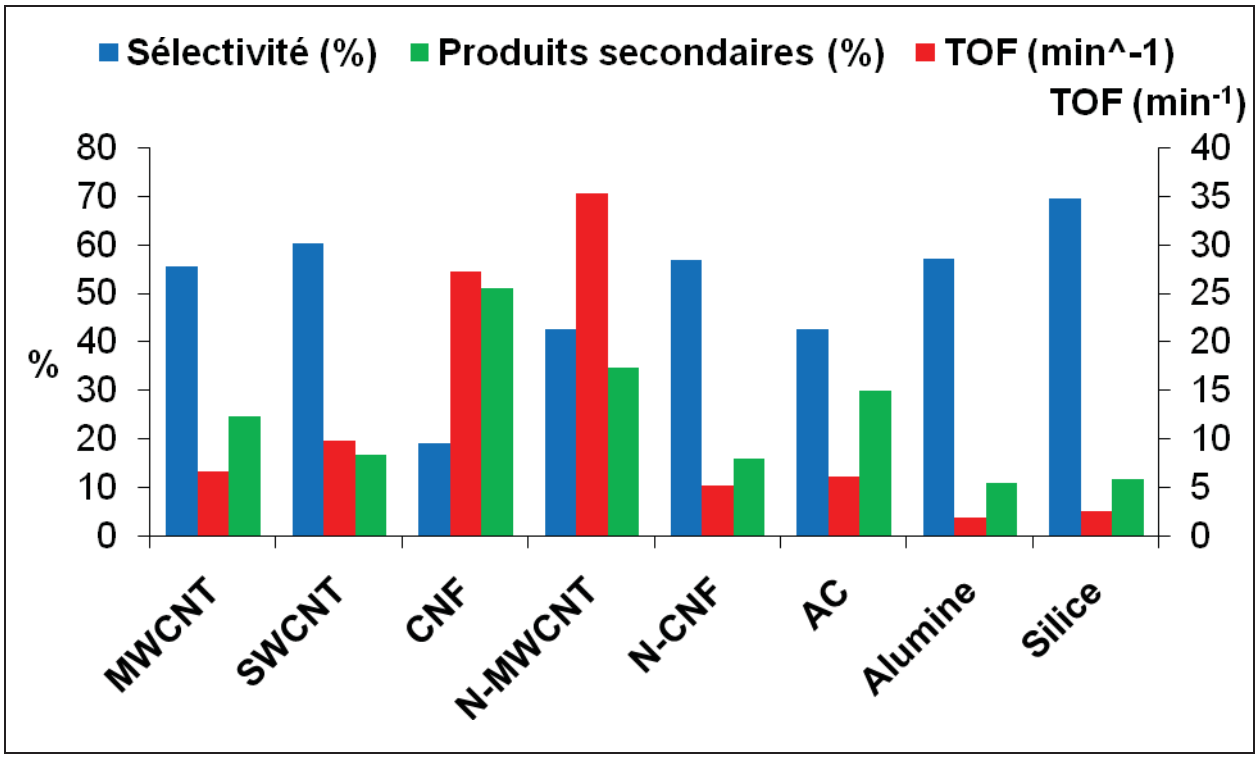

Figure 12 : Variation de la sélectivité et de l'activité en fonction d la nature du support

Au niveau de la sélectivité, la silice c'est avéré la plus sélective. La sélectivité à été aussi attribué à l'effet de variation de la taille des nanoparticules. Selon les travaux théoriques de P. Sautet une molécule de cinnamaldéhyde ne pourra pas se rapprocher via son cycle aromatique d'une surface plane de moins de 0,3 nm due à des répulsions stériques. De se fait la molécule est orienté d'une façon à favoriser la fonction carbonyle. Plus la nanoparticule est grosse plus sa surface devient plane par rapport à la dimension de la molécule de cinnamaldehyde (Fig. 13)

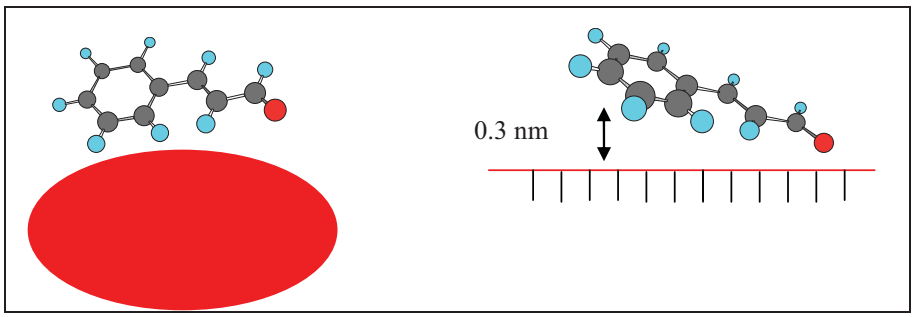

Figure 13 : Adsorption de CAL en fonction de la taille de la nanoparticule

En plus de la variation des diamètres des nanoparticules, les propriétés électronique de transfère d'électrons et d'enrichissement de la nanoparticule qui repousse la liaison C=C et favorise la liaison C=O et l'orientation des plans de graphène qui affaiblie ou augmente la

force d'adsorption du cinnamaldehyde sur le support et donc favorise ou non la sélectivité envers le cinnamylalcool (Fig. 14).

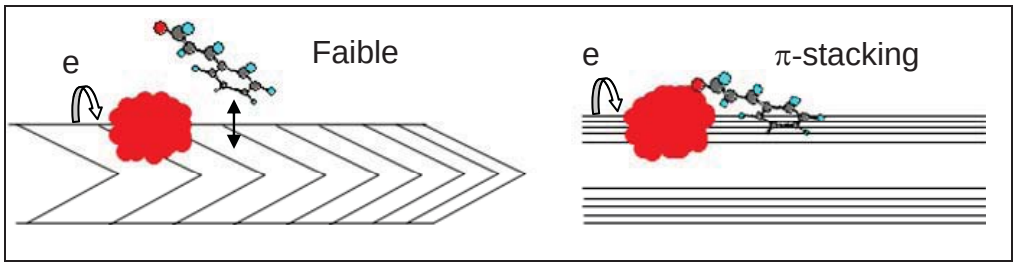

Figure 14 : Rôle du transfère électronique et de l'orientation des plans de graphène dans la sélectivité

La variation de la sélectivité en fonction de la taille des nanoparticules a été vérifié en tracent la variation de la sélectivité en cinnamylalcool en fonction du diamètre des nanoparticules mesuré par microscopie électronique à transmission. On trouve une bonne corrélation linéaire entre le diamètre des nanoparticules et la sélectivité (Fig. 15). Cependant, les nanofibres de carbones et le charbon actif constituent des exceptions. Ceci pourrait être lié à leurs hautes surfaces spécifiques ou leurs microporosités.

La différence de l'interaction entre les nanofibres de carbone et les nanoparticules de métaux de platine-ruthénium supportés à été mise en évidence par le faite que ces nanoparticules se sont détachés de la surface des nanofibres par sonication dans l'alcool pendant la préparation de la grille de microscopie électronique. Cette interaction faible pourrait être liée à la faible concentration en groupements carboxyliques de surface, due à un traitement à l'acide nitrique à froid pour éviter la destruction des fibres. Une faible interaction diminue la sélectivité.

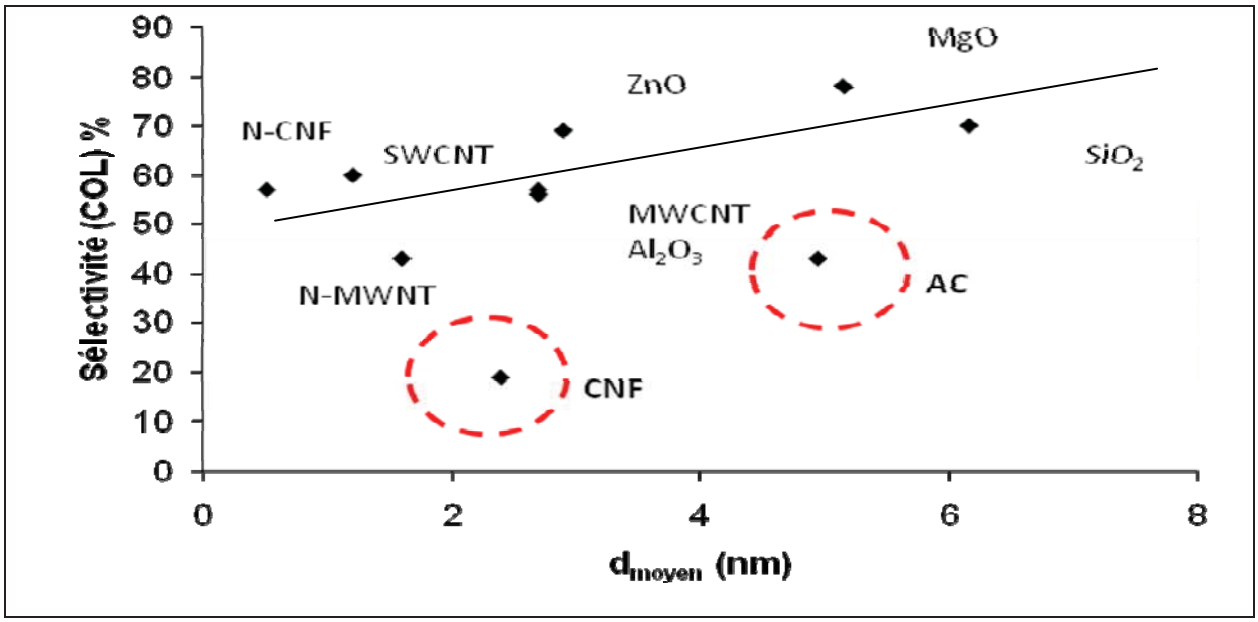

Figure 15 : Variation de la sélectivité en fonction de la taille de la nanoparticule

III-2-Effet de l'activation thermique

Pour la suite de l'étude nous avons choisit de travailler avec le catalyseur de PtRu/MWCNT. Dans la littérature, il a été démontré que la chauffe d'un catalyseur supporté sur un support carboné sous azote pourra augmenter sa sélectivité. C'est dans cette optique que notre catalyseur à été chauffé sous azote à 350, 700, 850 et 1000 °C et la performance catalytique étudié. On observe une augmentation de l'activité catalytique de 350 à 700 °C suivit d'une chute à 850 et 1000°C due à la perte des fonctions de surface et le frittage qui augmente la taille des nanoparticules.

En ce qui concerne la sélectivité, cette dernière augmente linéairement en fonction de la température d'activation et atteint 90 % pour le catalyseur activé à 1000°C.

Pour expliquer l'augmentation de la sélectivité en fonction de la température d'activation nous avons mené une étude paramétrique, et des études de spectroscopie WAXS, EXAFS, EDX et microscopie électronique à haute résolution, ainsi que des calculs théoriques par DFT.

Les résultats de l'étude paramétrique prouvent que le modèle cinétique pour l'hydrogénation du cinnamaldehyde en cinnamylalcool est le modèle Langmuir – Hinshelwood, et que l'adsorption du cinnamaldehyde était en compétition avec celle de

l'hydrogène. En faisant varier la température de catalyse, et en appliquant la loi d'Arrhenius nous trouvons une énergie d'activationn de 25 kj/mol.

Les méthodes spectroscopiques nous montrent que les nanoparticules doublent de diamètre par frittage à partir de 850 °C et que ce phénomène est responsable de l'augmentation de la sélectivité. Tandis que de 350 à 700 °C on a une modification de la structure de la nanoparticule. Cette dernière s'enrichie en ruthénium et passe du caractère fcc dominant au caractère hcp. L'enrichissement en ruthénium augmente la sélectivité par le biais d'un effet électropositive, en enrichissant le platine en électron qui repoussent la liaison C=C, ou par un effet électrophile, en pompant une paire d'électron de l'oxygène de la fonction carbonyle du cinnamaldéhyde et ainsi l'active.

ChIV- Electrocatalyseurs pour des électrodes de piles à combustible à membrane de polyélectrolyte

Notre travail consiste à l'élaboration d'électrocatalyseurs pour constituer des électrodes en DAFC. Nous somme intéressés par l'oxydation des alcools, notamment le méthanol, éthanol et glycérol. Les catalyseurs au platine peuvent opérer en milieu basique ou acide mais présente l'inconvénient d'être sensibles à l'empoisonnement par le CO, et aussi d'être très cher. Le Pd est moins cher et plus résistant à l'empoisonnement, mais ne fonctionne qu'en milieu alcalin. Mais ceci constitue un avantage puisque le CO2 sera transformé en carbonate, un fertilisant qui pourra être utilisé pour régénérer du bio-fuel.

IV-I- Etudes en demi-cellules

Tout d'abord les catalyseurs on été étudié en demi-cellules. Les résultats sont rassemblés dans le tableau 4.

Substrate	**Jp (mA.cm^{-2})**	**Sa$_p$(mA.µg.Pd^{-1})**	**V$_p$^{b} (V)**	**V$_{onset}$ (V)**	**Tafel slope (mV dec^{-1})**
Méthanol	19.4	1.1	-0.15	-0.55	282 (α 0.21)
Ethanol	35.1	2.1	-0.12	-0.75	249 (α 0.24)
Glycerol	53.7	2.8	-0.08	-0.60	-

Table 4 : Différents paramètres électrochimiques obtenu en demi-cellule

Seul le catalyseur de Pd supporté sur des nanotubes de carbone présente des résultats intéressant vis-à-vis une application en tant qu'anode de pile à combustible. Une fois encore nous avons prouvé l'importance de la nanostructure carbonée sur sa performance catalytique.

Notre 3% Pd/MWCNT c'est avéré vingt fois plus active que ceux de la littérature pour l'oxydation des alcools en demi-cellule**.** Les MWCNT assurent une meilleure dispersion des nanoparticules de Pd et une meilleure conductivité électrique que le charbon actif.

La pente de Tafel slope et le coefficient de transfère de charges α ont été calculés. Les nanotubes de carbone multiparois présentent des pentes de Tafel élevés par rapport aux charbons actifs (190 mV dec^{-1}). Ces valeurs sont les mêmes pour le méthanol et l'éthanol indiquant que les deux alcools suivent le même mécanisme d'oxydation. La valeur élevée de la pente de Tafel indique que l'étape limitante est celle d'une cinétique électrochimique.

En ce qui concerne le glycérol, son oxydation s'effectue en plusieurs étapes, ce qui explique l'absence de la dépendance linéaire, et l'impossibilité de calcul du Tafel slope.

Finalement on trouve une stabilité de la performance par chronopotentiométrie selon l'ordre croissant suivant : glycérol, méthanol et puis l'éthanol (Figure 16).

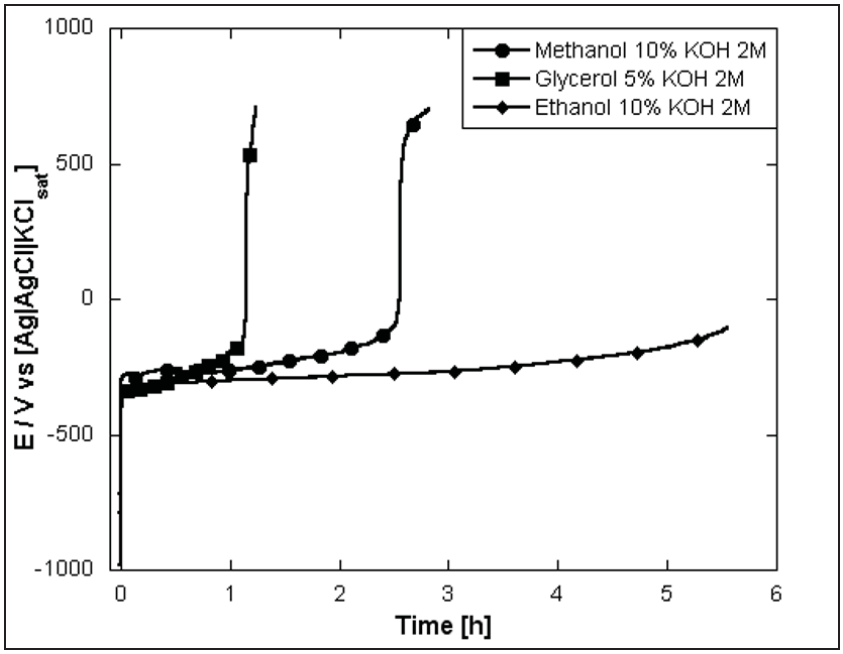

Figure 16 : Chronopotentiométrie du Pd/MWCNT avec différent alcools

On pourrait envisager un empoisonnement par le CO qui génère la surtension dans le cas du méthanol à 2,5 h et le glycérol à 1 h, mais comme par la suite les cellules on pu effectuer plusieurs cycles en DAFC, ceci est donc lié à des problèmes de diffusion de l'alcool à la surface des nanotubes de carbone.

IV-II- Etudes en DAFC

La performance du 3% Pd/MWCNT à été étudié en DAFC avec trois types d'alcools : le méthanol, éthanol et le glycérol. Les résultats sont présentés dans la figure 17.

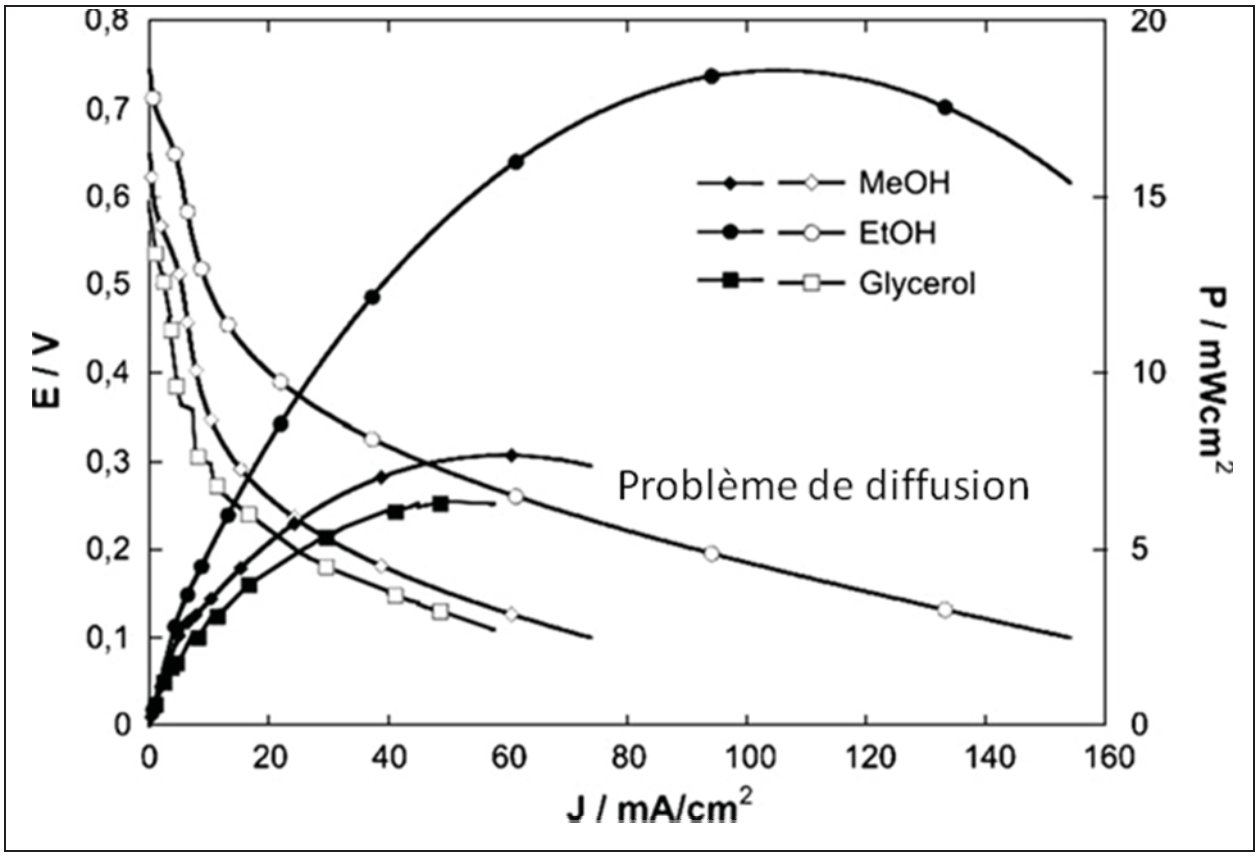

Figure 17 : Performance catalytique de 3% Pd/MWCNT en anode de DAFC

On observe que l'éthanol présente la meilleure performance avec une densité de puissance de 18 mW/cm^2. La cellule à été vidé et remplie à nouveau avec les diverses fuel et ceci pendant 4 cycles. Les résultats ont été les mêmes. Ceci indique que le problème lié au méthanol et au glycérol est un problème de diffusion à la surface des nanotubes de carbone multiparois et non pas lié à un empoisonnement au CO. Les mesures galvanostatiques et avec

l’éthanol comme fuel, montrent que la cellule peut délivrer un courent stable de 102 mA pendant 12 h.

IV-III-Pd/CNF,N-CNF,N-MWCNT

Aucun des CNF, N-CNF, N-MWCNT n’a aboutie à des résultats intéressant en demi-cellule ou en DAFC. Le rôle de la structure du support dans la détermination de la performance électrocatalytique est une fois encore vérifié.